Coupled finite difference and discrete element method for modelling the underground stopes backfilled with the cemented rockfill

by

Chong Wei

A thesis submitted in partial fulfilment of the requirements for the degree of

Doctor of Philosophy

in

Mining Engineering

Department of Civil and Environmental Engineering

University of Alberta

Abstract

Backfill columns and the adjacent rock pillars at the underground backfilled stopes are not isolated but mutually supported. Stress transmission and energy alternation occur between them ceaselessly due to the ubiquitous mechanical interactions at the frictional-bonded interfaces between backfill columns and the surrounding rocks when the backfilled stopes are subjected to the disturbance from the sequential mining activities. Consequently, the stress and displacement redistribution takes place in both backfill columns and the surrounding rocks, potentially influencing the stability of the backfilled stopes and the sequential mining activities at the adjacent underground mining area.

Thus, it is an imperative and fundamental task for engineers and researchers to have further study on the principle of the stress and displacement distribution at the backfilled stopes, both in backfill columns and the surrounding rocks, to make optimized designs in both backfill material and rock pillar, to avoid the potential risks in unwanted catastrophic failure and disasters. The main objective of this research is to develop a hybrid modelling approach with higher computation efficiency and precision to study the regime of the mechanical interaction between the CRF columns and the adjacent mining area by using the coupled FD-DE method. Based on a Canadian underground hard rock mine, at which the cemented rockfill (CRF) material was used to backfill the underground mine-out area, five main aspects were covered in this research to analyze the stress and displacement distribution, both in the CRF columns and the surrounding rocks during the entire mining/backfilling sequence at the backfilled stopes, by incorporating the laboratory tests and numerical simulations.

Firstly, the uniaxial and triaxial compression tests were conducted on the large-scale CRF specimens collected from the hard rock mine to study the heterogeneity in the mechanical properties and stress-strain behaviour of the field CRF material in the backfilled stopes. Secondly, the discrete element (DE) method, a discontinuum modelling approach, was used to simulate the CRF specimens according to a simplified particle size distribution to study the stress-strain behaviour, fracture evolution, and failure patterns of the CRF material during the uniaxial and triaxial compression processes. Thirdly, an advanced hybrid numerical modelling approach, the coupled finite difference (FD) and discrete element (DE) method, was applied to study the shear behaviour, stress and displacement distribution at the interface in the combined rock-cemented rockfill (R-CRF) specimen during the direct shear process. Next, the new Johnson-Kendall-Robert (JKR) contact model was employed by the coupled FD-DE method to study the consistency and flowability of the fresh CRF material during the slump test and dumping process at the single backfilled stope. Finally, the stress and displacement distribution and the stability at the multiple backfilled stopes were numerically analyzed with the coupled FD-DE method by considering the shear behaviour at the interfaces between the CRF columns and the surrounding rocks and the primary/secondary manner of the mining/backfilling activities at the hard rock mine.

Four aspects of the main contribution of this research can be highlighted here based on the results from the laboratory tests and numerical simulations. Firstly, this research has some practical laboratory references for assessing the required strength characteristics of backfill columns in the field by considering the heterogeneity in the mechanical properties of the field backfill material. Secondly, this research supplies an effective determination

process of the microstructural parameters of the contact model at the interfaces in the coupled FD-DE model which is involved with different geo-materials. Thirdly, this research provides some numerical modelling references for evaluating the flowability and consistency of the fresh backfill material in the backfilled stopes by simulating the coupled FD-DE method and the JKR contact model. Finally, this research provides valuable numerical modelling experience for applying the coupled FD-DE method in investigating the mechanical interaction between different geo-materials involved with frictional, cohesive and bonded interfaces.

Preface

This thesis is an original work by Chong Wei. This study was supported by the Natural Sciences and Engineering Research Council of Canada (NSERC) under the Collaborative Research and Development (CRD), the Chinese Scholarship Council (CSC), and the Itasca Education Partnership (IEP) run by the Itasca Consulting Group (ICG). Chapter 5 was based on the paper "Wei, C., Apel, D. and Katsaga, T., 2022. Coupled finite difference and discrete element method for modelling the direct shear tests on the combined rock-cemented rockfill specimens. Mining, Metallurgy & Exploration, 39(1), pp.89-109.". Professor Derek B. Apel led this collaborative research at the University of Alberta and with the guidance of Dr. Tatyana Katsaga at Itasca Consulting Canada.

Dedication

This thesis is dedicated to:

My Dear Parents:

WEI Wensheng (魏文生) & FAN Shumei (范淑梅)

My Dear Grandparents:

WEI Baoshan (魏宝山) & LIU Guorong (刘国荣)

FAN Enyi (范恩义) & ZHANG Qinghua (张庆华)

Acknowledgements

Foremost, I would like to express my sincere gratitude and appreciation to my supervisor Dr. Derek B. Apel, for his continuous support, patient guidance, and tremendous encouragement for my PhD study and research at the University of Alberta. It is a great honour to have him as my supervisor and one of my best friends in my life.

Besides my supervisor, I would like to greatly thank Dr. Wei Victor Liu, Dr. Hooman Askari Nasab, Dr. Nicholas Beier, Dr. Hassan Dehghanpour Hossein Abadi, Dr. Jeffery Boisvert at the University of Alberta, and Dr. Ferri Hassani at the McGill University, for their precious time, constructive criticisms, and insightful comments in my candidacy examination and thesis defence.

My great thanks also go to Mr. David DeGagne and Dr. Tatyana Katsaga at the Itasca Consulting Group (ICG), for offering me the precious opportunity of joining the Itasca Education Partnership (IEP) and for their patient guidance in my PhD study and research.

And next, I would like to give my sincere thanks to my dear colleagues who worked with me at the University of Alberta: Dr. Yuanyuan Pu, Dr. Huawei Xu, Dr. Mohammadali Sepehri, Mr. Jun Wang, Ms. Alicja Szmigiel, Dr. Guangping Huang, and Mr. Chao Liu for their kind help and suggestions in my PhD study and research. It was such a joyful time to work with you all.

Last but not least, I would like to express my love to my family, my friends, and my motherland China, and Canada, for all the beautiful, unforgettable, and unfaded memories.

Table of content

List of tables

List of figures

List of abbreviations

Abbreviation	Explanation
3D-DIC	Three-dimensional digital image correlation
AE	Acoustic emission
ASTM	American Society for Testing and Materials
BWZ	Ball-wall-zone
BHS	Blast-hole stoping
CCS	Central cross-section
CGB	Cemented gauge backfill
CHF	Cemented hydraulic fill
CPB	Cemented paste backfill
CRF	Cemented rockfill
DE	Discrete element
FD	Finite difference
FE	Finite element
FJ	Flat joint
FS	Factor of safety
FV	Finite volume
JKR	Johnson-Kendall-Robert
LVDT	Linear variable differential transformer
PB	Parallel bond
PSD	Particle size distribution
R	Rock
RMR	Rock Mass Rating
SEM	Scanning electron microscopy
UCS	Uniaxial compressive strength
VCL	Vertical central line

List of symbols

Symbols	Explanation
C_c	Uniform coefficient
C_u	Curvature coefficient
σ	Stress
ε	Strain
E	Young's modulus
η_p	Poisson's ratio
σ_3	Confining pressure
σ_p	Peak axial stress
τ	Shear strength
σ_m	principal stress
c	Cohesion
φ	Internal friction angle
σ_c	Uniaxial compressive strength
α	Failure plane angle
F_c	Contact force
M_c	Contact moment
F_l	Linear contact force
F_d	Dashpot force
F_p	Parallel bond contact force
M_p	Parallel bond contact moment

D_m	Mean particle diameter
$\overline{g}$	Bond installation gap
ρ	Bulk density
$\overline{E}$	Young's modulus of the parallel bond
k_n/k_s	Normal to shear stiffness ratio
$\overline{k}_n/\overline{k}_s$	Normal to shear stiffness ratio of the parallel bond
$\overline{\sigma}$	Normal strength of the parallel bond
$\overline{\tau}$	Shear strength of the parallel bond
μ	Friction coefficient
$\overline{\mu}$	Friction coefficient of the parallel bond
$\overline{\varphi}$	Internal friction angle of the parallel bond
σ_m	Principal stress
τ_s	Shear stress
A_s	Effective shear area
τ_i	Interface shear strength
σ_n	Normal stress
φ_i	Interface internal friction angle
c_i	Interface cohesion
k_i	Interface shear stiffness
μ_i	Interface friction coefficient
τ_p	Peak shear stress

δ_c	Critical shear displacement
τ_r	Residual shear strength
N_m	Finite zone numbers
d_s	Shear displacement
d_m	Magnitude displacement
F	Applied contact force
M_b	Applied contact moment
M	Total moment
F^l	Local applied contact force
M^l	Local applied contact moment
σ_n^c	Normal contact force
τ_{zx}^p	Peak shear stress
τ_{zx}^r	Residual shear stress
h_s	Stacking height
D_s	Stacking diameter
φ_r	Repose angle
F^{JKR}	Non-linear JKR contact force
F^{adh}	JKR attractive force
M^r	Rolling resistance moment
G	Effective shear modulus
γ_s	Surface energy

μ_r	Rolling-friction coefficient
p_v	Overburden pressure
p_h	Lateral earth pressure
n	Porosity
W	Backfill layer weight
C_i	Lateral compressive force
K_{ci}	Lateral earth pressure coefficient
α_i	Lateral earth pressure angle
S_i	Longitudinal shear force
σ_h	Horizontal stress
σ_v	Vertical stress
γ	Unit weight
k	Horizontal to vertical stress ratio
σ_m	Maximum principal stress
W_n	Wedge block net weight
c_r	Required cohesion
$(UCS)_r$	Required uniaxial compressive strength

Chapter 1 Introduction

1.1 Background

The backfilling process at an underground mine consists of returning geomaterials to the underground mined-out voids. These geomaterials include tailings, waste rocks and sands, which are removed during the extraction process of the orebody (Sivakugan et al., 2006). Modern backfilling technologies have been widely utilized in the mining industry for decades since the 1900s (Fall and Nasir, 2010; Qi and Fourie, 2019). Consolidated backfill columns can create a safer working platform for the subsequent mining activities, provide a better supporting effect for the underground stope stability, improve the recovery rate of ore pillars, and contribute to the environmental protection at the mine site (Belem and Benzaazoua, 2008; Heib et al., 2010; Zhang and Wang, 2007; Li and Aubertin, 2015). Furthermore, as the mining depth drastically increases nowadays, the backfilling process has become indispensable to guarantee the sustainable development of modern underground mines.

The waste rock backfilling method using the cemented rockfill (CRF) is a traditional technology adopted in many Canadian underground mines (Lingga, 2018; Jiang et al., 2019; Emad et al., 2012). Backfilling operation in this method can be flexible and has a high capacity (Wang et al., 2013). The CRF mainly comprises waste rock and cement (Sainsbury et al., 2014; Vennes, 2014). The waste rock, which behaves as the primary aggregate, usually comes from the abandoned gangue and the surrounding rocks at the mine, and Portland cement is mixed in as the binder material. The CRF is a weak, porous, and concrete-like material (Vennes, 2014). In this method, waste rock can be crushed, sieved and mixed with cement according to a specific particle size distribution and then

transported to the underground mined-out voids by mechanical equipment (Yao et al., 2012). In addition to the CRF, other popular backfill materials include cemented hydraulic fill (CHF) and cemented paste backfill (CPB), depending on different mining methods, geomaterial types and economic conditions at different underground mines (Sheshpari, 2015). As backfill materials are placed into the voids, aggregate particles begin to settle and consolidate. As the drainage and hydration processes occur continuously, backfill columns finally gain strength after being cured in the field for at least 28 days (Cui and Fall, 2018).

Strength characteristics and deformation properties of backfill materials have always been the focus of research that determines the stability of backfill columns and significantly affect the production schedule of the orebody extraction. The general way to study the stress-strain behaviour of backfill materials is to conduct physical laboratory tests such as uniaxial compression, triaxial compression, direct shear and Brazilian tests on backfill specimens, which are usually artificially made and cured in the laboratory using the aggregate and binder collected from the underground mines (Lingga and Apel, 2018; Koupouli et al., 2016; Kaklis et al., 2018). However, the inhomogeneity in the strength characteristics and deformation properties of backfill materials collected from the field are still very clear. In very few studies, core samples drilled from backfill columns were sawed and polished as field specimens (Johnson et al., 2015).

One of the mining engineers' very-high concerns is how the stress distributes inside backfill columns and around the stopes in underground mines. Backfill columns and the surrounding rocks are mutually supported and not self-isolated. Energy alternation and stress transmission happen through the frictional-bonded interfaces between them when

underground mined-out areas undergo disturbance. However, the research on how the backfill columns and surrounding rocks influence each other in the stress/displacement distribution and stability is still insufficient. The only existing method for measuring the in-situ stress inside backfill columns is pre-installing those cubic test frames attached with total earth pressure cells and piezometers into backfilled stopes before the columns consolidate and gain strength (Ouellet et al., 2005; Thompson et al., 2012). However, this method can be limited for the CRF columns since the non-uniform and discrete distributed particle sizes of the CRF aggregates can make the measuring results inaccurate and unrepresentative. Meanwhile, large CRF aggregate particles can damage the pre-buried instruments during the dumping process of the fresh CRF material.

Numerical modelling is a popular and effective way to comprehensively understand the stress distribution law inside backfill columns and around the surrounding rocks. These numerical models can be validated or calibrated with analytical solutions to predict the instability and potential geohazards induced by underground mining activities (Liu et al., 2017; Sepehri et al., 2017). Generally, typical numerical modelling methods can be classified into two categories of the continuum and the discontinuum approaches. The continuum approach mainly includes the finite element (FE), the finite difference (FD) and finite volume (FV) methods, which treat modelled geomaterials as homogenous and elastoplastic (Belinha and Dinis, 2006). Plenty of research has adopted the continuum approach to simulate the stress redistribution around the stopes induced by the adjacent orebody extraction, backfilling process and blasting vibrations due to the high computation performance of the continuum approach (Falaknaz et al., 2015; Emad et al., 2018; Liu et al., 2017). For the discontinuum approach, such as the discrete element

method, the modelled geomaterials are treated as assemblies of discrete blocks or particles that can be inhomogeneous in mechanical properties. However, very few studies have selected the discontinuum approach to monitor the stress distribution at multiple backfilled stopes (Hasan et al., 2017), while most of the research mainly focuses on the stress-strain behaviour of backfill materials and the instability of underground stopes induced by blasting vibrations due to the domination of the discontinuum approach in modelling large-strain deformation and post-failure behaviour (Suazo and Villavicencio, 2018; Wu et al., 2018; Martin et al., 2003). Meanwhile, many researchers have used the coupled FD-DE or FE-DE method to simulate the rock damage zones induced by blasting vibrations or the adjacent excavations to combine the advantages of the two approaches (Saiang, 2010; Cai et al., 2007). However, no relevant studies are found in which the simulation of the stress distribution and stability of underground backfilled stopes was involved with the hybrid continuum-discontinuum modelling approach.

1.2 Problem statement

Just like many other underground mines, the blasthole stoping (BHS) method was used at a hard-rock mine in Canada to extract the orebody. The mining/backfilling activities at this mine were in a primary/secondary manner. The primary stopes were extracted and then backfilled with the cemented rockfill to provide a supporting effect and confining pressure for the adjacent secondary stopes (rock pillars) mining activities. During the mining/backfilling sequence, the frictional-cohesive interfaces between the CRF columns and the surrounding rocks formed as the CRF columns consolidated and gained strength. The author is very interested in the law of how the backfilling process, mining/backfilling

sequence and the mechanical interaction at the interfaces influence the stress/displacement distribution and the stability of the underground mining area.

The stress measurement in the backfill columns can be very tough, and numerical modelling is an efficient way to study the stress/displacement distribution at the underground backfilled stopes. The finite difference method is very popular in modelling elastoplastic behaviour and has a very high computation efficiency, but it is very hard to simulate the large strain/deformation, especially at the post-failure stage. On the other hand, the discrete element method has great advantages in modelling the fracture evolution and failure mode with high simulation precision, but it is very time-consuming. The author is very interested in how to couple them in a hybrid way and combine the advantages of the two methods.

1.3 Objectives

The main objective of this research is to develop a hybrid modelling approach with higher computation efficiency and precision to study the regime of the mechanical interaction between the CRF columns and the adjacent mining area by using the coupled FD-DE method. As an innovative attempt that remains unexplored in numerical analysis in mining engineering, in this doctoral research thesis, the coupled FD-DE method, a hybrid continuum-discontinuum approach, was adopted to simulate the underground stopes backfilled with the cemented rockfill. This doctoral thesis, titled “Coupled finite difference and discrete element method for modelling underground stopes backfilled with the cemented rockfill, " has six main chapters, and each chapter's objectives are described here. In Chapter 3, physical laboratory tests were carried out on the field CRF core specimens to study the mechanical properties and stress-strain behaviour of the field CRF

material. In Chapter 4, by summarizing the mechanical properties gained from the laboratory test results, two kinds of the DE model of the CRF specimens with the simplified particle size distribution and mean particle diameter, respectively, were created to analyze the stress-strain behaviour numerically and validate the feasibility of modelling the CRF material with the DE method. In Chapter 5, the newly designed numerical direct shear tests based on the coupled FD-DE method were conducted on the combined rock-CRF (R-CRF) specimens to study the shear behaviour at the frictional-bonded interfaces between the CRF column and the surrounding rocks. In Chapter 6, the numerical slump tests were conducted on the DE model of the fresh CRF material, which was applied with the new Johnson-Kendall-Robert (JKR) contact model, and the backfilling process was modelled with the coupled FD-DE method to study the flowability and the stacking state of the fresh CRF material in the stope at early curing age. In Chapter 7, the coupled FD-DE method was adopted to simulate a single stope backfilled with a CRF column to study the stress distribution at the backfilled stope subjected to the shear effect from the interfaces between the CRF column and the surrounding rocks. In Chapter 8, the coupled FD-DE method was adopted to simulate multiple stopes backfilled with the CRF columns to study the influence of the primary/secondary manner of the mining/backfilling activities on the stress distribution at the multiple backfilled stopes and the stability of the multiple CRF columns.

1.4 Limitations

This research work has three main limitations. Firstly, due to the limitation of the drilling machine used by the Canadian hard rock mine, the diameter of the field CRF specimens is 6 inches, which is only 3 times the maximum diameter of the granitic aggregates (2

inches) for the scale effect elimination. However, the diameter of the field CRF samples at the mine was the largest that can be drilled compared with other Canadian underground mines. Secondly, since the limitation of the amount of the field CRF material, the rheological properties of the fresh CRF slurry could not be measured in the laboratory or provided by the mine. Thus, a parametric study on the microstructural parameters in the JKR contact model assigned in the DE model was conducted to see how they influence the flowability and backfilling efficiency of the fresh CRF material rather than conducting the calibration of the DE model of the fresh CRF material. Thirdly, since the mechanical properties of the interfaces between the CRF columns and the surrounding rocks were not provided by the mine, the cohesion and internal friction angle of the interfaces were assumed by the author to be 1 MPa and 30 degrees, respectively.. Later, the stress distribution along the vertical central line of the CRF column, which was influenced by the shear effect at the frictional-bonded interfaces, agrees well with the values calculated from Li and Aubertin's analytical model.

Chapter 2 Literature review

2.1 Backfilling technologies and backfill materials

Backfill material refers to any waste material, such as tailings, rock and sand, which can be placed into the underground mined-out area for disposal, environmental protection and engineering support (Liu et al., 2017). Depending on different mining methods and infrastructures, backfill materials can have different aggregate preparation, transportation and placing methods (Helmes, 1988). The selection of backfilling technologies at an underground mine is determined by the mining method, mineral processing method, equipment availability, geomaterial types and economic conditions (Sheshpari, 2015). Rock backfilling, hydraulic backfilling, and paste backfilling methods are three leading traditional backfilling technologies adopted in the mining industry worldwide (Grice, 1998).

In the rock backfilling method, waste rock or other industrial solid waste is crushed, sieved and mixed according to the particle size distribution and then transported to the underground mined-out voids by gravity or mechanical equipment (Yao et al., 2012). The cemented rockfill (CRF) is a backfill material when Portland cement is mixed into the crushed rock as a binder to improve the strength and stability of the backfill column. Backfilling operation in this method is flexible and has a high capacity, while it may cause severe air pollution at the voids and critical wear in equipment (Wang et al., 2013). The hydraulic backfilling method uses water as the transport medium to convey tailings or waste sand through pipelines or filling boreholes drilled into the voids (Yao et al., 2012). This method allows the granular solid with fine particles to be the aggregate of backfill materials, and its operation is economical and with a high capacity (Potvin et al., 2005).

However, permeability and the solid-water ratio of the hydraulic backfill material should be designed optimally, and the drainage system at the voids should be constructed in advance to prevent severe incidents due to liquefaction, rush-in, and pipe blockage problems (Bloss and Chen 1998; Tolarch, 2000). Portland cement can also be mixed into the granular solid as a binder to form the cemented hydraulic fill (CHF). For the paste backfilling method, tailings, cement and water are mixed, stirred, and thickened to the paste slurry firstly with a high solid proportion and then transported through pipelines to the voids by pumping or gravity (Yao et al., 2012; Sheshpari, 2015). Backfilling operation in this method can consume little cement, minimize ground tailings storage, and control the geochemical reactivity of backfill columns. Thus, it is economical and environmental-friendly (Aldhafeeri et al., 2016). However, the cemented paste backfill (CPB) preparation process can be complicated. The particle size distribution of the CPB material should be appropriately designed to prevent particle settlement and segregation while conveyed in pipelines (Landriault, 1995; Klein and Simon, 2006; Tariq and Yanful, 2013). Cement and water contents of the CPB material should also be optimized to ensure the rheological properties of the CPB slurry meet the requirement of consistency and flowability in pipelines (Ramlochan et al., 2004; Tariq and Yanful, 2013; Wu et al., 2013).

In addition to these traditional methods, some underground mines can adopt a few modified technologies according to specific backfilling conditions at the mined-out voids, including high-water content backfilling, total tailings backfilling and paste-like backfilling methods (Yao et al., 2012). In the high-water content backfilling method, two ingredients of the binder material are sent through two separate pipelines to the voids for mixing, which allows the backfill slurry to solidify in underground stopes without losing

any water (Zhu et al., 2018). In the total tailings backfilling method, an optimal percentage of fine tailings is added into the CPB material made in graded tailings, which can be relatively low concentrated and turbulent, to improve the consistency and flowability of the CPB slurry when it is transported in pipelines (Benzaazoua et al., 2008). For the paste-like backfilling method, the binder mixed into the paste-like slurry is silica-alumina-based cement combined with additive agents such as fly ash, slag or gypsum, aiming to improve the durability of the paste-like backfill columns. In addition, an optimal proportion of fine tailings is also added to enhance the self-flow ability and workability of the paste-like backfill slurry (Sheshpari, 2015).

2.2 Stress-strain behaviour of backfill materials

Backfill materials can be either cemented or uncemented (Sivakugan et al., 2006). This part mainly focuses on the mechanical properties of the consolidated cemented backfill materials since fewer and fewer underground mines choose the uncemented strategy for backfill materials due to the instability of the uncemented backfill columns. The mechanical properties of the uncemented backfill materials can be studied using soil mechanics theories due to their granular flow characteristics. However, rock mechanics theories are dominated for cemented backfill materials because they can be considered weak concrete-like materials (Pu et al., 2019; Zhang et al., 2018). Previous studies show that the elastoplastic behaviour can be observed on the cemented backfill specimens under the uniaxial and triaxial compression, and the strength characteristics and deformation properties of the cemented backfill materials are strongly influenced by the particle size distribution, cement content, curing age and material components (Wu et al., 2018; Fall et al., 2007; Lingga, 2018; Ghirian and Fall, 2013; Deng et al., 2017). As a

typical traditional cemented backfill material, the CRF material shares similar laws in the stress-strain behaviour and strength characteristics with the CPB or CHF materials.

Talbot curve theory is always used in backfill material designing to optimize the particle size distribution (Swan, 1985). Previous studies show both containing more coarse or fine aggregate particles can influence the binder hydration and microcrack evolution among the aggregate particles, leading to relatively lower compressive strength and deformation modulus of the cemented backfill specimens (Wu et al., 2018; Lingga, 2018). Higher cement content results in higher uniaxial compressive strength and Young's modulus since the increase in the cement content reduces the ductility and stiffness of the cemented backfill materials. Meanwhile, a lower water-cement ratio can cause a lower porosity and lead to a higher Young's modulus (Fall et al., 2007). The Mohr-Coulomb strength criterion has been widely used in previous research to characterize the failure envelope of cemented backfill materials under triaxial compression (Cui and Fall, 2016; Yang et al., 2020). It can also predict the compressive strength of the cemented backfill materials under different confining pressures by evaluating the cohesion and internal friction angle. Previous studies show that the cohesion of the cemented backfill materials increases while the internal friction angle decreases as the cement content increases (Belem et al., 2001; Cui and Fall, 2016). Generally, scanning electron microscopy (SEM) tests also reveal that microcracks inside these specimens can accumulate and propagate until the ultimate destruction during the entire compression process (Ghirian and Fall, 2013; Du et al., 2019). Previous studies (Liu et al., 2017; Chen et al., 2020; Lingga, 2018; Yang et al., 2020) show that failure patterns such as diagonal shear, columnar split and corner fracture modes, which are described in ASTM Standard C39 (2018), can all emerge

on backfill specimens under the uniaxial compression. The diagonal shear and tensile modes are the main failure pattern observed on the specimens under the triaxial compression (Yang et al., 2020). At the post-failure stage, cemented backfill specimens can either show strain hardening or softening behaviour, controlled by the binder hydration and strain development, and affected by the curing age and confining pressures (Cui and Fall, 2016; Yang et al., 2020).

Backfill columns and the surrounding rocks at the underground stopes are not self-isolated but mutually supported (Koupouli et al., 2016). Energy alternation and stress transmission happen through the frictional-bonded interfaces between them when underground mined-out areas undergo disturbance from the sequential orebody extraction. Many researchers have performed direct shear tests on the artificially combined rock-backfill or backfill-backfill specimens in the laboratory to study the interface shear behaviour, which can strongly influence the stress distribution and stability around the underground backfilled stopes. The laboratory test results reveal that the shear failure envelope of the interface also obeys the Mohr-Coulomb strength criterion, and the shear strength of these combined specimens can be smaller than the corresponding backfill material (Fall and Nasir, 2010). Major influence factors on the interface shear behaviour are the cement content, applied normal stress, surface roughness, curing time and conditions (Fang and Fall, 2019, 2020; Nasir and Fall, 2008; Lingga and Apel, 2018). Perfect elastoplastic behaviour can be observed on the interfaces in the combined rock-backfill specimens, while for the combined backfill-backfill specimens, the interfaces show evident strain-hardening shear behaviour, especially at the lower applied normal stress. As the cement content increases, the shear stress-

displacement curve can transform from a strain-hardening to a strain-softening shape (Koupouli et al., 2016). The higher normal stress applied to the combined specimens can weaken the interface dilation effect, resulting in higher shear strength and higher interface shear stiffness (Fall and Nasir, 2010). As the curing time increases, the degree of binder hydration at the interfaces increases, leading to a higher shear strength of the combined specimens (Guo et al., 2020). Meanwhile, a higher interface roughness can also contribute to an increased shear strength due to a larger interlock structure (Fang and Fall, 2020).

2.3 Stress state of backfill columns and the backfilled stopes

The stress distribution inside backfill columns and around the backfilled stopes can be significantly affected by the arching phenomenon, which occurs in backfill columns due to the shear behaviour at the frictional-bonded interfaces between backfill columns and the surrounding rocks (Li and Aubertin, 2009). As backfill materials in the underground stopes settle, dewater, and consolidate, the differential strain mobilizes the shear stress at the interfaces, and then a portion of pressure from the yielding backfill columns is transferred to the relatively stable neighbour non-yielding surrounding rocks (Ting et al., 2011). Traditional measuring methods for the in-situ stress in surrounding rocks can be classified into two categories: one consists of the methods that induce strain, deformation or crack opening of the rocks, such as hydraulic fracture, borehole relief and surface relief methods (Ljunggren et al., 2003; Cai and Peng, 2011), and the other one consists of the methods based on rock behaviour observation, such as the statistics of measured data, acoustic, strain recovery and geological observational methods (Ljunggren et al., 2003; Martin et al., 2003). However, there is still a shortage of studies in measuring the in-situ

stress inside backfill columns. The only existing popular method is to pre-install cubic test frames attached with the total earth pressure cells and piezometers into the backfilled stopes before the columns consolidate and gain strength (Ouellet and Hassani, 2005; Thompson et al., 2009; Hasan et al., 2014). The test results demonstrate that the total pressure at the center of the backfill column initially increased hydrostatically during the backfill slurry pouring process. And as the binder hydration continuously occurred, the backfill column gained shear strength gradually, and the total pressure was deduced to a value smaller than the theoretical overburden pressure due to the arching phenomenon. The measurement also indicates that high cement content and narrow stope geometry can increase the arching effect potential, leading to a smaller barricade pressure at the bottom of the backfilled stopes (Thompson et al., 2011, 2012).

Primary influence factors on the arching phenomenon and stress distribution in backfill columns and around the backfilled stopes include the stope geometry, mechanical properties of backfill materials and the surrounding rocks, and the mining/backfilling sequences. In very few studies (Ting et al., 2012; Pirapakaran and Sivakugan, 2007), physical laboratory models of the backfilled stopes with different shapes are created to study the stope geometry effect on the arching phenomenon. The test results reveal that the aspect ratio and stope inclination are critical factors in predicting the stress distribution in backfill columns. Meanwhile, there is plenty of research in which several representative analytical models have been proposed based on the limit equilibrium analysis to study the arching effect inside backfill columns. Firstly, in the early Marston's 2-dimensional analytical model (Marston, 1930), the interface between the backfill column and the surrounding rocks is considered cohesionless, and only the friction force

functions in the shear resistance. Terzaghi (1943) proposed a 2-dimensional analytical model like Marston's model but included cohesion into the interface shear parameters. And then, Li et al. (2005) proposed a 3-dimensional analytical model to cover the aspect ratio and stope inclination, which strongly affect the arching phenomenon in backfill columns. In Li's model, the equivalent internal frictional angle and cohesion differ for each interface, and the coefficient of earth pressure at the backfilled stope can be considered anisotropic. Li and Aubertin (2009) proposed a modified 3-dimensional analytical model to predict the effective stress in the backfill column by considering the hydrostatic pressure based on Li's model. Previous research has validated all these analytical models are reasonable and feasible in predicting the stress distribution inside backfill columns according to different backfilling situations.

Numerical modelling is an effective way to comprehensively understand the stress distribution law inside backfill columns and around the backfilled stopes. Furthermore, these numerical models can be validated or calibrated with analytical solutions to predict the instability and potential geohazards induced by underground mining activities (Liu et al., 2016; Sepehri et al., 2017). Generally, typical numerical modelling methods can be classified into continuum and discontinuum approaches. The continuum approach mainly includes the finite element (FE), the finite difference (FD) and finite volume (FV) methods, which treat modelled geomaterials as homogenous and elastoplastic (Belinha and Dinis, 2006). For the discontinuum approach, such as the discrete element (DE) method, the modelled geomaterials are treated as assemblies of discrete blocks or particles that can be inhomogeneous in mechanical properties.

Most researchers created the FD or FE models of a single backfilled stope to study the effects of the stope geometry and mechanical properties of backfill materials and the surrounding rocks on the stress distribution inside backfill columns (Jahanbakhshzadeh et al., 2017; Ting et al., 2011; Li and Aubertin, 2009). The modelling results indicate that the stope inclination angle and aspect ratio are key factors that influence the arching phenomenon in backfill columns. As the inclination angle increases, the vertical stress along the vertical central line (VCL) of the column at each elevation can decrease significantly, while relatively little change in the horizontal stress can happen. Meanwhile, the arching effect is more significant in the backfilled stopes with higher aspect ratios (height/width), and in the 3-dimensional models, the stress at each elevation increases as the length of backfilled stopes increases due to a weakened arching effect (Ting et al., 2011; Jahanbakhshzadeh et al., 2017). Previous studies show that the Poisson's ratio, internal friction angle, and cohesion of the cemented backfill materials are three key factors influencing the stress distribution in backfill columns. The vertical and horizontal stress along the vertical central line of the column at each elevation can slightly decrease as the internal friction angle increases, while the stress can be more insensitive to changes in these factors when the internal friction angle gets higher (Li and Aubertin, 2009; Jahanbakhshzadeh et al., 2015; Ting et al., 2011). Previous studies show that changing the cohesion and Poisson's ratio of the backfill column can impact the regularity of the stress distribution curves at the hanging walls of the backfilled stope (Li and Aubertin, 2009), while the vertical and horizontal stress are relatively insensitive to these two factors along the vertical central line of the column (Liu et al., 2016). As the effective internal friction angle and cohesion of the interface increase, the vertical and horizontal stresses along the

vertical central line of the column at each elevation increase, while the stresses can become entirely insensitive to the interface cohesion when it gets higher (Liu et al., 2016).

Meanwhile, some researchers created the FD or FE models of the multiple backfilled stopes to study the effect of the mining/backfilling sequence on the stress redistribution inside backfill columns and around the surrounding rocks. In Mkadmi's FE model, the saturated backfill layers were added to the pre-drained and settled backfill layers until the stope was wholly backfilled (Mkadmi et al., 2013). The test results show that a higher sequential backfilling rate results in a higher total stress at the base of the backfilled stopes due to the accumulation of the pore water pressure, and a lower normal stress can be observed at a slower backfilling rate since the drainage and binder hydration can occur sequentially in backfill columns. In some other FD models, two adjacent stopes were extracted adjacently and backfilled in a primary/secondary manner (Falaknaz et al., 2015). The modelling results indicate that the stress distribution in the second backfilled stope tends to behave like in a single backfilled stope and is in good agreement with the analytical solution developed by Li and Aubertin (2009), while the stress in the first backfilled stope can show an evident redistribution, which is significantly influenced by neighbouring excavation and backfilling operations (Newman, 2018). Previous studies by Newman (2018) and Falaknaz (2015) both show that during the excavation of the second stope, in the first backfilled stope, the vertical stress tends to decrease, especially near the mid-height of the column, while the horizontal stress increases first and then decreases owing to the movement of the surrounding walls. Therefore, during the backfilling process of the second stope, the horizontal stress in the first backfilled stope tends to increase, while the corresponding vertical stress becomes insensitive to the backfilling

process. It should be mentioned here that most of the previous studies adopted the continuum approach due to its high computation performance (Falaknaz et al., 2015; Emad et al., 2018; Liu et al., 2016), while in very few studies (Hasan et al., 2017), the discontinuum approach has been selected to evaluate the stress redistribution within the stopes backfilled with the uncemented backfill materials.

2.4 Stability of backfill columns and the backfilled stopes

At an underground mine, gaining an in-depth understanding of the stability of the backfilled stopes is one of the most crucial research objectives for mining engineers. Backfilling the underground mined-out area can reduce the ground subsidence, ore dilution, pillar failure and rockburst risks (Abdellah et al., 2020; Heib et al., 2010; Yang et al., 2015). To study the stability of the backfilled stopes, firstly, the backfill column strength in the primary stope should be determined by considering the extraction of the adjacent secondary stopes. Mitchell (1982) proposed an analytical solution for this case based on a limit equilibrium analysis of a wedge block model. In Mitchell's analytical model, the required uniaxial compressive strength of the backfill column is only related to the stope geometry and the height of the exposed sidewall. However, his model is inconsistent with the experimental observations for the drained cemented backfill columns (Fall and Nasir, 2010). Li and Aubertin (2012) proposed a modified Mitchell solution, which can be applied to the backfilled stopes with rectangular shapes and can overcome several limitations of the original model. In the modified Mitchell's model, the internal friction angle of the backfill column can be nonzero, and the interface cohesion can be considered a portion of the cohesion of the backfill column. Meanwhile, A safety factor was introduced to the modified model to evaluate the stability of the backfill

column, which can be calculated as the ratio of resistant force and driving force on the failure plane (Li and Aubertin, 2012).

Many previous studies have shown that underground mined-out voids are backfilled to minimize the ground subsidence and control the overlying strata movement, especially in many coal and iron mines. The main factors that influence the overburden stability of the backfilled stopes include the deformation modulus and thickness of the stope roof, the overlying strata pressure, the advancement distance and work face width, and the foundation coefficients of backfill columns (Sun et al., 2019). Yang et al. (2017) built a FE model of the backfilled stopes with the same geometry at an underground iron mine to evaluate the subsidence parameters, such as the vertical and horizontal deformation at the mine site surface. The modelling results indicate that as the underground stopes get backfilled, the ground deformation can be lower than critical values and fall into a controllable range. It shows that backfilling with the cemented paste backfill can feasibly be used in subsidence control. Zhang et al. (2018) created a physical model of the multiple backfilled stopes in the laboratory with the same cemented paste backfill and rock materials from a coal mine to reproduce the movement of overlying strata in the mining/backfilling sequence. The test results indicate that the overburdened stress on the top of backfill columns increases first and then stays stable. Backfilling the underground stopes can limit the overlying strata's deformation and avoid the caved zones' appearance. Yang et al. (2015) created a physical model of two adjacent backfilled stopes in the laboratory with the same cemented paste backfill material from an iron mine to study the stability of the multiple backfilled stopes at different stages in a primary/secondary manner of the mining/backfilling activities. The test results reveal that the stability of the

primary backfilled stope can be the worst when the secondary stope is extracted as the sidewall of the primary backfill column is exposed to the air. Lu et al. (2018) conducted field monitoring and numerical modelling to study the stress redistribution at the multiple backfilled stopes. The study indicates that shear stress can be concentrated at the interfaces between the columns and the surrounding rocks, and the corners at the boundaries of backfill columns are also the critical positions of the shear stress concentration zones.

Pillar failure is a common engineering disaster in underground mined-out voids. Many researchers combined in-situ monitoring and numerical modelling to study the effect of the backfilling process on the stability of rock pillars and the backfilled stopes. Heib et al. (2010) instrumented total earth pressure cells on rock pillars based on a gypsum mine and found that the adjacent backfill columns can induce confining pressures on rock pillars. Building the DE model of the backfilled stopes adjacent to fractured rock pillars indicates that backfill columns can induce the horizontal and vertical pressures that contribute to the fracture closure inside rock pillars. The induced stress depends on the backfill material consolidation, pillar deformation, pillar fracture presence, and the mechanical properties of the rock-backfill interfaces (Heib et al., 2010; Yin et al., 2017). Tesarik et al. (2009) analyzed the monitoring data from the biaxial stress meters instrumented in rock pillars to study the long-term stability of the backfilled stopes in an underground lead-zinc mine. The test results indicate that backfill columns can limit rock pillars' dilation and contribute to rock pillars' stability. The total strain measured inside rock pillars supported by backfill columns is significantly smaller than the unconfined rock pillars (Tesarik et al., 2009; Zhang et al., 2017).

Meanwhile, very few studies have focused on the effect of backfill columns on the rockburst risk. Feng et al. (2020) established underground backfilled stopes with overlaying rock strata based on a coal mine to identify and evaluate the instability of the surrounding rocks. The modelling results show that backfill columns can efficiently control dynamic disasters such as rockburst by decreasing the stress concentration coefficient and energy accumulation in the surrounding rocks. As the required energy to trigger rockburst increases, the damage time for surrounding rocks is prolonged (Feng et al., 2020).

Chapter 3 Mechanical properties of the field cemented rockfill

In this chapter, the uniaxial and triaxial compression tests were conducted on the large-scale cylindrical specimens made of the field cemented rockfill (CRF) core samples collected using the diamond saw drilled from a backfilled stope at a Canadian hard rock mine. The stress-strain curves obtained from the test results revealed that the strength characteristics and deformation properties of the field CRF material exhibit heterogeneity inside the CRF columns and along the borehole-drilling directions at different depths of the backfilled stope due to the segregation phenomenon and multi-stages of compression and consolidation during the CRF dumping process. This study can supply practical laboratory references for assessing the required axial compressive and shear strengths of the CRF column in the field.

3.1 Introduction

The cemented rockfill (CRF) comprises waste rock and cement slurry (Sainsbury, 2014; Vennes, 2014; Lingga and Apel, 2018). It is a primary backfill material used for underground mined-out areas. The waste rock is usually produced during the development of the drifts done in the host rock as the primary aggregate of the CRF material (Sepehri et al., 2017), and Portland cement is always mixed to provide the binding effect among the aggregate particles (Lingga and Apel, 2018). The CRF material is considered weak concrete (Vennes, 2014) due to the low content of cement. Many researchers (Swain, 1985; Lingga and Apel, 2018; Wu et al., 2018; Zhang and Wang, 2007) conducted multiple sieving tests and used the Talbot curve method (Talbot et al., 1923) to describe and optimize the particle size distribution of the aggregate of the CRF

and other concrete-like materials. Meanwhile, the cement and water contents of the fresh CRF slurry are two important physical parameters to determine the strength and mechanical properties of the consolidated CRF column in the backfilled underground stope (Wu et al., 2018; Kumar et al., 2016; Lingga et al., 2019).

Backfilling with the cemented rockfill has been widely implemented at many North American underground mines from early on (Peterson et al., 1996; Turichshev et al., 2017; Sepehri et al., 2017). The CRF mixture with different physical-mechanical properties can be transported to the specific underground stope with the conveyor belt haulage, tracks, or pipeline systems according to different preparation and storage methods (Helms, 1988). The CRF material used in this study was collected from a hard rock mine in northern Canada. This mine used the blast-hole stoping (BHS) mining method to extract the orebody and then backfill the underground openings with the CRF material (Sepehri et al., 2017; Lingga and Apel, 2018). The consolidated CRF columns can create safe working platforms for the subsequent mining activities, provide better support effect for the underground stability, improve the recovery rate of the ore pillars, and decrease the dilution rate of the ore production (Belem et al., 2008; Heib et al., 2010; Zhang and Wang, 2007; Li et al., 2015). Meanwhile, backfilling with the CRF column contributes significantly to the environmental protection of the mine site because it efficiently reduces the discharge amount of the mining waste stored on the surface and eliminates the hidden geohazard danger related to the failure of tailings dams (Yilmaz and Fall, 2007).

To study the mechanical properties of the backfill materials, many researchers and engineers conducted numerous laboratory tests on the cemented rockfill (Lingga et al., 2019), cemented paste backfill (CPB) (Fall et al., 2007; Johnson et al., 2015; Wu et al.,

2018) and cemented gangue backfill (CGB) (Sun et al., 2017; Zhang and Wang, 2007). These necessary tests include the uniaxial compression test (Lingga et al., 2019; Fall et al., 2007), triaxial compression test (Belem et al., 2001; Fall et al., 2007; Rankine and Sivakugan, 2007), direct shear test (Lingga and Apel, 2018; Fang and Fall, 2019) and Brazilian test (Johnson et al., 2015; Komurlu et al., 2016). They provide valid laboratory references for designing the backfilling system and monitoring the stability of the underground backfilled stopes. Previous studies have revealed that these different backfill materials' strength characteristics and deformation properties are in various ranges due to different particle size distributions and chemical compositions (Fall et al., 2005; Ghirian and Fall, 2013). Although these backfill materials show evident elastoplastic deformation during the uniaxial and triaxial compression tests, the stress-strain behaviour can be quite different. For example, ductile failure mode can occur at the post-failure stage on some cemented paste backfill (Rankin and Sivakugan, 2007). Most CRF material and cemented gangue backfill show obvious brittle failure response (Lingga et al., 2019; Wang et al., 2009). Meanwhile, the confining pressure and in-situ geological conditions at the underground stopes can also significantly influence the mechanical properties and failure behaviour of backfill materials (Rankin and Sivakugan, 2007). For the direct shear test on backfill materials, previous studies (Koupouli et al., 2016; Nasir and Fall, 2008) mainly focused on the shear stress-strain behaviour at the rock-backfill and backfill-backfill interfaces. Furthermore, for the Brazilian test, the tensile strength of backfill materials can vary widely according to different test methods and conditions (Kaklis et al., 2018; Johnson et al., 2015).

Meanwhile, other advanced test methods and apparatuses were also employed by many researchers as auxiliaries to study the mechanical properties of the backfill materials. For instance, many studies (Gong et al., 2014; Wu et al., 2018; Belem et al., 2001; Fall et al., 2007; Ercikdi et al., 2014; Johnson et al., 2015) conducted the acoustic emission (AE) monitoring test, ultrasonic test, and scanning electron microscope (SEM) test to learn the microstructure quality and the microcrack evolution inside the backfill materials under compression. Moreover, some other researchers (Lingga et al., 2019; Du et al., 2019) used the measuring system with the three-dimensional digital image correlation (3D-DIC) technique to investigate the visible cracks on backfill materials at the post-failure stage.

However, most of these previous laboratory tests were conducted on artificial backfill specimens, of which the aggregate and binder were mixed, cured, and consolidated under laboratory conditions (Lingga et al., 2019). In contrast, the temperature and humidity in the laboratory can be quite different from those in underground mined-out areas (Roux et al., 2005). Furthermore, in very few studies (Johnson et al., 2015), small-scale core samples with a diameter of 7.0 cm were drilled from a CPB column under field conditions and then used for laboratory tests. Compared with the well-mixed laboratory-made backfill specimens, particles inside the field core backfill samples are relatively more nonuniformly distributed, and the segregation phenomenon can be more prone to occur. Especially for the CRF material, the particle size distribution is very inhomogeneous, and the mechanical properties at different parts of the CRF column can be highly variable. Thus, the test data obtained from the artificial CRF specimen made in the laboratory may not be very representative (Liu et al., 2017). Hence, in this study, field CRF core samples were collected from a CRF column at an underground stope of a hard rock mine.

Moreover, by conducting the uniaxial and triaxial compression tests on these specimens, the strength and deformation parameter distributions of the CRF core samples drilled along the vertical and horizontal directions at different depths were then analyzed.

3.2 Material and methodology

3.2.1 Field-cemented rockfill

The field CRF core samples were collected from a hard rock mine located in Northwest Territories, Canada, of which the sampling method and locations are shown in Fig. 3.1. The dimension of the single backfilled stope at the mine is 30 × 7.5 × 30 m (length × width × height). Two 21-meter-long and 6-inch-wide diamond boreholes, B1 and B2, were drilled along the horizontal and vertical directions from the CRF discharge point, respectively, in an entirely dewatered and consolidated CRF column at a backfilled stope, which is located 200-meter-deep underground. Fig. 3.3a shows that the CRF samples from the borehole B1 and B2 were sawed and polished into 16 and 12 pieces of the cylindrical specimens, respectively, and then numbered according to the buried depth in the column at the backfilled stope.

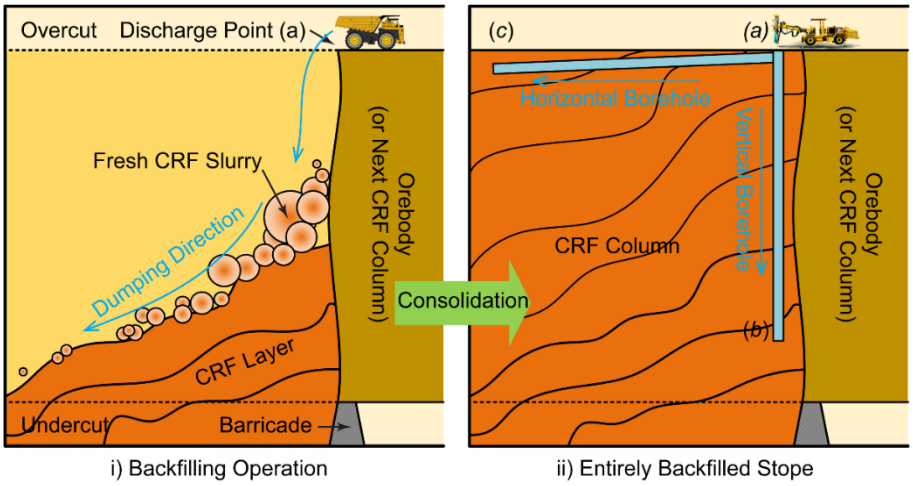

Fig. 3.1 Sampling method and locations of the field CRF core samples at the Canadian hard rock mine.

The mechanical-physical properties of the CRF samples are shown in Table 3.1. With a dry unit weight of 2281.8 kg/m^3, the CRF material mainly consists of the aggregate of granitic particles and the Portland cement binder. Meanwhile, the fresh CRF slurry's cement-aggregate, water-cement, and water-solid ratios are 8.0%, 1.0 and 9.6%, respectively. The granitic aggregate particle size distribution (PSD) is shown in Fig. 3.2, indicating that the CRF particles are sieved into twelve intervals according to the diameter, and the mass fractions are listed in Table 3.2.

According to the particle size distribution, the uniform coefficient C_u and curvature coefficient C_c of the granitic particles are 12.0 and 0.81, respectively. Compared with Swan's optimal theory of the CRF aggregate in 1985, the suitable exponent value for the granitic aggregate particle size distribution is 0.35, which is smaller than the recommended optimal of 0.5 for the backfill material (Swan, 1985). It indicates that the CRF samples have a slightly rapid transition from the large to fine aggregate particles, accounting for 40% and 60% by weight, respectively.

Table 3.1 Physical-mechanical properties of the field CRF core samples.

Category	Values
Dry unit weight (kg/m^3)	2281.8
Cement-aggregate mass ratio	0.08:1
Water-cement mass ratio	1:1
Water-solid mass ratio	0.096:1

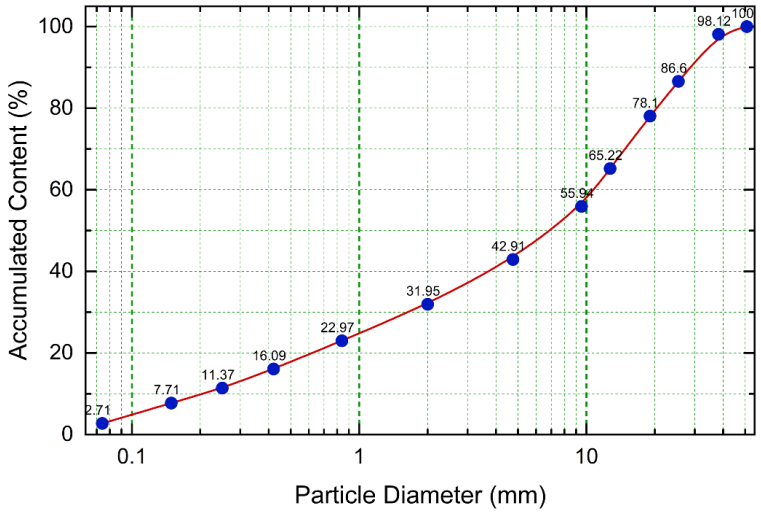

Fig. 3.2 Particle size distribution of the CRF aggregates.

Table 3.2 Mass fractions of the CRF aggregates with different particle diameters.

Intervals (mm)	Mass fraction
(0, 0.074)	2.71%
(0.074, 0.149)	5.00%
(0.149, 0.250)	3.66%
(0.250, 0.420)	4.72%
(0.420, 0.840)	6.88%
(0.840, 2.000)	8.98%
(2.000, 4.750)	10.96%
(4.750, 9.525)	13.03%
(9.525, 12.70)	9.28%
(12.70, 19.05)	12.88%
(19.05, 25.40)	8.50%
(25.40, 38.10)	11.52%
(38.1, 50.8)	1.88%

3.2.2 Specimen preparation

Fig. 3.3a shows that the CRF samples were cut into large-scale cylindrical specimens by a diamond saw and then labelled according to the buried depths in the CRF column along the vertical and horizontal directions at the backfilled stope. The upper and lower surfaces of the field CRF specimens were polished using abrasive papers to ensure a smooth-and-level initial status for the following tests. The diameter of the field CRF specimens was 6.0 inches, which was more than three times the maximum particle size in the CRF samples. The height of the field CRF specimens varied from 304.8 mm to 335.28 mm to keep a minimum aspect ratio of 2:1 to eliminate the size effect, according to the American Society for Testing and Materials (ASTM C39, 2018; ASTM C192, 2013). Meanwhile, the field CRF specimens were cured in the laboratory at a temperature of 25 ℃ and a humidity of 95% (Fall and Samb, 2009).

3.2.3 Laboratory test method

Fig. 3.3b and Fig. 3.3c show that the uniaxial and triaxial compression tests were carried out on the large-scale CRF core specimens using a 1,000-ton servo-hydraulic controlled INSTRON loading frame, which has a maximum axial pressure of 6,230 KN. For both the uniaxial and triaxial compression tests, the axial pressure was loaded under the constant displacement control until the field CRF specimens reached the failure load, with a quasi-static compression rate of 0.5 mm/min (ASTM C39, 2018). Two linear variable differential transformers (LVDTs) were placed at two opposite points at the mid-height of each specimen diametrically to measure the radial deformation for the uniaxial compression test. For the triaxial compression test, to simulate the natural stress condition, the hydraulic confining pressure was applied to the field CRF specimens by

placing them in a large-scale Hoek triaxial cell. The cell consists of a hollow steel cylinder with an embedded rubber membrane and a pair of spherical seat platens installed at the top and bottom of the field CRF specimens. A 260D Syringe Pump was used to provide the hydraulic confining pressure for the triaxial compression test, with a pressure capacity range of 0.69 MPa to 5.17 MPa and a refill depressurization range of 1.0 μl/min to 107 ml/min. The Hoek triaxial cell was saturated to be completely air-free by pumping oil into the cell before the tests started. The specific hydraulic confining pressures of 1.5 MPa and 2.5 MPa were applied to the cell after the field CRF specimens were placed in the rubber membrane. During both the uniaxial and triaxial compression tests, the specimens' axial load, axial, and radial deformations were collected through data loggers and then converted to axial stress, axial, and radial strains, respectively, and then recorded by using MTS Series 793 Control System.

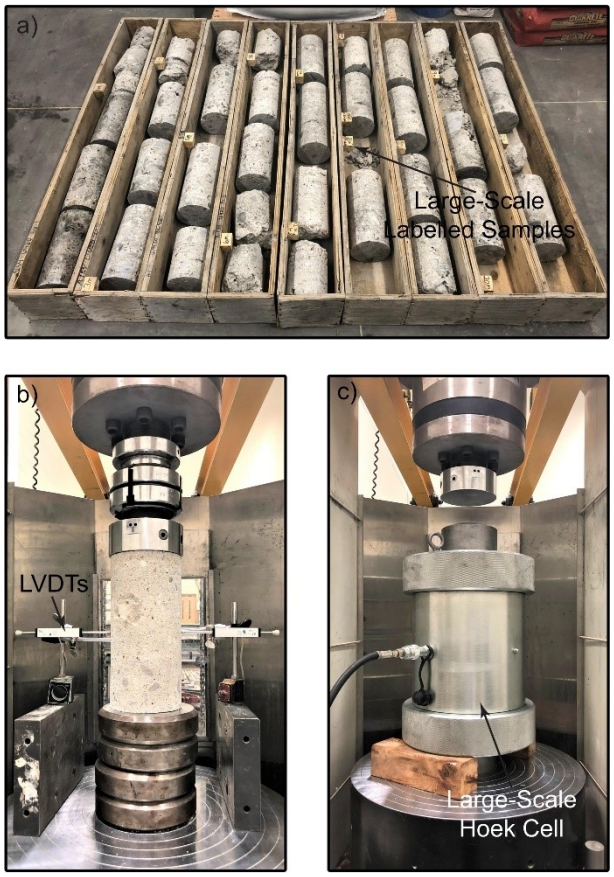

Fig. 3.3 Preparation of the field CRF specimens and the test apparatus setups: a) field CRF specimens, b) large-scale uniaxial compression test, and c) large-scale triaxial compression test.

3.3 Results and discussion

3.3.1 Stress-strain behaviour and the deformation properties of the field CRF specimen

Fig. 3.4 shows the stress-strain (σ-ε) curve of a representative field CRF core specimen under the uniaxial compression. As with most kinds of the geomaterials, such as concrete and rock (Zhao et al., 2019; Cai and Kaiser, 2014), the curve can be divided into four main stages, which are marked as oa to cd, respectively, according to the different stress-strain behaviour during the entire uniaxial compression test.

First, during the pore compaction stage (oa), the specimen experienced a self-adjustment period. It became stiffer with initial micro-fissures and pores getting compacted to close gradually, leading to a linear rather than a concave curve shape. Second, the specimen showed visible elastic deformation during the ab stage, with Young's modulus (E) of the specimen maintained constant, which was reflected from the linear positive correlated stress-strain behaviour at this stage. Third, the micro-cracks inside the specimen were initiated to expand at point b on the curve, propagated during stage bc, and then caused an apparent decrease in deformation modulus, leading to a nonlinear stress-strain behaviour at this stage. Finally, starting at the peak stress point c on the curve, the specimen was destroyed and underwent a strain-softening failure stage of cd, during which micro-cracks converged rapidly. And then, the peak stress of the specimen decreased gradually to a stable level.

What is more, some studies (Zhao et al., 2019; Cai and Kaiser, 2014; Wu et al., 2018) made more distinct divisions on stages of bc and cd, which can be both divided into two substages according to the stabilization of micro-cracks and damage propagation states inside some specific geomaterials. However, in this study, for σ-ε curves of the CRF specimens under the uniaxial compression, there is no need to make such a precise division on stages of bc and cd, because it can be observed in Fig. 3.4 that no unstable micro-crack propagation appeared neither near the peak stress point nor at the post-failure stage during the tests. Moreover, for σ-ε curves of the CRF specimens under the triaxial compression, the substages were divided at the corresponding bc and cd stages and not shown in this paper.

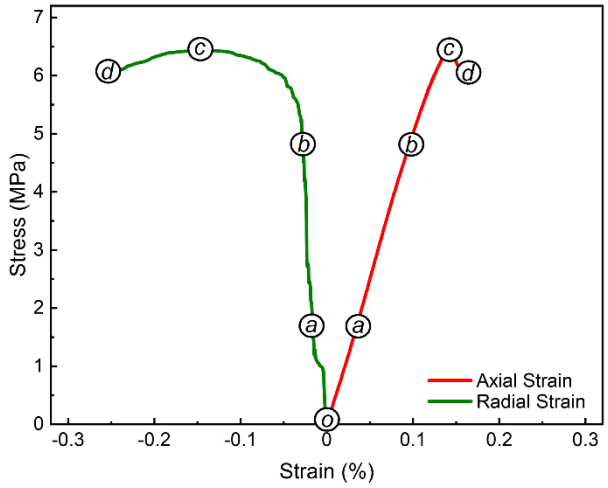

Fig. 3.4 σ - ε curve of a representative field CRF specimen under the uniaxial compression.

Fig. 3.5 depicts the distributions of the uniaxial compressive strength (UCS), Young's modulus (E), and Poisson's ratio (η_p) of the field CRF core samples drilled along the vertical and horizontal directions at the borehole locations in the corresponding CRF column at the backfilled stope. As shown in Fig. 3.5a, the average UCS for 15 groups of the field CRF specimens is 6.69 MPa, with a standard deviation (s_d) of 1.12 MPa and a coefficient of variation (c_v) of 17%, which is proved to be within the acceptable range (Johnson et al., 2015). Generally, as dewatering and consolidation inside the field CRF material occur continuously during the backfilling process, the UCS is expected to increase as the depth increases (Yilmaz et al., 2015). In this study, along the vertical drilling direction, the highest UCS of the specimens appears at point b of the maximum drilling depth in the backfilled stope. However, the UCS shows a fluctuant distribution from 4.95 MPa to 8.78 MPa along the depth due to the segregation phenomenon inside the CRF column. A previous study (Liu et al., 2017) has observed that the segregation phenomenon, which commonly occurs in hydraulic backfill materials, can easily result in

the rearrangement of the backfill material particles. It means that more coarse aggregate particles settle down, and more fine aggregate and binder particles rise to the top, leading to lower porosity and a higher UCS at the shallow depth of the backfilled stope. In this study, the segregation phenomenon can be easily observed by directly finding the unevenly distributed pores and particles on the field CRF specimens. Finally, due to the segregation phenomenon's combined effects and the CRF material's ununiform particle size distribution, the UCS of the specimens fluctuated dramatically along the vertical drilling direction. However, the highest UCS still appears at the maximum drilling depth in the CRF column at the backfilled stope due to multi-stages of overburden compression and consolidation.

Meanwhile, although a slight fluctuation exists in the UCS distribution of the specimens drilled in the horizontal direction, a significant downtrend can be easily observed along the horizontal distance from the CRF discharge point a to point c of the maximum drilling depth. Moreover, the lowest and highest UCS, 5.56 MPa and 8.46 MPa, respectively, appear at the maximum horizontal drilling depth and the CRF discharge point in the CRF column at the backfilled stope, respectively. The reason for this downtrend distribution is that as the multi-stage pouring of fresh CRF material continues, the CRF column at the backfilled stope withstands a multi-stage compression and consolidation process (Grabinsky, 2010). Thus, the closer the material gets to the CRF discharge point, the more compacted the material can be, and the less porosity the material acquires due to the impact from the subsequently poured fresh CRF material and the settlement driven by gravity. In contrast, the CRF material away from the CRF discharge point can undergo only minor disturbance from the subsequent pouring. Thus, it can be consolidated

naturally, leading to a lower UCS of the CRF material. Meanwhile, the segregation phenomenon can also contribute to the dispersed distribution of the UCS of the field CRF specimens along the horizontal drilling direction in the CRF column at the backfilled stope (Liu et al., 2017).

Fig. 3.5b shows that the average E for 15 groups of the CRF core specimens is 4.45 GPa, with an s_d of 0.82 GPa and a c_v of 18%. Thus, it depicts that E of the field CRF specimens drilled along the vertical and horizontal directions fluctuated and distributed dispersedly. However, E of the horizontal-drilled specimens can distribute more uniformly, with a lower c_v of 15%, then the specimens were drilled along the vertical direction. It means the multi-stage pouring of the fresh CRF material can exert less influence on the distribution of E along the horizontal drilling direction in the backfilled stope. Meanwhile, compared with the UCS distribution, the distribution of E of the field CRF specimens is much more uniform.

Fig. 3.5c shows that the average value of η for 15 groups of the field CRF specimens is 0.24, with a s_d of 0.17 and a c_v of 70%. This average value is reasonable for concrete-like materials such as cemented rockfill, cemented paste backfill and cemented coal gangue (Deng et al., 2017; Sun et al., 2017). Whether for the specimens drilled along the vertical or horizontal direction at the borehole locations, no evident regularities of the distribution in η are found. Both values fluctuate dramatically due to the individual difference of the specimens caused by the ununiform particle size distribution of the CRF material and the segregation phenomenon inside the CRF column. Another critical cause for these distribution irregularities is the errors from the measuring apparatus for the radial strains of the field CRF specimens during the uniaxial compression tests. Due to the relatively

large dimensions of the specimens, the LVDTs adopted the point measurement method, of which the probes were placed at two opposite points at the mid-height of each specimen diametrically. Suppose one point is located at the failure zone or a sizeable granitic aggregate particle on the specimen. In that case, the instability and asymmetry of the measurement can be generated, leading to a high c_v and inconsistent results of η of the field CRF specimens.

Fig. 3.6 depicts the distribution contours of the UCS and E at the cross-section of the CRF column, which is plotted with the mapping software Surfer by using the Kriging gridding method. It indicates that the CRF slurry's dumping method and dumping frequency can profoundly influence the arrival time when the CRF column is entirely consolidated and settled, leading to significant non-uniform distributions in the UCS and E. As seen at the bottom of the backfilled stope, the UCS and E of the CRF column can be higher due to the multi-stage compression from the overburden CRF layers. At the top of the backfilled stope, the further away from the CRF discharge point, the lower the UCS and E can be. The predicted contours are highly coincidental with the laboratory test results on the field CRF specimens.

a)

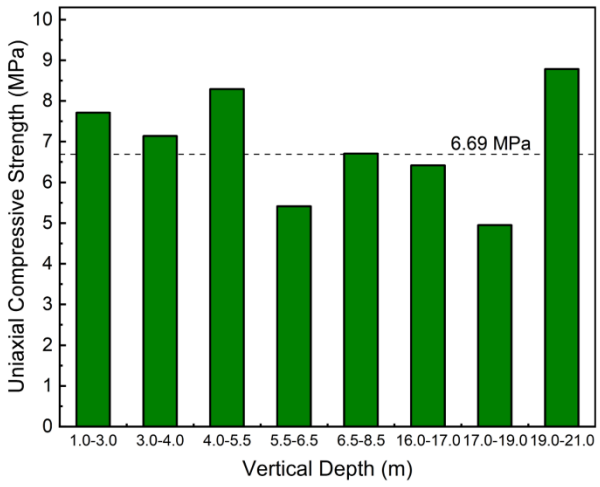

i) Vertical Distribution

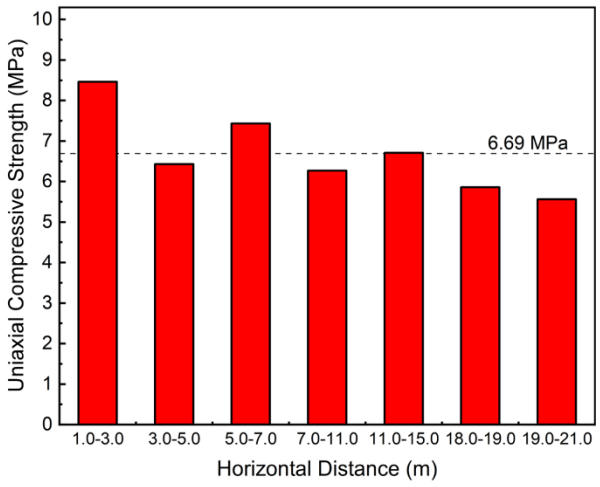

ii) Horizontal Distribution

b)

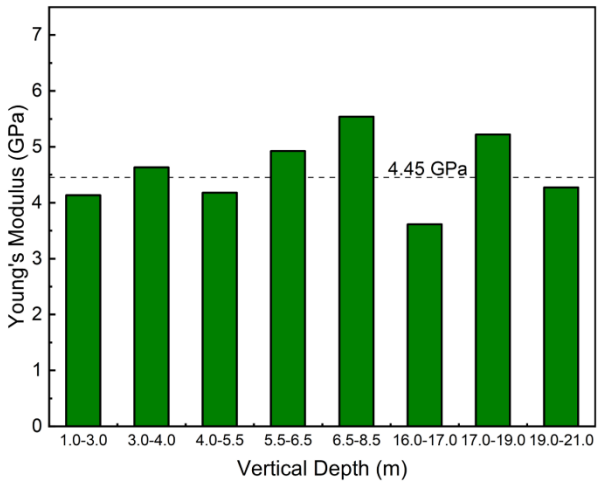

i) Vertical Distribution

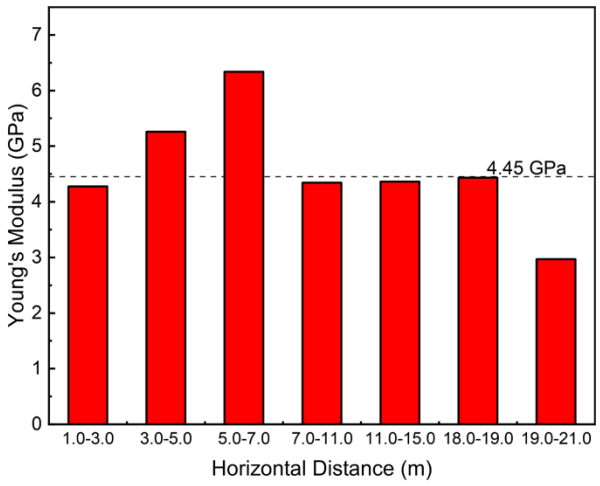

ii) Horizontal Distribution

c)

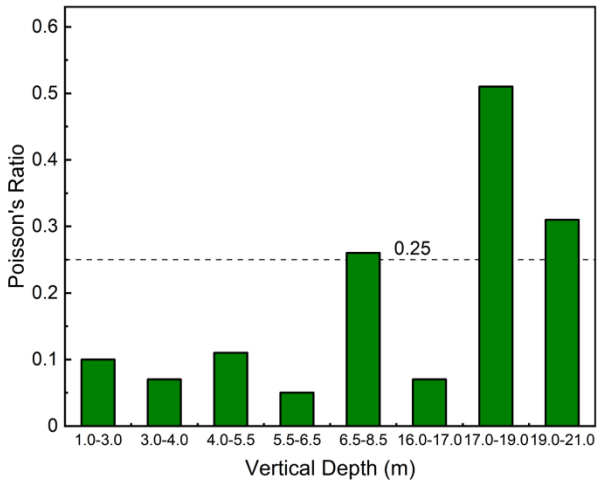

i) Vertical Distribution

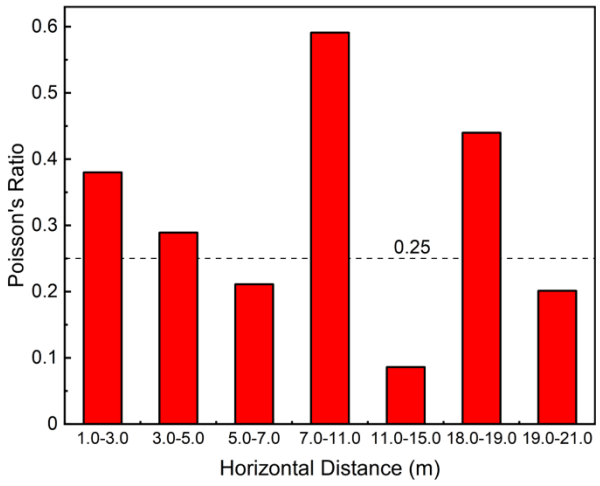

ii) Horizontal Distribution

Fig. 3.5 Distribution of the mechanical properties of the field CRF specimens along the drilling directions: a) UCS, b) E, and c) η.

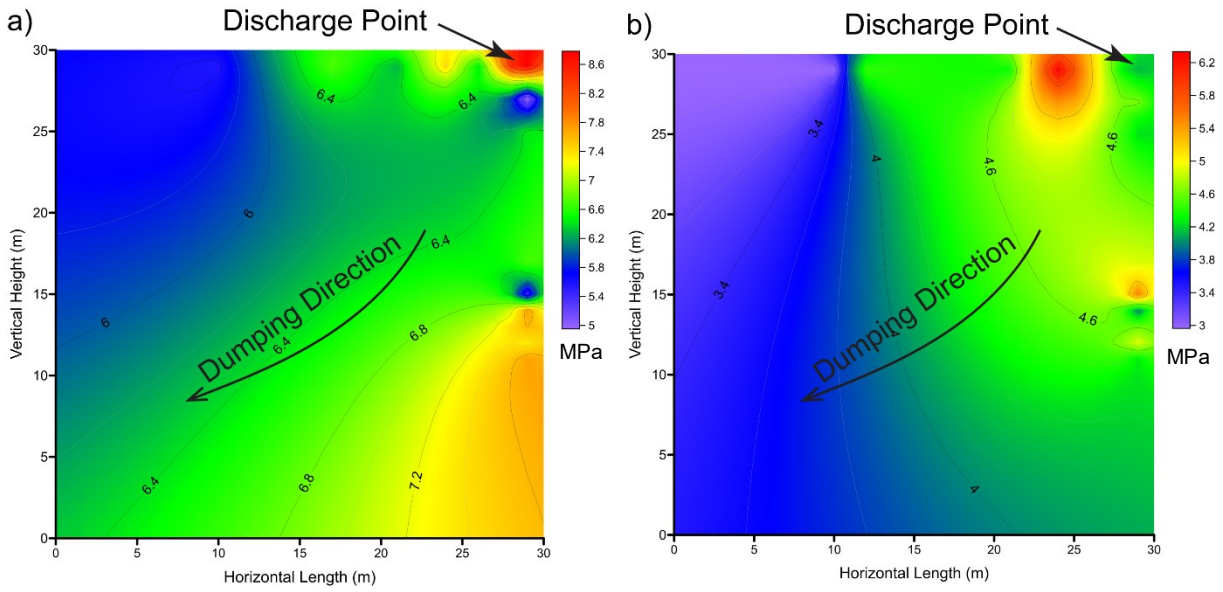

Fig. 3.6 Distribution of the mechanical properties of the field CRF material at the CCS of the CRF column: a) UCS, and b) E.

3.3.2 Strength characteristics and the failure pattern of the field CRF specimen

Fig. 3.7 compares the average UCS of Lingga's artificial CRF specimens with the field CRF specimens in this study. The average UCS of the artificial CRF specimens with different cement contents of 4.5% and 10% are 3.39 MPa and 9.22 MPa, respectively. Previous studies on cemented soil (Jongpradist et al., 2010) show that the average UCS can linearly increase as the cement content increases within a slight variation of cement content. Thus, the average UCS of the artificial CRF specimens when the cement content is 8% can be calculated as 7.1% using the interpolation method. As can be seen, the average UCS of 15 groups of the field CRF specimens is 6.69 MPa when the cement content is 8%, with an error of 5.8%, compared with the expected value calculated from Bob's artificial CRF

specimens. It indicates that the strength requirement of the CRF column is still met at the hard rock mine, although a significant non-uniform distribution exists in the UCS at different parts of the CRF column.

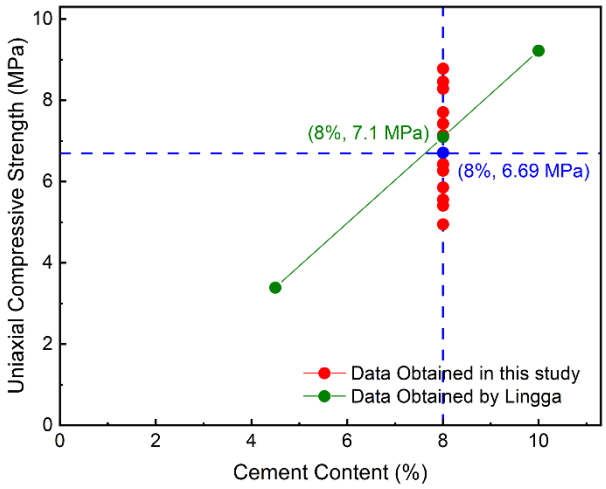

Fig. 3.7 Effect of the cement content on the UCS of the field CRF specimens.

Due to the limitation of the CRF sample quantity and laboratory test conditions, only five and three groups of triaxial compression tests at the confining pressure of 1.5 MPa and 2.5 MPa, respectively, were carried out on the field CRF specimens. Meanwhile, five uniaxial compression tests on the field CRF specimens buried at the same corresponding depths are chosen to match the triaxial compression tests, which can ensure the accuracy and rationality of the following calculations. Fig. 3.9 shows the peak axial stress (σ_p) of the field CRF specimens under the uniaxial and triaxial compression and the fitting curve of their average values at the confining pressures (σ_3) of 0 MPa, 1.5 MPa and 2.5 MPa.

The corresponding fitting formula is presented in Eq. 3.1 with a correlation coefficient (R^2) of 0.997:

$$\sigma_p = 7.56\sigma_3 + 6.55 \quad \textbf{(Eq. 3.1)}$$

At σ_3 of 1.5 MPa, the average value of σ_p is 17.53 MPa, with an s_d of 2.07 MPa and an c_v of 11%. When σ_3 is 2.5 MPa, the average value of σ_p is 25.66 MPa, with a s_d of 3.19 MPa and a c_v of 12%. These laboratory test data indicate that the individual difference between the triaxial compression tests on different field CRF specimens under the same confining pressure is relatively small, and the σ_p distribution is relatively uniform. It is mainly because the confining pressure constricts the microstructure inside the CRF material and automatically adjusts the micro-fissure and pore convergence degree of the specimen to be more uniform at different sub-stages of the triaxial compression test (Fall et al., 2007).

Fig. 3.8 depicts the Mohr-Coulomb strength criterion for the field CRF specimens under the uniaxial and triaxial compression at different σ_3 of 0 MPa, 1.5 MPa, and 2.5 MPa. The fitting formula of the linear envelope curve of the Mohr-Coulomb circles (Parry, 2004) is shown in Eq. 3.2, where τ is the shear strength of the field CRF specimens under different σ_3, and σ_m is the principal stress of the field CRF specimens during the compression tests. Through Eq. 3.2, the cohesion (c) and internal friction angle (φ) of the field CRF specimens can be calculated as 1.45 MPa, and 51.13°, respectively, and these values are within the reasonable ranges, compared with the previous studies (Lingga and Apel, 2018) in which the artificial CRF specimens with the same CRF material were tested.

$$\tau = 1.24\sigma_m + 1.45 \quad \textbf{(Eq. 3.2)}$$

Meanwhile, according to the previous studies (Farnam et al., 2010), the normalized form of the Mohr-Coulomb criterion can be expressed as Eq. 3.3:

$$\frac{\sigma_p}{\sigma_c} = 1 + k\left(\frac{\sigma_3}{\sigma_c}\right) \quad \textbf{(Eq. 3.3)}$$

In this equation, σ_c is the UCS of the field CRF specimen, with a value of 7.43 MPa chosen from the laboratory test data according to Fig. 3.8, σ_p/σ_c and σ_3/σ_c represent the triaxial strength ratio and confinement ratio of the field CRF specimen, respectively, and k_0 does Eq calculate a correlation factor. 3.4 as a value of 8.03:

$$k_0 = \frac{1 + sin\ \varphi}{1 - sin\ \varphi} \quad \textbf{(Eq. 3.4)}$$

Two fitting curves of σ_p-σ_3 the relationship derived from the normalized Mohr-Coulomb criterion and obtained from the OriginLab software, respectively, are also plotted in Fig. 3.9, and their corresponding formulas are expressed in Eq. 3.5 and Eq. 3.6, respectively:

$$\sigma_P = 8.03\sigma_3 + 7.43 \quad \textbf{(Eq. 3.5)}$$

$$\sigma_P = 8.38\sigma_3 + 7.51 \quad \textbf{(Eq. 3.6)}$$

It is proven that the relationship between σ_p and σ_3 of the field, CRF specimens conformed to the previous research (Fall et al., 2007; Zhao et al., 2019) on the cemented paste backfill or concrete as expected. As σ_3 increases, the average value of σ_p under the triaxial compression can significantly linearly-like increase. Meanwhile, R^2 of Eq. 3.5 and Eq. 3.6 are 0.989 and 0.998, respectively, which demonstrate that both curves can be used to predict σ_p of the field CRF specimens under the triaxial compression at different σ_3. It can also be validated that with a corresponding reasonable k_0 of 8.38, Eq. 3.6 has a good correlation and imitative effect on the relationship between σ_p and σ_3 when

compared with Eq. 3.5, which is derived from the normalized Mohr-Coulomb strength criterion.

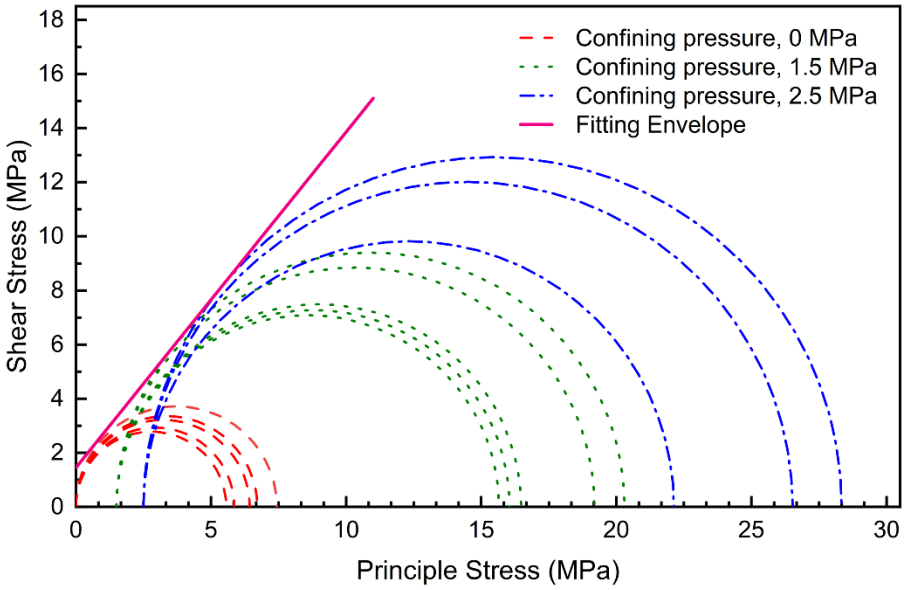

Fig. 3.8 Mohr's circles and Mohr-Coulomb strength criterion for the field CRF specimens.

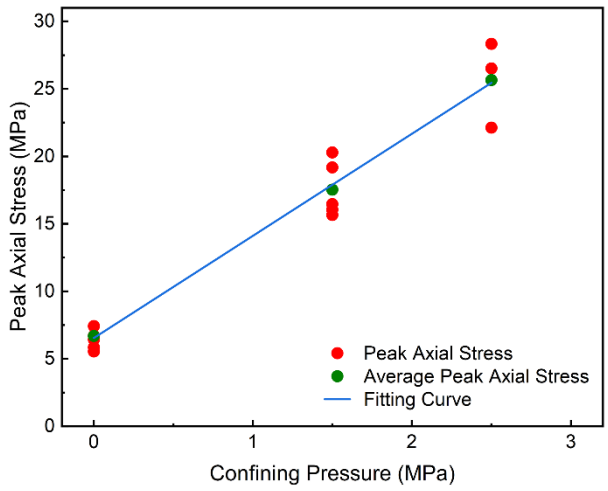

Fig. 3.9 σ_p - σ_3 curves of the field CRF specimens under the uniaxial and triaxial compression.

Fig. 3.10 indicates different failure modes of the representative field CRF specimens under the uniaxial and triaxial compression at σ_3 of 0 MPa, 1.5 MPa and 2.5 MPa. For the specimens under the uniaxial compression, several typical failure modes of concrete or concrete-like materials such as the cemented rockfill cemented paste backfill, rock-concrete mixture or cemented soil have been observed by previous studies (Liu et al., 2017; ASTM C39, 2018), including the diagonal shear, 'X'-cone shear, single or columnar split, and 'Y'-cone shear modes. A failure mode called corner fracture pattern is also discussed in ASTM Standard C39 for the concrete specimen under the uniaxial compression (ASTM C39, 2018).

In this study, among 15 groups of the field CRF specimens under the uniaxial compression, seven groups of the specimens show columnar failure mode (Fig. 10b), which is the most typical mode among these specimens. Moreover, 'Y'-cone shear mode appears in six groups of the specimens (Fig. 10a). Two groups of the specimens showed a failure mode of diagonal shear (Fig. 10c), while no 'X'-cone shear mode was observed among the specimens. During the uniaxial compression tests, as the same as the cemented paste backfill and concrete materials (Rankine and Sivakugan, 2007; Zhao et al., 2019), the specimens also show a brittle behaviour when reaching failure, with the stress-strain curves indicating the strain-softening effect. Meanwhile, microscopically from the failure surface of these specimens, it can be observed that micro-cracks mainly occur at the interface of coarse granitic particles of the CRF material and then converge into fractures with crushed fragments on the specimens. Compared with other concrete-like materials such as the cemented paste backfill and cemented soil, failure modes of the field CRF

material under the uniaxial compression depict more change due to the non-uniform particle size distribution.

As for triaxial compression tests, the diagonal shear is the most typical failure mode for brittle materials such as rock, concrete, and concrete-like materials under all levels of confining pressures (ASTM C39, 2018; Farnam et al., 2010; Zhang and Li, 2019). In this study, all eight groups of the specimens under the triaxial compression at σ_3 of 1.5 MPa and 2.5 MPa show a failure mode of diagonal shear (shown in Fig. 10d). The average observed angle (α) of the failure plane between the directions of axial stress and failure surface of the specimens is 68.5°. According to the Mohr-Coulomb strength criterion, the relationship between α and the internal friction angle (φ) is shown in Eq. 3.7, Eq. 3.8, and Eq. 3.9.

$$\tau = c + \sigma_m \tan\varphi = \frac{1}{2}(\sigma_1 - \sigma_3)\sin 2\alpha \quad \textbf{(Eq. 3.7)}$$

$$\sigma_1 = \frac{2c + \sigma_3[\sin 2\alpha + \tan\varphi\,(1 - \cos 2\alpha)]}{\sin 2\alpha - \tan\varphi\,(1 + \cos 2\alpha)} \quad \textbf{(Eq. 3.8)}$$

$$\alpha = \frac{\pi}{4} + \frac{\varphi}{2} \quad \textbf{(Eq. 3.9)}$$

Using Eq. 3.9, the calculated value of the orientation angle was 70.6°, which ideally corresponds with the observed average value on the field CRF specimens. Through microscopical observation on the failure surface of these field CRF specimens, the breakage and crushed fragments of the coarse granitic particles of the CRF material can be found along the surface. It indicated that the microstructure and micro-cracks inside these specimens under the triaxial compression are constricted to develop along the diagonal shear failure surface due to the confining pressure. Meanwhile, the effect of the

confining pressure on the micro-fissure convergence is much more significant than the effect of the uniform particle size distribution of the CRF material.

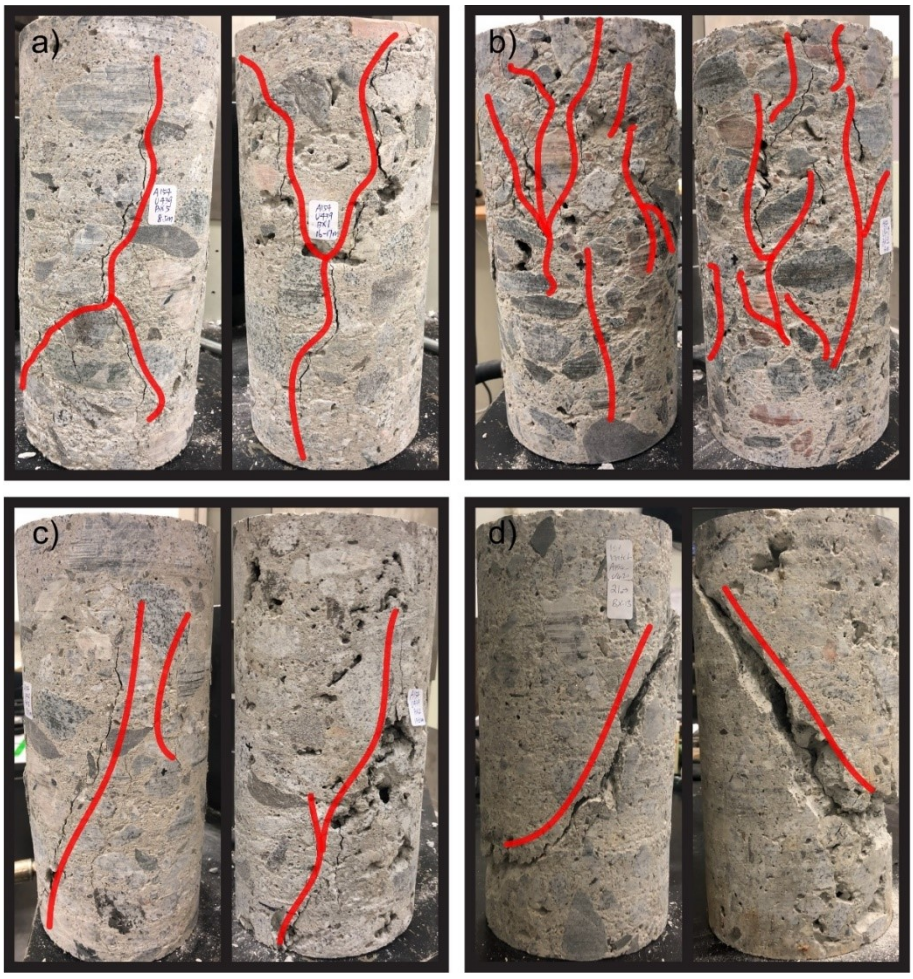

Fig. 3.10 Failure pattern of the representative field CRF specimens under the uniaxial and triaxial compression: a) corner failure mode, b) columnar failure mode, c) diagonal failure mode under the uniaxial compression, and d) diagonal failure mode under the triaxial compression.

3.4 Conclusions

In this study, the uniaxial and triaxial compression tests were carried out on the large-scale cylindrical specimens made of the field cemented rockfill (CRF) core samples drilled

at two boreholes in the horizontal and vertical directions in a backfilled stope from a Canadian hard rock mine.

The CRF material collected from the Canadian hard rock mine is a concrete-like material, and the stress-strain behaviour of the CRF core specimens under the uniaxial compression can be divided into four main stages of pore compaction, elastic deformation, stable micro-crack propagation and strain-softening post-failure, during which the CRF material shows obvious elastoplastic deformation due to the continuous micro-crack generation and convergence.

Along the vertical drilling direction, the segregation phenomenon inside the CRF columns causes the rearrangement of the CRF material particles and the appearance of lower porosity and higher cement content at the top column part. Finally, it leads to the fluctuating distribution of the uniaxial compressive strength of the CRF core specimens that the higher values appear at the shallow depth of the underground backfill stope. However, along the horizontal drilling direction, the uniaxial compressive strength of the specimens showed a significant downtrend distribution that the nearer the point in the column is from the CRF discharge point, the higher the uniaxial compressive strength can be, due to the multi-stage compression and consolidation processes. Young's modulus of the specimens fluctuates and distributes dispersedly along the vertical drilling direction due to the multi-stage pouring of the fresh CRF material. However, it shows a much evener distribution along the horizontal drilling direction. The Poisson's ratio of the specimens fluctuates dramatically either along the vertical or horizontal drilling direction, and no evident distribution regularities were found.

Meanwhile, the limitation from the point measurement method adopted by the LVDTs is an actual cause for the unstable laboratory test data of Poisson's ratio. Compared with previous research by Lingga and Apel (2018), it indicates that the strength requirement of the CRF column is still met at the hard rock mine. However, a significant non-uniform distribution exists in the UCS at different parts of the CRF column.

The peak axial stress of the specimens shows a linear-like positive correlation with the confining pressure. Their fitting formula has a good correlation and imitative effect on their relationship, which is highly agreed with the normalized equation of the Mohr-Coulomb strength criterion of the specimens. For the CRF core specimens under the uniaxial compression, the failure modes of columnar failure, 'Y'-cone shear, and diagonal shear can be observed, and for the specimens under the triaxial compression, all the specimens show an evident failure mode of diagonal shear, of which the observed orientation angle between the directions of axial stress and the failure surface of the specimen is highly agreed with the value calculated by the Mohr-Coulomb strength criterion.

The lowest UCS value of the CRF column at the Canadian diamond mine is much greater than the calculated required UCS according to the modified Mitchell's analytical model. It indicates that the CRF column has an excellent stability condition and no potential failure risks occur. Even the segregation phenomenon was found in the CRF column, leading to the dispersed distribution of the UCS of different parts of the CRF column.

Chapter 4 Discrete element method for modelling the uniaxial and triaxial compression tests on the cemented rockfill specimen

In this chapter, numerical the uniaxial and triaxial compression tests were carried out on two discrete elements (DE) models of the cemented rockfill (CRF) specimens, which are with the simplified particle size distribution and mean particle diameter, respectively. The microstructural parameters of the two DE models were well calibrated to ensure the overall mechanical properties perfectly coincide with the laboratory test results of the real CRF specimens under the uniaxial and triaxial compression. This study first calibrated the strength characteristics and failure pattern of the DE models of the CRF specimens under the triaxial compression. According to the Mohr-Coulomb failure criterion, the modelling results highly agreed with the laboratory test results. Meanwhile, the modelling results indicate that the particle size distribution and the model-particle diameter ratio significantly influence the overall mechanical properties and fragment evolution of the DE models of the CRF specimens.

4.1 Introduction

Numerical modeling is an effective technique to comprehend the stress-strain behaviour and the mechanical properties of backfill materials and predict the stability of backfill columns and underground mined-out areas under different geological conditions. Three main numerical modeling approaches were adopted by plentiful previous research to study the backfill mechanics, including the finite difference (FD) method (Nasir and Fall, 2010, 2008; Li and Aubertin, 2015), finite element (FE) method (Helinski et al., 2010, 2010; Cui et al., 2016), and discrete element (DE) method (Potyondy, 2015; Ding et al., 2014; Li et al., 2014; Liu et al., 2017; Wu et al., 2018). For the FD and FE methods, which

are categorized as continuum methods (Ding et al., 2014), most previous studies on the backfill materials mainly focused on the mechanical interaction between the underground backfilled stopes and the backfill columns (Falaknaz et al., 2015, 2015), the stress-strain behaviour at the backfill-rock and backfill-backfill interfaces (Liu et al., 2017; Li and Aubertin, 2015), and the stress distribution at the backfill columns and underground backfilled stopes (Pirapakaran and Sivakugan, 2007; Li and Aubertin, 2015; Falaknaz et al., 2015). The results from these numerical simulations revealed that the backfill columns largely enhance the stability of the underground mined-out areas, and the arching phenomenon occurred inside the backfill columns significantly influences the stress distribution at the underground backfilled stopes, which commences at the rock-backfill interfaces and is related to the stope geometry. Meanwhile, some research (Emad et al., 2012; Emad et al., 2014) focused on the dynamic characteristics of backfill columns under impact loading and blast-induced vibration by constructing numerical models of adjacent excavated and backfilled stopes underground.

Although these conventional continuum approaches of FD and FE methods show high computational efficiency when conducting numerical simulations, they may generate serious errors when model the large-strain deformation and post-failure behaviour in geotechnical problems (Li and Liu, 2002), compared with the FD and FE methods, the discontinuum approach of the DE method has advantages in simulating the large discontinuous deformation and exhibiting the fracture initiation and propagation explicitly (Li et al., 2018; Zhang and Wong, 2012) due to the model realization with separate units and bonds (Potyondy and Cundall, 2004), although the work on the calibration process of the microstructural parameters may require a higher computational ability. A lot of

previous numerical research has adopted the DE method to study the mechanical properties and stress-strain behaviour of concrete and concrete-like materials (Camborde et al., 2000; Hentz et al., 2004; Hentz et al., 2004). In these studies, the laboratory tests were reconstructed numerically in the Software PFC or PFC3D, such as the uniaxial compression test (Suchorzewski et al., 2018; Wang et al., 2008) and triaxial compression test (Tran et al., 2011; Liu et al., 2017; Onate et al., 2015), to simulate the micro-crack propagation and macro-fracture evolution. Furthermore, through the calibration process of the microstructural parameters of these DE models (Lian et al., 2011; Tran et al., 2011), the strength characteristics and overall deformation properties were validated with the laboratory test data obtained from the real specimens. The most concerning areas involved in the previous research were the effects of particle size distribution and model scale (Suchorzewski et al., 2018; Liu et al., 2012), the particle shape and microstructure reconstruction (Sun et al., 2017; You et al., 2009; Zelelew and Papagiannakis, 2010) and the selection of the contact model among the discrete particles in the DE models (Liu et al., 2019; Liu and You, 2009).

However, very few studies based on the backfill materials of CPB and CRF used the discontinuum approach of the DE method. Sun et al. (2017) reconstructed the microstructure of the CPB specimens numerically using the DE method Software PFC, according to the X-ray CT scanned images in the laboratory, to study the effect of the pore structure on the stress-strain behaviour. Liu et al. (2019) proposed a new microstructural hydration model to study the internal sulfate attacks to the strength evolution of the CPB material using the DE method. In a previous study from Liu et al. (2017), the cement and tailings particles inside the CPB specimens were created separately with software PFC3D

and the numerical triaxial compression tests were conducted to study the influence of the cement particle numbers on the stress-strain behaviour of the CPB material. According to the Talbot Theory, Wu et al. (2018) conducted uniaxial compression tests on artificial CRF specimens with different particle size distributions. Then, the numerical models were created in PFC3D to validate the effects of particle size distribution on the mechanical properties of the CRF materials. These studies revealed the important role of the microstructure in the strength evolution of the backfill materials, and the modelling results all highly agreed with the corresponding laboratory test results, such as the uniaxial compressive strength and Young's modulus and the shape of the stress-strain curves of the backfill specimens under the uniaxial compression.

However, in these previous studies, the mechanical properties and stress-strain behaviour of backfill materials under the triaxial compression were not calibrated. In underground backfilled stopes, backfill columns undergo the confining pressure which is from the surrounding walls and present an obvious shear failure mode. So, it may not be very representative if only the backfill material's uniaxial compressive strength of the DE model is calibrated. Thus, it is essential to calibrate the internal friction angle and cohesion according to the Mohr-Coulomb failure criterion (Brady and Brown, 2013) when simulating the stress-strain behaviour of backfill materials under the triaxial compression by using the discontinuum approach of the DE method in PFC (Huang et al., 2016). In this study, the mechanical properties and stress-strain behaviour of the DE models of the CRF specimens under both the uniaxial and triaxial compression will be calibrated by comparing the numerical modelling with the laboratory test data.

4.2 Material and methodology

4.2.1 Cemented rockfill

The cemented rockfill, comprised of aggregate particles with variously distributed sizes and bonded by the cement particles, can be considered a porous-bonded material (Jongpradist, 2010; Wu et al., 2018). In this study, the cemented rockfill (CRF), which was collected from a hard rock mine in Northwest Territories, Canada (Sepehri et al., 2017), was simulated with the DE method to study the stress-strain behaviour by conducting numerical the uniaxial and triaxial compression tests under different confining pressures on the DE model of the CRF specimen. The stress-strain behaviour, strength characteristics, and deformation properties of the field CRF material have been discussed in Chapter 3, and the mechanical properties of the CRF material that will be simulated in this study are listed in Table 4.1. The mechanical properties of the DE model of the CRF specimen were the average values of the real CRF specimens on which the uniaxial and triaxial compression tests were conducted in the laboratory. In addition, microstructural parameters of the parallel bond contact model applied among the discrete particles in the DE model of the CRF specimen were determined to ensure the overall mechanical properties of the DE model are the same as the real representative CRF specimen in the laboratory.

Table 4.1 Physical-mechanical properties of the CRF specimens.

Category	Values
Young's modulus (GPa)	4.45
Poisson's ratio	0.24
Uniaxial compressive strength (MPa)	7.43
Peak axial stress (MPa) under confining pressure of 1.5 MPa	20.3

Peak axial stress (MPa) under confining pressure of 2.5 MPa	28.2

4.2.2 Parallel bond contact model

In PFC3D Version 6.0, twelve built-in contact models are provided to simulate different microstructural contact behaviours between particles and walls, including four linear-based models, namely the linear contact bond, linear parallel bond, flat joint, and smooth joint contact models. They can be employed in numerical simulations to create bonded-particle models to mimic the bonded materials. In this study, the linear parallel bond (PB) contact model in PFC3D Software was adopted to simulate the mechanical behaviour and binding effect of the cement among aggregate particles of the CRF material due to its anastomotic mechanical behaviour with the field CRF core samples.

The behaviour summary, rheological components, and the activity-deletion criterion of the linear PB contact model have been shown in Fig. 4.1. Within the PB contact model, virtual cement-like bonds, which are deformable and breakable, exist at the contact positions among the discrete particles. Two interfaces are created at the contact position with groups of parallel springs, bonds, and dashpots. Interface one is linear elastic frictional without tension, representing the linear bond, and interface two is linear elastic bonded, representing the parallel bond. The contact force ($\boldsymbol{F}_c$) and the motion ($\boldsymbol{M}_c$) at the bond follow the force-displacement law:

$$\boldsymbol{F}_c = \boldsymbol{F}_l + \boldsymbol{F}_d + \boldsymbol{F}_p \qquad \textbf{(Eq. 4.1)}$$

$$\boldsymbol{M}_c = \boldsymbol{M}_p \qquad \textbf{(Eq. 4.2)}$$

where $\boldsymbol{F}_l$ is the linear contact force, $\boldsymbol{F}_d$ is the dashpot force and $\boldsymbol{F}_p$ is the parallel bond contact force. $\boldsymbol{M}_p$ is the parallel bond contact moment. The governing equations and activity-deletion criteria for the update mechanism of $\boldsymbol{F}_c$ and $\boldsymbol{M}_c$ in the PB contact model are not reiterated here since they have been studied in many previous studies (Wu et al., 2018). By following the force-displacement and motion laws, forces and moments can be transmitted between the discrete particles through the virtual interfaces. Then, with the positions of the discrete particles and walls updated, the stress state in the DE model changes. Microstructural breakage occurs when the bond's maximum stress exceeds the shear or normal strength at the contact position.

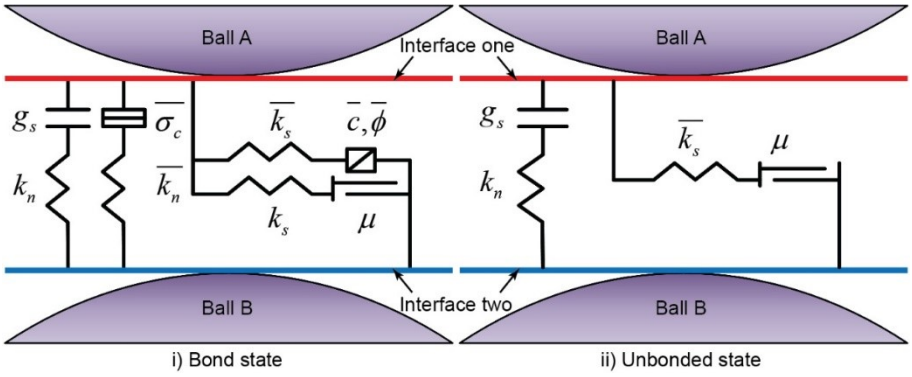

Fig. 4.1 Parallel bond contact model.

4.3 Numerical simulation

4.3.1 Model establishment

It can be seen from Fig. 4.2a that the DE model of the cylindrical CRF specimens, with dimensions of 152.4 mm × 304.8 mm (diameter × height), was constructed, conforming to the sizes of the CRF specimens used in large-scale the uniaxial and triaxial compression tests in the laboratory. Also, to eliminate the size effect, the length-diameter ratio of these DE models of the CRF specimens was designed to be 2:1, and the model diameter was

three times the maximum size of the particles of these DE models of the CRF specimens, following the recommendations in American Society for Testing and Materials (ASTM Standard C39, 2012). Furthermore, the ball clouds in these created DE models of the CRF specimens were generated randomly by the boundary contraction method with an initial void ratio of 0.58, according to the simplified particle size distribution shown in Fig. 4.2. Compared with the true particle size distribution of the CRF specimens, a group of small particles with diameters smaller than 2.0 mm were magnified to those particles with a medium diameter of 3.375 mm in the simplified particle size distribution. Hence, the total number of particles generated in the DE model of the CRF specimens was reduced and the calculation time of the simulation process was saved (Wu et al., 2018; Bock and Prusek, 2015; Liu, 2012).

It should be noted here that previous studies have indicated that it was quite hard to comprehend the determination of the mass fraction of the binder particles in the numerical simulation with the discrete element method due to the multiple stages of the complex hydration process (Wu et al., 2018). Thus, in this study, the density and mass fraction of the Portland cement particles were converted into those of the balls in the DE model of the CRF specimens since their sizes were much finer than the granitic aggregate particles of CRF core samples. And the binding effects among the Portland cement particles were also converted into those among the particles inside the DE model of the CRF specimens. After the bonds were installed and microstructural parameters set, all the velocities, spins, contact forces and moments were nulled and fixed at zero initially with a few cycles of calculations to ensure that the DE model of the CRF specimens finally reach an equilibrium with no internal stresses remained.

The uniaxial and triaxial compression tests were simulated to carry out on the DE model of the CRF specimens using software PFC3D to calibrate the microstructural parameters and investigate the influence of model and particle sizes on the overall mechanical properties of the DE model of the CRF specimens. Fig. 4.3a has shown that for numerical triaxial compression tests, a rigid cylindrical vessel was created to wrap the DE model of the CRF specimens to simulate the large-scale Hoek triaxial cell to maintain a stable confining pressure through calling embedded servo-control functions in the PFC3D Software. Meanwhile, two horizontal walls were created at the top and bottom surfaces of the DE model of the CRF specimens, respectively, to simulate the pair of spherical seat platens. While for numerical uniaxial compression tests, the rigid cylindrical vessel was deleted before the test started and then no confining pressure was applied to the DE model of the CRF specimens. Same with the laboratory experiments, the axial pressure continued loading under constant displacement control until the CRF specimens' DE model reached the failure, by squeezing the top and bottom horizontal walls. In this study, to ensure the quasi-static loading states to be sufficiently provided and to save the calculation time during the numerical tests, the axial strain rate was set to be 0.05 m/s and the loading velocity of the top-bottom wall pair was set to be 0.00762 m/s, of which the values are sufficiently low to maintain the DE model of the CRF specimens staying at a quasi-static equilibrium during the entire compression process of the tests (Ding et al., 2014; Li et al., 2018; Wu et al., 2018). During the numerical tests, the axial stress, axial, and radial strain of the DE model of the CRF specimens were measured through three spherical measurement regions that were placed symmetrically along the axis of the largest vessel dimension, which is described in PFC3D Version 6.0 Manual. Meanwhile, the force-chain fabric, cracking, and fragment development in the DE model of the CRF

specimens was also observed and monitored during the numerical uniaxial and triaxial compression tests.

Meanwhile, to investigate the influence of model and particle sizes on the overall mechanical properties of the CRF specimens, six groups of the DE model of the CRF specimens with different diameter ratios (D/d) of 10, 15, 20, 25, 30, and 35 were constructed, shown in Fig. 4.3b. The sizes of the particles in each model were uniform, and the D and d here refer to the diameter of each numerical model and the maximum diameter of the particles inside the DE model of the CRF specimens, respectively (Ding et al., 2014). It should be mentioned here that for the DE model with a D/d of 15, the diameter of the particles is 10.0 mm, which is precisely the mean particle diameter of the real CRF core samples with an accurate particle size distribution, calculated by the formula Eq. 4.3 (Kemper and Rosenau, 1986). In this equation, D_m represents the mean diameter of the particles inside the DE model of the CRF specimens, and d_i and ω_i are the mean diameter and mass fraction of each aggregate class, respectively.

$$D_m = \sum_{i=1}^{n} d_i \omega_i \qquad \textbf{(Eq. 4.3)}$$

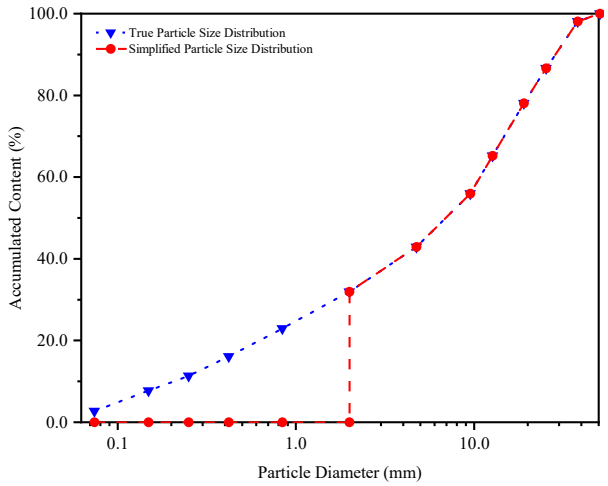

Fig. 4.2 Simplified particle size distribution of the CRF aggregates.

Table 4.2 Microstructural parameters of PB contact model in the DE model of the CRF specimens with the simplified particle size distribution.

Category	Values
Bulk Density (kg/m^3)	2281.8
Initial particle-cloud porosity	0.58
Installation gap of the parallel bond (m)	0.001
Young's modulus of the particles (GPa)	6.59
Young's modulus of the parallel bond (GPa)	6.59
Stiffness ratio of the particles	4.5
Stiffness ratio of the parallel bond	4.5
Normal strength of the parallel bond (MPa)	7.35
Shear strength of the parallel bond (MPa)	4.99
Internal friction angle of the parallel bond (°)	51.0
Friction coefficient of the particles	0.87

Friction coefficient of the parallel bond	0.87

Table 4.3 Microstructural parameters of PB contact model in the DE model of the CRF specimens with the mean particle diameter.

Category	Values
Bulk Density (kg/m^3)	2281.8
Initial particle-cloud porosity	0.20
Installation gap of the parallel bond (m)	0.001
Young's modulus of the particles (GPa)	3.67
Young's modulus of the parallel bond (GPa)	3.67
Stiffness ratio of the particles	4.0
Stiffness ratio of the parallel bond	4.0
Normal strength of the parallel bond (MPa)	15.5
Shear strength of the parallel bond (MPa)	2.61
Internal friction angle of the parallel bond (°)	51.0
Friction coefficient of the particles	0.87
Friction coefficient of the parallel bond	0.87

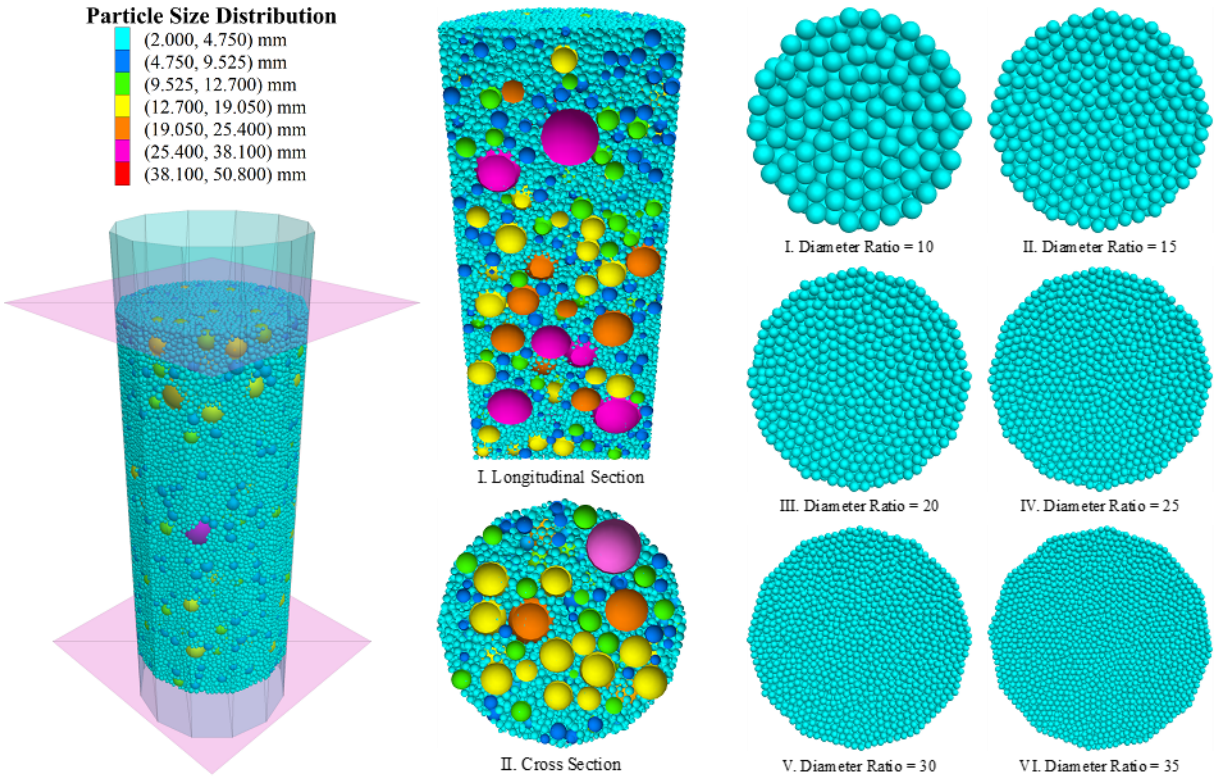

Fig. 4.3 Uniaxial and triaxial compression tests on the DE model of the CRF specimens with a) simplified particle size distribution and b) different particle diameter ratios.

For the DE model of the CRF specimens with the simplified particle size distribution, 42,547 balls were generated using the grain scaling method, according to the seven intervals of the mass fractions of the CRF particles, with an initial ball-cloud porosity of 0.58. While for the DE model of the CRF specimens with the mean particle diameter, the boundary contraction method was adopted, and a total of 8,128 balls were generated with an initial ball-cloud porosity of 0.2. Both packing methods can produce the same dense-packed contact state of bonded materials. The chosen initial ball-cloud porosity values corresponded with the initial loose and dense contact states of the two kinds of granular CRF material, respectively, before the grain scaling and boundary contraction procedures, commenced. Installation gap ($\bar{g}$) is an important parameter to determine the bond

numbers and the grain connectivity inside the DE model of the CRF specimens. To choose an appropriate value, it should be less than the ratio of the smallest to the largest diameter of the particles inside the DE model of the CRF specimens and ensure a fit average coordination number of the generated DE model of the CRF specimens (Fan et al., 2018). The Young's modulus, stiffness ratio and strengths of the particles and bonds are considered as three groups of the dominant microstructural parameters to influence the overall mechanical properties of the DE model of the CRF specimens, which mainly control Young's modulus, Poisson's ratio, and strength behaviour of the DE model of the CRF specimens (Ding et al., 2014; Li et al., 2018). Although the two kinds of the DE model of the CRF specimens showed a high degree of consistency in overall mechanical properties with each other, the microstructural parameters were significantly different due to the huge difference in particle and bond numbers and particle size distributions. Meanwhile, the calibrated overall mechanical properties of the DE model of the CRF specimens were not very sensitive to the bond friction angle and friction coefficient of the particles and bonds of the DE model of the CRF specimens, which were set to be 51° and 0.87, respectively, and equal to the corresponding internal friction angle and friction coefficient of the CRF specimens, respectively.

4.3.2 Parameter determination

In the numerical simulations with the DE method, the calibration between the microstructural parameters of the DE model of the CRF specimens to the overall mechanical properties of the CRF specimens obtained from the laboratory tests is considered a key fundamental procedure. The common microstructural parameters of the DE model of the CRF specimens mainly include the grain density (ρ), which is the bulk

density after the mass fraction of cement particles being converted, and the initial void ratio (n_c) before the particle packing process through grain scaling and boundary contraction methods. Additionally, for the DE model of the CRF specimens employed with the PB contact model, the microstructural parameters mainly consist of two groups, namely the linear material group and the parallel bonded material group, according to the different mechanical functions of the two groups of the rheological components.

The flowcharts of the modified calibration procedures for the microstructural parameters of the DE model of the CRF specimens are shown in Fig. 4.4 (Li et al., 2018; Wu et al., 2018). First, the installation gap ($\hat{g}$) of the parallel bonds inside the DE model of the CRF specimens was determined so that the parallel bonded contact number was determined. Second, Young's modulus (E), Poisson's ratio (η_p), uniaxial compressive strength (σ_c) and post-peak behaviour of the CRF specimens under uniaxial compression were calibrated by assigning appropriate values of particle and bond Young's modulus (E and $\bar{E}$), particle and bond normal to shear stiffness ratio (k_n/k_s and $\bar{k}_n/\bar{k}_s$), bond normal and shear strength ($\bar{\sigma}$ and $\bar{\tau}$), and particle and bond friction coefficient (μ and $\bar{\mu}$) of the DE model of the CRF specimens. Third, the peak axial stress (σ_p) under different confining pressures (σ_3), internal friction angle (φ) and cohesion (c) of the specimens were calibrated by mainly adjusting the bond normal and shear strength ($\bar{\sigma}$ and $\bar{\tau}$) of the DE model of the CRF specimens. Finally, the main overall mechanical properties and behaviour of the calibrated DE model of the CRF specimens were highly consistent with the laboratory test results of the real CRF specimens, of which the typical values for the numerical calibration process are shown in Table 4.2.

It should be mentioned that for the Young's modulus and Poisson's ratio of the specimens, their average values obtained from the 15 groups of the uniaxial compression tests were selected as the standard values, while for the uniaxial compressive strength and peak axial stress under different confining pressures of the specimens, the standard values were chosen specifically from three groups of the laboratory test data obtained from the uniaxial and triaxial compression tests, with which the internal friction angle and cohesion of the specimens can be calculated, as they matched with the Mohr-Coulomb strength criteria ideally and their Mohr's circles were tangent to the envelope curve of the criterion. The category of the relevant microstructural parameters and their calibration results for the DE model of the CRF specimens with the simplified particle size distribution and mean particle diameter of 10 mm, are shown in Table 4.2. Meanwhile, different microstructural parameter values of bond friction angle ($\bar{\varphi}$) were assigned to the DE model of the CRF specimens with the mean particle diameter to study the sensitivity of overall mechanical properties and stress-strain curve shape to the changes in microstructural parameters.

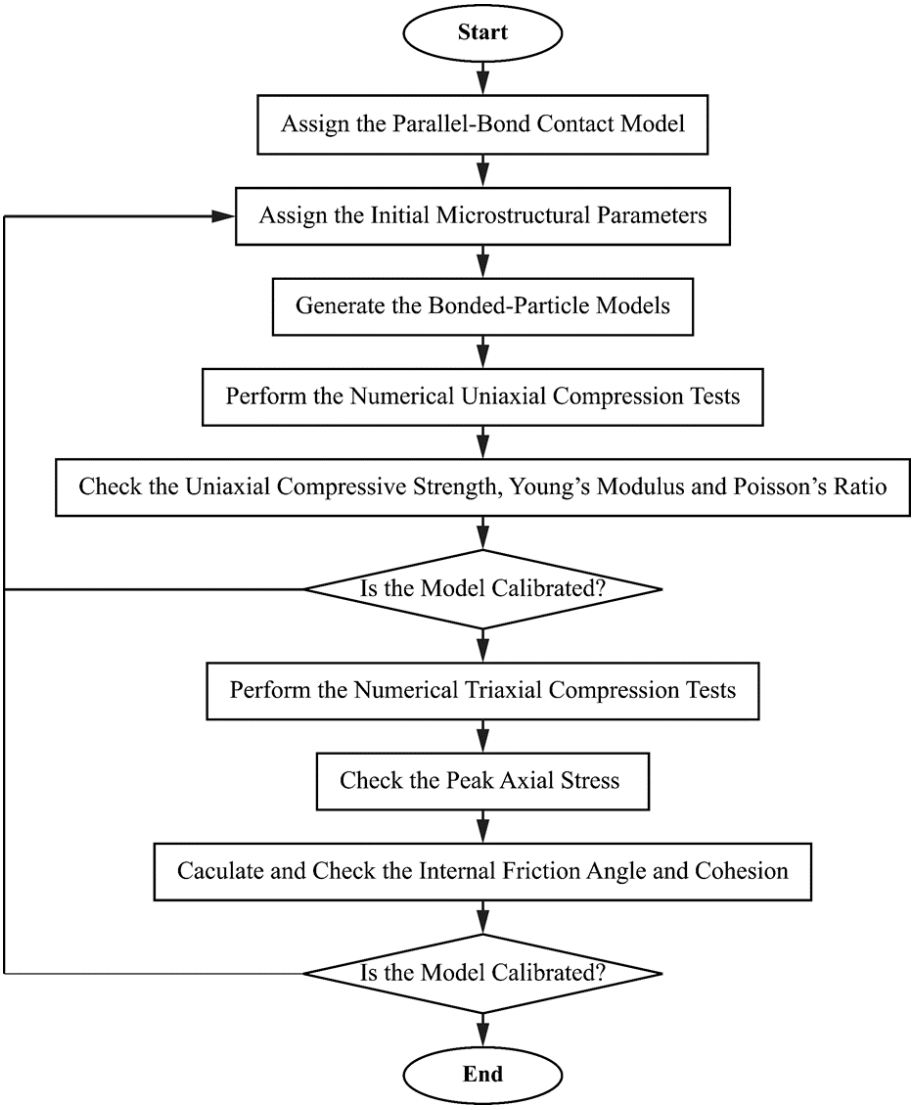

Fig. 4.4 Determination process of the microstructural parameters of the PB contact model in the DE model of the CRF specimens.

4.4 Results and discussion

4.4.1 Stress-strain behaviour and the mechanical properties of the DE model of the CRF specimen

According to the calibration results of the microstructural parameters of the DE model of the CRF specimens shown in Table 4.2, the complete stress-strain curve pairs of the DE

model of the CRF specimens with the simplified particle size distribution and mean particle diameter under numerical the uniaxial and triaxial compression are shown in Fig. 4.5a and Fig. 4.5b, respectively. For both the DE model of the CRF specimens with the simplified particle size distribution and mean particle diameter under the numerical uniaxial compression, the overall mechanical properties and the stress-strain behaviour of two kinds of the DE model of the CRF specimens were both well calibrated and in good agreement with those of the real CRF specimens. The Young's modulus and Poisson's ratio of these DE models of the CRF specimens, reflected by the slope of the axial stress-strain curves and radial-axial strain ratio of the stress-strain curves (Zhao et al., 2019), respectively, during the elastic deformation stage of the numerical uniaxial compression tests, were ideally conforming to the standard average values which were calculated from those laboratory test data of the CRF specimens. The peak axial stress of the two kinds of the DE model of the CRF specimens under the numerical uniaxial compression, with values of 7.47 MPa and 7.44 MPa, both ideally matched with the uniaxial compressive strength of the specimens selected from laboratory test data according to the Mohr-Coulomb strength criterion of the specimens (Brady and Brown, 2013). Compared with the laboratory stress-strain curve pairs of the specimens under the uniaxial compression, no evident pore compaction stages were observed on the two corresponding numerical curve pairs of the DE model of the CRF specimens shown in Fig. 4.5a and Fig. 4.5b, although both the slopes of the axial stress-strain curves of the two kinds of the DE model of the CRF specimens experienced very tiny and smooth increase at the initial period of the stress-strain behaviour. This is mainly because the strength of the parallel bonds between the particles was assigned to be homogenous inside the DE model of the CRF specimens, and the initial internal stress and strain were zeroed at the beginning. Thus,

no bond breakage occurred when the axial compressive load was quite low, and no micro-fissure and pore convergence occurred during the initial period of the numerical uniaxial compression tests. However, inside the real CRF material, the binding effect of the Portland cement among the granitic aggregate was inhomogeneous, and the initial micro-fissures and pores were ununiformly generated and then distributed at the beginning of the laboratory tests. The same situations occurred in previous studies (Fall et al., 2007; Zhao et al., 2019) on cemented paste backfill and concrete-like materials. During the post-failure stage of the numerical uniaxial compression tests on the DE model of the CRF specimens, both two kinds of the DE model of the CRF specimens showed obvious brittle response behaviour, and the curves indicated obvious strain softening (Rankine and Sivakugan, 2007), which were highly consistent with those curves obtained from the laboratory tests on the real CRF specimens.

For the DE model of the CRF specimens with the simplified particle size distribution and mean particle diameter under the numerical triaxial compression, the evolution law of the stress-strain behaviour of the DE model of the CRF specimens conformed to the previous laboratory and numerical studies on cemented paste backfill, concrete or concrete-like materials (Liu, et al., 2017; Huang, et al., 2016; Zhao et al., 2019). Similar to the DE model of the CRF specimens under the numerical uniaxial compression, no evident pore compaction stages were found at the initial period of the stress-strain behaviour of both the two kinds of the DE model of the CRF specimens under the numerical triaxial compression at confining pressures of 1.5 MPa and 2.5 MPa. Meanwhile, during the elastic deformation stage of numerical triaxial compression tests on the DE model of the CRF specimens, regardless of different confining pressure

conditions, the slope of the axial stress-strain curves maintained stable with values of elastic modulus of 7.38 GPa and 4.66 GPa, respectively, for the DE model of the CRF specimens with the simplified particle size distribution and mean particle diameter. It showed that during the numerical triaxial compression tests, increases in the confining pressure exerted very little influence on the elastic modulus of the DE model of the CRF specimens, while for the laboratory tests, the situations were different according to various geo-materials (Huang et al., 2016; Zhao et al., 2019). Under the confining pressure of 1.5 MPa, the micro-cracks inside the two kinds of the DE model of the CRF specimens started to expand when the axial strain reached around 0.25%. This value was postponed to 0.30% when the confining pressure increased to 2.5 MPa, and then the micro-crack propagation stage of the numerical triaxial compression tests on the two kinds of the DE model of the CRF specimens commenced. However, compared with the DE model of the CRF specimens with the simplified particle size distribution, the model with the mean particle diameter demonstrated a smaller elastic modulus at the elastic deformation stage and a more concave curve shape at the micro-crack propagation stage of the numerical triaxial compression test. This phenomenon resulted from a synthetical effect of the particle size distribution, particle and bond numbers, and microstructural parameter settings of the DE model of the CRF specimens. Meanwhile, unstable micro-crack propagation can be observed around the peak axial stress of the two kinds of the DE model of the CRF specimens under numerical triaxial compression, regardless of different confining pressure conditions of 1.5 MPa and 2.5 MPa, and the two kinds of the DE model of the CRF specimens both experienced a rapid stable deformation period before unstable failure occurred during the post-failure stage of the numerical tests.

It should be noted that previous studies have shown that for the DE model of the CRF specimens employed with the flat-joint contact model, the bond friction angle usually depends linearly on the macroscopic friction angle (Li et al., 2018). While due to the unquantifiability of the stress-strain curve shape of the specimens, a parametric study was carried out on the DE model of the CRF specimens to analyze the effects of these two microstructural parameters on the stress-strain behaviour of the DE model of the CRF specimens employed with PB contact model, during the micro-crack propagation and the post-failure stages in this study. Fig. 4.6 shows the complete stress-strain curve pairs of the DE model of the CRF specimens with the mean particle diameter under the numerical uniaxial compression, with different bond friction angles ($\bar{\varphi}$) of 49, 51, 53, 55, 57 and 59 degrees. Apparently, with the bond friction angle increased from 49° to 59°, there is a relatively small decrease of 11.2% in the uniaxial compressive strength of the DE model of the CRF specimens. However, Young's modulus and Poisson's ratio were neither sensitive to the changes in bond friction angle of the DE model of the CRF specimens, which remain the same at 4.45 GPa and 0.242, respectively. It can be seen from Fig. 4.6 that the larger the bond friction angle was, the earlier the micro-crack inside the DE model of the CRF specimens started to expand, and the more concave the curves were at this stage. Meanwhile, at the post-failure stage of the numerical uniaxial compression tests on the DE model of the CRF specimens, as the bond friction angle increased, the axial stress of the DE model of the CRF specimens after the peak value decreased more gently, which showed more gentle brittle failure response. It means that the bond friction angle is the main microstructural parameter that can control the stress-strain curve shape of the DE model of the CRF specimens at the micro-crack expansion and post-failure stages during the numerical tests.

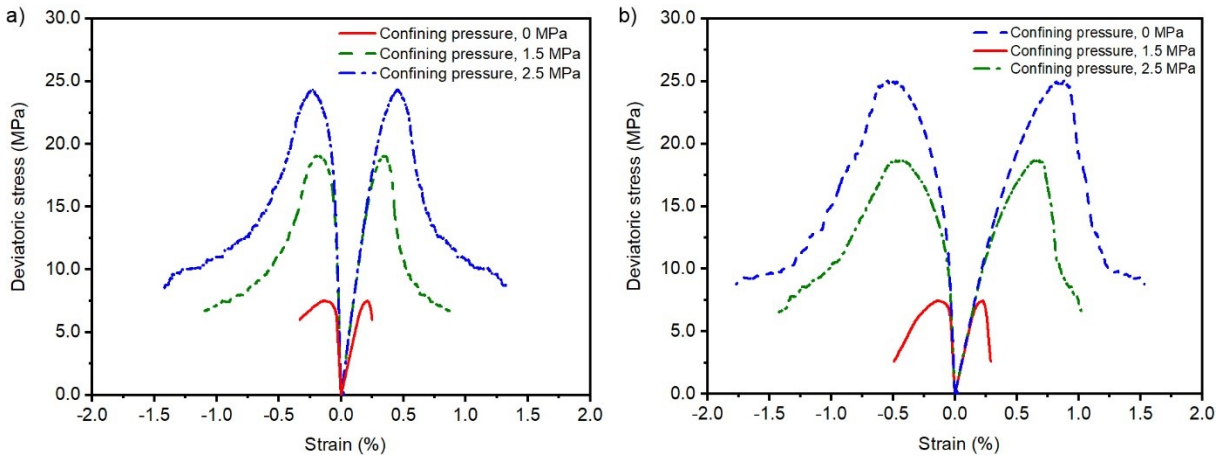

Fig. 4.5 $\sigma-\varepsilon$ curves of the DE model of the CRF specimens with a) simplified particle size distribution and b) mean particle diameter under the uniaxial and triaxial compression.

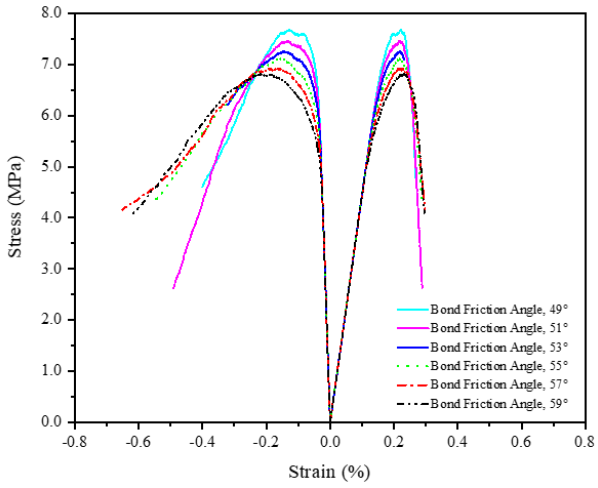

Fig. 4.6 Effect of $\bar{\varphi}$ of the PB contact model on the stress-strain behaviour of the DE model of the CRF specimens with the mean particle diameter under the uniaxial compression.

4.4.2 Strength characteristics and the failure pattern of the DE model of the CRF specimen

Fig. 4.7 depicts the peak axial stress (σ_p) and their fitting curves of the DE model of the CRF specimens with simplified particle size distribution and mean weighted particle

diameter under numerical uniaxial and triaxial compression at confining pressures (σ_3) of 0 MPa, 1.5 MPa and 2.5 MPa. The corresponding fitting formulas of the two kinds of the DE model of the CRF specimens are presented in Eq. 4.4 and Eq. 4.5 below, with correlation coefficients (R^2) of 0.994 and 0.998, respectively.

$$\sigma_p = 7.87\sigma_3 + 7.78 \quad \textbf{(Eq. 4.4)}$$

$$\sigma_p = 8.07\sigma_3 + 7.64 \quad \textbf{(Eq. 4.5)}$$

These peak axial stress values of the two kinds of the DE model of the CRF specimens were both in high agreement with those corresponding standard values selected from laboratory testing data of the specimens under uniaxial and triaxial compression according to the Mohr-Coulomb strength criterion. And the relationship between the σ_p and σ_3 of the two kinds of the DE model of the CRF specimens both ideally accorded with the previous numerical and laboratory studies (Camborde et al., 2000; Fall et al., 2007) on concrete or concrete-like material, as expected, that the σ_p increased linearly-like with the σ_3 increasing under numerical triaxial compression. It should be noted that although the simulated particles inside the DE model of the CRF specimen with mean particle diameter were homogenously distributed balls, and the ball numbers and microstructure were also totally different with those of the real CRF specimens, the peak axial stress values and their variation law still perfectly matched with the laboratory testing data of the specimens due to the microstructural parameter calibration process, which is considered as a key fundamental process for numerical modeling of the granular geomaterials (Potyondy et al., 2015). The Mohr-Coulomb strength criterion of the two kinds of the DE model of the CRF specimens under numerical triaxial compression are

shown in Fig. 4.8 and the corresponding fitting formulas of the linear envelope curves of the Mohr-Coulomb circles of the two kinds of the DE model of the CRF specimens are shown in Eq. 4.6 and Eq. 4.7, respectively, where τ_m is the shear strength of the DE model of the CRF specimens under different confining pressures, and σ_m is the principal stress of the DE model at the failure surface during the numerical tests (Brady and Brown, 2013).

$$\tau = 1.29\sigma_m + 1.32 \qquad \textbf{(Eq. 4.6)}$$

$$\tau = 1.28\sigma_m + 1.29 \qquad \textbf{(Eq. 4.7)}$$

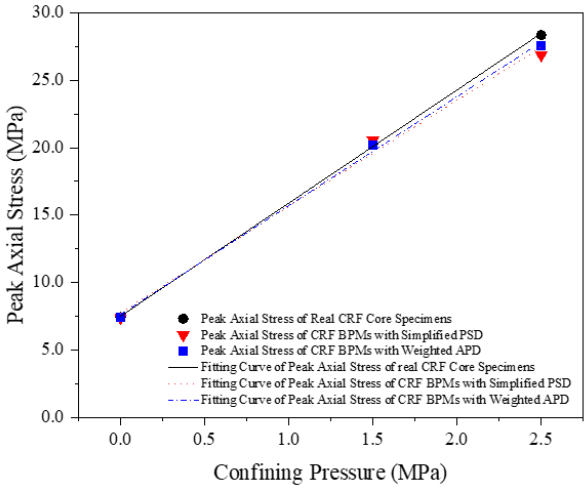

Fig. 4.7 σ_p-σ_3 curves of the DE model of the CRF specimens under the uniaxial and triaxial compression.

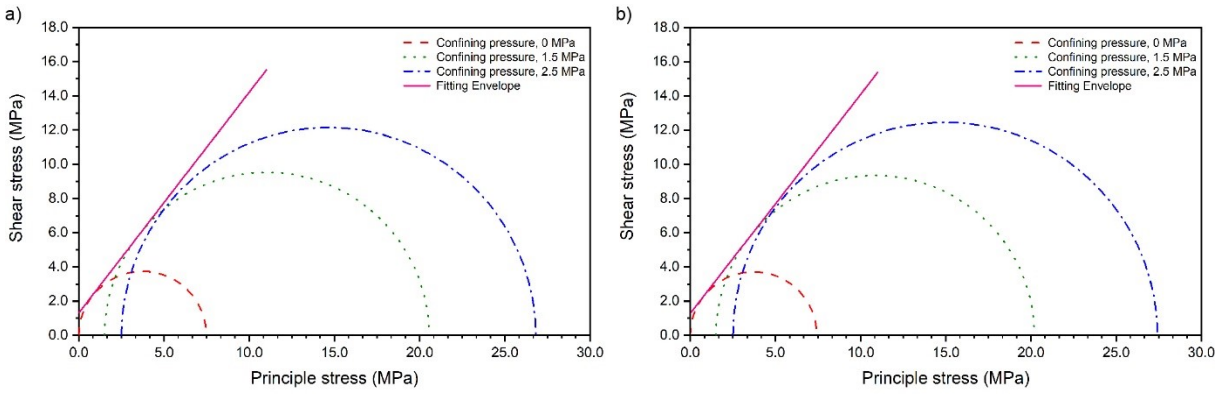

Fig. 4.8 Mohr's circles and Mohr-Coulomb strength criterion for the DE model of the CRF specimens with a) simplified particle size distribution and b) mean particle diameter.

The cohesion (c) and internal friction angle (φ) of the DE model of the CRF specimens with the simplified particle size distribution calculated from the Mohr-Coulomb strength criterion are 1.32 MPa and 52.2°, respectively. For the DE model of the CRF specimens with the mean particle diameter, these values are 1.29 MPa and 52.0°, respectively. These values obtained from the two kinds of the DE model of the CRF specimens were both highly conforming to the corresponding standard values selected from the laboratory test data of the CRF specimens under the triaxial compression, with average error values of 1.85% and 9.8% for the cohesion and internal friction angle, respectively. Compared Eq. 4.6 and Eq. 4.7 with Eq. 3.2, the curves from two kinds of the DE model of the CRF specimens can both simulate and predict the peak axial stress and the shear strength of the specimens under different confining pressures. Particularly, the k_0 value in Eq. 4.5 for the DE model of the CRF specimens with the mean particle diameter almost equal to the k_0 value calculated by Eq. 3.4 demonstrates the good correlation and imitative effects of the DE model of the CRF specimens on the specimens under the uniaxial and triaxial compression laboratory test data.

Fig. 4.9a and Fig. 4.9b depict the parallel bond states inside the DE model of the CRF specimens with the simplified particle size distribution and mean particle diameter, respectively, under numerical the uniaxial and triaxial compression at confining pressures of 0 MPa, 1.5 MPa and 2.5 MPa. For both the two kinds of the DE model of the CRF specimens employed the parallel bond contact model, three main bond states, including the bonded, unbonded-and-broke in shear, and unbonded-and-broke in tension, all existed inside the DE model of the CRF specimens under different confining pressures, which were denoted in the colour of light blue, dark blue and red, respectively in Fig. 4.9.

Under the numerical uniaxial compression, for both the two kinds of the DE model of the CRF specimens, the unbonded and broken parallel bonds are mainly located at the bottom, with a few bonds broken in shear distributed along some specific planes to the upper part of the DE model of the CRF specimens. Meanwhile, the quantities of tensile and shear failure of the bonds inside the DE model of the CRF specimens with the simplified particle size distribution were relatively balanced. However, the shear failure dominated the bond breakage inside the DE model of the CRF specimens with the mean particle diameter, which mainly resulted from the microstructural parameter assignment in the calibration process. It is much easier to break in shear than in tension for the bonds inside the DE model of the CRF specimens with the mean particle diameter, with a normal bond strength of 15.5 MPa, which is almost six times the bond shear strength of the DE model of the CRF specimens. In previous studies (Liu et al., 2017; Wu et al., 2018) on the cemented rockfill, this imbalance in strength values existed commonly, which mainly came from the relatively fewer particle and bond numbers, leading to large numbers of

bonds broke in shear at the early stages during the numerical uniaxial compression tests, compared with the DE model of the CRF specimens with the simplified particle size distribution.

Under the confining pressure of 1.5 MPa, for both the two kinds of the DE model of the CRF specimens, the unbonded and broken bonds mainly appeared near the diagonal surface, with some bonds broken in shear distributed throughout the DE model of the CRF specimens. Meanwhile, a few bond breakage dominated by tensile failure occurred along an inclined surface intersected with the diagonal surface of the two kinds of the DE model of the CRF specimens, which was more evident to be observed on the DE model of the CRF specimens with the simplified particle size distribution due to the ununiformly distributed particle size and numbers. Under the confining pressure of 2.5 MPa, the bond breakage inside the two kinds of the DE model of the CRF specimens became more intense, compared with the parallel bond states of the DE model of the CRF specimens under the numerical triaxial compression at the confining pressure of 1.5 MPa, and the unbonded and broken bonds still distributed along the diagonal surface and the corresponding intersected inclined surface for both the two kinds of the DE model of the CRF specimens. While a significant increase in the number of bonds broken in shear can be observed during the later period of the numerical triaxial compression tests, the tensile failure no longer dominated the bond breakage. This is mainly because the higher confining pressure influenced the normal and shear strength of the bonds and constricted the bond breakage inside the DE model of the CRF specimens, which conforms to the failure behaviour evolution of the CRF specimens under the triaxial compression in laboratory (Fall et al., 2007).

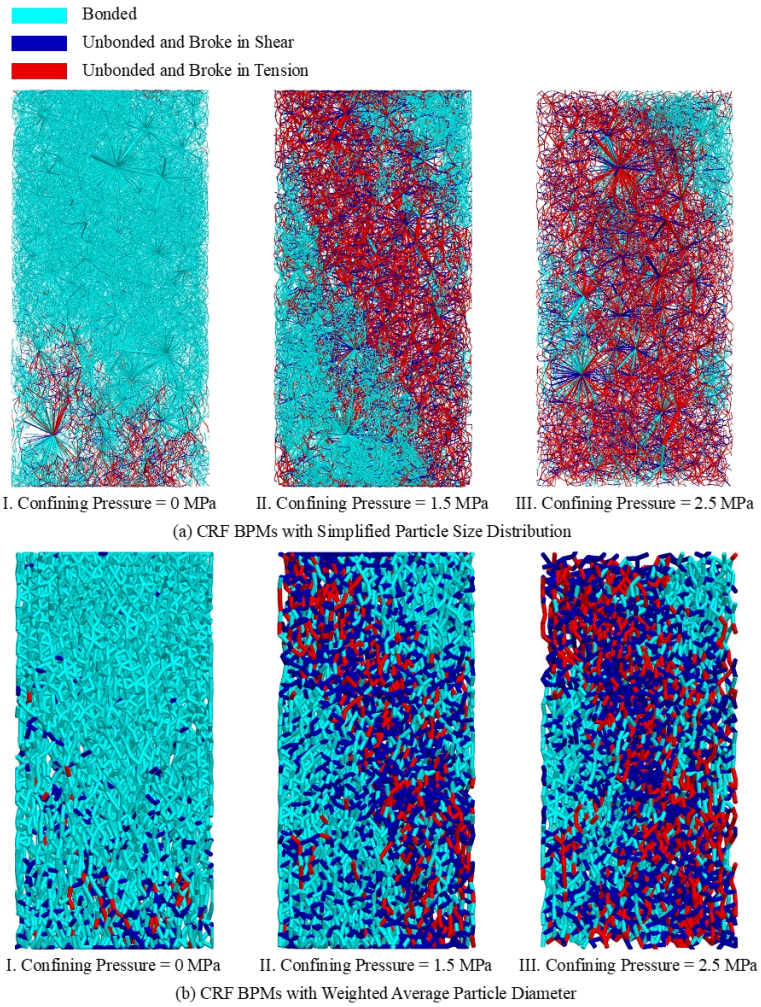

Fig. 4.9 Parallel bond state in the DE model of the CRF specimens with a) simplified particle size distribution and b) mean particle diameter under the uniaxial and triaxial compression.

Fig 4.10 and Fig. 4.11 present the fracture evolution inside the DE model of the CRF specimens with the simplified particle size distribution and mean particle diameter, respectively, under numerical uniaxial and triaxial compression at confining pressures of 0 MPa, 1.5 MPa and 2.5 MPa. It should be mentioned here that in the legends of Fig. 4.10 and Fig. 4.11, the colour and the number of the balls indicate the order of occurrence of the ball fragments and the total number of the balls involved in the fracture inside the DE

model of the CRF specimens, respectively, and the redder the colour of the balls was, the later the fragments inside the DE model of the CRF specimens appeared (Wu et al., 2018). In order to show a comprehensive observation of the overall failure mode of the DE model of the CRF specimens, both two kinds of the DE model of the CRF specimens were rotated 0, 90, 180 and 270 degrees along their central axis, and typically longitudinal profiles were made to demonstrate the internal fracture evolution inside the DE model of the CRF specimens.

Under the numerical uniaxial compression, for both the two kinds of the DE model of the CRF specimens, the overall fractures mainly occurred and developed at the bottom initially. Then some ball fragments extended rapidly to the middle part of the DE model of the CRF specimens, which ideally corresponded to the parallel bond states inside the DE model of the CRF specimens shown in Fig. 4.9a. Trends of surface peeling and volume dilatancy can be easily observed at the edges of the top and bottom surfaces of the DE model of the CRF specimens, and some particles fell off from the DE model of the CRF specimens at the concentrated damage zones. Meanwhile, it has been marked in the figures that both the two kinds of the DE model of the CRF specimens presented a failure mode of corner fracture pattern at the end of the numerical uniaxial compression tests, which also perfectly matched with the failure mode of three groups of the CRF specimens under uniaxial compression in the laboratory. Similarly, previous researchers (Tran et al., 2011; Sun et al., 2017) conducted numerical uniaxial compression tests on the DE models of the concrete and cemented paste backfill, and the failure modes of corner fracture and 'X'-cone shear can be observed at the post-peak stage at the end of their numerical tests.

Fig. 4.10b and Fig. 4.11b show that under the confining pressure of 1.5 MPa, same as the five groups of specimens under triaxial compression in the laboratory, both the two kinds of the DE model of the CRF specimens demonstrated a failure mode of diagonal shear pattern with failure plane angles of the diagonal failure surfaces (Brady and Brown, 2013) of 66° and 65.5°, respectively, which highly accorded with the values obtained from the laboratory test data of the CRF specimens. For the DE model of the CRF specimens with the mean particle diameter, the overall fractures occurred along the diagonal failure surface initially, then extended to one side of the failure surface and formed an obvious concentrated damage zone in yellow colour in the figure. This is because the particles and bonds were homogenously distributed inside the DE model of the CRF specimens, and the ball fragments can quickly converge to develop into large overall fractures. Previous researchers (Ding et al., 2014; Li et al., 2018) also found that the large DE model of the CRF specimens can make the particles to be well distributed and properly connected and then have better-balanced contact through observing the contact force chains of the DE model of the CRF specimens. However, for the DE model of the CRF specimens with the simplified particle size distribution, the overall fractures mainly occurred among the fine particles initially and then developed into the balls located at the coarse particles' periphery. Finally, the balls with large diameters involved in the overall fracture evolution with the bonds around them broke in shear and tension (Wu et al., 2018). No evident concentrated damage zones were found on the DE model of the CRF specimens because the unbalanced distributed particle size and bond numbers and the unbroken bonds between the balls with large diameters significantly hampered the convergence of the ball fragments, resulting in the integrity of the DE model of the CRF specimens.

Fig. 4.10c and Fig. 4.11c show that when the confining pressure increased from 1.5 MPa to 2.5 MPa, both the two kinds of the DE model of the CRF specimens demonstrated a failure mode of diagonal shear pattern, with similar failure plane angles of the diagonal failure surfaces of 66.0° and 67.0°, respectively. Previous studies (Zhang and Li, 2019) have shown a small decrease in the fracture angle of the marble and granite rock under the triaxial compression as the confining pressure increases, while more studies on concrete and concrete-like materials are needed. For the DE model of the CRF specimens with the mean particle diameter, the concentrated damage zone on one side of the diagonal failure surface was observed, which was extended and converged from the initial overall fractures distributed along the failure surface of the DE model of the CRF specimens. Meanwhile, for the DE model of the CRF specimens with the simplified particle size distribution, evidently concentrated damage zone can be observed on both sides of the failure surface of the DE model of the CRF specimens, and some coarse particles located at the failure surface also involved into a further overall fracture evolution. This is mainly because, under the influence of a higher confining pressure of 2.5MPa, much more bonds around the coarse particles broke in tension and shear during the numerical triaxial compression tests to reach a higher triaxial compressive strength of the DE model of the CRF specimens, which means that higher confining pressures can significantly promote the convergence of the ball fragments inside the DE model of the CRF specimens to form overall fractures. The same situations occurred in previous studies (Huang et al., 2016) in that concentrated crack zone can be observed on the DE model of rock specimens under the numerical triaxial compression at higher confining pressures.

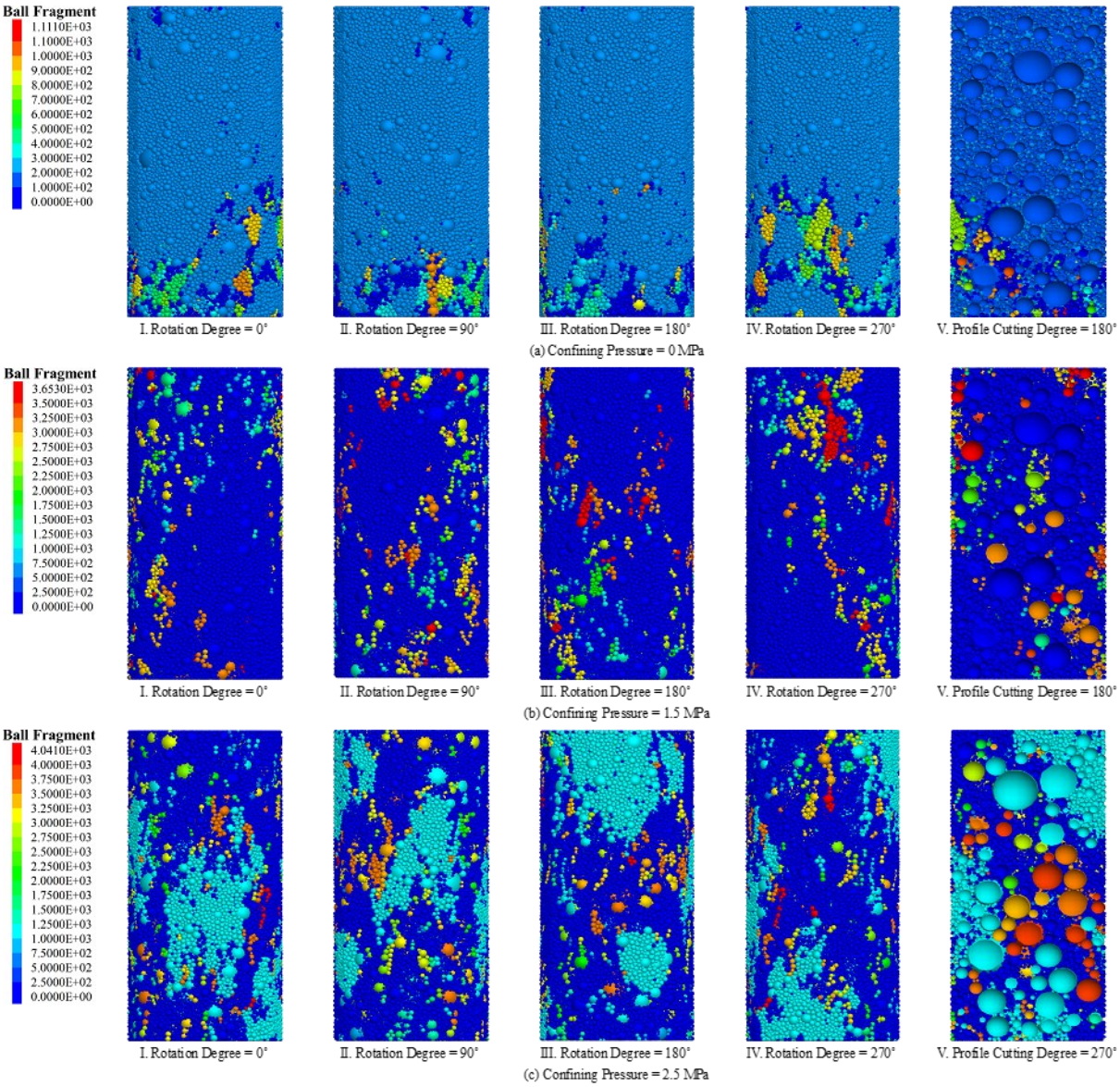

Fig. 4.10 Fracture evolution in the DE model of the CRF specimens with the simplified particle size distribution under different σ_3 of: a) 0 MPa, b) 1.5 MPa, and c) 2.5 MPa.

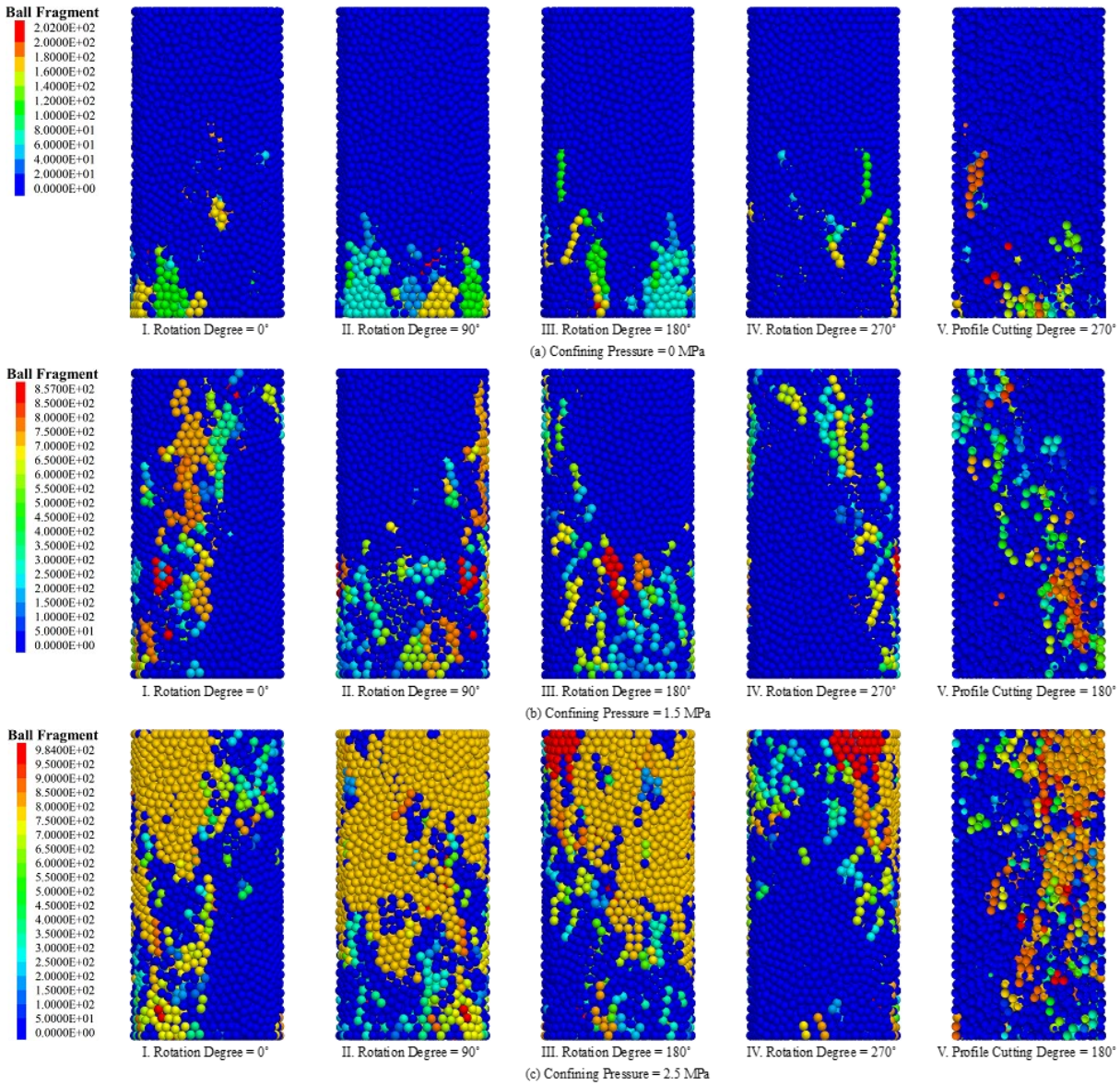

Fig. 4.11 Fracture evolution in the DE model of the CRF specimens with the mean particle diameter under different σ_3 of: a) 0 MPa, b) 1.5 MPa, and c) 2.5 MPa.

4.4.3 Effects of the microstructural parameters of the PB contact model on the mechanical properties of the DE model of the CRF specimen

In this study, the DE model of the CRF specimens with different average particle diameters (d) of 15.2, 10.0, 7.6, 6.1, 5.1, and 4.4 mm were simulated, with the corresponding diameter ratios (D/d) of 10, 15, 20, 25, 30 and 35, respectively, shown in

Fig. 4.3b. Curves in Fig. 4.12a demonstrate the relationship between the peak axial stress and the average particle diameter of the DE model of the CRF specimens under numerical uniaxial and triaxial compression. In high agreement with the previous studies (Li et al., 2018; Ding et al., 2014; Potyondy and Cundall et al., 2004), it can be proved that as the average particle diameter of the DE model of the CRF specimens decreased, the corresponding diameter ratio increased and the peak axial stress of the DE model of the CRF specimens increased significantly as power functions with higher coefficients of variation under higher confining pressures, due to the evident increase in particle and bond numbers.

Fig. 4.12b and Fig. 4.12c depict the relationship between Young's modulus, Poisson's ratio and the average particle diameter of the DE model of the CRF specimens under the numerical uniaxial compression, respectively. As the average particle diameter decreased, the corresponding diameter ratio increased, and Young's modulus of the DE model of the CRF specimens increased as a power function, while the Poisson's ratio decreased logarithmically (Ding et al., 2014; Potyondy and Cundall et al., 2004). The average particle diameter significantly influences the overall mechanical properties of the DE model of the CRF specimens. Previous studies (Li et al., 2018) recommended that a diameter ratio of 20 or larger is reasonable to reduce this influence if a change in the particle size distribution of the DE model of the CRF specimens is needed through numbers of numerical uniaxial compression and Brazilian tests on the DE model of the rock specimens employed with Flat-Joint (FJ) contact model. In this study, with the diameter ratio increasing from 10 to 35, the uniaxial compressive strength, Young's modulus, and Poisson's ratio of the DE model of the CRF specimens under the uniaxial

compression increased by 66.9%, 49.3%, and 12.7%, respectively, and under confining pressures of 1.5 MPa and 2.5 MPa, the peak axial stress of the DE model of the CRF specimens under the triaxial compression increased by 85.7% and 87.1%. It shows that the peak axial stress at higher confining pressures and the Poisson's ratio are the most and the least sensitive to the changes in average particle diameter of the DE model of the CRF specimens, respectively.

Meanwhile, through a comprehensive observation of the DE model of the CRF specimens with different model scales, the bond installation gap ($\bar{g}$) is also a very important parameter to influence the overall mechanical properties of the DE model of the CRF specimens. The average particle diameters were different for the DE model of the CRF specimens with different model scales but with the same diameter ratio. To maintain the highly agreed overall mechanical properties of the DE model of the CRF specimens with each other, the ratio between the bond installation gap and the average particle diameter of the DE model of the CRF specimens should keep unchanged (Li et al., 2018).

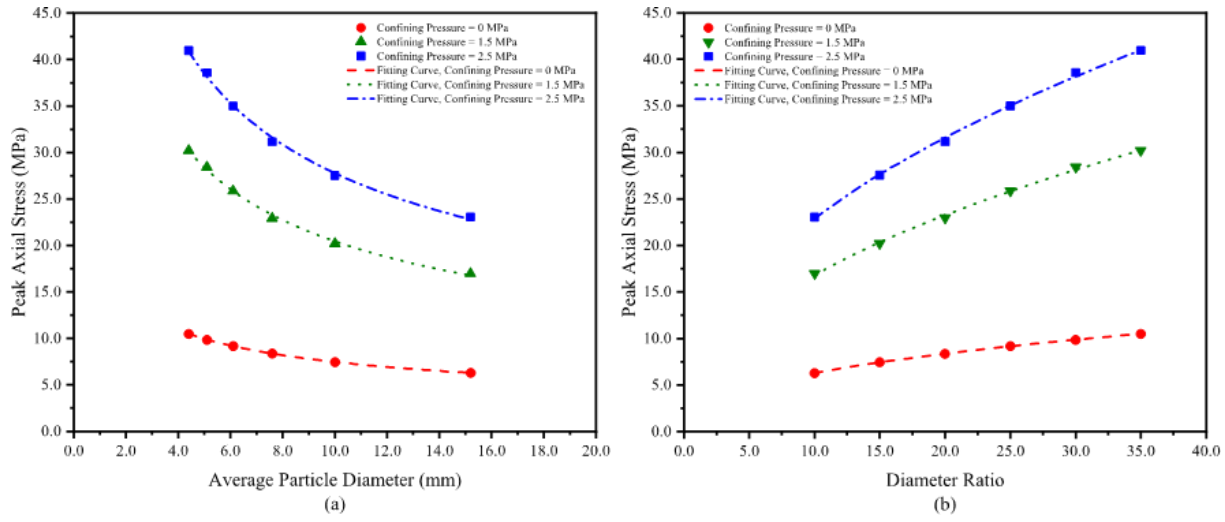

(a)

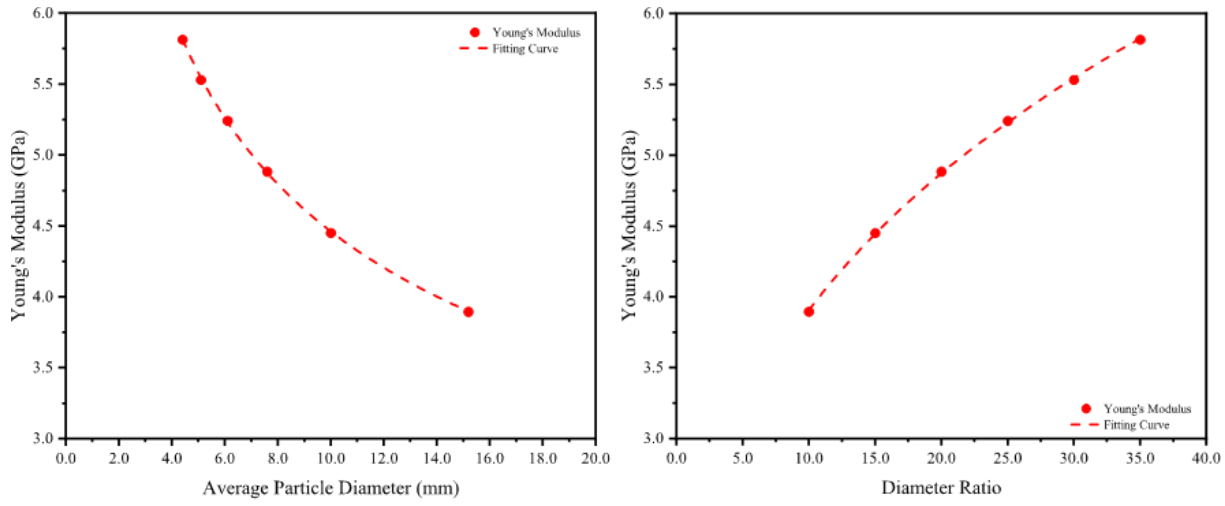

(b)

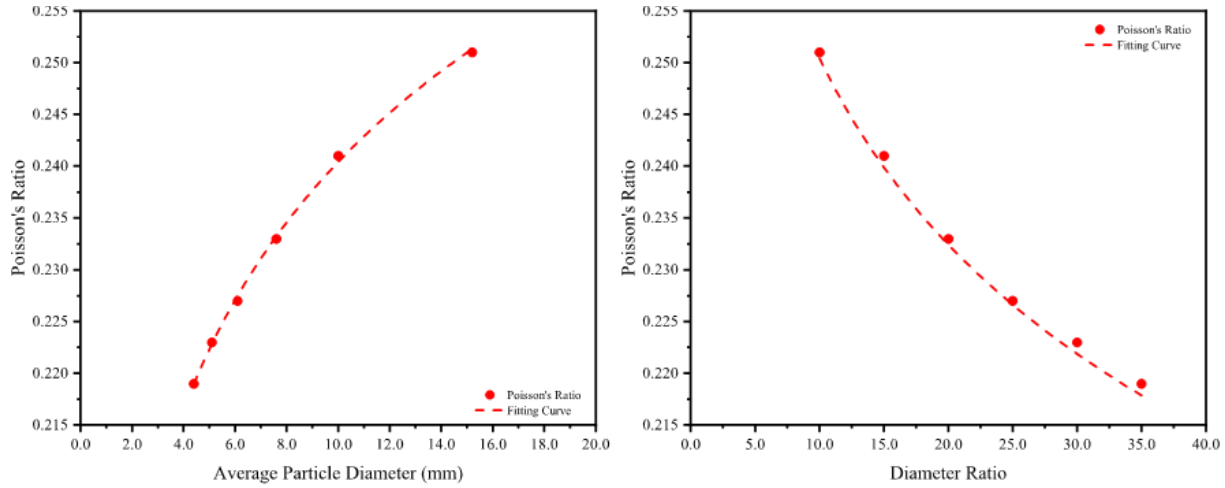

(c)

Fig. 4.12 Effect of the average particle diameter on the mechanical properties of the DE model of the CRF specimens: a) σ_p, b) E, and c) η.

4.4 Conclusions

In this study, based on the discrete element (DE) method, two kinds of the DE model of the CRF specimens, with the simplified particle size distribution and mean particle diameter, which adopted the parallel bond (PB) contact model among the particles were

constructed in the software PFC3D. And then, the numerical uniaxial and triaxial compression tests were conducted on these DE models of the CRF specimens to calibrate the microstructural parameters and validate the feasibility of using these DE models of the CRF specimens in future numerical simulations. Finally, the DE model of the CRF specimens with different average particle diameters was simulated to study the effects of different diameter ratios (D/d) on the overall mechanical properties of the DE model of the CRF specimens under numerical uniaxial and triaxial compression. The following conclusions can be drawn:

For both the two kinds of the DE model of the CRF specimens under numerical uniaxial and triaxial compression, the overall mechanical properties and stress-strain behaviour were well calibrated and in good agreement with these of the real CRF specimens in the laboratory. Meanwhile, the calibrated DE model of the CRF specimens with the mean particle diameter can be used as an adequate substitute for the DE model of the CRF specimens with the simplified particle size distribution in future numerical modelling due to good imitation effect and high computational efficiency with fewer particle and bond generations.

The bond friction angle ($\bar{\varphi}$) is one of the main microstructural parameters that control the shape of the stress-strain curve of the DE model of the CRF specimens under the uniaxial compression during the micro-crack expansion and post-failure stages. As the bond friction angle increases, the uniaxial compressive strength of the DE model of the CRF specimens decreases slightly, while Young's modulus and Poisson's ratio remain unchanged due to their insensitivity to the bond friction angle of the DE model of the CRF specimens. Importantly, for the DE model of the CRF specimens under numerical

uniaxial compression, as the bond friction angle increases, the micro-crack expansion stage begins earlier, and the shape of the stress-strain curve of the DE model of the CRF specimens during this stage becomes more concave. Meanwhile, as the bond friction angle increases, the decrease rate of the axial stress after the peak value decreases, and the DE model of the CRF specimens show a gentler strain-softening brittle failure response during the post-failure stage.

For both kinds of the DE model of the CRF specimens, the fracture evolution ideally matches with the parallel bond contact state inside the DE model of the CRF specimens and the corresponding failure modes observed on the real CRF specimens in the laboratory. For both the two kinds of the DE model of the CRF specimens, under the numerical uniaxial compression, a failure mode of corner fracture pattern with surface peeling and volume dilatancy at the top and bottom surface edges of the DE model of the CRF specimens can be observed. And under the numerical triaxial compression, a failure mode of diagonal shear pattern can be observed, of which the observed failure plane angles between the directions of axial stress and failure surface of the DE model of the CRF specimens highly accorded with the average value obtained from laboratory test data of the real specimens. For the DE model of the CRF specimens with the mean particle diameter, the macro-fractures occurred along the diagonal failure surface and extended to form a concentrated damage zone because the homogenously distributed particles and bonds contributed to the ball fragment convergence. And for the DE model of the CRF specimens with the simplified particle size distribution, the macro-fractures initially occurred among the fine particles and then developed into the coarse particles and the particles at their peripheries. As a result, no evident concentrated damage zone was

formed due to the hamper from the coarse particles to the ball fragment convergence. However, increasing the confining pressure can significantly promote the convergence of the ball fragments inside the CRF specimens' DE model to form a concentrated damage zone.

The diameter ratio (D/d) of the DE model of the CRF specimens with average particle diameter highly influences the strength characteristics and deformation properties. As the diameter ratio increases, the peak axial stress and Young's modulus of the DE model of the CRF specimens increase significantly as power functions and the Poisson's ratio decrease logarithmically. The peak axial stress at higher confining pressures and the Poisson's ratio are the most and the least sensitive to the changes in the average particle diameter of the DE model of the CRF specimens, respectively. Meanwhile, the bond installation gap is also a very important parameter to influence the overall mechanical properties of the DE model of the CRF specimens. Therefore, the ratio between the bond installation gap and the average particle diameter of the DE model of the CRF specimens should keep unchanged to maintain highly agreed overall mechanical properties of the DE model of the CRF specimens with different model scale but the same diameter ratio.

Chapter 5 Coupled finite difference and discrete element method for modelling the direct shear test on the combined rock-cemented rockfill specimen

This chapter provides an effective determination process of the interface microstructural parameters in the numerical modelling of the mechanical interaction between two different geomaterials involved with frictional-bonded interfaces, such as the interaction between backfill columns and the surrounding rocks, or the soil-structure interaction, by using the coupled finite difference and discrete element (FD-DE) method. Three-dimensional numerical direct shear tests were conducted on the coupled FD-DE model of the combined rock-cemented rockfill (R-CRF) specimens with the frictional-bonded interface. With the microstructural parameters determined, the macro-mechanical properties of the interface of the coupled model were calibrated to fit well with the theoretical values of the combined specimen under the direct shear condition assumed according to the Mohr-Coulomb strength criterion. Evident elastoplastic shear behaviour was observed on the interfaces, and excellent agreement was attained between the shapes of theoretical and simulated shear stress-displacement curves of the coupled models at different servo-controlled normal stresses. Particulate-scale force chains inside the DE model of the CRF specimen were highly consistent with the force contour on the FD model of the rock specimen, demonstrating the shear stress evolution of the coupled model at different shear displacements. Parametric studies verified the effects of the deformation properties of the interface parallel bonds on the shape of shear stress-displacement curves of the coupled models. The test results validated the feasibility and rationality of the coupled FD-DE method for modelling the combined specimens with frictional-bonded interfaces or joints. Furthermore, this study provides valuable numerical modelling

experience for investigating the shear behaviour at the interface between cemented backfill columns and surrounding walls by using the coupled FD-DE method.

5.1 Introduction

Backfill columns and the surrounding rocks at underground stopes are not self-isolated but mutually supported (Koupouli et al., 2016). Energy alternation and stress transmission happen through the frictional-bonded interfaces between them when underground mined-out areas undergo disturbance from the sequential orebody extraction. Many researchers have performed direct shear tests on the artificially combined rock-backfill or backfill-backfill specimens in the laboratory to study this interface shear behaviour, which can strongly influence the stress distribution and stability around underground backfilled stopes. The test results reveal that the shear failure envelope of these interfaces also obeys the Mohr-Coulomb failure criterion, and the shear strength of these combined specimens can be smaller than the corresponding backfill material (Fall and Nasir, 2010). Major influence factors on the interface shear behaviour are the cement content, applied normal stress, surface roughness, curing time and conditions (Fang and Fall, 2019; Fang and Fall, 2020; Nasir and Fall, 2008; Lingga and Apel, 2018). Perfect elastoplastic behaviour can be observed on the combined rock-backfill specimens' interfaces, while for the combined backfill-backfill specimens, the interface shows evident strain-hardening shear behaviour, especially at lower applied normal stress. As the cement content increases, the shear stress-displacement curve can transform from a strain-hardening to a strain-softening shape (Koupouli et al., 2016). Higher normal stress applied to the combined specimens can weaken the interface dilation effect, resulting in higher shear strength and higher interface shear stiffness (Fall

and Nasir, 2010). As the curing time increases, the degree of binder hydration at the interfaces increases, leading to the combined specimens' higher shear strength (Guo et al., 2020). Meanwhile, a higher interface roughness can also contribute to an increased shear strength due to a larger interlock structure (Fang and Fall, 2020).

Numerical modelling is always a popular and effective way to comprehensively understand the mechanical properties and stress-strain behaviour of the interface between the backfill column and the surrounding rocks. Various engineering disciplines have used numerical modelling, ranging from bioengineering to mining engineering (Apel et al., 2021). Generally, typical numerical modelling methods can be classified into two categories: the continuum and discontinuum approaches. The continuum approach treats modelled geomaterials as homogenous and elastoplastic, mainly including the finite element (FE), the finite difference (FD) and finite volume (FV) methods (Belinha and Dinis, 2006). For the discontinuum approach, such as the discrete element (DE) method, modelled geomaterials can be treated as assemblies of discrete blocks or spheres with inhomogeneous mechanical properties (Hasan et al., 2017). When modelled the direct shear tests on geomaterials, such as rock, soil and concrete-like materials, few researchers adopted the continuum approach, although this approach has very high computation efficiency (Wu, 2015; Lin et al., 2010). Instead, most studies selected the discontinuum approach due to its domination in modelling the large-strain deformation and post-failure behaviour (Suazo and Villavicencio, 2018; Wu et al., 2018).

During these years, with further development in numerical modelling techniques, more and more researchers have applied the coupled continuum-discontinuum approach, including the coupled finite difference and discrete element (FD-DE) method and the

coupled finite-element and discrete element (FE-DE) method, into the numerical simulation on large-scale geotechnical-related engineering projects, such as the landslide disaster or tunnel excavation and railway stability (Feng et al., 2017; Ma et al., 2019; Nishiura et al., 2018). The coupled approach can combine the advantages of the two single approaches and efficiently interpret the mechanical interaction at the interface between two geomaterials, such as rocks and rock beds or foundation soil and concrete, which can be considered granular and continuous. Furthermore, using the wall-zone or sphere-zone coupling scheme, the coupled approach can connect the finite zones or finite elements to the discrete particles, resulting in smooth stress and displacement transmission between the continuum and discontinuum models.

In mining engineering, to successfully simulate the mechanical interaction and the stress distribution law between backfill columns and the surrounding rocks with the coupled approach, the microstructural parameters at the frictional-bonded interface between them need to be determined. However, there are no previous studies about the numerical simulation of the direct shear tests on geomaterials with interfaces or joints by using the coupled FD-DE or FE-DE methods. Thus, in this study, the coupled FD-DE models of the combined rock-cemented rockfill (R-CRF) specimens were designed for numerical direct shear tests to study the shear behaviour of the frictional-bonded interfaces between the CRF columns and the surrounding rocks. These interfaces' microstructural parameters were determined for future numerical modelling on the stability and stress distribution of underground stopes backfilled with the CRF columns. This study can provide an effective determination process of the interface microstructural parameters in the numerical modelling of the mechanical interaction between two different geomaterials

involved with frictional-bonded interfaces, such as the interaction between backfill columns and the surrounding rocks, or the soil-structure interaction, by using the coupled finite difference and discrete element (FD-DE) method.

5.2 Material and methodology

5.2.1 Direct shear test

Many researchers have conducted direct shear tests in the laboratory to study the shear behaviour of the frictional-bonded interface inside the combined rock-backfill or backfill-backfill specimens (Nasir and Fall, 2008; Fang and Fall, 18; Fang and Fall, 2019; Fang and Fall, 2020; Koupouli et al., 2016; Koupouli et al., 2017). These combined specimens include the combined cemented paste backfill (CPB-CPB), combined rock-cemented paste backfill (R-CPB) and combined cemented rockfill-cemented rockfill (CRF-CRF) specimens (Lingga and Apel, 2018). The schematic diagram of the direct shear apparatus simulated in this study is shown in Fig. 5.1 (Koupouli et al., 2016). In this apparatus, the shear box is divided into a top portion, movable, and a bottom portion, fixed. A hydraulic pump maintains constant normal loads on the top box in vertical and horizontal directions. Normal and tangential linear variable differential transformers (LVDT) are incorporated with the apparatus to monitor the normal and shear displacement. Pressure transducers are used to record the normal and shear stress. The data acquisition system can automatically obtain the combined specimen's shear strength characteristics and deformation properties. The top box moves at a low shear displacement rate during the shear process to ensure a quasi-equilibrium shear system under the servo-controlled normal stress. Along the shear direction, the top of the combined specimen interacts with the confining walls of the shear box until normal wall reaction forces (N_1 and N_2) and

shear force (T) at the interface reach dynamic equilibrium (Zhang and Thornton, 2007; Salazar et al., 2015). Meanwhile, three shear wall reaction forces (T_1, T_2 and T_3) can be ignored since the combined specimen is bonded to the box with encapsulating material and no relative displacement occurs during the test. Thus, the shear stress (τ_s) at the interface of the combined specimen can be given by:

$$\tau_s = \frac{T}{A_s} = \frac{N}{A_s} \qquad \textbf{(Eq. 5.1)}$$

where N is the resultant normal wall reaction force along the shear direction and A_s is the effective shear area that progressively decreases while the shear displacement increases. Meanwhile, in Fig. 5.1b, σ_x, σ_z and τ_{zx} (τ_{xz}) represent the x-, z- and zx-component of the average stress tensor at a differential element on the interface, respectively.

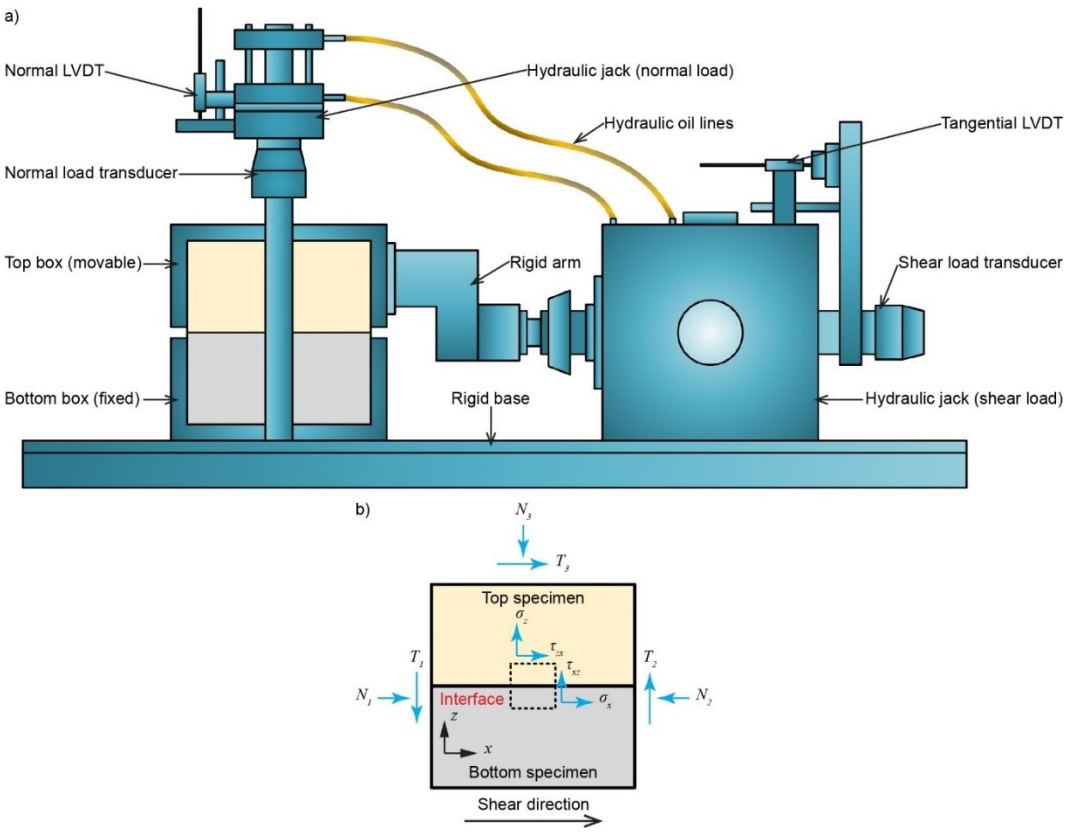

Fig. 5.1 Direct shear test on a typical combined specimen: a) apparatus setup, and b) direct shear mechanism.

5.2.2 Combined rock-cemented rockfill specimen

Three-dimensional numerical models of the combined rock-cemented rockfill (R-CRF) specimens were created with Itasca's software PFC3D 6.0 and FLAC3D 7.0 in this study. In the combined R-CRF specimens, the basic physical-mechanical properties of kimberlite rock and the CRF are determined based on the laboratory test results and previous studies from Sepehri et al. (Sepehri et al., 2017), which are shown in Table 5.1 and Table 4.1 in Chapter 4. The kimberlite properties were estimated based on the average Rock Mass Rating (RMR) system and the generalized Hoek-Brown criterion (Sepehri et al., 2017). The CRF properties were weight-averaged from the laboratory test results of the uniaxial and triaxial compression tests on the field CRF core samples after 28 days of curing age. The CRF material mainly consists of the granitic aggregate mixed with the Portland cement as the binder, with a uniform coefficient of 12.0 and a curvature coefficient of 0.81. The true particle size distribution of the CRF aggregate is shown in Fig. 3.2 in Chapter 3, and the simplified particle size distribution adopted in the simulation of the DE model of the CRF specimen is shown in Fig. 4.2 in Chapter 4.

Table 5.1 Physical-mechanical properties of the kimberlite specimens.

Category	Values
Unit weight (MN/m^3)	0.028
Elastic modulus (GPa)	30.0
Poisson's ratio	0.3
Cohesion (MPa)	4.48
Internal friction angle (°)	31.0

Friction coefficient	0.7
Uniaxial compressive strength (MPa)	69.0
Tensile strength (MPa)	3.54

Koupouli et al. (Koupouli et al. 2017) performed the direct shear tests on the combined R-CPB specimens with natural rock joint interfaces. The test results proved that under the direct shear condition, the shear behaviour of the combined R-CPB specimen is dominated by the frictional-bonded interface, and the Mohr-Coulomb strength criterion can be adopted to describe the relationship between the interface shear strength (τ_i) and the normal stress (σ_n):

$$\tau_i = c_i + \sigma_n \tan\varphi_i \qquad \textbf{(Eq. 5.2)}$$

where c_i and φ_i are the cohesion and internal friction angle of the interface, respectively. Similarly, the natural interfaces between the CRF columns and surrounding rocks are rough, unclear, and nonplanar. Thus, the Mohr-Coulomb strength criterion can also be used in this study to make strength parameter assumptions for the interface of the modelled combined R-CRF specimen. For the direct shear test on the combined R-CPB specimen, previous studies indicated that the ratio between φ_i and the CPB material's internal friction angle is higher than 0.6, and c_i is always smaller than the CPB material's cohesion (Fall and Nasir, 2010). In this study, c_i and φ_i are assumed to be 1.0 MPa and 30.0°, respectively, to describe the frictional weakly bonded state at the interface of the modelled combined R-CRF specimen. Meanwhile, to determine the shape of the shear stress displacement curve, it is necessary to quantify the interface shear stiffness (k_i) and

the interface friction coefficient (μ_i) of the modelled combined specimen. Previous studies (Fang and Fall, 2020; Manaras, 2009) indicate that k_i and μ_i can be defined as:

$$k_i = \frac{\tau_p}{\delta_c} \quad \textbf{(Eq. 5.3)}$$

$$\mu_i = \frac{\tau_r}{\sigma_n} \quad \textbf{(Eq. 5.4)}$$

where τ_p, δ_c, τ_r, and σ_n represent the peak shear stress, critical displacement when the shear failure occurs, residual shear strength, and normal stress, respectively. Nasir and Fall (2008) also found that the initial shear stiffness slightly increases along with σ_n. Thus, to simplify the simulation procedure and quantify the interface's deformation properties efficiently, average values of 70.0 MPa and 0.70 are selected for k_i and μ_i, respectively, at the interface of the modelled combined specimen. These values are based on previous studies by Lingga and Apel (Lingga and Apel, 2018), where the direct shear tests were carried out on the artificial combined CRF-CRF specimens in the laboratory using the same CRF material in this study. The assumptions of deformation properties and expected strength parameters of the interface are listed in Table 5.2.

Table 5.2 Physical-mechanical properties of the interfaces in the combined R-CRF specimens.

Category	Values
Shear stiffness (MPa/m)	70.0
Cohesion (MPa)	1.0
Internal friction angle (°)	30.0
Friction coefficient	0.7

5.2.3 Coupled finite difference and discrete element method

In this study, finite zones were created to simulate the FD model of the rock specimen, and the DE model of the CRF specimen was formed by randomly generated discrete particles with a simplified particle size distribution. The interface of the combined specimen was modelled with the coupled finite difference and discrete element (FD-DE) method. The coupling mechanism at the modelled interface is shown in Fig. 5.2a. At the interface, coupled walls with edge-connected triangular facets were created to coincide with the FD model's zone faces. Then, following the force-displacement law, the contact forces and moments from the discrete particles are equivalently transferred to the corresponding grid points of the finite zones as nodal forces and moments during iterations at the interface. Meanwhile, the nodal displacements in the finite zones are transferred to the coupled walls at the interface in return, the contact forces and moments on the discrete particles are updated consistently. These information transfers between the FD and DE models are implemented with the ball-wall-zone (BWZ) coupling method using a Socket Input/Output (I/O) Function at the coupled wall.

The algorithms and governing equations developed to implement the coupled FD-DE method at the modelled combined specimen's interface are presented here. Fig. 5.2b demonstrates that a discrete sphere is in contact with a triangular wall facet wrapping a finite zone face. In this figure, position C represents the sphere-wall contact point, and position CP is the closest point to C on the wall facet. x_i (i = 1, 2, 3) denotes three vertex locations of the triangular wall facet. By connecting x_i with CP, the area that is nonadjacent to x_i is defined as A_i (i = 1, 2, 3), and the total area of the wall facet is A. Then, the contact forces and translational stiffness values at CP can be barycentrically

extrapolated to x_i, which coincide with the three corresponding gridpoints of the finite zone, by multiplying a weighting factor of $\xi_i = A_i/A$. The following equations are given to ensure extrapolated forces and moments at CP are consistent with the contact forces and C. In Fig. 5.2b, $\boldsymbol{r}_i$ (i = 1, 2, 3) represents the vectors pointing from CP to x_i, and the force applied at each gridpoint is defined as $\boldsymbol{F}_i$ (i = 1, 2, 3). $\boldsymbol{F}$ and $\boldsymbol{M}_b$ are the applied contact force and contact moment due to the binding effect at C. The total moment ($\boldsymbol{M}$) applied on the wall facet is given by:

$$\boldsymbol{M} = \boldsymbol{M}_b + (C - CP) \times \boldsymbol{F} \qquad \textbf{(Eq. 5.5)}$$

where × denotes the cross product, with full computation mode activated, an entirely consistent equivalent force system is then determined by the coupling scheme:

$$\sum \boldsymbol{F}_i = \boldsymbol{F} \qquad \textbf{(Eq. 5.6)}$$

$$\sum \boldsymbol{r}_i \times \boldsymbol{F}_i = \boldsymbol{M} \qquad \textbf{(Eq. 5.7)}$$

$\boldsymbol{n}$ is defined as the unit vector pointing in the normal direction of the wall facet, and then the shear force vector ($\boldsymbol{F}_s$) and its corresponding unit vector ($\boldsymbol{s}$) pointing along the wall facet are given by:

$$\boldsymbol{F}_s = \boldsymbol{F} - \|\boldsymbol{F}\| \cdot \boldsymbol{n} \qquad \textbf{(Eq. 5.8)}$$

$$\boldsymbol{s} = \frac{\boldsymbol{F}_s}{\|\boldsymbol{F}_s\|} \qquad \textbf{(Eq. 5.9)}$$

The equivalent force system is determined in the local axis system at the wall facet where the x-component and y-component of $\boldsymbol{F}$ coincide with the $\boldsymbol{n}$ and the $\boldsymbol{s}$ direction, respectively. Then, $\boldsymbol{r}_i^l$, $\boldsymbol{F}_i^l$, $\boldsymbol{F}^l$, $\boldsymbol{M}_i^l$ and $\boldsymbol{M}^l$ are defined to be the force and moment

parameters in the local axis system corresponding to $\boldsymbol{r}_i$, $\boldsymbol{F}_\mathrm{i}$, $\boldsymbol{F}$, $\boldsymbol{M}_\mathrm{i}$, and $\boldsymbol{M}$, respectively. The rules of transferring x-, y- and z- components of $\boldsymbol{F}^l$ to corresponding components of $\boldsymbol{F}_i^l$ at each gridpoint are given by:

$$\sum \boldsymbol{F}_{i,x}^l = \boldsymbol{F}_x^l \qquad \textbf{(Eq. 5.10)}$$

$$\sum \boldsymbol{F}_{i,y}^l = \boldsymbol{F}_y^l \qquad \textbf{(Eq. 5.11)}$$

$$\sum \boldsymbol{F}_{i,z}^l = \boldsymbol{F}_z^l = 0 \qquad \textbf{(Eq. 5.12)}$$

$$\sum \left(\boldsymbol{r}_{i,y}^l \times \boldsymbol{F}_{i,z}^l - \boldsymbol{r}_{i,z}^l \times \boldsymbol{F}_{i,y}^l\right) = \boldsymbol{M}_x^l \qquad \textbf{(Eq. 5.13)}$$

$$\sum \left(\boldsymbol{r}_{i,z}^l \times \boldsymbol{F}_{i,x}^l - \boldsymbol{r}_{i,x}^l \times \boldsymbol{F}_{i,z}^l\right) = \boldsymbol{M}_y^l \qquad \textbf{(Eq. 5.14)}$$

$$\sum \left(\boldsymbol{r}_{i,x}^l \times \boldsymbol{F}_{i,y}^l - \boldsymbol{r}_{i,y}^l \times \boldsymbol{F}_{i,x}^l\right) = \boldsymbol{M}_z^l \qquad \textbf{(Eq. 5.15)}$$

As CP is located on the wall facet, $\boldsymbol{r}_{i,x}^l$ equals 0. Thus, Eq. 5.14 and Eq. 5.15 can be simplified to Eq. 5.1 6 and Eq. 5.17, respectively, and $\boldsymbol{F}_{i,x}^l$ at each gridpoint is then determined with Eq. 5.10, Eq. 5.16 and Eq. 5.17:

$$\sum \boldsymbol{r}_{i,z}^l \times \boldsymbol{F}_{i,x}^l = \boldsymbol{M}_y^l \qquad \textbf{(Eq. 5.16)}$$

$$\sum \boldsymbol{r}_{i,y}^l \times \boldsymbol{F}_{i,x}^l = -\boldsymbol{M}_z^l \qquad \textbf{(Eq. 5.17)}$$

With $\boldsymbol{F}_y^l$ barycentrically distributed to each gridpoint, the weighting factor described above is applied in the direction of the maximum contact force along the wall facet, namely $\boldsymbol{r}_{i,y}^l = \omega_i \boldsymbol{F}_y^l$, and Eq. 5.13 can be simplified to Eq. 5.18:

$$\sum \boldsymbol{r}_{i,y}^{l} \times \boldsymbol{F}_{i,z}^{l} = \sum \left(\boldsymbol{r}_{i,z}^{l} \xi_i \boldsymbol{F}_{y}^{l} \right) + \boldsymbol{M}_{x}^{l} \qquad \textbf{(Eq. 5.18)}$$

Eq. 5.18 provides an additional constraint for the equivalent force system to find a particular solution from the governing equations described above:

$$\sum \boldsymbol{r}_{i,z}^{l} \times \boldsymbol{F}_{i,z}^{l} = 0 \qquad \textbf{(Eq. 5.19)}$$

With Eq. 5.12, Eq. 5.18, and Eq. 5.19, $\boldsymbol{F}_{i,y}^{l}$ and $\boldsymbol{F}_{i,z}^{l}$ at each gridpoint of the finite zone are determined. Subsequently, the resultant forces are converted into the global axis system and applied to corresponding gridpoints, triggering force, velocity, and displacement updates simultaneously in the finite zone.

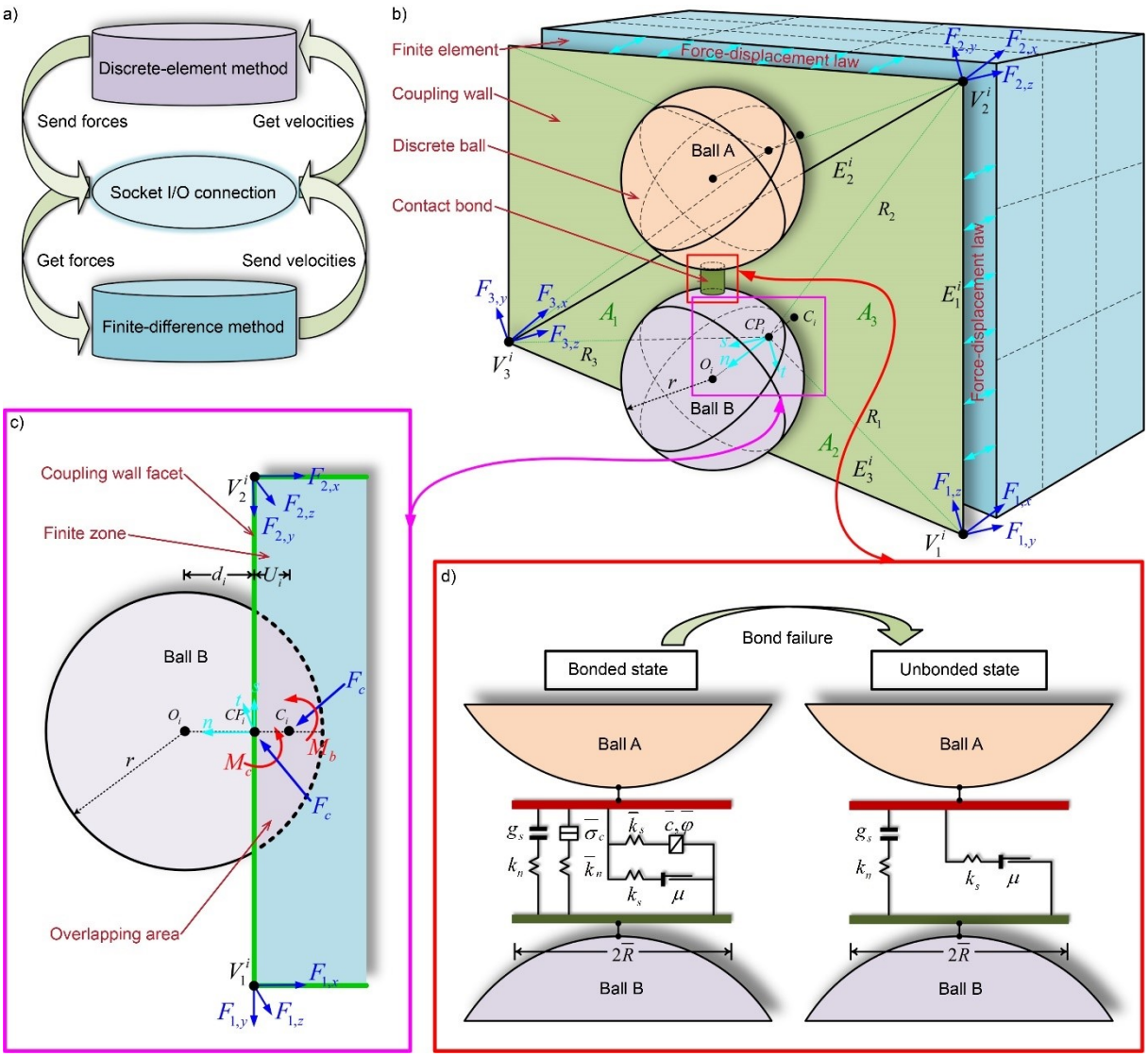

Fig. 5.2 Coupled FD-DE method: a) coupling mechanism, b) ball-wall-zone coupling method, c) cross-section at the ball-wall contact and d) parallel bond contact model.

5.3 Numerical simulation

5.3.1 Model establishment

Fig. 5.3 shows the geometry, boundary conditions and creation procedures of a combined R-CRF specimen's three-dimensional coupled FD-DE model. The dimensions of the coupled model were designed to be 15 m × 15 m × 7.5 m (length × width × height), which

were large enough to coincide with future numerical studies on the simulation of underground stopes backfilled with the CRF columns. In the coupled model, 15 m × 15 m × 3.75 m finite zones, representing the FD model of the rock specimen, were initially constructed with FLAC3D, a finite difference program using an explicit LaGrangian calculation scheme and a mixed discretization zoning technique. The optimal mesh sizes were set to be 1/10, 1/10 and 1/8 of the length, width, and height, respectively, of the FD model. The physical-mechanical properties of the rock specimen in Table 5.1 were then applied to the finite zones directly. A coupled wall with edge-connected triangular facets was then created to cover the top face of the finite zones. Each wall facet coincides with the corresponding finite zone, and the vertexes of wall facets act consistently with the zone gridpoints. Next, five more rigid walls connected to the coupled wall were generated to form a box of 15 m × 15 m × 3.75 m to contain the discrete particles of the DE model.

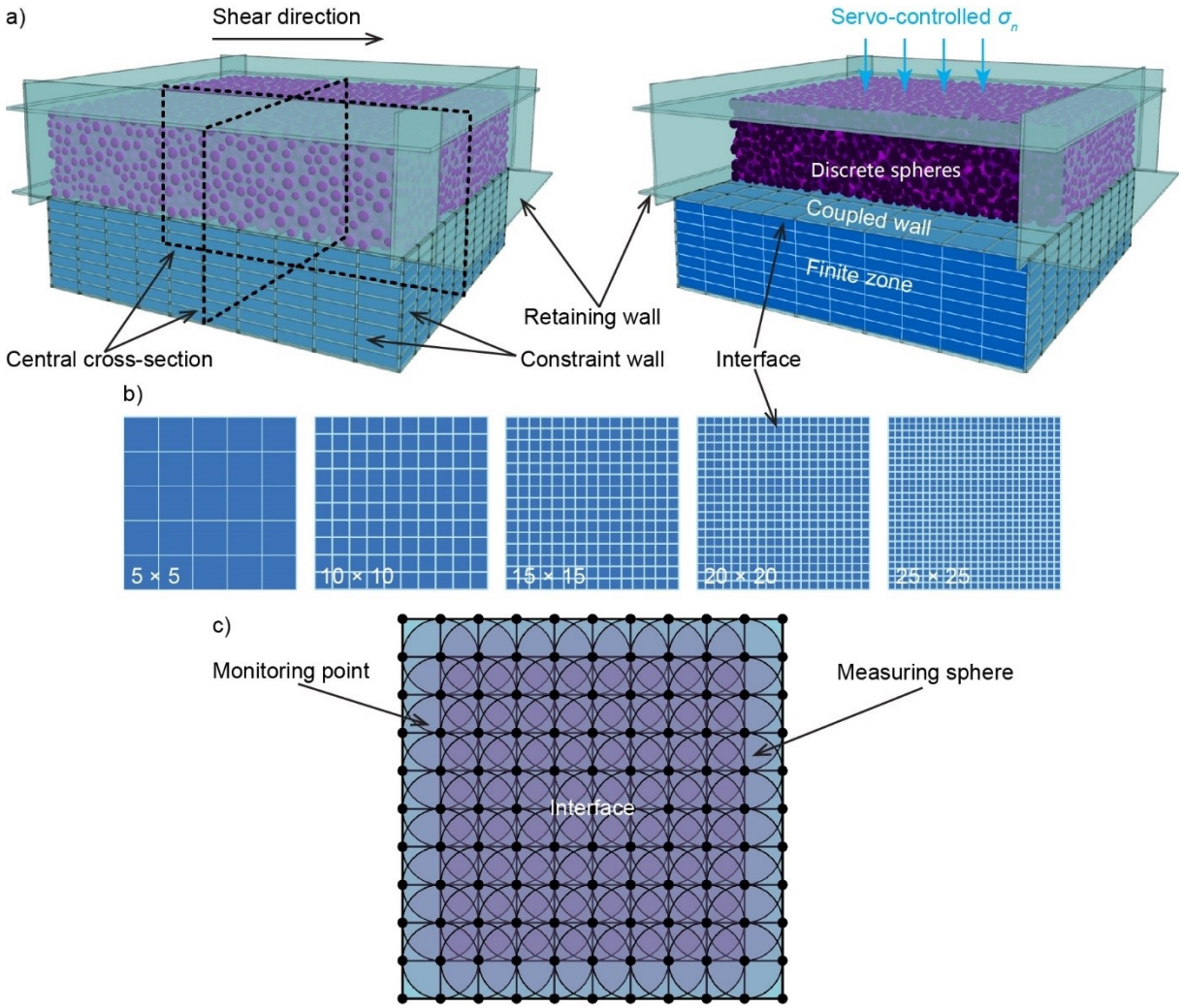

Fig. 5.3 Direct shear test on the coupled FD-DE model of the combined R-CRF specimen: a) full and cross-section view, b) different mesh sizes of the FD model of the rock specimen, and c) measuring method of the DE model of the CRF specimen.

5.3.2 Parameter determination

Unlike the FD method, the overall mechanical properties of the geo-material that one wants to simulate using the DE method cannot be directly assigned to the DE model. This is because the DE model consists of a large number of discrete blocks or spheres, and the mechanical interaction reflects the overall mechanical properties of the geo-material

among the discrete particles at the microscopic level, which are controlled by the microstructural parameters of the contact model applied to the virtual bonds that connect the discrete particles. Thus, to ensure the DE model and the following simulation are precise and correct, the microstructural parameters of the contact model need to be determined until the DE model's overall mechanical properties are the same as those values of the corresponding real geo-material.

In this study, the particle scaling method was adopted to simplify the generation of the discrete particles in the DE model using PFC3D, software that provides a discrete element modelling framework. Empirically, to eliminate the scale effect on the modelling results, the ratio between the maximum model scale and maximum sphere radius (r_{max}) should be no less than 50, and the ratio between r_{max} and the minimum sphere radius (r_{min}) should be no less than 1.66 (Ding et al., 2014; Wu and Xu, 2016). Thus, in this study, optimal r_{max} and r_{min} of the discrete particles were determined as 0.18 m and 0.3 m, respectively, and a total of 9,639 discrete particles were generated. The DE model employed the PB contact model to provide the virtual binding effect from Portland cement among the discrete particles. The microstructural parameters for the DE model were determined by conducting the uniaxial and triaxial compression tests on the modelled CRF cylindrical specimens, shown in Table 4.2 in Chapter 4. These tests can ensure the strength parameters and deformation properties of the DE model coincide with the corresponding values of the CRF specimen shown in Table 4.1 in Chapter 4. Furthermore, to determine the interface's microstructural parameters, groups of newly designed numerical direct shear tests were carried out to ensure the coupled model's stress-strain

behaviour and macro-mechanical properties coincide with the assumptions described in the methodology section. The determined results are shown in Table 5.3.

Table 5.3 Microstructural parameters of the PB contact model at the interfaces in the coupled FD-DE model of the combined rock-CRF specimens.

Category	Values
Effective modulus (GPa)	0.15
Bond effective modulus (GPa)	0.015
Stiffness ratio	1.0
Bond stiffness ratio	1.0
Bond normal strength (MPa)	0.09
Bond shear strength (MPa)	1.1
Bond internal friction angle (°)	30.0
Contact friction coefficient	0.7
Bond gap (m)	0.024

The direct shear tests were performed on the coupled models under three different values of σ_n: 0.25 MPa, 0.5 MPa and 1.0 MPa. Initial servo-controlled σ_n was applied to the lateral and top walls surrounding the discrete particles, and the velocities at the lateral and bottom faces of the finite zones were fixed in the corresponding normal directions to provide constraints. During the shear process, servo controlling in the x-direction was realized, and the DE model moved rightward at a low displacement rate of 0.05 m/s to ensure a quasi-equilibrium shearing system. Two extended retaining walls were created

along the shear direction to prevent unbonded discrete particles from flying out of the shear box. Meanwhile, the interface meshed into different numbers (N_m) of 25, 100, 225, 400, 625 of finite square zones, with the corresponding mesh sizes of 3.0 m, 1.5 m, 1.0 m, 0.75 m, and 0.6 m, respectively, to study the effect of the mesh size on the shear behaviour and macro-mechanical properties of the coupled model. Groups of measuring spheres were created at the interface, and two central cross-sections of the coupled model to obtain the stress and displacement distributions. The ij-component of the average stress tensor (σ_{ij}) acting on the center location of each measuring sphere can be calculated as:

$$\sigma_{ij} = \frac{1}{V}\sum_{i=1}^{n} \boldsymbol{f}_i^C \times \boldsymbol{l}_j^C \qquad \textbf{(Eq. 5.20)}$$

In this equation, at the contact position C between two discrete particles, $\boldsymbol{f}_i^C$ is the i-component of the contact force, $\boldsymbol{l}_j^C$ is the corresponding j-component of the branch vector connecting the center locations of two discrete particles (Wang et al., 2007).

5.4 Results and discussion

5.4.1 Shear behaviour and the mechanical properties of the coupled FD-DE model of the combined R-CRF specimen

Fig. 5.4a demonstrates the shear stress displacement (τ_s-d_s) curves of the coupled model under different values of σ_n. As can be seen, under the direct shear condition, the coupled model shows evident elastoplastic shear behaviour, and each τ_s-d_s curve can be divided into five main stages. At stage one (oa), when the shear begins, d_s increases from 0 to 0.003 m, and a slight decrease in k_i can be observed due to the breakage of a small group of bonds that exceed the normal strength limit. At stage two (ab), τ_s keeps increasing

while d_s increases from 0.003 m to around 0.015 m. Evident elastic deformation can be observed at the interface, and k_i of each τ_s-d_s curve maintains a stable value. At stage three (bc), shear failure begins to dominate the bond breakage, with a slight decrease in k_i occurs at the interface, and τ_s under each σ_n reaches a peak stress value, with d_s increasing to around 0.019 m. At stage four (cd), the propagation of the bond breakage at the interface occurs significantly, leading to a rapid collapse of τ_s, as d_s increases from around 0.019 m to 0.04 m. Finally, at stage five (de), with the binding effect at the interface entirely disappearing, frictional sliding occurs between the DE and the FD models, and τ_s under each σ_n maintains a stable value of τ_r. As d_s increases to 0.1 m, the shape of τ_s-d_s curves indicate a perfect plateau, and the shear behaviour of the strain-softening can be observed at the interface.

Meanwhile, the coupled model's strength parameters and deformation properties under the direct shear condition highly coincide with the expected results, with the determined microstructural parameters shown in Table 4.3 in Chapter 4 and Table 5.3 applied to the discrete particles and the interfaces. During the shear process, under σ_n of 0.25 MPa, 0.5 MPa and 1.0 MPa, τ_p reaches 1.17 MPa, 1.32 MPa and 1.58 MPa, respectively, with a maximum relative error of 2.4%. According to the Mohr-Coulomb strength criterion, the coupled model's failure envelope can then be plotted by linearly relating τ_p to σ_n. Non-zero apparent c_i and φ_i are calculated as 1.04 MPa and 29.5°, respectively, with relative errors of 4% and 1.6%. As σ_n increases from 0.25 MPa to 1.0 MPa, k_i under each σ_n increases by 25% from 62.8 MPa to 78.8 MPa. A weighted average value of k_i is calculated as 73.5 MPa, with a relative error of 5%. These observations are highly consistent with previous studies by Fall and Nasir (2010), which found that higher σ_n is associated with

higher τ_p and k_i at the interface of the coupled model. Under σ_n of 0.25 MPa, 0.5 MPa and 1.0 MPa, τ_r maintains stable at 0.18 MPa, 0.33 MPa and 0.63 MPa, respectively, and the corresponding μ_i is calculated as 0.63, 0.66 and 0.72, respectively, with a maximum relative error of 9%. It must be mentioned that a slight increase in δ_c is also observed as σ_n Increases from 0.25 MPa to 1.0 MPa.

Fig. 5.4b and Fig. 5.4c demonstrate that as d_s increases from 0 to 0.1 m, both σ_n The y- and z- directions are stably servo-controlled at 0.25 MPa, 0.5 MPa and 1.0 MPa on the constraint walls of the DE model. When the servo-controlling scheme realizes, the average contact forces between the discrete particles and the walls are gradually adjusted to balance with the target values of σ_n cyclically servo-controlling the velocities of the lateral and top constraint walls surrounding the discrete particles. Fig. 5.5a presents the contour of σ_n in the y-direction at the central cross-section of the DE model when d_s reaches 0.02 m. It should be mentioned here that in FLAC3D, the compressive and tensile stresses are plotted as negative and positive, respectively. As can be seen, due to different diameters and effective bond gaps of the discrete particles, the contact stress among the spheres induced by σ_n indicates a non-uniform distribution, leading to an unbalanced distribution in the normal stress in the y-direction at different parts of the central cross-section. Fig. 5.5b shows the contour of σ_n in the z-direction at the interface of the coupled model when σ_n reaches 0.02 m. The figure indicates that σ_n transferred from the discrete particles to the top face of the finite zones also exhibits a non-uniform distribution. The boundary effect from the fixed faces during the shear process also contributes to this unbalanced distribution. However, either the calculated average normal stress applied to the central cross-section in the y-direction or transferred to the finite zones in the z-

direction still highly coincides with servo-controlled σ_n applied to the constraint walls of the coupled model. It indicates that servo-controlling the normal stress with the coupled FD-DE method can reflect the true nature of the laboratory operation more factually than the FD method alone.

Fig. 5.4d demonstrates the relationship between the normal displacement (d_n) and d_s of the coupled model under different σ_n. As can be seen at the stage of elastic deformation, d_n under different values of σ_n all increase rapidly, as d_s increases from 0 to around 0.02 m. It indicates that the shear condition causes significant shear dilation at the interface of the coupled model (Wang et al., 2018), and the effect can be weakened at higher values of σ_n due to the higher constraint effect. Then, during the collapse of τ_s, d_n decreases stably as d_s increases from around 0.02 m to 0.04 m. Finally, under lower σ_n of 0.25 MPa and 0.5 MPa, as d_s increases from 0.04 m to 0.1 m, d_n maintains plateau, but shear dilation still exists. However, under a higher σ_n of 1.0 MPa, d_n decreases to a value lower than 0, and the constraint effect gradually diminishes shear dilation.

Fig. 5.6 shows the distribution of magnitude displacement (d_m) in the coupled model under different values of σ_n at the central cross-section. The length of the displacement vector represents the magnitude and the acting direction of d_m is pointing from the initial position of the discrete sphere or the gridpoint of the finite zone. For the DE model, significant rightward motions can be observed on the discrete particles due to the relatively low displacement rate during the entire shear process. Before τ_s reaches τ_p, the binding effect at the interface hinders the rightward motions of the discrete particles, leading to a relatively lower d_m at the bottom of the DE model. After the collapse of τ_p, the gradient of d_m from the top to the bottom of the DE model significantly decreases due

to the disappearance of the interface's binding effect. However, while the frictional sliding dominates the shear behaviour, the gradient of d_m still exists at the right end of the DE model. For the FD model, before τ_s reaches τ_p, an evident convex thrust of d_m caused by shear dilation can be observed in the finite zones along the motion direction of the grid points. After the collapse of τ_p, the interface's binding effect disappears, leading to the weakening of shear dilation and the diminution of the convex thrust. It also indicates that a higher σ_n is associated with a larger convex thrust and a higher d_m. Meanwhile, at the frictional sliding stage, a vortex zone of d_m is formed gradually by the combined action of shear dilation and the constraint effect on the right side of the FD model. During the shear process, the discrete particles in this zone undergo shear compression and generate the shear strain localization.

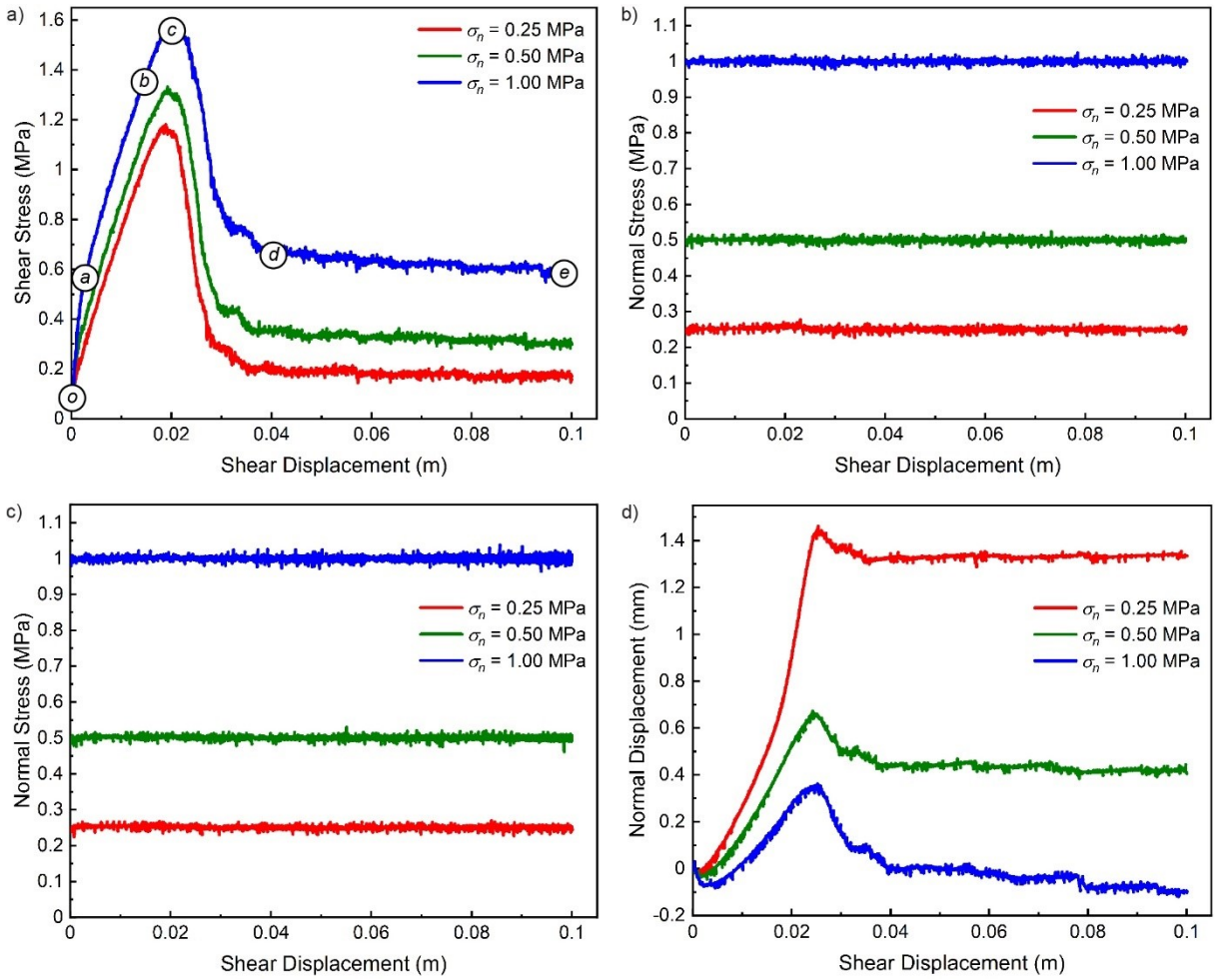

Fig. 5.4 Results of the direct shear tests on the coupled FD-DE model of the combined R-CRF specimens: a) τ_s-d_s curves, b) σ_n-d_s curves in the z-direction, c) σ_n-d_s curves in the y-direction, and d) d_n-d_s curves.

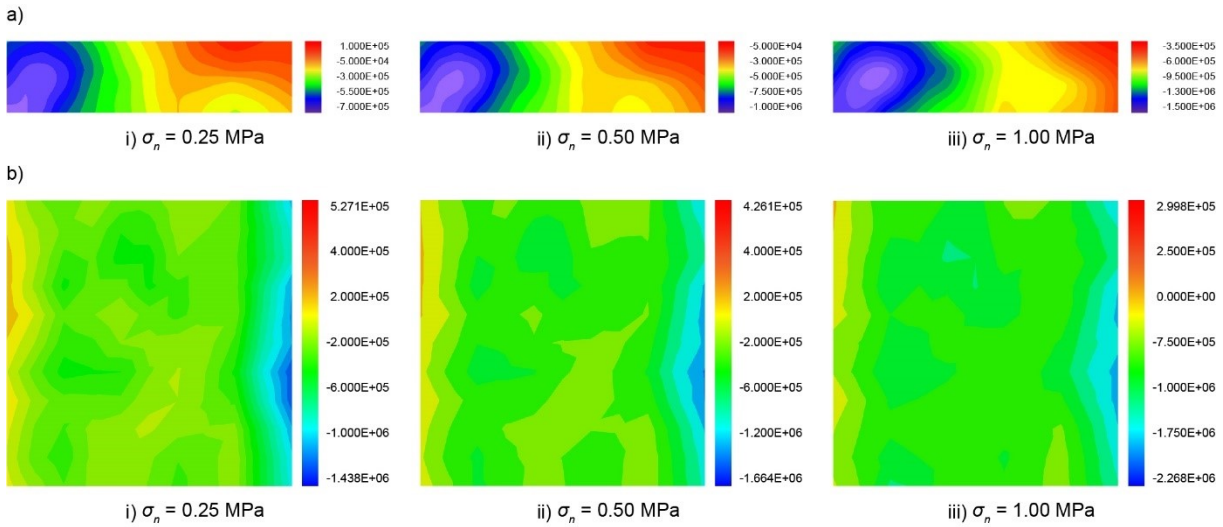

Fig. 5.5 Distribution of σ_n on the coupled FD-DE model of the combined R-CRF specimens in: a) y-direction and b) z-direction.

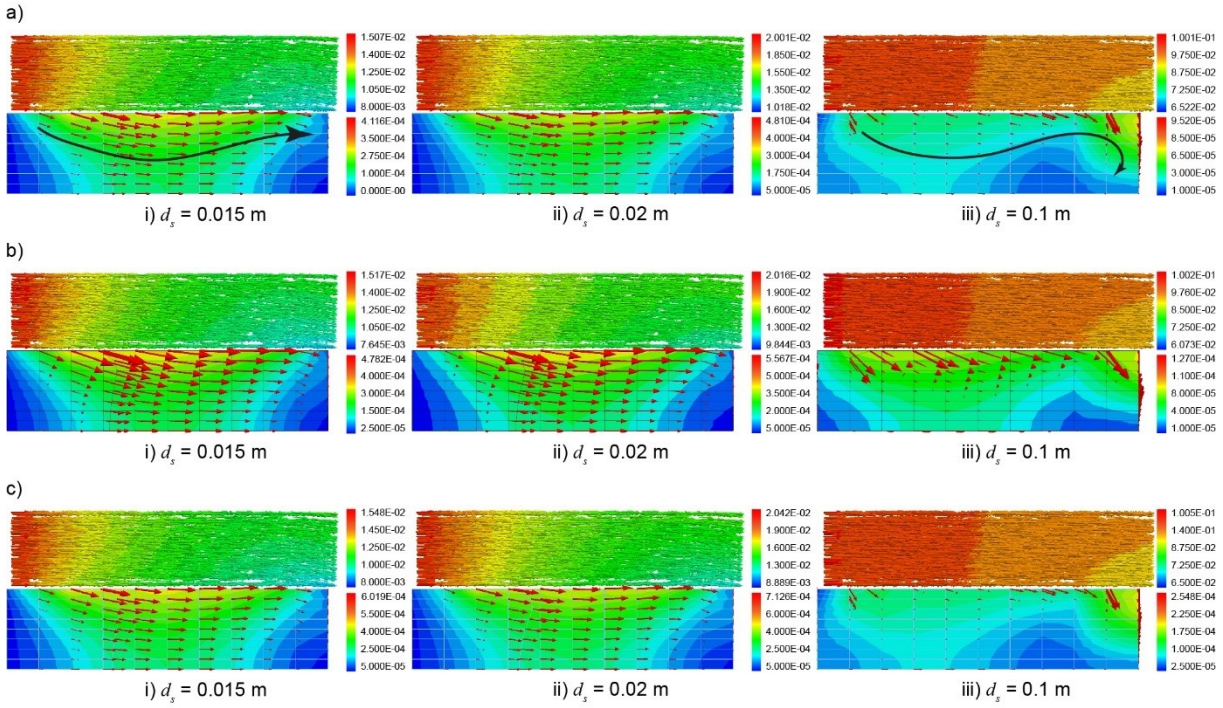

Fig. 5.6 Distribution of d_m at the CCS of the coupled FD-DE model of the combined R-CRF specimens under different σ_n of: a) 0.25 MPa, b) 0.50 MPa, and c) 1.00 MPa.

Fig. 5.7 indicates the evolution of normal contact force (σ_n^c) chain formed among the discrete particles at the DE model's central cross-section during the entire shear process. The mutually connected cylinders represent the force chain at the contact positions. Meanwhile, the thickness and axial direction of cylinders reflect the magnitude and direction of σ_n^c, respectively. The cylinders are marked in red and blue to identify the stress state of σ_n^c in compression and tension, respectively. As can be seen, before the shear begins, the DE model is only subjected to the servo-controlled σ_n applied on the constraint walls, and either the magnitude or the direction of σ_n^c in compression shows uniform distribution in the DE model. Due to the constraint effect, the discrete particles are squeezed, and the stress state of σ_n^c in the DE model is dominated by compression and no evident σ_n^c in tension is observed. Then, during the elastic deformation stage, as d_s increases from 0 to around 0.02 m, the force chain of σ_n^c in compression progressively distributes unevenly. A concentration band of σ_n^c in compression can then be formed diagonally from the left top corner to the right bottom corner of the central cross-section under the combined action of shear displacement rate and the binding effect at the interface. While d_s increases from around 0.02 m to 0.1 m, the interface's binding effect gets weakened and the band gradually diminishes. Finally, the band disappears when the frictional sliding dominates the shear behaviour of the coupled model. However, there is a significant trend in the direction of the force chain of σ_n^c in compression at this stage, which is the same as the shear direction, compared with the chain under the initial servo-controlled σ_n. During the elastic deformation stage, a concentration band of σ_n^c in tension is also formed diagonally in the DE model from the bottom left corner to the top right corner of the central cross-section. It shows the force chain of σ_n^c in tension formed in the

discrete particles, which results from the gradient of τ_s along the height of the DE model, which always acts as an inhibition to the rightward motion of the discrete particles. However, the inhibition effect is not significant. Finally, the force chain of σ_n^c in tension diminishes when virtual bonds at the interface entirely break and the binding effect disappears.

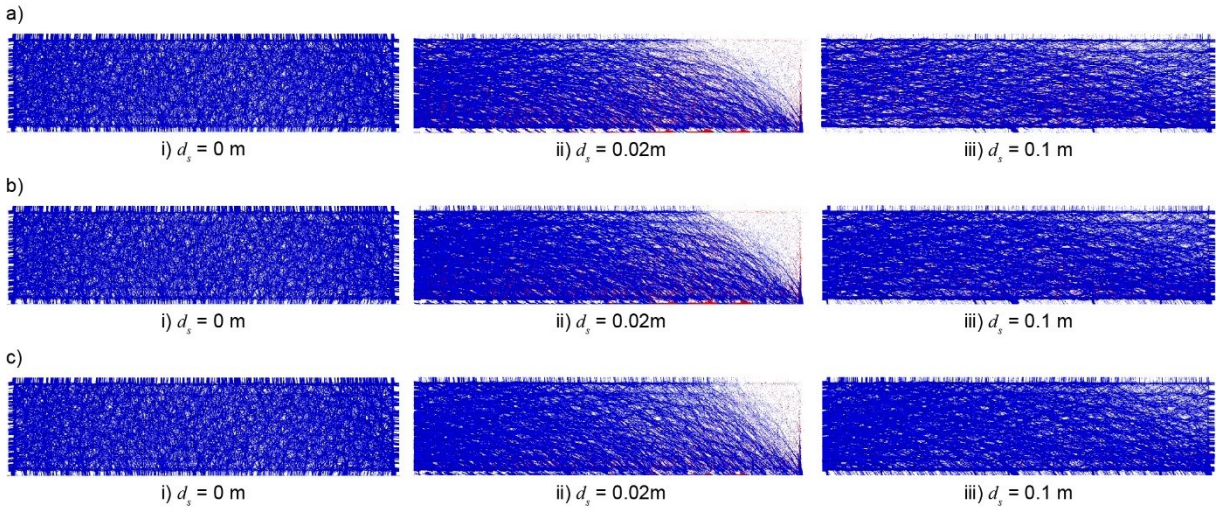

Fig. 5.7 Force chain of σ_n^c at the CCS of the DE model of the CRF specimens under different σ_n of: a) 0.25 MPa, b) 0.50 MPa, and c) 1.00 MPa.

Fig. 5.8 demonstrates the distribution of σ_{xx} in the coupled model under different values of σ_n during the entire shear process. As can be seen, σ_{xx} can be nonuniformly distributed in the coupled model, even if under a stable and even shear displacement rate. During the elastic deformation stage, a significant stress concentration zone of σ_{xx} is formed on the right side of the DE model. The maximum value of σ_{xx} at the core of the zone gradually increases as d_s increases from 0 to around 0.02 m. An evident gradient in σ_x can be observed along the DE model's height, which leads to a larger σ_{xx} at the interface of the coupled model due to the binding effect. Meanwhile, the gradient causes evident σ_{xx} in

tension at the right top corner of the DE model, which highly coincides with the force chain of σ_n^c plotted in Fig. 5.7. Then, after the collapse of τ_s, the stress concentration zone of σ_x progressively diminishes and moves to the bottom right corner of the DE model. The maximum value of σ_{xx} at the core of the zone significantly decreases, as d_s increases from around 0.02 m to 0.05 m. It also indicates that the redistribution of σ_{xx} at this stage is not evident under higher values of σ_n, as a higher frictional force can significantly inhibit the motion of discrete particles in the DE model. However, for the FD model, the distribution of σ_x is passively controlled by the fixed boundary conditions at the constraint walls. During the entire shear process, the FD model's finite zones are dragged by the DE model and potentially have a rightward motion trend. Thus, the stress state of σ_{xx} The finite zones transform from tension to compression along the shear direction from left to right. As can be seen in Fig. 5.8, the stress concentration zones of σ_{xx} in tension and in compression both expand during the elastic deformation stage. After the collapse of τ_s, σ_{xx} rapidly decreases and the stress concentration of σ_{xx} in compression on the left almost disappears under the domination of the frictional sliding at the interface of the coupled model.

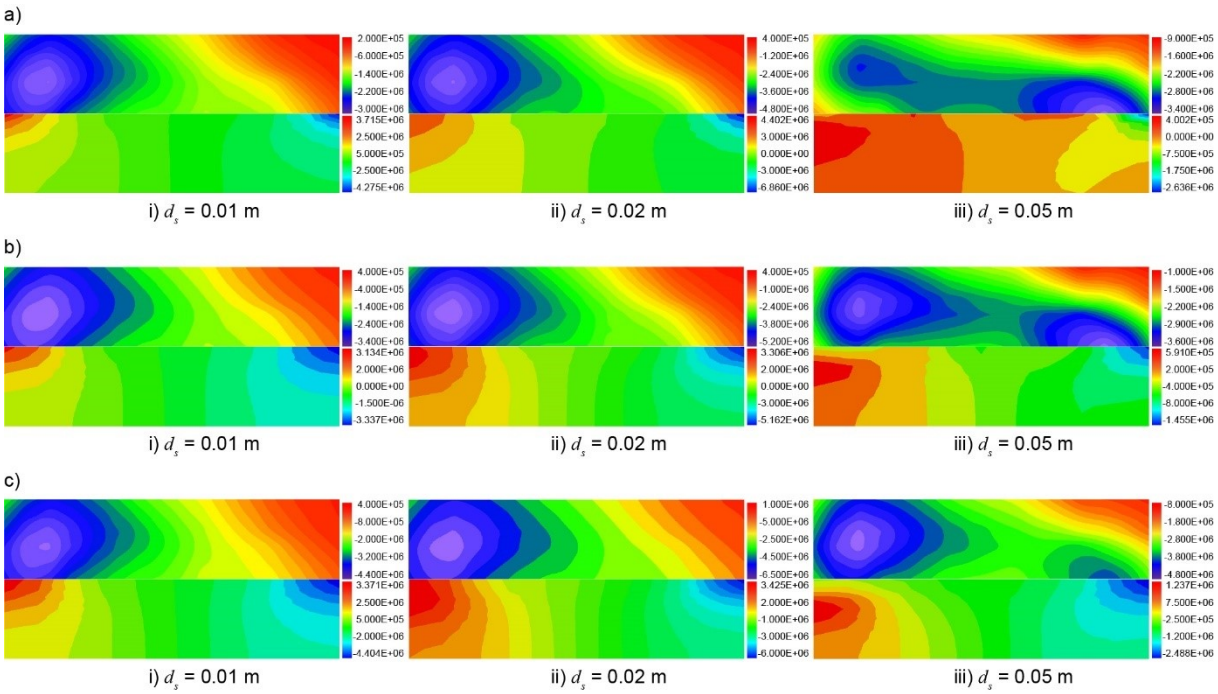

Fig. 5.8 Distribution of σ_{xx} at the CCS of the coupled FD-DE model of the combined R-CRF specimens under different σ_n of: a) 0.25 MPa, b) 0.50 MPa, and c) 1.00 MPa.

Fig. 5.9 and Fig. 5.10 demonstrate the three-dimensional contours of the zx-component of the average peak and residual stress tensors (τ_{zx}^{p} and τ_{zx}^{r}) at the interface when τ_s reaches τ_p and τ_r, respectively, under different σ_n. The figures illustrate the comparison between the contours plotted using the FD and DE methods. For the FD model, the data of τ_{zx}^{p} and τ_{zx}^{r} are directly collected from 81 groups of the monitoring gridpoints that are uniformly located on the top face of the finite zones at the interface. It also should be mentioned here that in Fig. 5.9 and 5.10, the compressive stress is plotted as positive to make the distribution of the stress peaks and valleys clear and easily focused from the three-dimensional contours. For the DE model, the same number of measuring spheres with the exact locations of the corresponding monitoring gridpoints are created on the bottom face of the discrete particles to measure the stress data. Finally, τ_{zx}^{p} and τ_{zx}^{r} are

gained from each monitoring gridpoint and the corresponding measuring sphere. The mapping software Surfer 18.0 is adopted to plot the data into three-dimensional contours with the Kriging gridding method. It has been validated in Fig. 5.4a that the stress-strain behaviour and the coupled model's macro-mechanical properties under the direct shear condition highly coincide with the expected results. However, in this case, the contours of τ_{zx}^{p} and τ_{zx}^{r} reflect that a dynamic equilibrium exists between τ_{zx}^{p} , τ_{zx}^{r} and τ_{s}. τ_{zx} is nonuniformly distributed at different locations on the interface during the entire shear process due to the constraint effect and the random generation method of the discrete particles, even under the servo-controlled σ_n and low shear displacement rates.

As shown in Fig. 5.9, under σ_n of 0.25 MPa, 0.5 MPa and 1.0 MPa, τ_s reaches τ_p when d_s is 0.018 m, 0.019 m, and 0.02 m, respectively. The contours of τ_{zx}^{p} plotted from the DE and the FD models highly coincide with each other. Both the contours have an excellent presentation of the distribution of τ_s with the coupling scheme successfully applied at the interface. The figures indicate that the peak value of τ_{zx}^{p} under each value of σ_n is relatively the same, although higher σ_n values can be associated with the higher bottom limit value of τ_{zx}^{p}. As can be seen in Fig. 5.9, τ_{zx}^{p} demonstrates a relatively lower value at the shear box boundaries due to the constraint effect. Moreover, because the discrete particles with different diameters randomly generate in the shear box, the number of contacts and discrete particles in each measuring sphere is variable, and groups of stress concentration zones of τ_{zx}^{p} appear at the interface. This indicates that the coupled model can effectively interpret the true nature of the combined R-CRF specimen with a nonplanar and rough interface more factually than modelling with the FD method alone.

Fig. 5.10 shows the contours of τ_{zx}^{r} when d_s reaches 0.05 m. As can be seen, under σ_n of 0.25 MPa, 0.5 MPa and 1.0 MPa, τ_r is 0.18 MPa, 0.33 MPa, and 0.63 MPa, respectively. However, both the contours of τ_{zx}^{r} plotted from the DE and the FD models show significantly uneven distribution. Groups of the stress concentration zones of τ_{zx}^{r} appear at the interface, and higher σ_n values can be associated with higher peak values of τ_{zx}^{r}. Meanwhile, due to the breakage of virtual bonds at the interface, the coincidence between the two contours of τ_{zx}^{r} disappears, and the contour from the DE model shows a more imbalanced distribution in τ_{zx}^{r} with frictional sliding dominating the shear behaviour. An evident increasing trend in τ_{zx}^{r} can be observed at the interface from left to right along the shear direction. This phenomenon can result from the leftward motion of the stress concentration zone of σ_{xx} in the DE model caused by frictional sliding. Moreover, the trend is not significant in the FD model due to the constraint effect at the shear box boundaries.

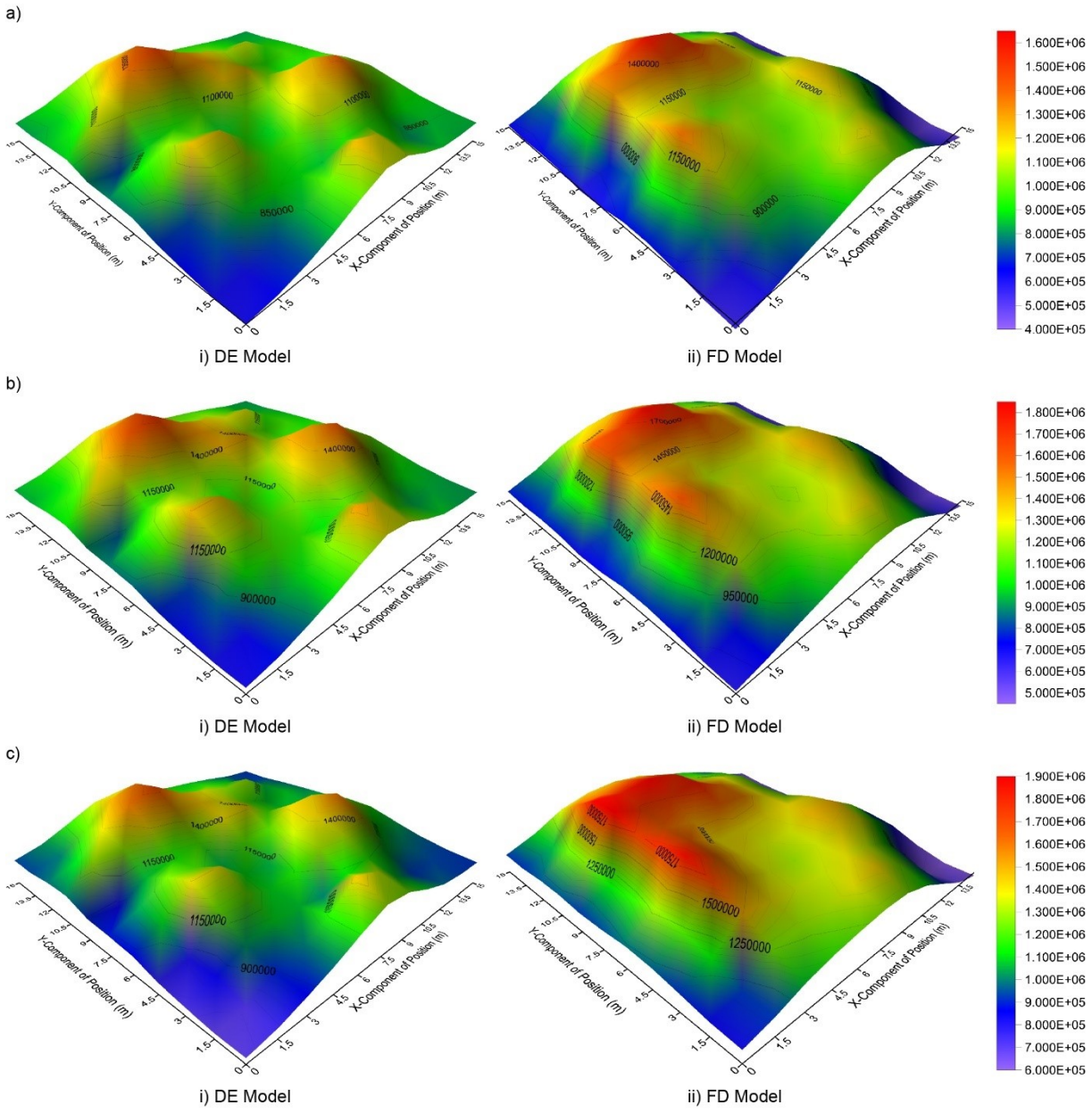

Fig. 5.9 Distribution of τ_{zx}^{p} at the interfaces in the coupled FD-DE model of the combined R-CRF specimens under different σ_n of: a) 0.25 MPa, b) 0.50 MPa, and c) 1.00 MPa.

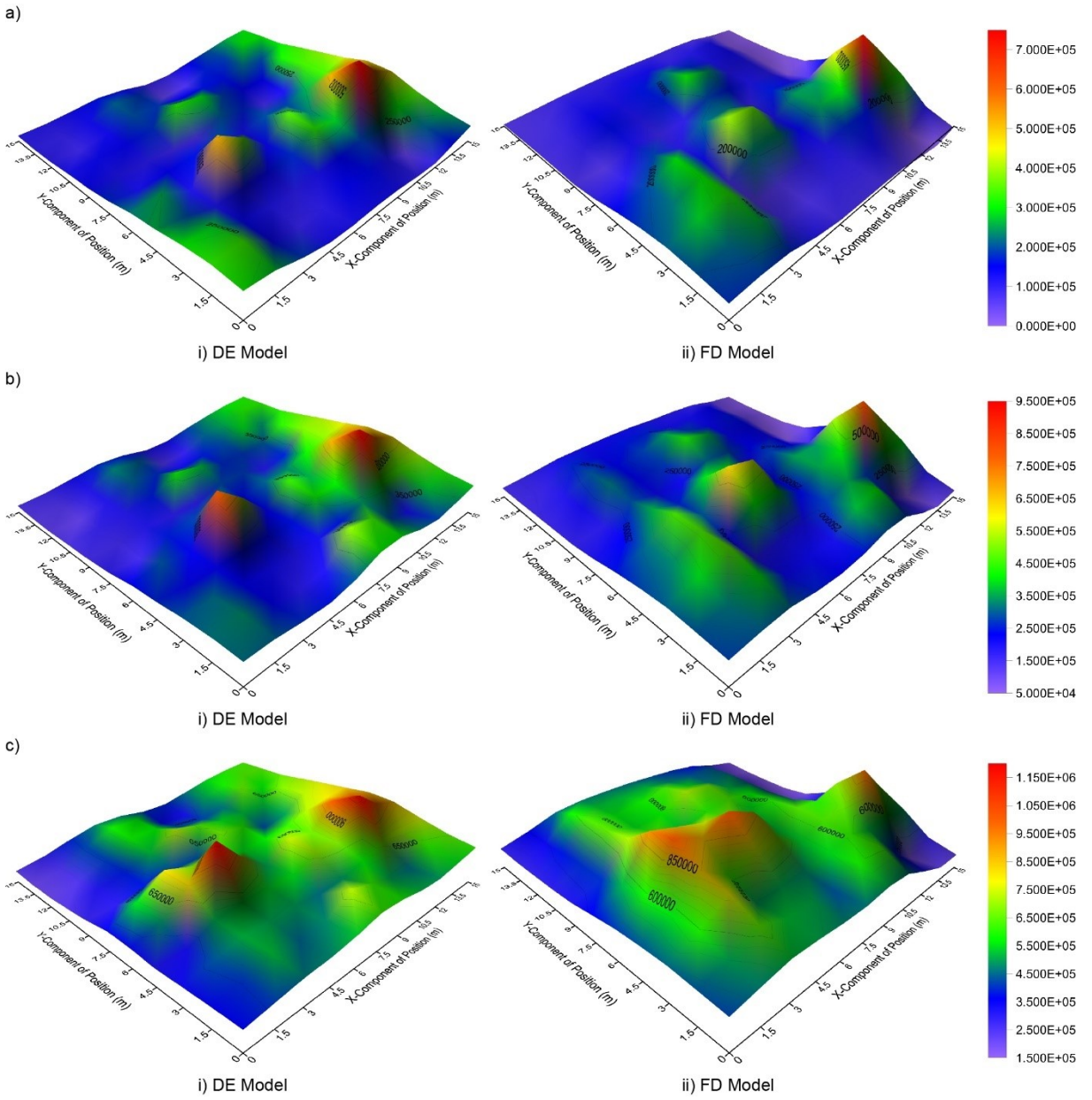

Fig. 5.10 Distribution of τ_{zx}^{r} at the interfaces in the coupled FD-DE model of the combined R-CRF specimens under different σ_n of: a) 0.25 MPa, b) 0.50 MPa, and c) 1.00 MPa.

5.4.2 Effects of the microstructural parameters of the PB contact model on the shear behaviour of the coupled FD-DE model of the combined R-CRF specimen

This section will study the effects of the interface's microstructural parameters on the shear behaviour and macro-mechanical properties of the coupled model. Different orders of magnitude were assigned. Five groups of numerical tests for each parameter were carried out under σ_n of 0.5 MPa to monitor the changes in the shape of τ_s-d_s curves, strength parameters and deformation properties. The effects of $\overline{\sigma}$, $\overline{\tau}$, $\overline{\varphi}$, and μ are only briefly described in this section, as their effects have good agreement with previous parametric studies (Bahaaddini et al., 2015, 2013, 2012) on the DE models, which indicate that $\overline{\sigma}$ and $\overline{\tau}$ can directly impact τ_p of the coupled model. In the parallel bond contact model, due to the parallel bonds following the Mohr-Coulomb strength criterion, a significant increase in τ_p can be observed when either $\overline{\sigma}$ and $\overline{\tau}$ increases. $\overline{\varphi}$ mainly influences the shape of the τ_s-d_s the curve at stages three and four, which are described in Fig. 4.6 in Chapter 4, indicating that as $\overline{\varphi}$ increases, a slight increase in τ_p can be observed, and the increasing and decreasing rates of τ_s at stages three and four, both decrease slightly, resulting in a relatively smooth curve shape. Meanwhile, μ can be highly consistent with the natural friction coefficient of the interface, only influencing the shear behaviour of the coupled model when frictional sliding occurs. As μ_i increases, τ_r increases significantly.

The microstructural parameters of E, $\overline{E}$, η, and $\overline{\eta}$ can significantly impact the shear behaviour and macro-mechanical properties at the interface of the coupled model under the direct shear condition. Fig. 5.11a to Fig. 5.11d demonstrate τ_s-d_s curves of the coupled model under σ_n of 0.5 MPa, with the order of magnitude of changes in E, $\overline{E}$, η and $\overline{\eta}$,

respectively. Fig. 11a shows that as E increases from 1.5 MPa to 15.0 GPa, k_i increases, leading to a steeper curve shape at the elastic deformation stage. Meanwhile, at higher E values, the decreasing rate of τ_s after the collapse of τ_p decreases. However, as E increases, both τ_p and τ_r first increase and then decrease. Fig. 11b indicates that $\overline{E}$ has a tremendous impact on the shape of τ_s-d_s curves. While $\overline{E}$ increases from 0.15 MPa to 1.5 GPa, k_i significantly increases, and the shear behaviour of the coupled model transforms from strain-hardening to strain-softening. When $\overline{E}$ is below 1.5 MPa, no evident τ_p or τ_r appears. However, while $\overline{E}$ increases from 15.0 MPa to 1.5 GPa, τ_p decreases dramatically, and τ_p maintains a stable value. As shown in Fig. 11c, as η increases from 0.1 to 1000, no evident changes in k_i or the curve shape are observed, while both τ_p and τ_r decrease significantly. Fig. 11d indicates that $\overline{\eta}$ can also remarkably impact the shape of τ_s-d_s curves. While $\overline{\eta}$ increases from 0.1 to 1000, k_i decreases dramatically, leading to a smoother and flatter curve at the elastic deformation stage. As $\overline{\eta}$ increases, both τ_p and τ_r first increase and then decrease. However, unlike the effect of $\overline{E}$, at higher $\overline{\eta}$ values, τ_p still exists and the shear behaviour of the coupled model is strain-hardening. To summarize, all four microstructural parameters of E, $\overline{E}$, η and $\overline{\eta}$ can impact the macro-mechanical properties of the interface while only $\overline{E}$ and $\overline{\eta}$ can remarkably influence the shear behaviour of the coupled model.

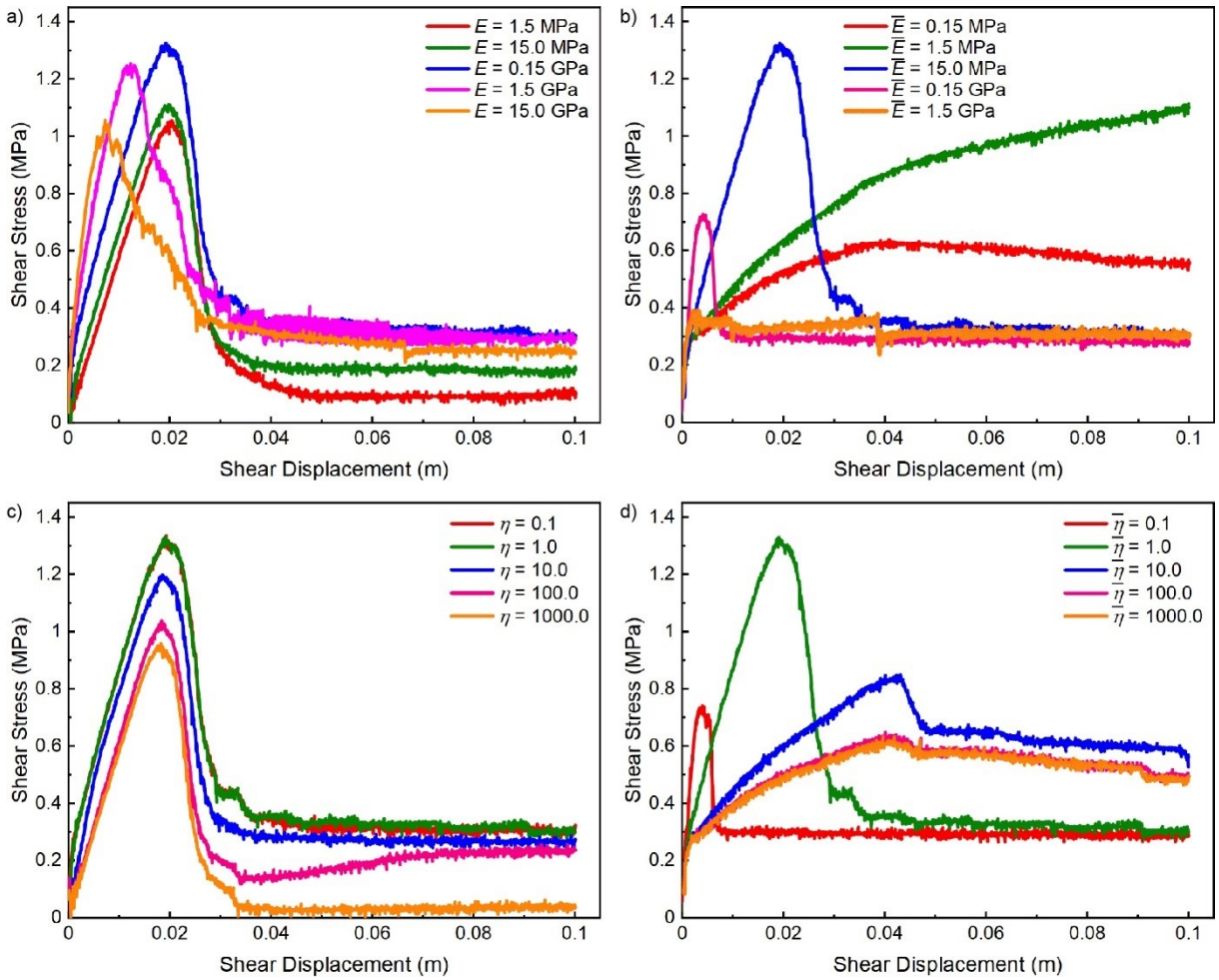

Fig. 5.11 Effects of the microstructural parameters of the PB contact model on the shear behaviour of the FD-DE model of the combined R-CRF specimens: a) E, b) $\overline{E}$, c) φ, and d) $\overline{\varphi}$.

5.4.3 Effects of the mesh size of the interface on the shear behaviour of the coupled FD-DE model of the combined R-CRF specimen

Fig. 5.12 presents the effects of the mesh size of the FD model's top face on the coupled model's shear behaviour and macro-mechanical properties. It indicates that with N_m increasing from 25 to 625, both k_i and τ_p increase, leading to a steeper curve shape at stages two and three, while no evident changes in τ_r at stage five are observed.

Meanwhile, as N_m increases, the shape of τ_s-d_s curves maintain strain-softening and the decreasing rate of τ_s after the collapse of τ_p has no changes at stage four. It must be mentioned that the mesh size along the height of the FD model does not influence the coupled model's shear behaviour or macro-mechanical properties. Thus, these figures are not presented in this section.

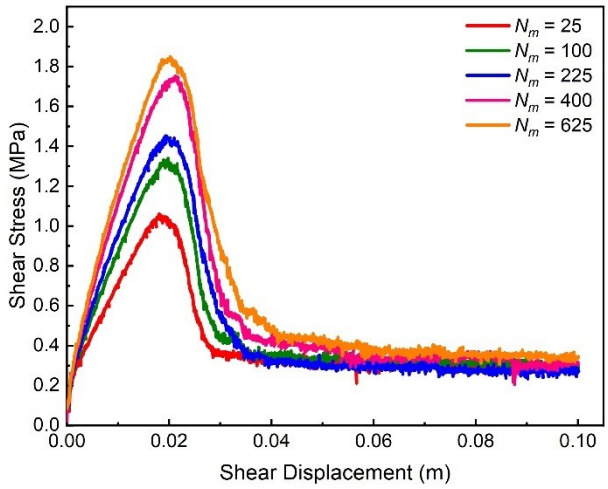

Fig. 5.12 Effect of N_m of the FD model of the rock specimen on the shear behaviour of the FD-DE model of the combined R-CRF specimens.

5.5 Conclusions

In this study, three-dimensional numerical direct shear tests were carried out on the modelled combined rock-cemented rockfill (R-CRF) specimens based on the coupled finite difference and discrete element (FD-DE) method by using Itasca's software FLAC3D 7.0 and PFC3D 6.0. The simulation provided an efficient scheme to determine the microstructural parameters of the coupled model of the combined specimen with a frictional-bonded interface. Meanwhile, the simulation validated the feasibility of using the coupled FD-DE method to model the binding effect at the interface between two geo-

materials, such as the CRF column and the surrounding rocks. The primary observations and conclusions are as follows.

Under the direct shear condition, the coupled FD-DE model of the combined R-CRF specimen shows evident elastoplastic shear behaviour of the strain-softening, including five main stages of the initial bond breakage, elastic deformation, bond breakage propagation, shear strength collapse and frictional sliding. With the microstructural parameters of the DE model of the CRF specimen determined, the coupled model's strength parameters and deformation properties under the different servo-controlled normal stresses highly coincide with the expected results. The coupled model's failure envelope under the direct shear condition also agrees with the Mohr-Coulomb strength criterion. The servo-controlled normal stress monitored in either the y- or z- direction maintains a stable value during the entire direct shear process. However, it can nonuniformly distribute at different locations on the corresponding central cross-section of the coupled model, indicating that the numerical servo-controlling scheme based on the coupled FD-DE method can reflect the true nature of the laboratory operation more factually than the FD method alone.

A significant shear dilation phenomenon can be observed at the interface of the coupled model during the entire direct shear process, which leads to a rapid increase in the normal displacement during the elastic deformation stage, and then a stable plateau value during the frictional sliding stage. During the entire shear process, the magnitude displacement of the discrete particles is higher at the top while lower at the bottom of the DE model since the binding and frictional effects at the interface hinder the rightward motion of discrete particles. For the FD model, during the elastic deformation stage, an evident

convex thrust of the magnitude displacement can be observed in finite zones due to shear dilation. The convex thrust gradually diminishes after the collapse of the peak shear stress. A vortex zone of the magnitude displacement can be formed during the frictional sliding stage by shear dilation and the constraint effect from boundary walls.

During the elastic deformation stage, a concentration band of the normal contact force in compression can be formed diagonally from the top left corner to the bottom right corner of the DE model. After the peak shear stress collapse, the concentration band gradually diminishes due to the weakened binding effect at the interface. During the frictional sliding stage, a significant rightward trend can be observed in the chain of the normal contact force in compression, with the binding effect disappearing. During the elastic deformation stage, a significant stress concentration zone in the x-direction can be formed and expanded on the left of the DE model. This concentration zone progressively diminishes and moves to the bottom right corner of the DE model after the peak shear stress collapse due to the weakened binding effect at the interface. However, for the FD model, the stress in the x-direction passively transforms from tension to compression along the shear direction from left to right during the entire shear process, during which the zx-component of the stress in the coupled model shows a non-uniform distribution at different locations on the interface due to the constraint effect and the random generation method of the discrete particles. For the peak shear stress at the interface, contours plotted from the DE and the FD models highly coincide, and both contours have an excellent interpretation of the peak shear stress distribution of the coupled model. For the residual shear stress, an evident increasing trend in the zx-component of the stress can be observed in the contour from left to right in the DE model. This trend results from the

rightward motion of the concentration zone of the stress in the x-direction caused by the frictional sliding. However, no corresponding trend can be observed in the contour plotted from the FD model due to the constraint effect at the boundary walls.

The interface microstructural parameters significantly impact the shape of the shear stress displacement curve and macro-mechanical properties, including the peak shear stress, residual shear stress and the shear stiffness of the coupled model under the direct shear condition. The peak and residual shear stress can significantly increase when the bond normal or shear strength at the interface increases. As the contact friction coefficient at the interface increases, the residual shear stress increases. While the effective modulus, bond effective modulus or bond stiffness ratio at the interface increases, both the peak and residual shear stress increase and decrease. However, when the interface's stiffness ratio increases, the peak and residual shear stress decrease. The increase in the bond's internal friction angle at the interface can contribute to a smoother curve shape during bond breakage propagation and peak shear stress collapse. The shear stiffness increases significantly with increases in either the effective modulus or bond effective modulus. However, when the effective bond modulus increases, the coupled model's shear behaviour can transform from strain-softening to strain-hardening. As the stiffness ratio increases, the shear stiffness maintains a stable value, while when the bond stiffness ratio increases, the shear stiffness decreases significantly. Meanwhile, as the mesh size at the interface decreases, the shear stiffness and peak stress increase. Moreover, the residual shear stress maintains a stable value.

Chapter 6 Coupled finite difference and discrete element method for modelling the dumping process of the freshly cemented rockfill

In this Chapter, the Johnson-Kendall-Robert (JKR) contact model was adopted in the discrete element (DE) model of the fresh CRF material to simulate the adhesion among the aggregate particles that results from the liquid-bridge forces and binding effect of the Portland cement. First, the slump test, which is used to evaluate the flowability and workability of the fresh concrete-like material, was simulated with the DE method, and the effects of the microstructural parameters on the flowability of the DE model of the fresh CRF material were studied. After that, the backfilling process of the fresh CRF material at a single stope was modelled with the coupled finite difference (FD) and discrete element (DE) method, and the stress, displacement, and porosity distribution in the coupled FD-DE model were monitored and recorded during the dumping process. The modelling results indicate that the microstructural parameters of surface energy and friction coefficient in the JKR contact model are two main factors that significantly influence the flowability of the DE model of the fresh CRF material. Consequently, the flowability and consistency of the fresh CRF material can determine the CRF column shape, the backfilling quality, and the efficiency of the single stope.

6.1 Introduction

At a Canadian hard rock mine, the cemented rockfill (CRF) is a mixture of water, Portland cement, and granitic aggregates of crushed waste rocks (Sepehri et al., 2017). The fresh CRF material is mixed to a homogenous and workable condition on the ground and then dumped into an extracted stope by mining trucks. During the backfilling process, the fresh CRF material behaves like a fresh concrete-like material, and the composition, cement

ratio, and water ratio significantly influence the rheological properties of the fresh CRF material (Hou et al., 2017; Behera et al., 2019). Meanwhile, the flowability of the fresh CRF material determines the backfilling quality and backfilling efficiency of the mined-out area at the hard rock mine.

Fresh concrete is a mixture of concentrated aggregates suspended in a viscous liquid of cement material (Boulekbache et al., 2010). The Bingham model is the most popular constitutive model to describe concrete-like material. In the Bingham equation, the yield stress and the plastic viscosity coefficient are the two main indexes to indicate the rheological properties of the non-Newtonian flow, which are not constant during the shear time due to the development of thixotropy and the loss of workability (Roussel, 2005, 2006). Many types of the laboratory and field tests can be used to evaluate the flowability of concrete-like materials, such as the slump test, L-pipeline test, and viscosimeter test. However, the slump test is proved to be the most efficient way to classify concrete-like material in terms of their flowability in the laboratory and field, though no rheological properties were measured during the test (Boulekbache et al., 2010). In a traditional slump test, there is a slump bucket in a circular truncated cone shape and a hard, non-absorbent base plate which behaves as the measuring platform (Hoornahad and Koenders, 2012). The slump bucket will be filled with fresh concrete or concrete-like materials, and the bucket will be carefully lifted in the vertical direction to start the slumping process of the material. The slump of the fresh concrete or concrete-like material is defined as the distance from the slumped material's top to the slump bucket's top level. The higher the slump is, the greater the flowability of the fresh concrete-like material (Wu and Qu, 2009).

In recent years, the discrete element (DE) method has been rapidly developed and widely used in the numerical modelling of fresh concrete and concrete-like materials to study their rheological behaviour and flowability (Li et al., 2021). Guo et al. (2010) simulated workability tests on fresh concrete with the DE method and studied the effect of the microstructural parameters in the linear contact model on the rheological behaviour of the fresh concrete. Krenzera et al. (2019) simulated the mixing process of fresh concrete and realized the liquid transportation process between the wet and dry aggregate particles with the DE method. Mechtcherine and Shyshko (2015) related the microstructural parameters in the contact model to the yield stress based on the Bingham constitutive model and studied the effect of the microstructural parameters on the flow shape of the DE model of the fresh concrete. Zhang et al. (2020) simulated the filling performance and pouring process of the fresh concrete with the DE method by conducting numerical L-pipeline tests and studied the influence of the rockfill void rate on the passing ability of the fresh self-compacting concrete.

Some studies focus on the numerical modelling of the slump test on fresh concrete material based on the DE method, although the slump test is the most common and popular empirical test in both the laboratory and the field to evaluate the flowability of the fresh concrete material. Hoornahad and Koenders (2012) simulated the slump test on the DE model of the fresh concrete and calibrated the rheological behaviour of the model with the real fresh concrete material, and Deeb et al. (2014) studied the flowability of the self-compacting concrete by simulating the slump test with the DE method. Li et al. (2021) adopted the Johnson-Kendall-Robert (JKR) contact model in the DE model of the fresh

concrete to simulate the adhesion results from the liquid-bridge forces among the discrete particles.

These numerical slump tests on various fresh concrete with different aggregates and additives all showed great agreement with their corresponding laboratory test results on the real fresh concrete material. However, there are few numerical studies about using the DE method to simulate concrete-like materials, such as the cemented paste backfill (CPB) or cemented rockfill (CRF). In this study, firstly, a series of numerical slump tests were conducted on the DE model of the fresh CRF material, which was applied with the JKR contact model, to study the effects of the microstructural parameters on the flowability of the DE model of the CRF material. Secondly, a single stope was extracted in the FD model of the orebody, and the backfilling process of the DE model of the fresh CRF material was simulated by dumping the discrete particles into the stope in layers to study how the flowability and consistency can determine the backfilling efficiency and quality of the mined-out area.

6.2 Material and methodology

6.2.1 Mining and backfilling methods

As discussed in Chapter 3, the blasthole stoping (BHS) method was adopted in the hard rock mine, which is in Northwest Territories, Canada, and then the mined-out openings were backfilled with the cemented rockfill (CRF), which was a mixture of water, Portland cement and the crushed waste rock from the surrounding granitic rocks according to a modified solid-water ratio. The mining/backfilling process at the hard rock mine is presented in Fig. 6.1. The mechanical properties of the kimberlite rock (orebody) were evaluated based on the average Rock Mass Rating (RMR) system and the generalized

Hoek-Brown criterion (Sepehri et al., 2017), which are shown in Table 5.1 in Chapter 5. The stress-strain behaviour and the mechanical properties of the consolidated CRF material cured for 28 days were discussed in Chapter 3.

As shown in Fig. 6.1a, the mining activities with the BHS method and the backfilling activities using the CRF material are in a primary/secondary sequence. Before a single stope was extracted, two drifts, namely the overcut and undercut, were developed at the bottom and the top of the stope, respectively, which were used for drilling and blasting of the orebody and the transportation of the ore products, respectively (Sepehri et al., 2017). The stope was blasted in a retreated way. As the stope was entirely mined out, the backfill barricade was initially built at the undercut gate. Then, the fresh CRF material was dumped into the extracted stope to support the adjacent rock pillars and work platform for future mining activities.

Before the fresh CRF material entirely consolidates and gains strength, it behaves as a kind of fresh concrete-like slurry, and the consistency and flowability of the fresh CRF material can be significantly influenced by the particle size distribution of the CRF aggregates, the cement-water ratio, the characteristics of the additives, and the mixing quality of the binding material and the granitic aggregates (Hou et al., 2017). Fig. 6.1b shows that during the backfilling process at a single stope, the fresh CRF material was dumped into the stope by layers, of which the dumping frequency can be determined by the waste management plan at the mine, the stope geometry and the flowability of the fresh CRF material. And after multiple stages of compression and consolidation, the CRF material dewatered and gained strength with 28 days of curing under the field conditions. Meanwhile, the extracted stope cannot be entirely backfilled typically, leading to those

unbackfilled voids at the top of the stope due to the limitation of the flowability of the backfill material, the stope geometry, and the backfilling machinery.

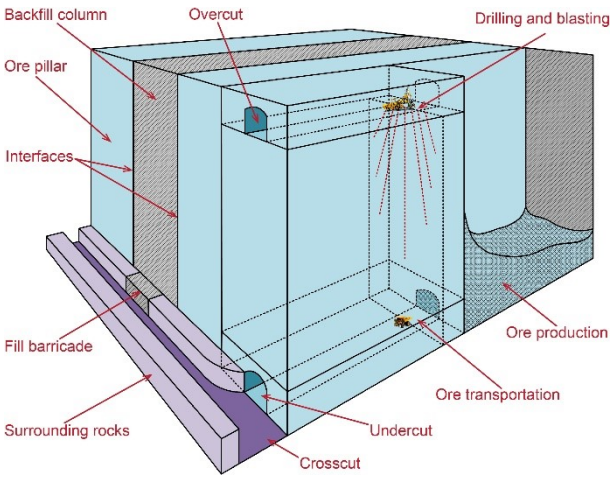

(a)

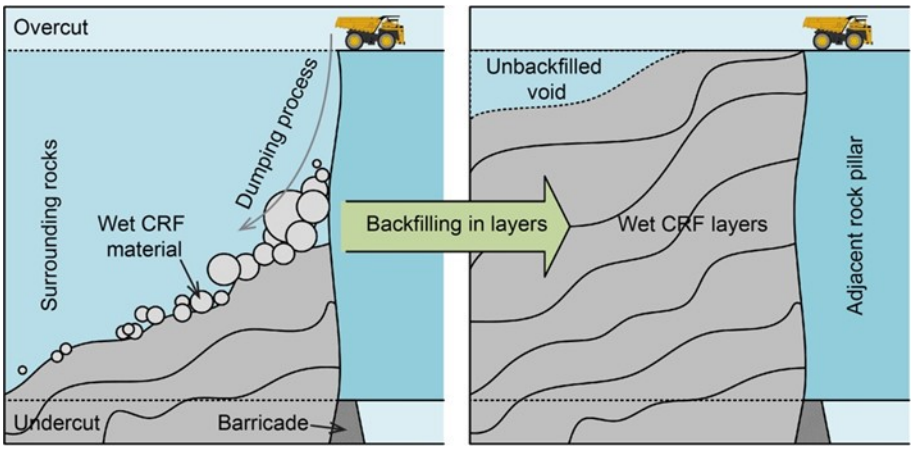

(b)

Fig. 6.1 Mining and backfilling methods at the Canadian hard rock mine: a) blasthole stoping method, and b) dumping process of the fresh CRF material.

6.2.2 Slump test

The slump test is popularly used in both the laboratory and field to evaluate the consistency and flowability of the fresh concrete or fresh concrete-like materials before

they set, such as the cemented soil, cemented rockfill (CRF), cemented tailings and cemented paste backfill (CPB) (Behera et al., 2019). As can be seen in Fig. 6.3, the main instruments used in a slump test include a slump bucket, which is in a circular truncated cone shape, and a measuring platform, which is a hard, non-absorbent base plate. In a standard slump test in the laboratory, the slump bucket has an internal diameter of 100 mm at the top, an external diameter of 200 mm at the bottom, and a height of 300 mm of the cone. Due to the adoption of the particle size scaling method in the DE modelling, in this study, the dimensions of the modelled slump bucket were also scaled up, which will be discussed in Section 6.3.3, to reduce the generation of the discrete particles and increase the computation efficiency.

In a standard slump test, the slump bucket will be filled with fresh concrete or concrete-like materials in several stages to make sure the material is naturally compacted, driven by gravity, and then the extra material will be struck off flush with the top of the slump bucket. At last, the bucket is carefully lifted in the vertical direction to start the slumping process of the material. The slump of the fresh concrete or concrete-like material is defined as the distance from the slumped material's top to the slump bucket's top level. Meanwhile, in this study, three geometric parameters of the slumped fresh CRF material, including the stacking height (h_s), stacking diameter (D_s), and repose angle (φ_r), are defined to evaluate how the microstructural parameters of the Johnson-Kendall-Robert (JKR) contact model to influence the consistency and flowability of the DE model of the fresh CRF material.

6.2.3 Johnson-Kendall-Robert contact model

The Johnson-Kendall-Robert (JKR) contact model, which is an extension of the Hertz-Mindlin contact model proposed by Johnson (1971), can be used to simulate the cohesion or adhesion among the aggregate particles of fresh material due to the van der Waals, capillary, or liquid-bridge forces, by introducing an attractive force component to the JKR contact model (Harvig et al., 2017; Xia et al., 2019).

Fig. 6.3 shows that in the JKR contact model when two discrete particles are in contact, there is a contact force $\boldsymbol{F}^c$, consisting of the non-linear JKR force $\boldsymbol{F}^{JKR}$ and damping force $\boldsymbol{F}^d$, and a contact moment $\boldsymbol{M}^r$, resulting from the rolling resistance. The elastic JKR force $\boldsymbol{F}^{JKR}$ can be divided into two components, $\boldsymbol{F}_n^{JKR}$ and $\boldsymbol{F}_s^{JKR}$, which act in the normal and shear directions, respectively. Thus, the contact force $\boldsymbol{F}^c$ can be expressed as:

$$\boldsymbol{F}^c = \boldsymbol{F}_n^{JKR} + \boldsymbol{F}_s^{JKR} + \boldsymbol{F}_n^d + \boldsymbol{F}_s^d \qquad \textbf{(Eq. 6.1)}$$

To describe the cohesion or adhesion between two in-contact discrete particles, an attractive force component, $\boldsymbol{F}^{adh}$, was introduced into the JKR contact model according to Johnson (1971) and Chokshi (1993), which acts over the circular contact patch area with a radius of a. Based on the Hertz-Mindlin contact model, the normal JKR contact force $\boldsymbol{F}_n^{JKR}$, which is the total normal contact force without considering the damping effect, is given by:

$$\boldsymbol{F}_n^{JKR} = \left(\frac{4E^*a^3}{3R^*} - 4\sqrt{\pi\gamma E^* a^3}\right)\hat{\boldsymbol{n}}_c \qquad \textbf{(Eq. 6.2)}$$

where E^* and R^* are the equivalent elastic modulus and contact radius of the two in-contact discrete particles, respectively, and γ represents the effective surface energy per

unit contact area of each in-contact discrete particle with the identical material. In this equation, the first term is identical to the elastic Hertz force and the second term is the attractive force component $\boldsymbol{F}^{adh}$. As can be seen from Fig. 6.3, due to the attractive force component $\boldsymbol{F}^{adh}$, the contact area between the two in-contact discrete particles assigned with the JKR contact model can be larger than that predicted by the Hertz theory, leading to an increase in the contact radius a.

The cohesion or adhesion between two in-contact discrete particles also influences the shear JKR contact force $\boldsymbol{F}_s^{JKR}$. The full shear process between two in-contact discrete particles consists of peeling and sliding stages. During the peeling stage, the contact area decreases continuously, and the shear JKR contact force $\boldsymbol{F}_s^{JKR}$ increases simultaneously from an initial JKR contact force $\boldsymbol{F}_s^{JKR^*}$, which only correlates with the shear-displacement increment $\Delta\boldsymbol{\delta}_s$ and the tangential shear stiffness k_s^t. And then, as the shear process continues, $\boldsymbol{F}_s^{JKR}$ reaches a critical shear JKR force $\boldsymbol{F}_{s,c}^{JKR}$, at which two in-contact discrete particles start to slide along the contact area. During the sliding stage, the shear JKR contact force $\boldsymbol{F}_s^{JKR}$ is only related to the friction coefficient μ and the critical shear JKR force $\boldsymbol{F}_{s,c}^{JKR}$. Thus, during the full shear process, $\boldsymbol{F}_s^{JKR}$ can be expressed as:

$$\boldsymbol{F}_s^{JKR} = \begin{cases} \boldsymbol{F}_s^{JKR^*} = \left(\boldsymbol{F}_s^{JKR}\right)_o + k_s^t\,\Delta\boldsymbol{\delta}_s\,, & \left|\boldsymbol{F}_s^{JKR^*}\right| \le \left|\boldsymbol{F}_{s,c}^{JKR}\right| \\ \boldsymbol{F}_{s,c}^{JKR}\left(\dfrac{\boldsymbol{F}_s^{JKR^*}}{\left|\boldsymbol{F}_s^{JKR^*}\right|}\right), & \text{otherwise} \end{cases} \qquad \textbf{(Eq. 6.3)}$$

Damping force $\boldsymbol{F}^d$ is also introduced into the JKR contact model to contribute to the kinetic energy dissipation between the two in-contact discrete particles. $\boldsymbol{F}^d$ can also be

divided into two components, $\boldsymbol{F}_n^d$ and $\boldsymbol{F}_s^d$, which act in the normal and shear directions, respectively. The normal damping force $\boldsymbol{F}_n^d$ is defined as:

$$\boldsymbol{F}_n^d = -2\beta_n\sqrt{m_c k_n^t}\,\dot{\boldsymbol{\delta}}_n \qquad \textbf{(Eq. 6.4)}$$

where m_c is the effective contact mass of the two in-contact discrete particles, k_n^t is the tangential normal stiffness, $\dot{\boldsymbol{\delta}}_n$ is the relative normal translational velocity, and β_n is the normal critical damping ratio. Meanwhile, the shear-damping force $\boldsymbol{F}_n^d$ is given by:

$$\boldsymbol{F}_s^d = \begin{cases} \left(-2\beta_s\sqrt{m_c k_s^t}\right)\dot{\boldsymbol{\delta}}_s\,, & \text{full} - \text{shear mode} \\ 0, & \text{slip} - \text{cut mode} \end{cases} \qquad \textbf{(Eq. 6.5)}$$

where k_s^t is the tangential shear stiffness, $\dot{\boldsymbol{\delta}}_s$ is the relative shear translational velocity, and β_s is the shear critical damping ratio. As can be seen that during the full shear process, shear damping force $\boldsymbol{F}_s^d$ is related to $\dot{\boldsymbol{\delta}}_s$ only, while at the slip-cut process, $\boldsymbol{F}_s^d$ maintains zero due to the formation of the shear failure plane between the two in-contact discrete particles.

In the JKR contact model, when two discrete particles are in contact, there is also a contact moment $\boldsymbol{M}^r$, resulting from the rolling resistance, which can be expressed as:

$$\boldsymbol{M}^r = \begin{cases} \boldsymbol{M}^{r^*} = (\boldsymbol{M}^r)_o - k_r^t\,\Delta\boldsymbol{\theta}_b\,, & \left\|\boldsymbol{M}^{r^*}\right\| \le \|\boldsymbol{M}_c^r\| \\ \boldsymbol{M}_c^r\left(\dfrac{\boldsymbol{M}^r}{\|\boldsymbol{M}^r\|}\right), & \text{otherwise} \end{cases} \qquad \textbf{(Eq. 6.6)}$$

where k_r^t is the tangential rolling resistance stiffness, $\Delta\boldsymbol{\theta}_b$ is the relative bend-rotation increment, μ_r is the rolling-friction coefficient, and $\bar{R}$ is the contact effective radius of the two in-contact discrete particles. During the full shear process, the rolling resistance

moment $\boldsymbol{M}^r$ relates to the initial contact moment $(\boldsymbol{M}^r)_o$ and the relative bend-rotation increment $\Delta\boldsymbol{\theta}_b$. As the shear process continues, $\boldsymbol{M}^r$ reaches a critical rolling resistance moment $\boldsymbol{M}_c^r$, and $\boldsymbol{M}^r$ can be only correlated with $\boldsymbol{M}_c^r$ only during the slip-cut process.

In the JKR contact model, tensile forces are allowed to develop due to the surface adhesion among the discrete particles of the DE model, incorporating the viscous damping and rolling resistance forces. As the JKR contact model is assigned to the DE model, a contact between two discrete particles forms when the surface gap becomes smaller than the reference gap and stays activated until the surface gap reaches a threshold tear-off distance.

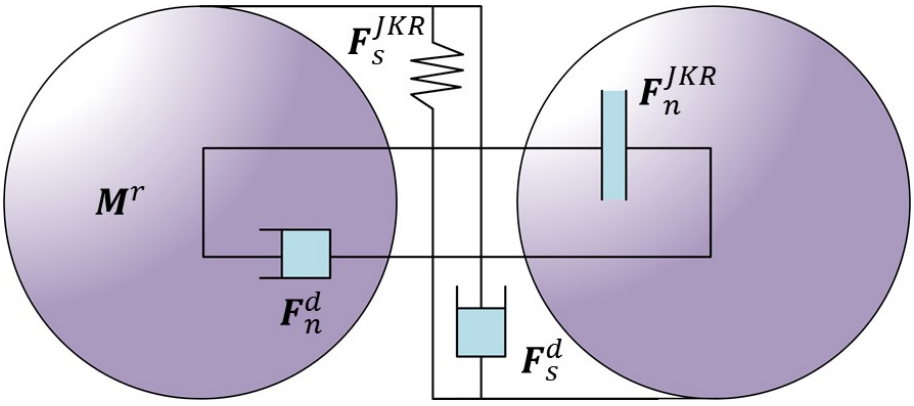

Fig. 6. 2 Johnson-Kendall-Robert contact model (Xia et al., 2019).

6.3 Numerical simulation

6.3.1 Model establishment

Fig. 6.3 shows the geometry and creation procedures of the slump test instruments for the DE model of the fresh CRF material. First, a slump bucket in the truncated cone shape was built by creating a series of rigid walls in the software PFC3D, with an internal diameter of 10 m, an external diameter of 20 m and a height of 30 m. A stiff planar wall

with dimensions of 120 m × 120 m (length × width) was then built as the measuring platform. And then, totally a group of 37,830 discrete particles with the mean particle diameter, described in Chapter 4, were generated in the slump bucket to simulate the fresh CRF material using the boundary contraction method. The JKR contact model and its microstructural parameters were then applied to these discrete particles, and the DE model of the fresh CRF material was initially set in the bucket before the slump test started. The determination of these microstructural parameters in the JKR contact model will be discussed in Section 6.3.2.

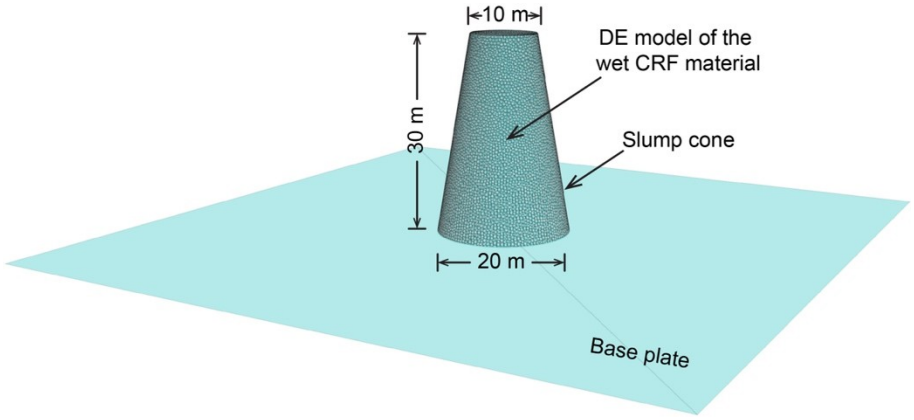

Fig. 6.3 Slump test on the DE model of the fresh CRF material.

Meanwhile, the dumping process of the fresh CRF material in a single stope was simulated in this study with the coupled finite difference (FD) and discrete element (DE) method. The dimensions of the FD model of the surrounding rocks (orebody) were designed to be 100 m × 100 m × 100 m (length × width × height), which are large enough to eliminate the scale effect from the boundary conditions of the FD model. Fig. 6.4 shows that the FD model of the orebody was initially constructed in the software FLAC3D, which is a finite difference program using an explicit LaGrangian calculation scheme and a mixed discretization zoning technique. The finite zones of the FD model meshed radially with an

optimal mesh size ranging from 1.0 m to 5.0 m. The Mohr-Coulomb constitutive model was then applied to the FD model, and the physical-mechanical properties which are listed in Table 5.1 in Chapter 5 were then applied to the FD model directly to realize the mechanical behaviour of the corresponding rock material.

The normal displacement at the bottom and lateral faces of the FD model were fixed at a very far distance from the mining zone to simulate the boundary conditions of the orebody. Next, the FD model was solved to a geo-stress equilibrium state, as the gravity and a lateral earth pressure coefficient of 0.4 were assigned, according to the field investigation results from the Canadian underground hard rock mine (Sepehri et al., 2017). A single vertical-narrow stope with dimensions of 15 m × 7.5 m × 30 m (length × width × height) was then excavated at the centre of the FD model. And then, the FD model was solved to gain a required unbalanced force ratio and reach a new geo-stress equilibrium state again. Finally, six coupling walls were created to cover the surrounding walls of the single stope before the dumping process of the DE model of the fresh CRF material to ensure the realization of the coupling mechanism between the FD and DE models.

The fresh CRF material was then simulated with the DE method in the software PFC3D. A discrete particle inlet was created at the top left corner of the extracted stope in the FD model of the surrounding rocks, with dimensions of 3.0 m × 3.0 m × 1.5 m (length × width × height) to simulate the actual size of the bucket of a mining truck. The periodic boundary condition was applied to the inlet, and a total of 12 layers of the discrete particles of the DE model of the fresh CRF material were generated and dumped into the stope with initial velocities of 0.02 m/s and 0.02 m/s in the x- and z- directions,

respectively, to simulate the entire backfilling sequence in a single stope. Each layer of the discrete particles was set and driven by gravity before the next layer was dumped. It should be mentioned here that the microstructural parameters of the JKR model can significantly influence the layer numbers of the discrete particles of the DE model of the fresh CRF material. During the test, the stress and displacement distribution in the coupled FD-DE model of the single stope backfilled with the fresh CRF material was monitored and recorded at predefined monitoring points, lines, and central cross-sections are marked in Fig. 6.4.

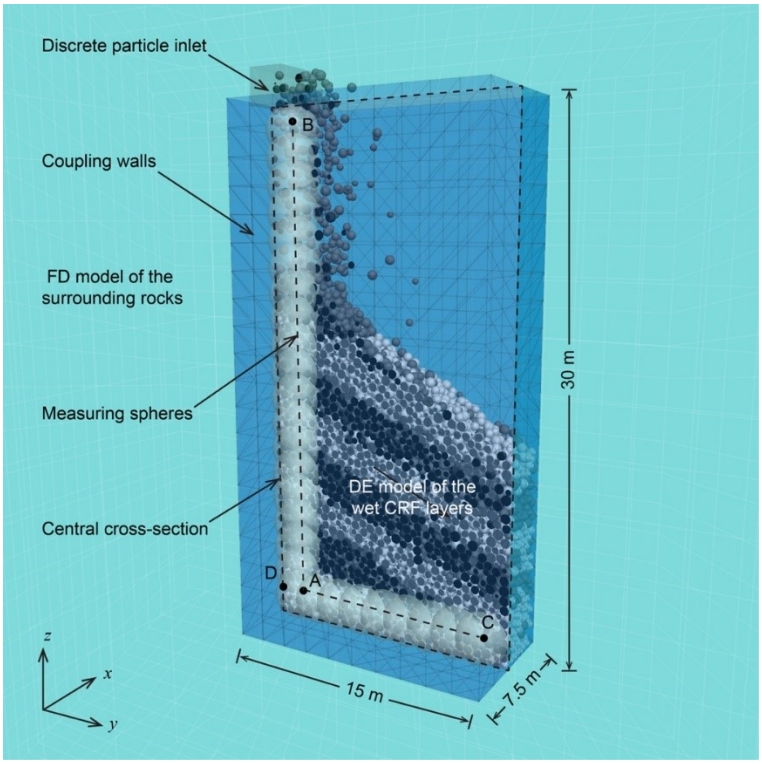

Fig. 6.4 Coupled FD-DE model of a single stope backfilled with the fresh CRF material.

6.3.2 Parameter determination

Similar to the fresh concrete slurry, the adhesion among the aggregates of the fresh CRF material can also be simulated by adopting the JKR contact model to the discrete particles

of its DE model. Due to the lack of the rheological properties of the fresh CRF material, a parametric study was conducted on the microstructural parameters of the JKR contact model to study their influence on the consistency and flowability of the DE model of the fresh CRF material. The mechanism of the JKR contact model has been discussed in Section 6.2.3. As can be seen in Fig. 6.3, there are mainly four microstructural parameters that control the rheological properties of the DE model of the fresh CRF material, the effective shear modulus (G), surface energy (γ_s), friction coefficient (μ), and rolling-friction coefficient (μ_r) of the discrete particles, which are listed in Table 6.1.

Table 6.1 Microstructural parameters of the JKR contact model in the DE model of the fresh CRF material.

Category	**Values**
Shear modulus (Pa)	1.2e6, 4.1e7, 8.1e7, 1.2e8, 3.9e8, 6.6e8, 9.3e8, **1.2e9**
Surface energy (KJ/m²)	5, 10, 50, **100**, 500, 1000, 5000, 10000
Friction coefficient	0.05, 0.1, 0.15, **0.2**, 0.25, 0.3, 0.35, 0.4
Rolling-friction coefficient	0.02, 0.04, 0.06, **0.08**, 0.10, 0.12, 0.14, 0.16

6.4 Results and discussion

6.4.1 Stress and displacement distribution in the DE model of the fresh CRF material during the slumping process

Fig. 6.5 presents the slumping process of one group of the DE model of the fresh CRF material, and the magnitude displacement (d_m) of these discrete particles were monitored during the slumping process. Initially, the DE model of the fresh CRF material was

compacted by gravity naturally and set in the slump bucket. And then, as the slump bucket was lifted up, the discrete particles of the DE model started to slump, driven by gravity. As the limitation from the stiff walls of the slump bucket disappeared, the outer discrete particles can have a larger d_m then the discrete particles near the vertical-central line (VCL) of the DE model of the fresh CRF material. Next, as the slump bucket had no contact area with the discrete particles, d_m was almost at the same level as the middle and top parts of the DE model. However, due to the friction and adhesion between the measuring platform and the discrete particles, there were still constraints to the slumping process of the discrete particles near the VCL of the DE model at the bottom part, leading to a relatively smaller d_m then the outer discrete particles, and finally, as the discrete particles set, the slumping process ended, and the displacement arches were displayed on the CCS of the fresh CRF material DE model.

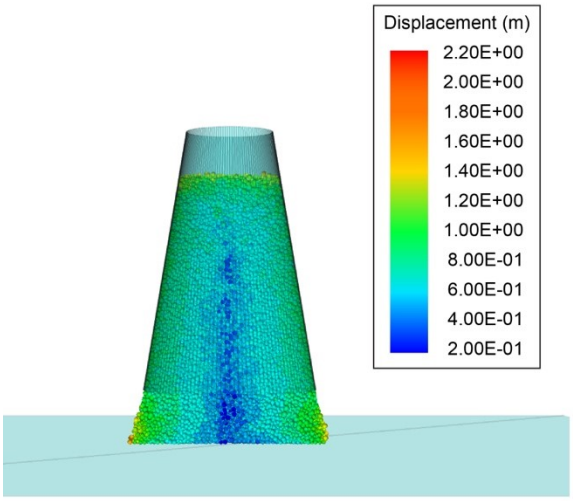

I) Mechanical timestep = 2611

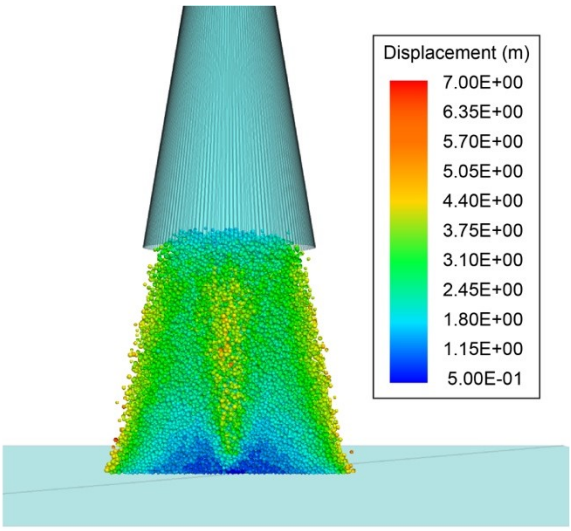

II) Mechanical timestep = 3026

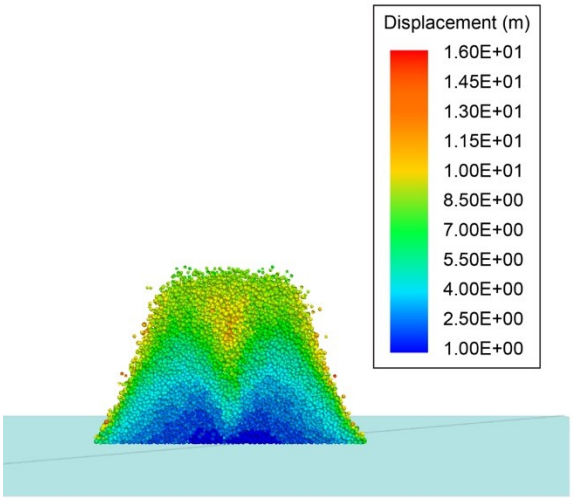

III) Mechanical timestep = 3714

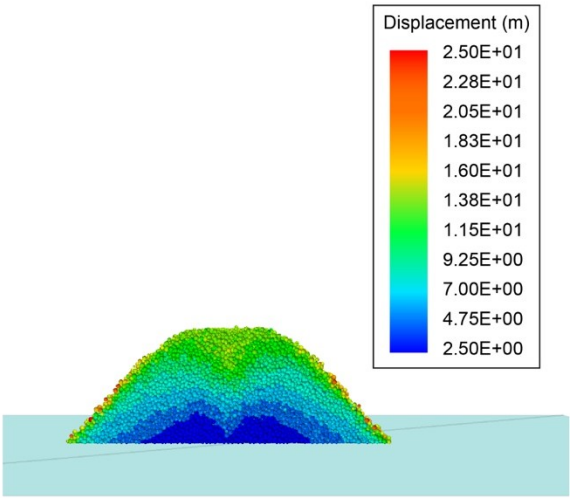

IV) Mechanical timestep = 5009

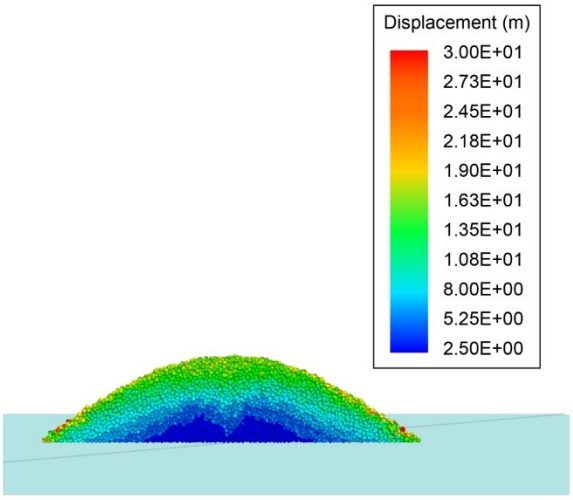

V) Mechanical timestep = 7117

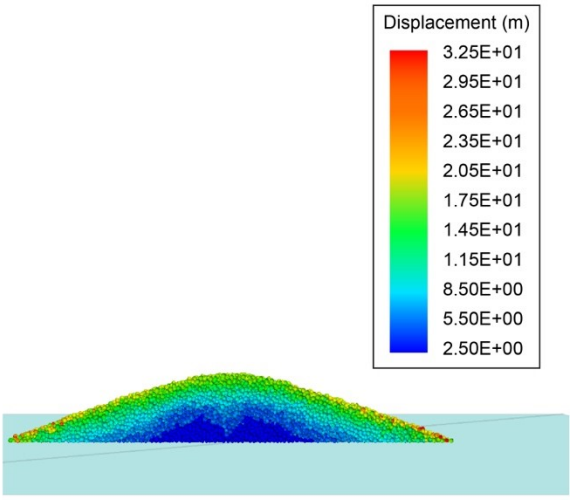

VI) Mechanical timestep = 25530

Fig. 6.5 Distribution of d_m at the CCS of the DE model of the fresh CRF material during the slumping process.

Fig. 6.6 shows the effects of the microstructural parameters of the JKR contact model on the stacking pattern of the DE model of the fresh CRF material during the slumping process. Fig. 6.6a indicates that the effective shear modulus (G) mainly influences the compressibility of the discrete particles and sequentially influences the slump of the DE model of the fresh CRF material. As G increased exponentially, the stacking height (h_s) increased slightly, the stacking diameter (D_s) decreased slightly, and the slope of the DE model concaved up as the stiffness and the compressibility of the discrete particles reduced, leading to an increase in the slope angle of the DE model.

Fig. 6.6b shows that the surface energy (γ_s), which reflects the adhesion and viscosity among the discrete particles, has a significant effect on the flowability of the DE model of the fresh CRF material. As γ_s increased exponentially, h_s and the repose angle (φ_r) both increased significantly while D_s decreased significantly. As γ_s increased to 10 KJ/m^2, the adhesion among the discrete particles increased and made the DE model of the fresh CRF material more viscous, hindering the downtrend slumping of the discrete particles and leading to an irregular cone shape stack of the discrete particles.

Fig. 6.6c and Fig. 6.6d show that the friction coefficient (μ) and rolling-friction coefficient (μ_r) both significantly influence the flowability of the DE model of the fresh CRF material. It shows that the increase in μ and μ_r both can hinder the slumping process of the discrete particles, leading to the smaller D_s, higher h_s and larger φ_r of the DE model of the fresh CRF material.

Fig. 6.7 presents the relationship between the JKR contact model's microstructural parameters and the DE model's geometric parameters of the fresh CRF material after the slumping process. Fig. 7a shows that G has a positive logarithmic relationship with h_s and φ_r, while γ_s, μ, and μ_r all have a positive linear relationship with h_s and φ_r. Meanwhile, D_s decreases linearly as any of the four microstructural parameters increases. As can be seen from Fig. 6.6 and Fig. 6.7, the increase in the four microstructural parameters in the JKR contact model all led to the decrease in the slump of the DE model of the fresh CRF material during the slumping process. The surface energy and friction coefficient can be the two most dominant microstructural parameters that influence the flowability of the discrete particles and determine the slumping process and stacking form of the DE model of the fresh CRF material.

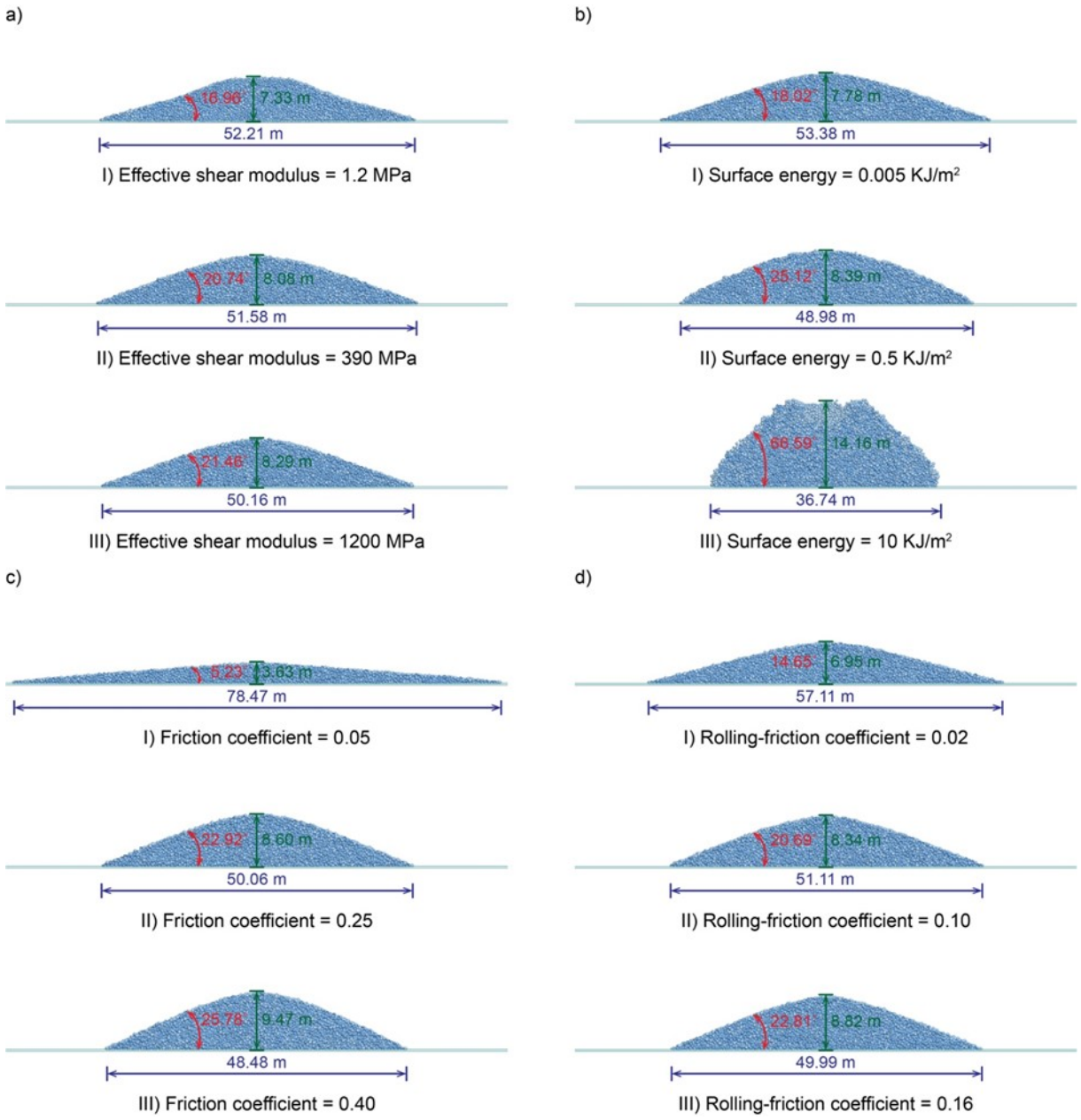

Fig. 6.6 Effects of the microstructural parameters of the JKR contact model on the stacking pattern of the DE model of the fresh CRF material during the slumping process: a) G, b) γ_s, c) μ, and d) μ_r.

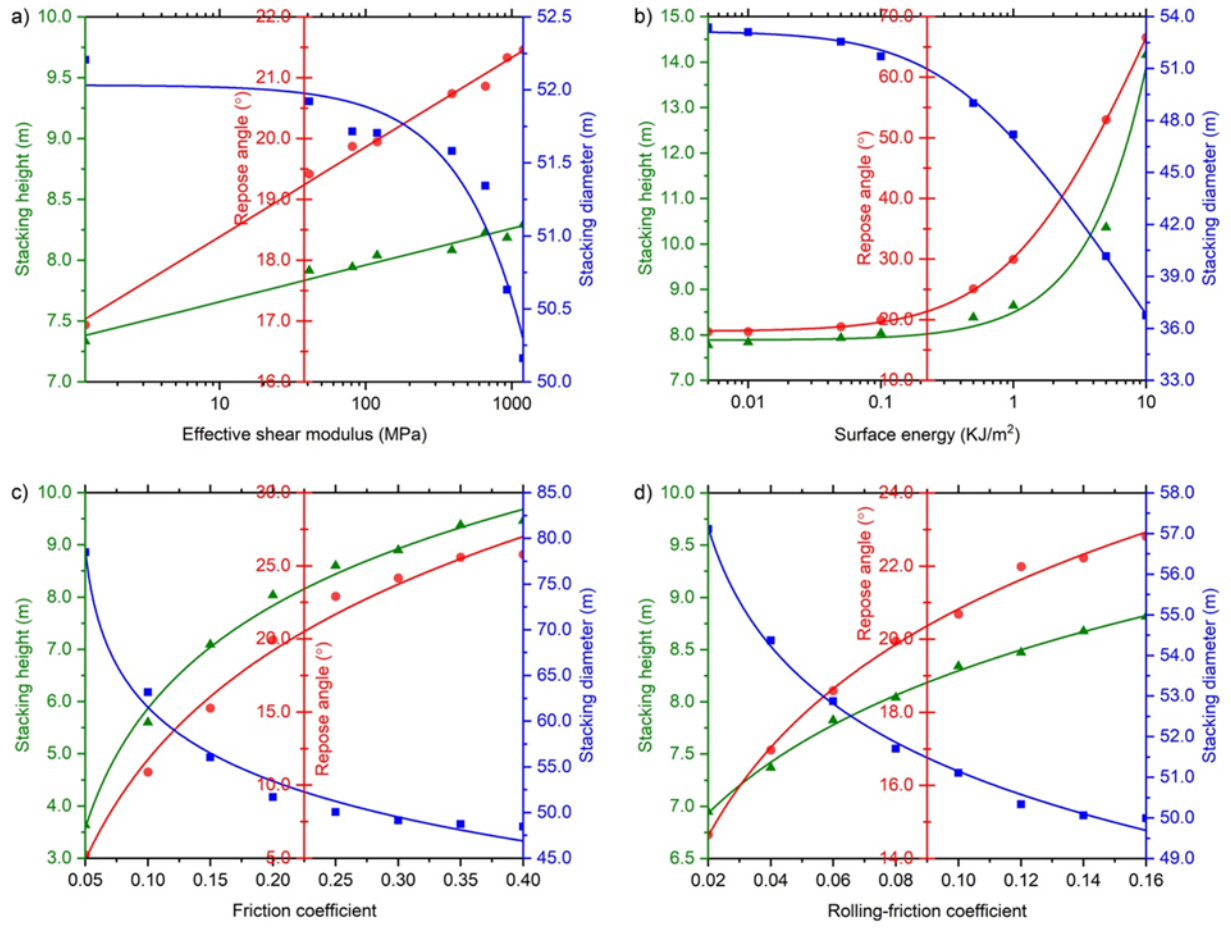

Fig. 6.7 Effects of the microstructural parameters of the JKR contact model on the flowability of the DE model of the fresh CRF material during the slumping process: a) G, b) γ_s, c) μ, and d) μ_r.

6.4.2 Stress and displacement distribution in the coupled FD-DE model of the single stope backfilled with the fresh CRF material during the dumping process

Fig. 6.8 presents the dumping process of one group of the DE model of the fresh CRF material at a single stope, and the distribution of d_m in the discrete layered particles, the FD model of the surrounding rocks was monitored during the dumping process. As can be seen from Fig. 6.8 that the coupling mechanism was successfully triggered and executed, and the displacement and force information can successfully be transmitted

between the DE model of the fresh CRF material and the FD model of the surrounding rocks. As the first layer of the discrete particles was dumped into the stope, the discrete particles could not entirely spread out and fill the bottom of the stope, and a slope was formed in the DE model of the fresh CRF material. As the dumping process continued and eight layers of the discrete particles were dumped into the stope, the height of the DE model of the CRF column increased, and the slope at the top of the DE model still existed. Finally, as 12 layers of the discrete particles were dumped into the stope, an unbackfilled void was formed at the top of the stope, and different parts of the DE model of the CRF column can have different d_m, due to multiple compression and consolidation stages and viscosity and consistency effects, which were generated from the JKR contact model.

The distribution of d_m in the FD model of the surrounding rocks indicates that the DE model of the fresh CRF material was at the active lateral earth pressure state. As more layers of the discrete particles were dumped into the stope, the displacement concentration zone of d_m started to move rightward at the bottom of the stope, and the discrete particles at the right bottom corner of the stope were compressed, resulting in the largest d_m among all the discrete particles in the DE model of the fresh CRF material.

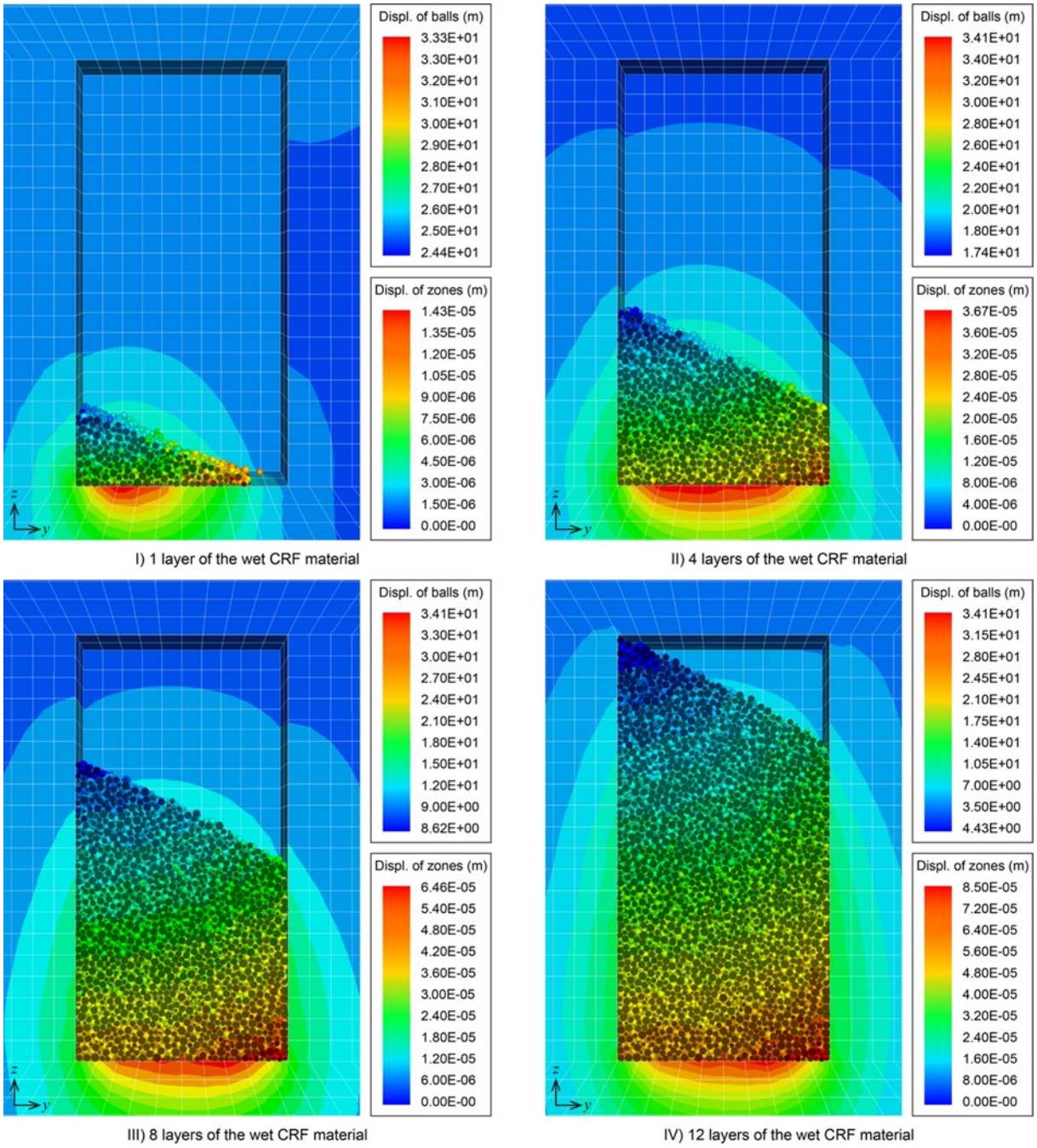

Fig. 6.8 Distribution of d_m at the CCS of the coupled FD-DE model of the single backfilled stope during the dumping process of the fresh CRF material.

Fig. 6.9 shows the stress distribution along the monitoring lines in the DE model of the CRF column during the dumping process of the fresh CRF material. As 12 layers of the

discrete particles were dumped into the stope, the stresses, σ_{xx} and σ_{zz}, which are in the x-, and z- directions, respectively, all increased along the monitoring line AB as the depth of the stope increased, while these stresses were slightly fluctuant along the monitoring line AC as the horizontal distance increased. Meanwhile, σ_{zz} and σ_{xx} were all smaller than the corresponding overburden and lateral earth pressures, p_v and p_h, respectively, due to the shear effect at the interfaces between the DE model of the CRF column and the FD model of the surrounding rocks, which the JKR contact model mainly contributed applied among the discrete particles.

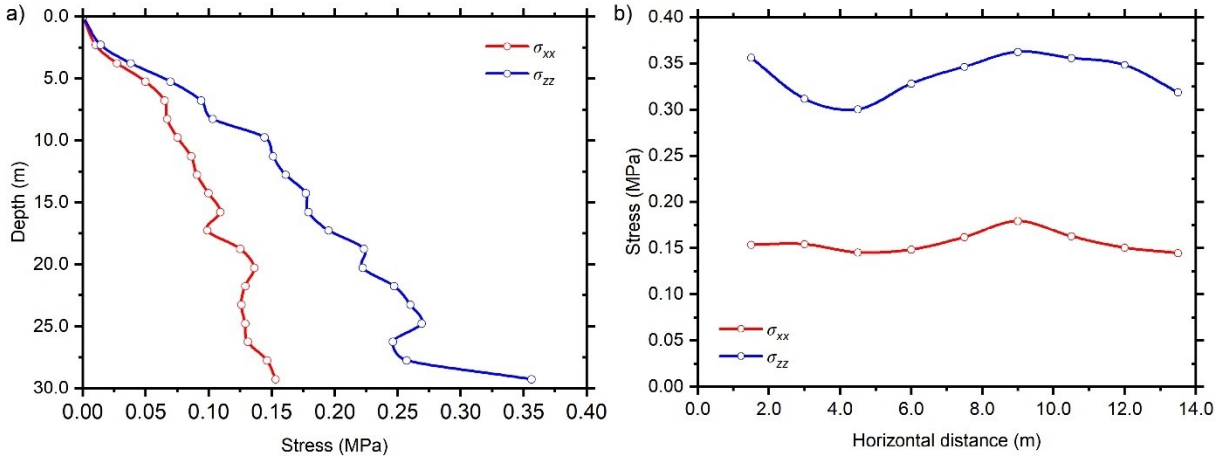

Fig. 6.9 Stress distribution along the monitoring lines in the DE model of the CRF column during the dumping process of the fresh CRF material: a) monitoring line AB, and b) monitoring line AC.

Fig. 6.10 shows the distribution of the porosity (n) of the discrete particles along the monitoring lines in the DE model of the CRF column during the dumping process of the fresh CRF material. As can be seen in Fig. 6.10a, along the monitoring line AB, the porosity n decreased by 12% as the depth of the column increased due to multiple stages of the compression and consolidation by the overburden pressure from the discrete

particles of the overlying CRF layers. FOn the other hand, fig. 6.10b shows that along the monitoring line AC, which is at the bottom of the DE model of the CRF column, n fluctuated slightly but maintained around 0.247, indicating that at the same height of the column, the column can have the same porosity.

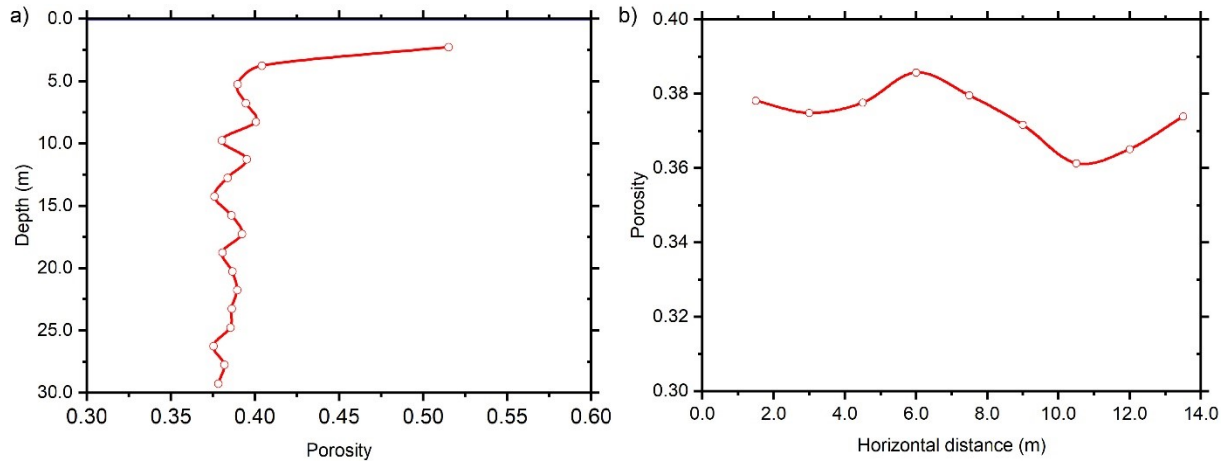

Fig. 6.10 Distribution of n along the monitoring lines in the DE model of the CRF column during the dumping process of the fresh CRF material: a) monitoring line AB, and b) monitoring line AC.

Fig. 6.11 presents the effects of microstructural parameters of the JKR contact model on the dumping process of the fresh CRF material in the single backfilled stope. As shown in Fig. 6.11a, as G increased, the compressibility of the discrete particles in the DE model of the fresh CRF material decreased, and the stacking height of the CRF column increased significantly, leading to a lower backfilling rate and a higher porosity in the column. Fig. 6.11b shows that the adhesion among the discrete particles in the DE model dramatically influences the stacking state and shape of the fresh CRF layers. As γ_s increased, a group of discrete particles were pasted on the FD model of the surrounding walls, and only eight layers of the discrete particles could be backfilled into the single stope, indicating a lower

backfilling rate and worse backfill quality. It can be seen in Fig. 6.11c that decreasing the discrete particles' friction coefficient can help decrease the angle of repose of the CRF column, resulting in a higher backfilling of the fresh CRF layers. Fig. 6.11d indicates that μ_r There is very little contribution to the backfilling rate and backfill quality of the fresh CRF material DE model.

Meanwhile, the effects of the microstructural parameters of the JKR contact model on the porosity of the fresh CRF material were also analyzed. The modelling results indicate that as G decreased, the DE model of the fresh CRF material became denser and could have a higher compression capacity, resulting in a significant decrease in n. As γ_s increased exponentially, the adhesion increased significantly, leading to higher resistance among the discrete particles during the dumping process and a higher n in the DE model of the fresh CRF material. And as μ and μ_r increased, n of the DE model of the fresh CRF material increased slightly since the energy significantly dissipated among the discrete particles during the dumping process of the DE model of the fresh CRF material.

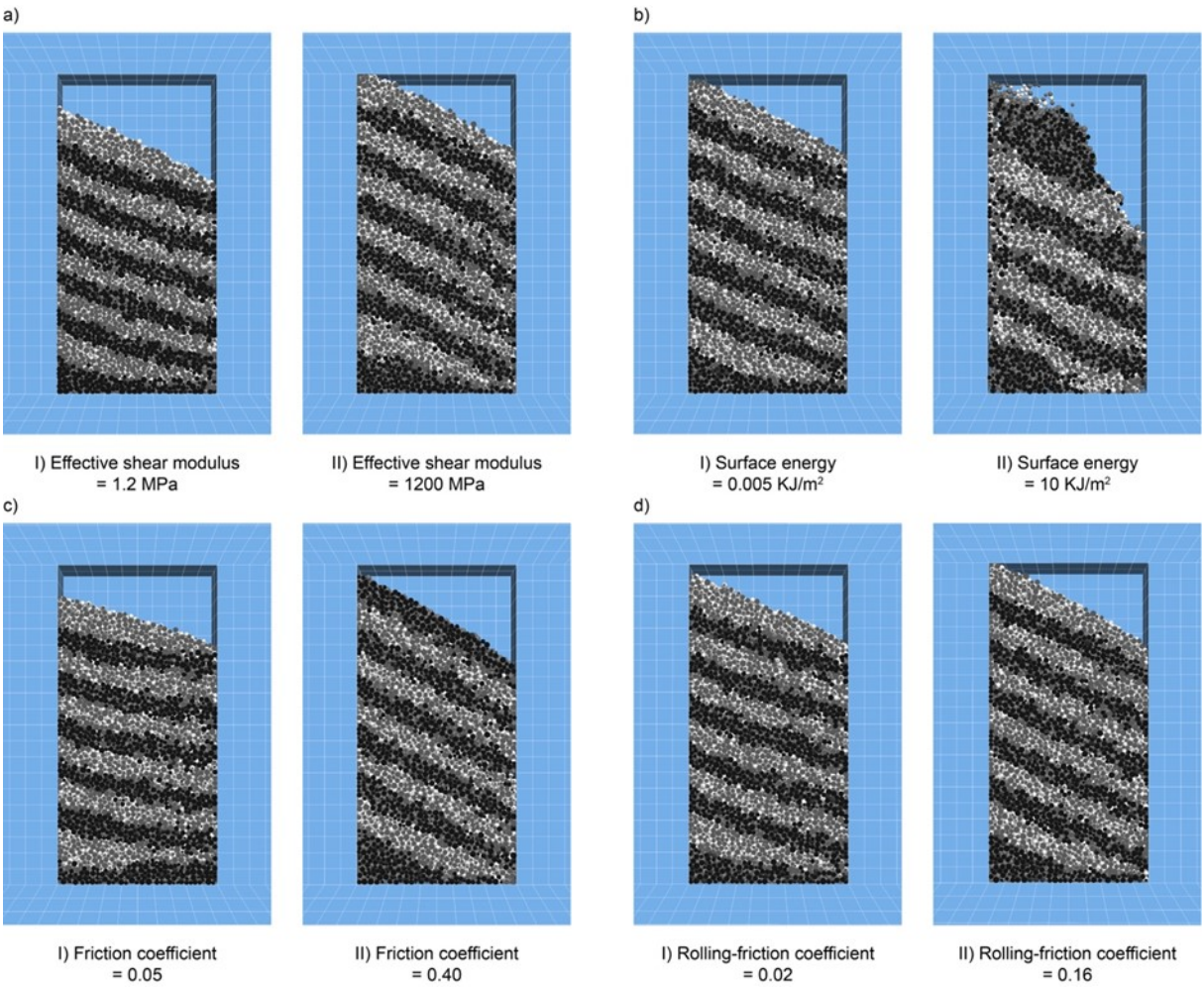

Fig. 6.11 Effects of microstructural parameters of the JKR contact model on the dumping process of the fresh CRF material in the single backfilled stope: a) G, b) γ_s, c) μ, and d) μ_r.

6.5 Conclusions

In this study, the Johnson-Kendall-Robert (JKR) contact model was adopted in the discrete element (DE) model of the fresh CRF material to simulate the adhesion among the aggregate particles that results from the liquid-bridge forces and binding effect of the Portland cement. First, the numerical slump test was conducted to evaluate the flowability and workability of the DE model of the fresh CRF material and the effects of the microstructural parameters of the JKR contact model on the flowability and

consistency. And then, the backfilling process of the fresh CRF material at a single stope was simulated with the coupled finite difference (FD) and discrete element (DE) method, and the stress, displacement, and porosity distribution in the DE model of the fresh CRF material were monitored and recorded during the dumping process.

The modelling results indicate that the flowability of the DE model of the fresh CRF material was mainly influenced by the microstructural parameters of surface energy and friction coefficient in the JKR contact model. The modelling results show that the increase in the microstructural parameters of the surface energy and friction coefficient can lead to a higher porosity, a lower backfilling rate and a worse backfill quality of the CRF column. This study provided some numerical modelling experience for the cemented backfill material's proportioning modification and backfilling process.

Chapter 7 Coupled finite difference and discrete element method for modelling a single stope backfilled with the cemented rockfill

In this chapter, the coupled finite difference (FD) and discrete element (DE) methods were adopted to simulate a single underground stope backfilled with a cemented rockfill (CRF) column at different lateral earth pressure states, considering the frictional-bonded interfaces between the DE model of the CRF column and the FD model of the surrounding rocks. By comparing with the analytical solution from previous studies (Li et al., 2005; Li and Aubertin, 2009), the modelling results show that the shear effect at the interfaces significantly influences the settlement and consolidation process of the CRF column, leading to the stress and displacement redistribution in both the CRF column and the surrounding rocks, and the occurrence of an arching phenomenon in the CRF column. The modelling results also indicate that backfilling with the CRF column can efficiently shrink the stress concentration zones, deduce the maximum principal stress in the surrounding rocks and improve the stability of the underground mined-out areas. This research can provide valuable numerical modelling experience for applying the coupled FD-DE method in studying the mechanical interaction between two different geo-materials involved with frictional-bonded interfaces.

7.1 Introduction

In underground mines, backfill columns and the surrounding rocks at the backfilled stopes are not self-isolated but mutually supported (Mitchell, 1989; Belem and Benzaazoua, 2008). Frictional-bonded interfaces exist between the backfill column in the primary backfilled stope and the ore pillar in the secondary unextracted stope (Lingga and Apel, 2018). They are formed during the settlement and consolidation processes of

the backfill materials. Through these interfaces, energy alternation and stress transmission occur ceaselessly between backfill columns and the surrounding rocks, especially when the underground mined-out areas undergo disturbance from the sequential mining activities.

Many researchers performed direct shear tests on the combined rock-backfill or backfill-backfill specimens to study the mechanical properties and stress-strain behaviour of the interfaces between the two parts of the combined specimens. It is considered a fundamental step to assess the mechanical response and interaction between backfill columns and the surrounding rocks at the backfilled stopes. The test results revealed that the shear failure envelopes of these interfaces obey the Mohr-Coulomb strength criterion (Lingga and Apel, 2018). Furthermore, the shear strength of those combined specimens is always smaller than the corresponding backfill specimens, and perfect elastoplastic behaviour can be observed on the interfaces of the combined rock-backfill specimens (Koupouli et al., 2016; Fall and Nasir, 2010). Major influence factors on the shear behaviour of these interfaces include the cement content, applied normal stress, surface roughness, curing time and condition (Fang and Fall, 2019, 2020; Nasir and Fall, 2008; Lingga and Apel, 2018; Guo et al., 2020).

The interfaces significantly influence the stress distribution and the stability of the underground mined-out areas. The shear interaction between backfill columns and the surrounding rocks leads to an arching phenomenon inside backfill columns (Lingga and Apel, 2018). The differential strain mobilizes the shear stress at the interfaces as backfill materials settle, dewater, and consolidate. As a result, a portion of the pressure from the backfill columns' yielding parts is transferred to the relatively stable neighbour non-

yielding parts of the surrounding rocks (Ting et al., 2011). Some researchers observed this phenomenon by measuring the in-situ total earth pressure at specific monitoring locations in cemented paste backfill (CPB) columns (Ouellet and Hassani, 2005; Thompson et al., 2009; Hasan et al., 2014). The measuring results indicate that the cement content significantly influences the arching effect on the stress distribution inside backfill columns. As cement hydration occurs continuously, backfill columns gain strength gradually, and the vertical stress at each location is reduced to the corresponding theoretical overburden pressure (Ting et al., 2011; Pirapakaran and Sivakugan, 2007).

Two very-high concerns from mining engineers and researchers are the stress distribution in the surrounding rocks and the improvement effect of backfill columns on the stability of the underground mined-out areas. Some previous studies showed that backfilling the extracted stopes helps minimize ground subsidence, control the overlying strata movement, and increase the rock pillar stability (Heib et al., 2010; Yin et al., 2017). For example, in underground coal mines, the main factors influencing the overburden stability of the backfilled stopes include the stope roof thickness, overlying strata pressure, advancement distance, work face width and foundation coefficient of backfill columns (Sun et al., 2019). In addition to the field stress monitoring, some researchers created physical models of multiple backfilled stopes in the laboratory to reproduce the entire process of the settlement and consolidation of backfill columns and study the stability of the backfilled stopes at different stages in a primary/secondary manner of mining and backfilling (Zhang et al., 2018; Yang et al., 2015). The test results indicated that the primary backfilled stope has the worst stability condition when the second stope gets extracted as the primary backfill column is exposed in the air. Furthermore, the

corners of the underground backfilled stopes at the surrounding rocks are the critical positions of shear stress concentration zones with high risks in potential rockburst geohazard.

However, it is not efficient enough to study the arching phenomenon inside backfill columns using the measuring or physical method, owing to the limitations of backfill material types, monitoring location numbers and the underground mined-out area dimensions (Thompson et al., 2009). Thus, many researchers studied the stress distribution inside backfill columns caused by the shear interaction at the interfaces through analytical solutions and numerical simulation. For example, Li and Aubertin (2009) proposed a three-dimensional analytical model based on earlier models from Marston (1930), Terzaghi (1943) and Li et al. (2005), which considers the interface shear parameters, stope geometry and hydrostatic pressure as influence factors. It calculates the effective stress distribution along the backfill columns' vertical-central lines (VCL). The equivalent internal frictional angle, apparent cohesion, and lateral earth pressure coefficient at each interface can be considered anisotropic in this analytical model. The analytical model also shows that the aspect ratio and inclination of the stope are critical factors influencing the stress distribution in backfill columns.

There is also plentiful research in which the numerical models of the backfilled stopes were established to validate these analytical solutions to predict the instability of backfill columns and potential geohazards induced by the sequential underground mining activities (Liu et al., 2016; Ting et al., 2011; Li and Aubertin, 2009). The modelling results showed that the key factors which affect the arching phenomenon in backfill columns include the mechanical properties of backfill materials and the interfaces, stope geometry,

excavation sequence and backfilling process (Jahanbakhshzadeh et al., 2017; Ting et al., 2011; Li and Aubertin, 2009; Liu et al., 2016; Mkadmi et al., 2014; Falaknaz et al., 2015; Emad et al., 2018). According to Liu et al. (2016), as the interfaces' effective internal friction angle and cohesion increase, both the vertical and horizontal stresses increase at each elevation along the VCL of a backfill column. However, the stresses become insensitive to the mechanical properties of the interfaces when they reach higher values. Furthermore, in Falaknaz et al.'s (2015) study, two adjacent stopes were simulated to be extracted and backfilled in a primary/secondary manner. The modelling results indicated that the stresses in the first backfilled stope show an evident redistribution, which is significantly influenced by the neighbouring excavation and backfilling operation. During the excavation process of the secondary stope, the vertical stress decreases along the VCL of the primary backfill column. In contrast, the corresponding horizontal stress increases initially and then decreases, owing to the movement of the surrounding rocks of the primary backfilled stope (Falaknaz et al., 2015; Newman, 2018).

Among these studies that adopted the numerical simulation, most researchers used the continuum approaches to simulate the underground backfilled stopes, including the finite-element (FE) method, finite difference (FD) method and finite-volume (FV) method (Liu et al., 2016; Mkadmi et al., 2014; Falaknaz et al., 2015; Emad et al., 2018). The continuous approaches treat the modelled backfill materials as homogeneous and elastoplastic, resulting in high computation efficiency. While for the discontinuum approaches, such as the discrete element (DE) method, very few studies simulated the stress redistribution at underground mined-out areas by considering backfill materials as assemblies of discrete blocks or particles (Hasan et al., 2017). Some other studies that

used the discontinuum approaches mainly focus on the stress-strain behaviour of backfill materials and the instability of underground stopes due to their advantages in modelling large-strain deformation and the post-failure behaviour (Suazo and Villavicencio, 2018; Wu et al., 2018). Furthermore, some researchers used the coupled FE-DE or FD-DE method to simulate the rock damage zones induced by blasting vibration or the adjacent stope excavation to combine the advantages of the two approaches (Saiang, 2010; Cai et al., 2006).

However, there are no relevant studies regarding the stress distribution inside backfill columns and the stability of the backfilled stopes by using the hybrid continuum-discontinuum approach. In previous studies, most researchers only focused on the stress distribution inside backfill columns, and there are no studies that emphasized the supporting effect of backfill columns on the backfilled stopes and the improvement effect on the stability of the underground mined-out areas. On the other hand, the coupled FD-DE method, a popular hybrid continuum-discontinuum approach, can easily overcome the hardness in modelling the underground mined-out areas with large dimensions by using the pure DE method without losing computation efficiency. Also, the coupled FD-DE method can conquer the problem of the pure FD method in modelling large-strain deformation and the post-failure without considering influences by meshing and zone numbers. Thus, it is necessary to fill this gap using the coupled FD-DE method to simulate the backfilled stopes considering the interfaces between backfill columns and the surrounding rocks.

7.2 Background and methodology

7.2.1 Mining and backfilling methods

As discussed in Chapter 3, the blasthole stoping (BHS) method was adopted in the hard rock mine, which is located in Northwest Territories, Canada, and then the mined-out openings were backfilled with the cemented rockfill (CRF) (Sepehri et al., 2017). The mining/backfilling activities at the hard rock mine were executed in a primary/secondary manner, shown in Fig. 6.1 in Chapter 6. Two drifts, including an overcut and an undercut, were developed at the bottom and the top of the stope before the extraction, respectively, for drilling/blasting the orebody and transporting the ore rocks. As the stope was extracted, the stope was then backfilled with the CRF material by layers. After at least 28 days of curing under the field conditions, the CRF column was entirely dewatered, consolidated, and gained strength, providing a working platform for future mining activities and improvement effects on the adjacent rock pillars.

7.2.2 Li and Aubertin's analytical model

Li et al. (2005) proposed a three-dimensional analytical model regarding the arching phenomenon to predict the stress distribution along the VCL of a backfill column by considering the shear behaviour at the frictional-bonded interfaces between the backfill column and the surrounding rocks. In Li et al.'s model, the aspect ratio and inclination of the backfilled stope are involved, which can strongly affect the arching phenomenon in the backfill column. Meanwhile, in Li et al.'s model, for each interface, the equivalent internal friction angle, apparent cohesion, and lateral earth pressure coefficient at the surrounding rocks of the backfilled stope can be considered anisotropic at any random elevation.

Fig. 7.1 depicts the schematic diagram of a vertical-narrow backfilled stope and a layer element from the backfill column at a random depth h, which is subjected to a series of uniformly distributed stresses from the walls formed by the surrounding rocks. In this figure, H, B, and L are the height, width, and length of the backfill column, respectively. The left, front, right and back surrounding walls are marked as 1, 2, 3 and 4, respectively. For a random backfill column depth h, the backfill layer element is subjected to the vertical overburden pressure V on the top surface, horizontal lateral compressive force C_i (i = 1, 2, 3, 4), longitudinal and transversal shear forces S_i and T_i (i = 1, 2, 3, 4) at the interfaces, where i represents the mark number of the corresponding surrounding walls.

The weight of the backfill layer element W can be calculated as:

$$W = \gamma BLdh \qquad \textbf{(Eq. 7.1)}$$

In this equation, γ is the unit weight of the consolidated backfill material and dh is the thickness of the backfill layer element.

The vertical overburden pressure V is assumed to be uniformly distributed on the top surface of the backfill layer element and can be obtained by:

$$V = \sigma_v^h BL \qquad \textbf{(Eq. 7.2)}$$

where σ_v^h is the vertical stress, which is assumed to be uniformly distributed in the backfill layer element at a random backfill column depth h.

The horizontal lateral compressive force C_i (i = 1, 2, 3, 4) at the interfaces between the backfill column and four surrounding walls can be expressed as:

$$C_i = \sigma_{hi}^h dhL = K_{ci}\sigma_v^h dhL = K_{ci} dh\, V/B \qquad \textbf{(Eq. 7.3)}$$

where σ_{hi}^h (i = 1, 2, 3, 4) is the horizontal stress, which is assumed to be uniformly distributed in the backfill layer element at a random backfill column depth h. In this equation, a linear relationship between σ_v^h and σ_{hi}^h is adopted. Thus, the lateral earth pressure coefficient K_{ci} (i = 1, 2, 3, 4) is calculated to represent the ratio between the horizontal and vertical stresses at the corresponding interface:

$$K_{ci} = \sigma_{hi}^h / \sigma_v^h \qquad \textbf{(Eq. 7.4)}$$

Meanwhile, a unified format of K_{ci} that considers three different lateral earth pressure states of at-rest, active and passive can be expressed as:

$$K_{ci} = K_i + \frac{2c}{\sigma_v^h} \tan \alpha_i \qquad \textbf{(Eq. 7.5)}$$

where c is the cohesion of the backfill column, K_i (i = 1, 2, 3, 4) is the reaction coefficient of the lateral earth pressure and α_i (i = 1, 2, 3, 4) is the state angle of the lateral earth pressure at the corresponding surrounding walls, which is only related to the internal friction angle φ of the backfill column (Frydman and Keissar, 1987). The definition of K_i and α_i are listed in Table 7.1.

Table 7.1 Coefficients and angles of different lateral earth pressure states.

Lateral earth pressure state	Lateral earth pressure coefficient	Lateral earth pressure angle
At-rest	$1 - \sin\varphi$	$0°$
Active	$(1 - \sin\varphi)/(1 + \sin\varphi)$	$\varphi/2 - 45°$
Passive	$(1 + \sin\varphi)/(1 - \sin\varphi)$	$\varphi/2 + 45°$

In Li et al.'s model, for a random backfill column depth h, the longitudinal shear stress which acts at the interfaces between the backfill column and the surrounding rocks is defined according to the Mohr-Coulomb strength criterion to determine the threshold values of the longitudinal shear force S_i (i = 1, 2, 3, 4) at the corresponding interface:

$$S_i = \left(\sigma_{hi}^h \tan \delta_i + c_i\right) L dh = (K_{ci}\sigma_v^h \tan \delta_i + c_i) L dh \quad \textbf{(Eq. 7.6)}$$

where δ_i and c_i (i = 1, 2, 3, 4) are the effective internal friction angle and apparent cohesion of the interfaces between the backfill column and the surrounding rocks, respectively.

The backfill layer element at a random backfill column depth h reaches its static stress equilibrium in the vertical direction as the backfill column entirely settles and consolidates. Thus, at the centroid of the backfill layer element, the equilibrium equation can be expressed as:

$$W = dV + \sum_{i=1}^{4} S_i \quad \textbf{(Eq. 7.7)}$$

Introducing Eq. 7.1 to Eq. 7.6 into Eq. 8.7, the unified format of the equilibrium equation can be obtained by:

$$\frac{d\sigma_v^h}{dh} + \sigma_v^h \left(\frac{\lambda_{1,3}}{B} + \frac{\lambda_{2,4}}{L}\right) + \left(\frac{\kappa_{1,3}}{B} + \frac{\kappa_{2,4}}{L}\right) - \gamma = 0 \quad \textbf{(Eq. 7.8)}$$

In this equation, $\lambda_{1,3}$, $\lambda_{2,4}$, $\kappa_{1,3}$, and $\kappa_{2,4}$ are defined as:

$$\lambda_{1,3} = K_1 \tan \delta_1 + K_3 \tan \delta_3 \quad \textbf{(Eq. 7.9)}$$

$$\lambda_{2,4} = K_2\, tan\, \delta_2 + K_4\, tan\, \delta_4 \quad \textbf{(Eq. 7.10)}$$

$$\kappa_{1,3} = c_1 + c_3 + 2c(\tan\alpha_1 \tan\delta_1 + \tan\alpha_3 \tan\delta_3) \quad \textbf{(Eq. 7.11)}$$

$$\kappa_{2,4} = c_2 + c_4 + 2c(\tan\alpha_2 \tan\delta_4 + \tan\alpha_2 \tan\delta_4) \quad \textbf{(Eq. 7.12)}$$

Combining with Eq. 7.4, the vertical and horizontal stresses (σ_v^h and σ_{hi}^h) which act at the centroid of the backfill layer element can be solved as:

$$\sigma_v^h = \frac{\gamma - \left(\kappa_{1,3}B^{-1} + \kappa_{2,4}L^{-1}\right)}{\left(\lambda_{1,3}B^{-1} + \lambda_{2,4}L^{-1}\right)}\left\{1 - exp\left[-h\left(\lambda_{1,3}B^{-1} + \lambda_{2,4}L^{-1}\right)\right]\right\} \quad \textbf{(Eq. 7.13)}$$

$$\sigma_{hi}^h = K_i\sigma_v^h + 2c\tan\alpha_i \quad \textbf{(Eq. 7.14)}$$

If the four surrounding walls of the backfilled stope have the same reaction coefficient K and state angle α of the lateral earth pressure state, the general solution to the vertical and horizontal stresses (σ_v^h and σ_{hi}^h) can be simplified as:

$$\sigma_v^h = \frac{\gamma(B^{-1} + L^{-1})^{-1} - 2c(1 + 2\tan\alpha\tan\delta)}{2K\tan\delta}\{1 - exp[-2hK(B^{-1} + L^{-1})\tan\delta]\} \quad \textbf{(Eq. 7.15)}$$

$$\sigma_h^h = K\sigma_v^h + 2c\tan\alpha \quad \textbf{(Eq. 7.16)}$$

As can be seen from Eq. 7.15, the vertical stress σ_v^h that acts at the centroid of the backfill layer element tends to approach the overburden pressure V when the scale of the backfilled stope is large enough to ignore the shear effect at the interfaces between the backfill column and the surrounding rocks. Meanwhile, naturally, for a typical vertical-narrow backfilled stope, the lateral earth pressure state of the backfill column is expected to be between the at-rest and active states, depending on the depth of the backfill layer

element in the backfill column. In this study, the reaction coefficient of the lateral earth pressure at the at-rest and active states (K_i^r and K_i^a) are calculated as 0.223 and 0.125, respectively, for the following numerical modelling of a single backfilled stope based on the coupled FD-DE method.

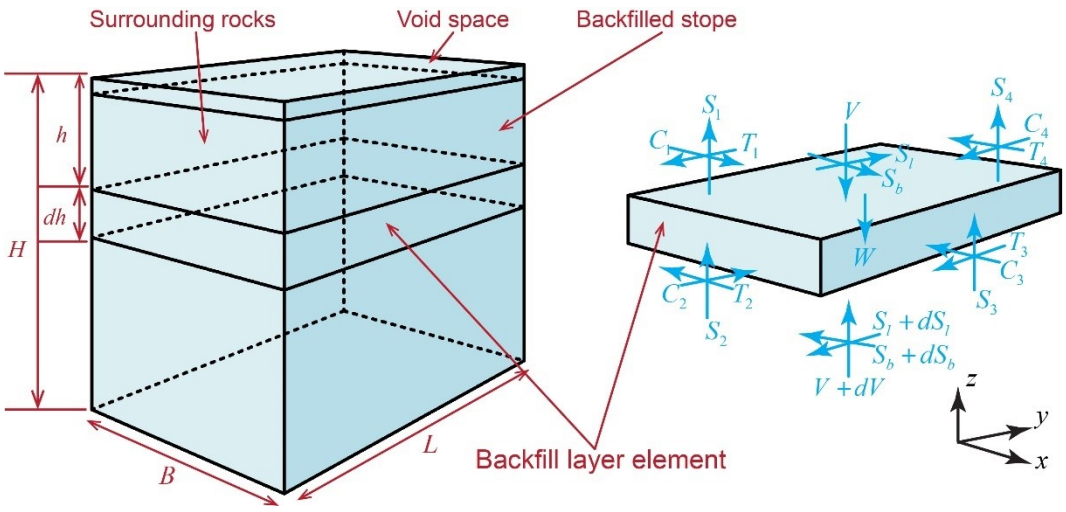

Fig. 7.1 Interaction between a typical cemented backfill column and the surrounding rocks.

7.3 Numerical simulation

7.3.1 Model establishment

Fig. 7.2 shows the geometry, boundary conditions, and establishment of the three-dimensional coupled FD-DE model of a single underground stope backfilled with a CRF column. The dimensions of the FD model of the orebody were designed to be 100 m × 100 m × 100 m (length × width × height), which are large enough to eliminate the scale effect from the boundary conditions of the FD model. As shown in Fig. 7.2b, the FD model was initially constructed with the FD method in FLAC3D, a finite difference program using an explicit LaGrangian calculation scheme and a mixed discretization zoning technique.

Initially, the finite zones of the FD model meshed radially with optimal mesh sizes ranging from 1.0 to 5.0 m. The Mohr-Coulomb constitutive model with the physical-mechanical properties of the surrounding rocks, listed in Table 8.1, was then applied to the FD model directly to realize the mechanical behaviour of rock-like materials. And then, the normal displacement of the bottom and lateral faces of the FD model was fixed to simulate the boundary conditions of the orebody at a very far distance from the underground mined-out areas. Next, the FD model was solved to a geo-stress equilibrium state, by assigning the gravity and a lateral earth pressure coefficient of 0.4, according to the field investigation results from the Canadian underground hard rock mine (Sepehri et al., 2017). A single vertical-narrow stope with dimensions of 30 m × 7.5 m × 30 m (length × width × height), of which the dimensions are the same as the mine (Sepehri et al., 2017), was then excavated at the centre of the FD model. And then, the FD model was solved to gain the required unbalanced force ratio and reach a new geo-stress equilibrium state again. Six coupling walls were created to cover the surrounding walls of the single stope before the creation of the DE model of the CRF column to ensure the realization of the coupling mechanism between the FD and DE models.

The CRF column was then modelled with the DE method in PFC3D software, which provides a discrete element modelling framework. Twelve layers of the discrete particles, representing the CRF granitic aggregates, were sequentially generated to form the DE model of a CRF column with dimensions of 30 m × 7.5 m × 29.5 m (length × width × height) in the single stope in the FD model. The primary layer of the discrete particles was firstly generated in the single stope and solved to gain the required porosity and unit weight, which coincide with the real CRF material in the laboratory. Secondly, the PB

contact model was assigned to the primary layer of the discrete particles, and the microstructural parameters listed in Table 4.2 in Chapter 4 and Table 5.3 in Chapter 5 were assigned to the DE model of the discrete particles and its interfaces with the FD model of the surrounding rocks, respectively, to simulate the binding effect from the Portland cement among the granitic aggregate in the CRF material. Thirdly, gravity was assigned to the discrete particles' primary layer to simulate the CRF column's settlement and consolidation process. Next, the discrete particles' secondary layer was generated on top of the discrete particles' primary layer by following the same generation procedures. These steps were repeated until the last layer of the discrete particles was successfully generated and the DE model of the CRF column entirely formed. As can be seen from Fig. 7.2a, an unfilled void with a thickness of 0.5 m was left at the top of the single stope, representing the incompleteness of the backfilling process due to the dewatering, settlement, and compression processes of the CRF column. In this study, the particle size scaling method was adopted to simplify the generation of the discrete particles in the DE model of the CRF column. Empirically, to eliminate the scale effect on the DE model, the ratio between the maximum model scale and the maximum ball radius r_{max} should be no less than 50, and the ratio between the maximum ball radius r_{max} and the minimum ball radius r_{min} should be no less than 1.66 (Ding et al., 2014; Wu and Xu, 2016). Thus, in this study, optimal r_{max} and r_{min} The discrete particles were determined as 0.18 and 0.3 m, respectively, and a total of 75,659 discrete particles were generated.

Meanwhile, two kinds of the lateral earth pressure states of the CRF column during the settlement and consolidation process were simulated, namely the fully at-rest and natural states. For the backfill columns at the natural state, especially the uncemented backfill

columns, the lateral earth pressure can transfer from the at-rest state at the shallow depth to the active state at the bottom of the backfill columns. The difference in the movement magnitude of the surrounding walls along the depth of the single stope can result in the difference in the horizontal pressure transferring (Aubertin et al., 2003). In this study, if no modifications were made to the coupled FD-DE model, then the DE model of the CRF column was simulated to be at the natural state. For some cemented backfill materials with very high strength, such as the CRF material, can settle and consolidate very fast in the early curing stage, and the column can quickly gain a great self-supporting ability, resulting in a fully at-rest lateral earth pressure state, with a very small portion of horizontal pressure from the backfill column transferred to the surrounding rocks. In this study, to simulate the fully at-rest state, the normal displacement of the surrounding walls of the single stope in the FD model was fixed until the displacement in the primary layer of the discrete particles of the DE model, which was caused by its weight, was eliminated. After the normal displacement of the surrounding walls was freed, the secondary layer of the discrete particles was generated, and these steps were repeated until the DE model of the CRF column was entirely formed and consolidated.

In this study, six monitoring lines of AB, AC, AD, EF, GH and IJ in the FD model, a vertical-central line (VCL) and two central cross-sections (CCS) in the DE model were created to monitor the redistribution of the stress and displacement in the coupled FD-DE model of the single stope backfilled with the CRF column. Furthermore, Fig. 8.6d shows that groups of measuring spheres were created at the CCSs of the DE model to obtain the contours of the stress and displacement distributions, of which the measuring mechanism has been described in Wei et al.'s research (2022).

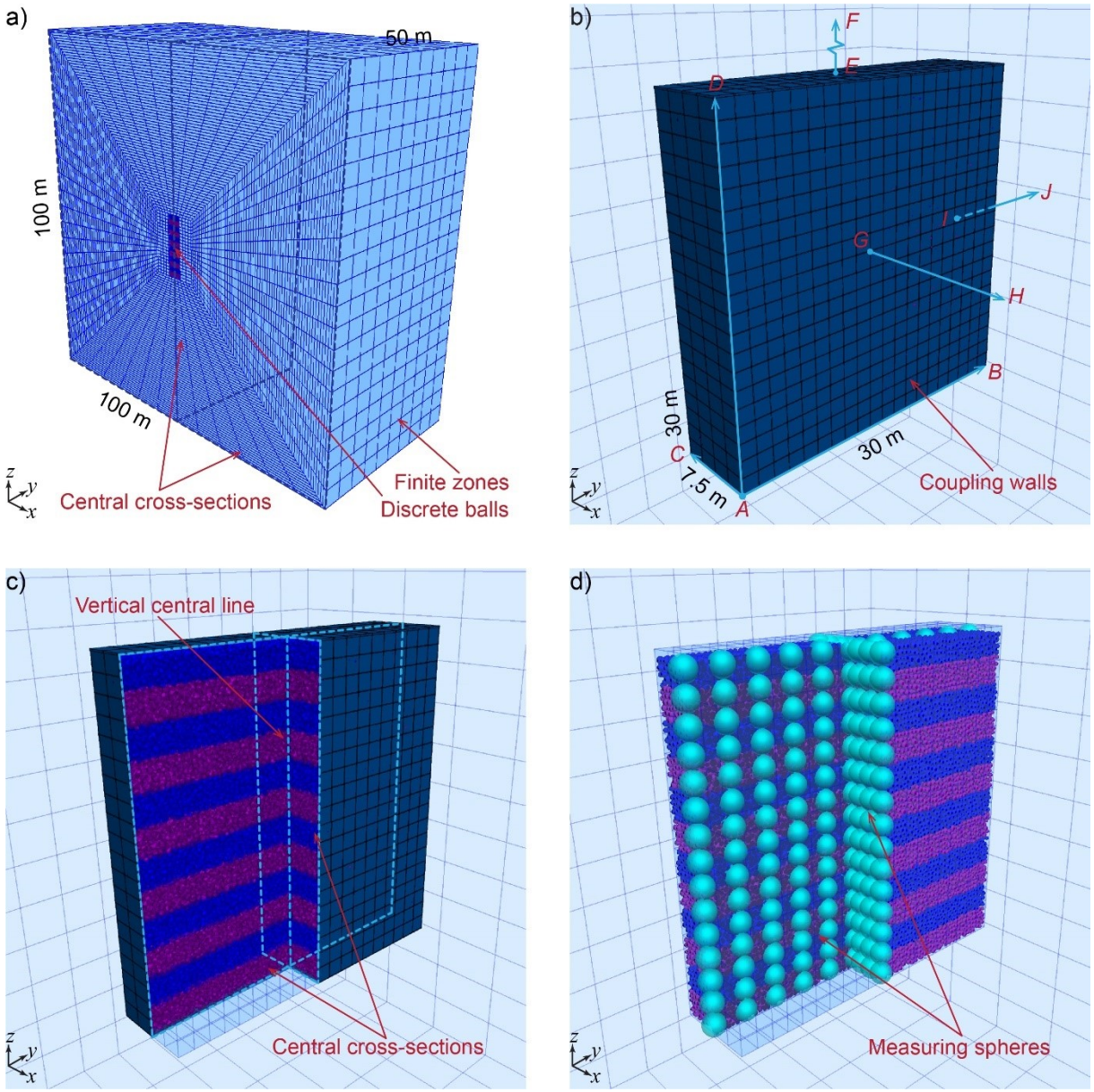

Fig. 7.2 Coupled FD-DE model of a single stope backfilled with a CRF column: a) perspective view, b) coupling walls and monitoring lines, c) vertical-central lines and cross-sections, and d) measuring spheres.

7.3.2 Parameter determination

The cemented rockfill is a porously bonded concrete-like material (Wu et al., 2018; Jongpradist et al., 2011). Thus, the linear parallel bond (PB) contact model was assigned

to the DE model of the CRF column and its interfaces with the FD model of the surrounding rocks to simulate the binding effect from the Portland cement among the granitic aggregate particles in the CRF material. The rheological components in the PB contact model are shown in Fig. 4.1b in Chapter 4. As can be seen, two virtual interfaces exist at the contact position between two discrete particles in the DE model, consisting of groups of parallel springs, bonds, and dashpots. Interface one is linear, elastic, and frictional without tension, representing the linear bond, and interface two is linear-elastic bonded, representing the parallel bond. These cement-like bonds are deformable and breakable, transferring forces and moments between the discrete particles in the DE model. Since the implementation mechanism of the PB contact model has been studied in many previous studies (Wu et al., 2018; Ding et al., 2014), the algorithms, governing equations and the update mechanism of the contact forces and moments among the discrete particles in the DE model are not reiterated here.

Unlike the FD method, the overall mechanical properties of the backfill material, which needs to be simulated using the DE method, cannot be assigned to the DE model directly. Instead, they are controlled by the microstructural parameters of the bonds in the PB contact model, which is assigned to the DE model at the microscopic level. Thus, before modelling the backfill material by using the DE method, these microstructural parameters need to be determined until the overall mechanical properties of the DE model have a good agreement with the corresponding real backfill material. In this study, the microstructural parameters of the DE model of the CRF material were determined by conducting numerical uniaxial and triaxial compression tests on the DE model of the cylindrical CRF specimens, and the test results are shown in Table 4.2 in Chapter 4. These

numerical tests can ensure the overall mechanical properties of the DE model of the CRF material have a good agreement with the corresponding values shown in Table 4.1 in Chapter 4, and the stress-strain behaviour of the DE model of the CRF specimens coincides with the real CRF specimens in the laboratory. It should be mentioned here that the establishment of the DE model of the CRF specimens and test procedures for the numerical uniaxial and triaxial compression tests are not reiterated here, as they have been studied in many previous studies (Wu et al., 2018; Ding et al., 2014). Meanwhile, in this study, numerical direct shear tests were conducted on the coupled FD-DE model of the combined rock-cemented rockfill (R-CRF) specimens to determine the microstructural parameters of the interfaces between the DE model of the CRF column and the FD model of the surrounding rocks (Wei et al., 2022). These numerical tests ensure that the interfaces' overall mechanical properties in the coupled FD-DE model of the single stope backfilled with a CRF column coincide well with the corresponding values shown in Table 5.2 in Chapter 5.

Fig. 5.3 and Fig. 5.4 in Chapter 5 show the establishment of the coupled FD-DE model of the combined R-CRF specimens and their stress-strain behaviour during the numerical the direct shear tests. More details about the implementation mechanism of the numerical direct shear test based on the coupled FD-DE method were presented in another research by the author (Wei et al., 2022). As can be seen in Fig. 5.3, the finite zones were constructed in FLAC3D, representing the FD model of the rock specimen, and the discrete particles were constructed in PFC3D, representing the DE model of the CRF specimen. A coupling wall, of which the microstructural parameters need to be determined, was generated at the interface to transfer the forces and displacements

between the FD and DE models. During the shearing process, normal stresses of 0.25 MPa, 1.50 MPa and 2.50 MPa were applied and servo-controlled on the lateral and top walls of the coupled FD-DE model, and the DE model was moved rightward at a very low displacement rate of 0.05 m/s to ensure a quasi-equilibrium direct shearing system. Fig. 5.4b and Fig. 5.4c show that the servo-controlled normal stresses were successfully applied to the lateral and top walls of the coupled FD-DE model, and as the numerical direct shear test repeated, the overall mechanical properties and stress-strain behaviour of the coupled FD-DE model finally coincided well with the corresponding real combined R-CRF specimen. The microstructural parameters of the interface in the coupled model were then successfully determined.

7.4 Results and discussion

7.4.1 Stress and displacement distribution in the DE model of the CRF column

Fig. 7.3 presents the stress distribution along the VCL of the DE model of the CRF column at different lateral earth pressure states in the single backfilled stope. The calculation results show that when the interfaces between the CRF column and the surrounding rocks are smooth and frictionless, no shear effect generates at the interfaces, and no arching phenomenon occurs in the column. Thus, the vertical overburden pressure p_v along the VCL of the column is only subjected to the unit weight γ and has a positive linear relationship with the depth h of the column. In this situation, two lateral earth pressure coefficients k of 0.233 and 0.125, were used to calculate the lateral earth pressure, p_h^r and p_h^a, respectively, along the VCL of the column at the at-rest and active states, respectively. Both p_h^r and p_h^a have a positive linear relationship with the depth h of the column at both states.

The predicted vertical stresses, σ_v^r and σ_v^a, along the VCL of the column at the at-rest and active states, respectively, are calculated from Li et al.'s analytical model and shown in Fig. 7.3a and Fig. 7.3b, respectively. The calculation results indicate that when the interfaces between the CRF column and the surrounding rocks are frictional and bonded, both σ_v^r and σ_v^a increase logarithmically, as the depth of the column increases, at both states. Due to the shear effect at the interfaces and the arching effect in the column, the apparent deduction is observed in σ_v^r and σ_v^a, which are both smaller than the corresponding p_v, along the VCL of the column at any depth of the column. And the larger the depth of the column is, the larger the deduction in σ_v^r and σ_v^a can be found.

Meanwhile, according to the calculation results from Li et al.'s model, the predicted horizontal stresses, σ_h^r and σ_h^a, along the VCL of the column at the at-rest and active states, respectively, are both smaller than the corresponding p_h^r and p_h^a, respectively, and increase logarithmically as the depth of the column increases. When the column is in the active state, a larger portion of p_h^a from the yielding parts of the column is transferred to the corresponding relatively stable neighbour surrounding rocks, leading to smaller k and C_i (i = 1, 2, 3, 4) values at the interfaces, compared with the column at the at-rest state. Thus, σ_h^a is smaller than the corresponding σ_h^r, and σ_v^a is larger than the corresponding σ_v^r due to a weaker shear effect at the interfaces and a weaker arching effect in the column. It should be mentioned here that σ_v^r, σ_v^a, σ_h^r, and σ_h^a, which are the predicted values calculated from Li et al.'s model, are considered the threshold values for the true vertical and horizontal stresses along the VCL of the column at the natural lateral earth pressure state, as S_i (i = 1, 2, 3, 4) at the interfaces are defined by the Mohr-Coulomb strength

criterion in Li et al.'s model, which is always larger than the real shear stresses in the vertical shear direction at the interfaces.

Fig. 7.3a shows that at the at-rest state, the stresses in the z-, x- and y- directions, σ_{zz}^{r}, σ_{xx}^{r}, and σ_{yy}^{r}, along the VCL of the column, which are modelled with the DE method, all increase logarithmically as the depth of the column increases, and have a good agreement with the corresponding σ_{v}^{r} and σ_{h}^{r}, respectively, which are calculated from Li et al.'s model. As can be seen from Fig. 7.3a, although the horizontal displacement caused by the settlement of the primary layer of the column has been eliminated, as the depth of the column increases, the overburden pressure from the second layer of the column can still lead an extra small portion of p_{h}^{a} from the yielding parts of the column to transfer to the corresponding relatively stable neighbour surrounding rocks, resulting in a slight increase in σ_{zz}^{r} and a slight decrease in σ_{xx}^{r} and σ_{yy}^{r} at the bottom of the column.

Fig. 7.3b shows that at the natural state, the stresses in the z-, x- and y- directions, σ_{zz}^{a}, σ_{xx}^{a}, and σ_{yy}^{a}, along the VCL of the column, which is modelled with the DE method, all increase logarithmically as the depth of the column increases. As can be seen in Fig. 7.3b, naturally, at the shallow and medium depth of the column, the column is at the at-rest state, and σ_{zz}^{a} also has a good agreement with σ_{v}^{r}, due to the high strength and great self-supporting ability of the column. As the depth of the column increases, the overburden pressure increases, and a slight increase in σ_{zz}^{a} can also be observed at the bottom of the column, which leads the lateral earth pressure to switch from the at-rest state to the active state at the bottom. Meanwhile, as can be seen in Fig. 7.3b, naturally, as the depth of the column increases, both σ_{xx}^{a} and σ_{yy}^{a} have a good agreement with the corresponding σ_{h}^{a}, which is calculated from Li et al.'s model, while σ_{yy}^{a} is slightly larger than the

corresponding σ_{xx}^{a} at the natural lateral earth pressure state due to the stope geometry with a narrow width and a long length and the high strength of the column. Under the same overburden pressure from the secondary layer, the portion of p_h^a from the yielding parts of the primary layer of the column transfers more in the x-direction rather than in the y-direction to the corresponding relatively stable neighbour surrounding rocks, resulting in a slightly higher k in the y-direction. Furthermore, as can be seen in Fig. 7.3b, at the active state, a slight increase can be observed in both σ_{xx}^{a} and σ_{yy}^{a} at the shallow depth of the column, resulting from the squeezing effect generated at the top of the surrounding walls during the downtrend movement of the layers of the column in the settlement process.

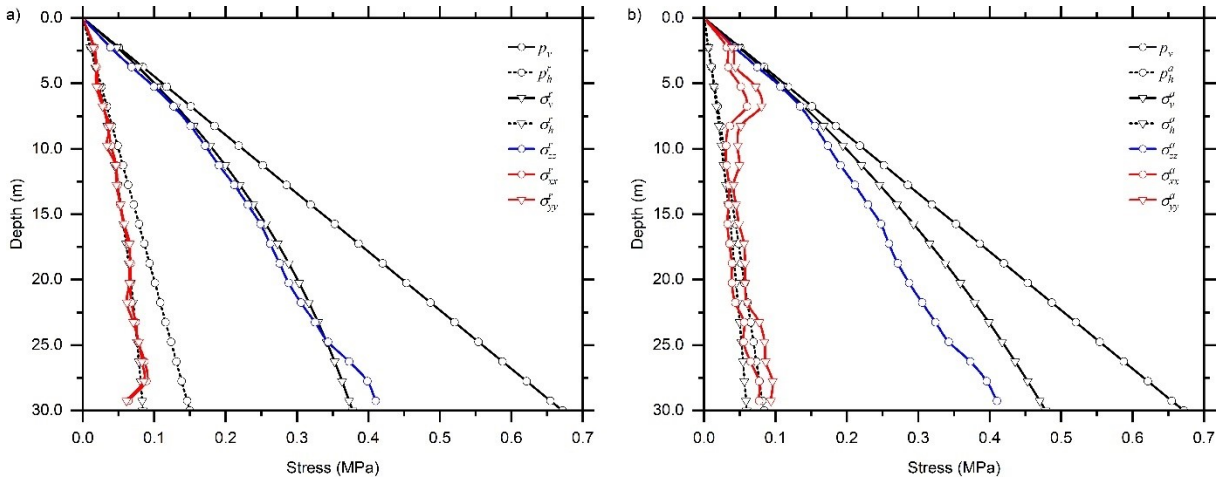

Fig. 7.3 Stress distribution along the VCL of the DE model of the CRF column at: a) at-rest, and b) natural lateral earth pressure states.

Fig. 7.4 presents the distribution of the *k* along the VCL of the DE model of the CRF column at different lateral earth pressure states in the single vertical backfilled stope. At the at-rest state, as the depth of the column increases, both *k* in the x- and y- directions start from the infinity and then approach the standard value of 0.233 gradually at the

medium depth of the column. At the natural state, as the depth of the column increases, k in the x-direction starts from infinity and then approaches the standard value of 0.125 gradually at the medium depth of the column. However, k in the y-direction is larger than the standard value of 0.125 at the medium depth and bottom of the column, due to the stope geometry with a narrow width and a long length, indicating a greater self-supporting ability of the column in the y-direction.

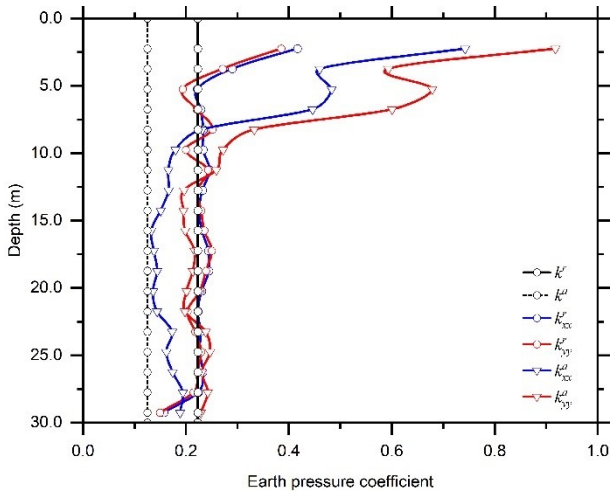

Fig. 7.4 Distribution of k along the VCL of the DE model of the CRF column at different lateral earth pressure states.

Fig. 7.5 and Fig. 7.6 present the stress distribution at the CCS of the DE model of the CRF column at different lateral earth pressure states in the single vertical backfilled stope. The modelling results indicate that at both the at-rest and active states, the stress distribution inside the CRF column is significantly influenced by the shear effect that generates at the frictional bonded interfaces between the column and the surrounding rocks, leading to the occurrence of the arching phenomenon inside the column. As can be seen in Fig. 7.5a and Fig. 7.5b, in the CRF column at the at-rest state, the stress in the z-direction, σ_{zz}, is smaller than the corresponding vertical overburden pressure p_v at both the CCS of the

column on the xz- and yz- planes. Meanwhile, at any depth of the column, σ_{zz} decreases gradually from the locations near the VCL of the column to the locations near the interfaces, and evident concave-down stress arches are observed in the distribution of σ_{zz} at both the CCS of the column on the xz- and yz- planes.

Fig. 7.5c and Fig. 7.5d show that in the CRF column at the at-rest state, the stresses in the x- and y- directions, σ_{xx}^{r} and σ_{yy}^{r}, are both smaller than the corresponding lateral earth pressure p_h^r at both the CCS of the column on the xz- and yz- planes. Meanwhile, at the locations near the surrounding rocks inside the column, both σ_{xx}^{r} and σ_{yy}^{r} are extremely small, and only a very small portion of p_h^r from the yielding parts of the column transfers to the corresponding relatively stable neighbour surrounding rocks because the horizontal displacement caused by the settlement of the primary layer of the column has been eliminated. Thus, both σ_{xx}^{r} and σ_{yy}^{r} at the locations near the VCL of the column are mostly influenced by the mechanical properties of the CRF column itself.

Fig. 7.6a and Fig. 7.6b present that, in the CRF column at the natural state, the stress in the z-direction σ_{zz} has the same distribution pattern with σ_{zz} at the at-rest state, and obvious concave-down stress arches are also observed in the distribution of σ_{zz}, at both the CCS of the column on the xz- and yz- planes. Naturally, at the shallow and medium depth of the column, the column is at the at-rest state, due to its high strength and great self-supporting ability, resulting in the same magnitude of σ_{zz} compared with the column at the at-rest state. As the depth of the column increases, the overburden pressure increases, and the lateral earth pressure switch from the at-rest state to the active state at the bottom of the column, resulting in an increased magnitude of σ_{zz} closed to the threshold value at the active state.

Fig. 7.6c and Fig. 7.6d show that, in the CRF column at the natural state, the stresses in the x- and y- directions, σ_{xx}^{a} and σ_{yy}^{a}, have a very similar distribution pattern with σ_{xx}^{r} and σ_{yy}^{r} at the at-rest state, and at the CCS of the column on the xz- and yz- planes, respectively. However, due to the ununiform particle size distribution of the DE model of the CRF column, some symmetric stress concentration zones in the distribution of σ_{xx}^{a} and σ_{yy}^{a} are observed on the CCS of the column on the xz- and yz- planes, respectively, during the settlement and consolidation processes of the column. As can be seen from Fig. 7.6c and Fig. 7.6d, at the natural state, the stress transmission and energy alternation occur ceaselessly at the interfaces between the column and the surrounding rocks. Thus, compared with the column at the at-rest state, at the locations near the interfaces inside the column, a relatively large portion of p_{h}^{a} from the yielding parts of the column transfers to the corresponding relatively stable neighbour surrounding rocks, resulting in relatively smaller σ_{xx}^{a} and σ_{yy}^{a} in the column especially at the bottom of the column at the natural state.

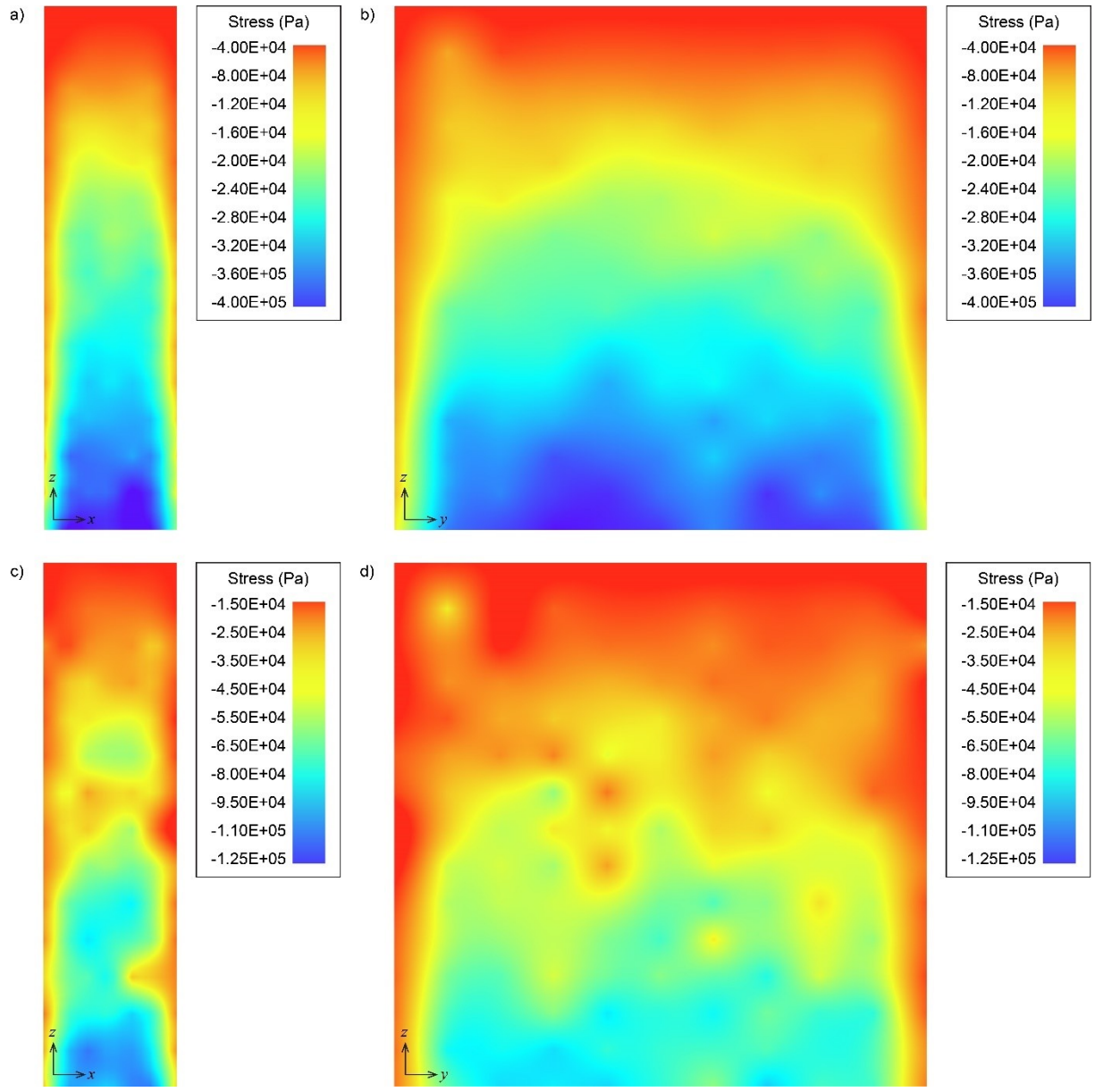

Fig. 7.5 Stress distribution at the CCS of the DE model of the CRF column at the at-rest lateral earth pressure state: a) σ_{zz}^{r} on the xz-plane, b) σ_{zz}^{r} on the yz-plane, c) σ_{xx}^{r} on the xz-plane, and d) σ_{yy}^{r} on the yz-plane.

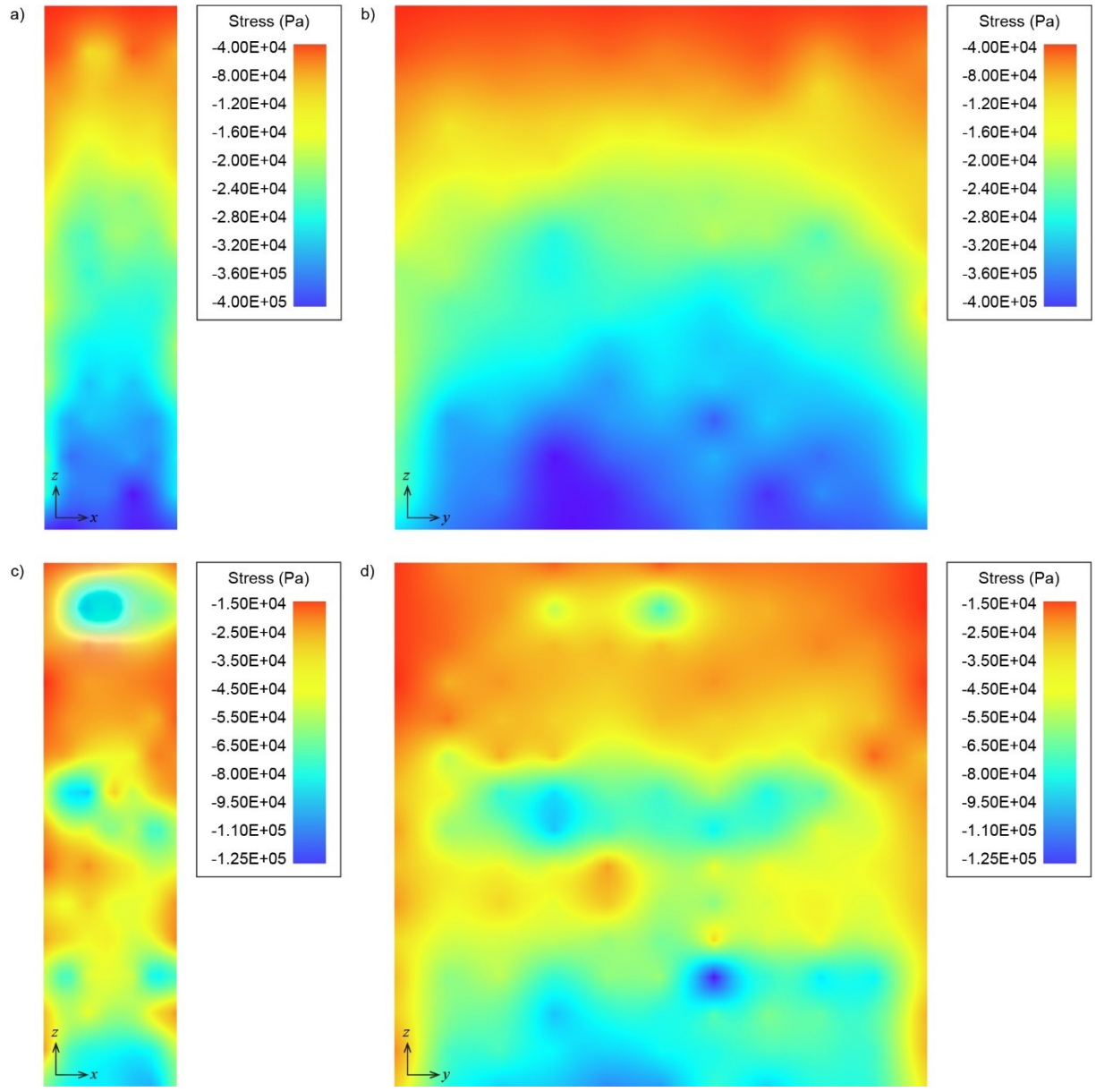

Fig. 7.6 Stress distribution at the CCS of the DE model of the CRF column at the natural lateral earth pressure state: a) σ_{zz}^{a} on the xz-plane, b) σ_{zz}^{a} on the yz-plane, c) σ_{xx}^{a} on the xz-plane, and d) σ_{yy}^{a} on the yz-plane.

Fig. 7.7 and Fig. 7.8 present the displacement distribution at the CCS of the DE model of the CRF column at different lateral earth pressure states in the single vertical backfilled stope. The modelling results indicate that at both the at-rest and natural states, the

displacement distribution inside the CRF column is significantly influenced by the shear effect that generates at the frictional bonded interfaces between the column and the surrounding rocks, resulting from the occurrence of the arching phenomenon inside the column. As can be seen in Fig. 7.7a and Fig. 7.7b, in the CRF column at the at-rest state, the displacement in the z-direction d_{zz}^{r}, is smaller at the locations near the interfaces and increase to be higher at the locations near the VCL of the column, at both the CCS of the column on the xz- and yz- planes at any depth of the column. Meanwhile, obvious concave-up displacement arches are observed in the distribution of d_{zz}^{r} at both the CCS of the column on the xz- and yz- planes, as the shear effect at the interfaces hinders the downtrend movement of the CRF particles and the settlement process of the column. Fig. 7.7c and Fig. 7.7d show that in the CRF column at the at-rest state, the displacement in the x- and y- directions, d_{xx}^{r} and d_{yy}^{r}, are both extremely small, and no obvious displacement arches are observed at the CCS of the column on either the xz- or yz- plane, because the horizontal displacement which is caused by the settlement of the primary layer of the column has been eliminated. Thus, due to the quick consolidation process and the good self-supporting ability of the column, both d_{xx}^{r} and d_{yy}^{r} in the column are mostly influenced by the mechanical properties of the column itself.

Fig. 7.8a and Fig. 7.8b show that in the CRF column at the natural state, the displacement in the z-direction d_{zz}^{a}, has the same distribution pattern with d_{zz}^{r} at the at-rest state, and obvious concave-up displacement arches are also observed in the distribution of d_{zz}^{a}, at both the CCS of the column on the xz- and yz- planes. Furthermore. Fig. 7.8c and Fig. 7.8d show that in the CRF column at the natural state, the displacement in the x- and y- directions, d_{xx}^{a} and d_{yy}^{a}, show an evident symmetrical distribution pattern at both the CCS

of the column on the xz- and yz- planes. At the natural state, in the corresponding x- and y- directions, d_{xx}^{a} and d_{yy}^{a} are both smaller at the locations near the VCL of the column and increase to be higher at the locations near the interfaces, leading the CRF particles to have a tendency of outward movement from the VCL of the column. Naturally, as the depth of the column increases, the outward movement tendency of CRF particles gets stronger, resulting in the lateral earth pressure switching from the at-rest state to the active state at the bottom of the column.

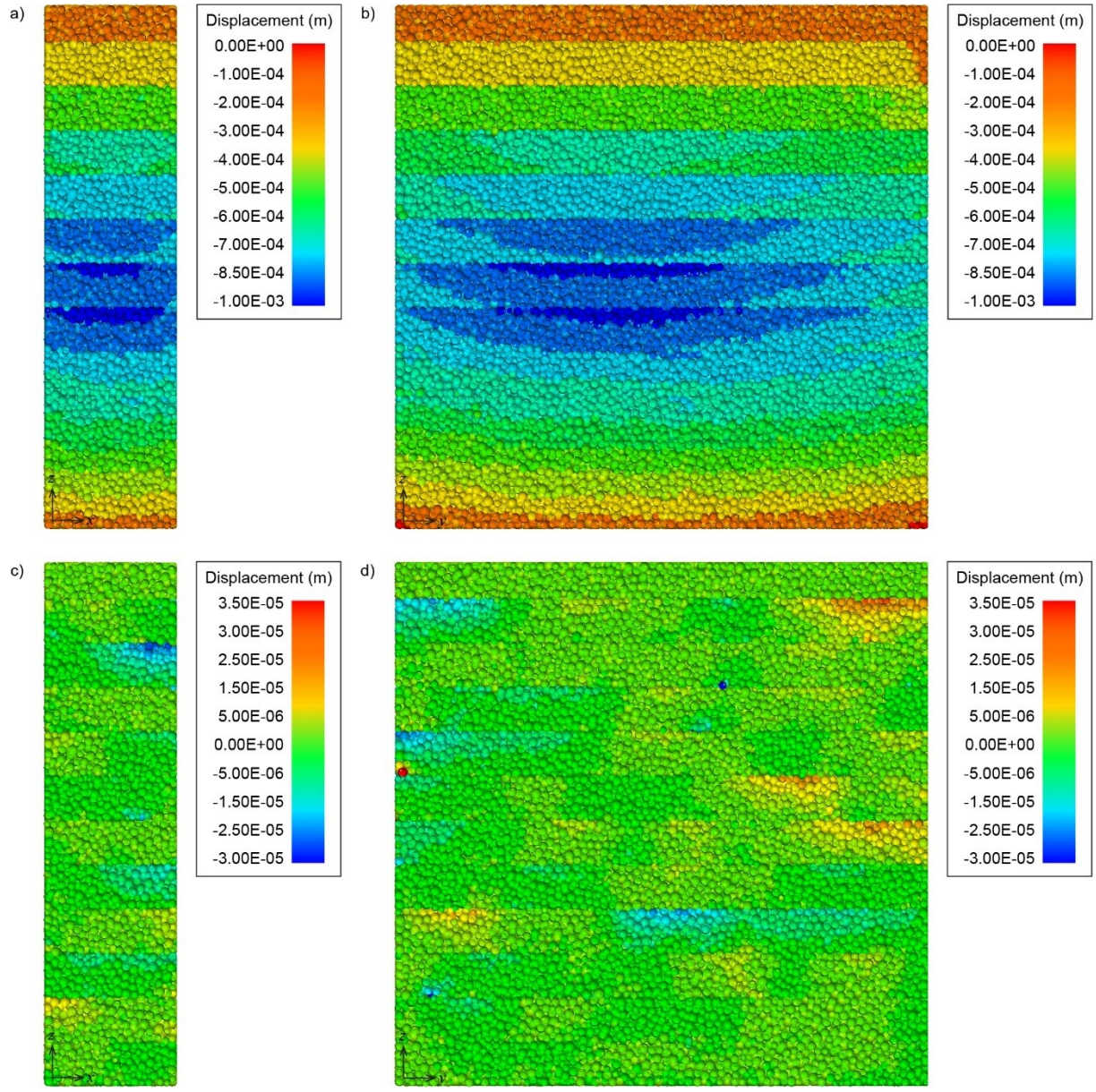

Fig. 7.7 Displacement distribution at the CCS of the DE model of the CRF column at the at-rest lateral earth pressure state: a) d_{zz}^{r} on the xz-plane, b) d_{zz}^{r} on the yz-plane, c) d_{xx}^{r} on the xz-plane, and d) d_{yy}^{r} on the yz-plane.

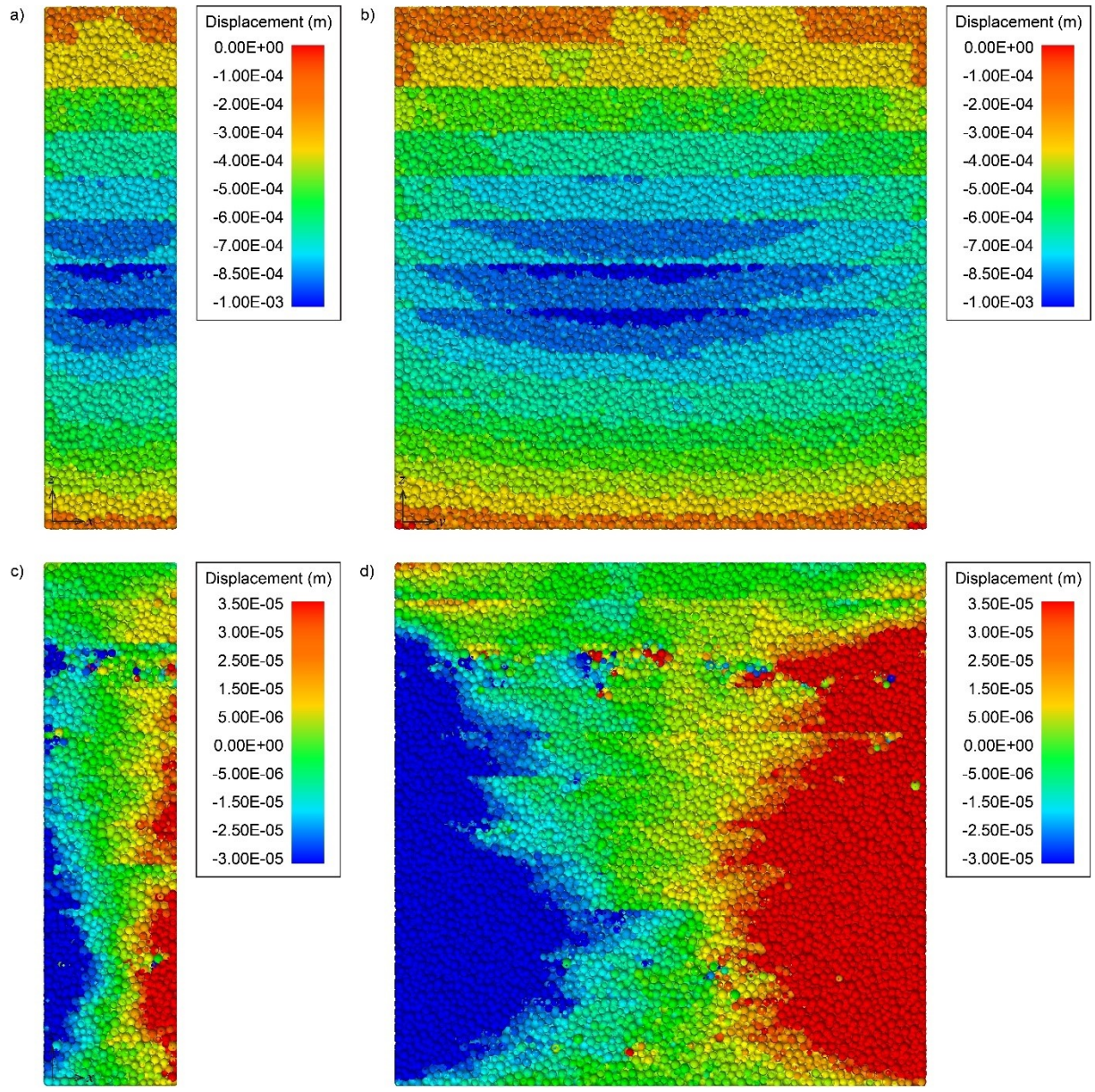

Fig. 7.8 Displacement distribution at the CCS of the DE model of the CRF column at the natural lateral earth pressure state: a) d_{zz}^{a} on the xz-plane, b) d_{zz}^{a} on the yz-plane, c) d_{xx}^{a} on the xz-plane, and d) d_{yy}^{a} on the yz-plane.

7.4.2 Stress and displacement distribution in the FD model of the surrounding rocks

Fig. 7.9 shows the stress distribution at the CCS of the FD model of the surrounding rocks at the natural lateral earth pressure state in the single stope after being backfilled with the

CRF column. It should be mentioned here that, at the at-rest state, the stress at the CCS of the surrounding rocks has the same distribution pattern as the natural state. Thus, it is not shown in this section. As can be seen in Fig. 7.9a and Fig. 7.9b, in the surrounding rocks at the natural state, the stress in the z-direction, σ_{zz}^{a}, increases significantly at both the CCS of the surrounding rocks on the xz- and yz- planes, due to the overburden pressure from the column and the shear effect at the interfaces during the settlement and consolidation processes of the column. Fig. 7.9c, and Fig. 7.9d indicate that, naturally, after the stope backfilled, the downtrend movement of the column provides the confining pressure and supporting effect to the adjacent surrounding rocks, increasing in σ_{xx}^{a} and σ_{yy}^{a} at the CCS of the surrounding rocks on the xz- and yz- planes, respectively.

Fig. 7.10 presents the zoomed-out view of the distribution of maximum principal stress σ_{m}^{a} at the stress concentration zones in the FD model of the surrounding rocks before and after backfilled with the CRF column at the natural lateral earth pressure state. As can be seen, the area of the stress concentration zones, which are located at the bottom corners of the surrounding rocks, evidently shrinks due to the confining pressure and the supporting effect from the column. It demonstrates that at the core the stress concentration zone located on the xz-plane shown in Fig.7.10, σ_{m}^{a} decreases by 4.0% after the stope is backfilled with the column. The modelling results indicate that, naturally, backfilling the primary extracted stope can efficiently provide the confining pressure to the surrounding rocks, reduce the potential rockburst risk and improve the stability of the underground mined-out areas.

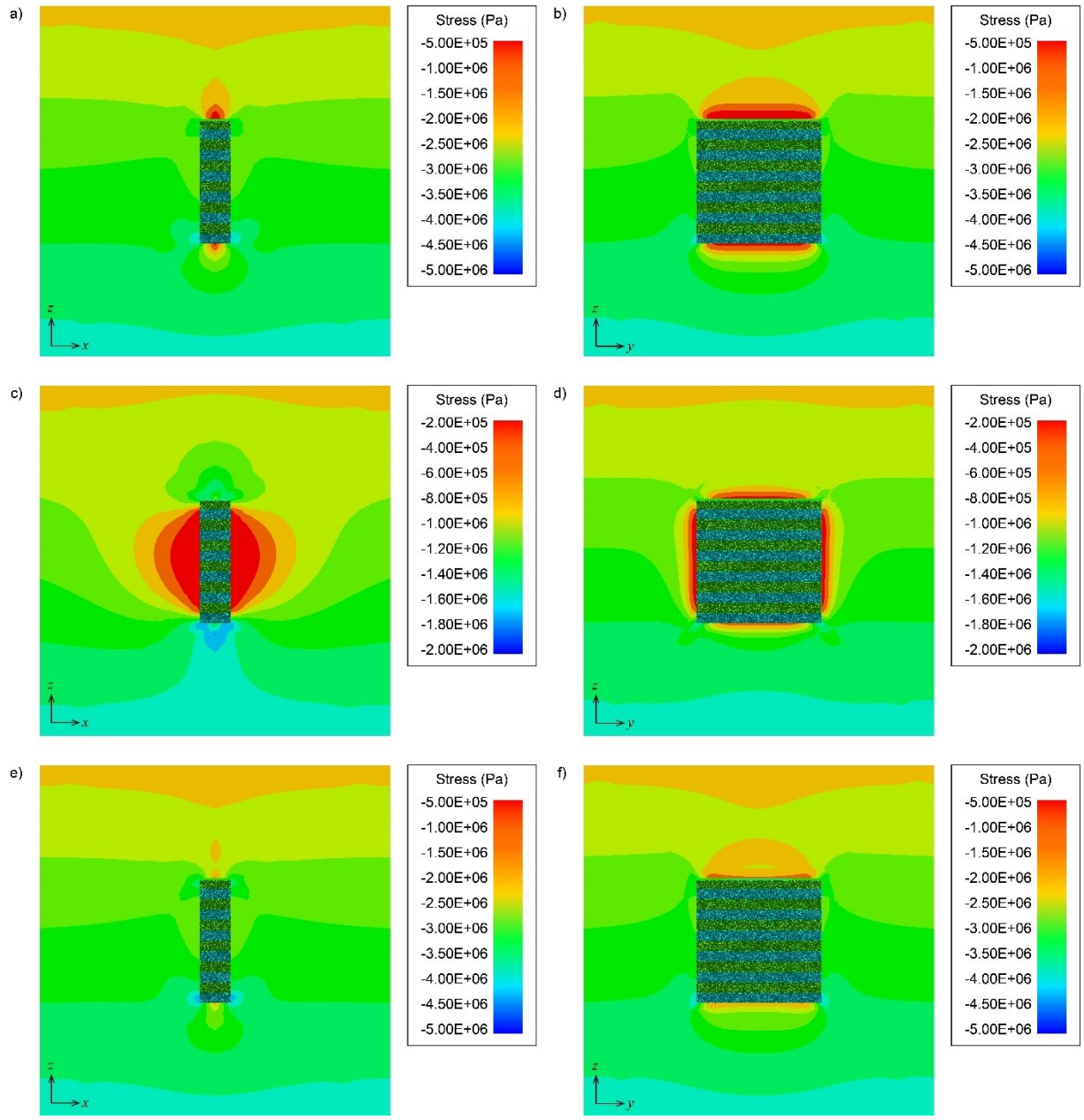

Fig. 7.9 Stress distribution at the CCS of the FD model of the surrounding rocks at the natural lateral earth pressure state: a) σ_{zz}^{a} on the xz-plane, b) σ_{zz}^{a} on the yz-plane, c) σ_{xx}^{a} on the xz-plane, and d) σ_{yy}^{a} on the yz-plane, e) σ_{m}^{a} on the xz-plane, and f) σ_{m}^{a} on the yz-plane.

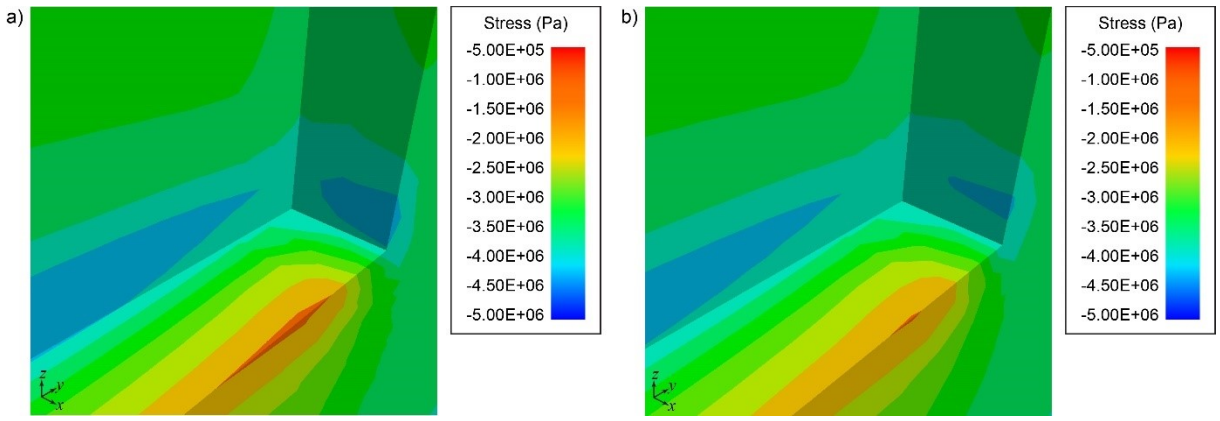

Fig. 7.10 Effect of the backfilling process on the distribution of σ_m^a at the stress concentration zones in the FD model of the surrounding rocks at the natural lateral earth pressure state.

Fig. 7.11 shows the changes in the stress distribution along the monitoring lines of the FD model of the single stope before and after backfilled with the CRF column at the natural lateral earth pressure state. As can be seen in Fig. 7.11a and Fig. 7.11b, before the stope backfilled, the maximum principal stress σ_m^e increases first and then decreases along the monitoring line BA and AC in the surrounding rocks, respectively, with the highest value of σ_m^e appearing at the mid-points of both the monitoring lines. Fig. 7.11c shows that before the stope backfilled, σ_m^e increases along the monitoring line DA in the surrounding rocks, as the depth of the stope increases, with the highest value of σ_m^e appearing at the bottom end of the monitoring line. Fig. 7.11a to Fig. 7.11c also show that after the stope backfilled, σ_m^a all decreases to be smaller than the corresponding σ_m^e, along the monitoring line BA, AC and DA at the surrounding rocks, with the maximum decrease rates of 3.9%, 4.0%, 1.8%, respectively. The modelling results indicate that the column significantly improves the stability of the underground mined-out areas, leading to the

efficient reduction in the maximum principal stress and the area of the stress concentration zones in the surrounding rocks.

Fig. 7.11d to Fig. 7.11f show that, before the stope backfilled, the stresses in the x-, y- and z- directions, σ_{xx}^{e}, σ_{yy}^{e}, and σ_{zz}^{e}, along the monitoring line IJ, GH and EF in the surrounding rocks, respectively, all start from zero at the interfaces and increase to the corresponding overburden pressure p_v and lateral earth pressure p_h^a, respectively, at the further end of the monitoring lines. And then, after the stope backfilled, the stresses in the x-, y- and z- directions, σ_{xx}^{a}, σ_{yy}^{a}, and σ_{zz}^{a}, all increases to be larger than the corresponding σ_{xx}^{e}, σ_{yy}^{e}, and σ_{zz}^{e}, along the monitoring line IJ, GH and EF in the surrounding rocks, especially near the interfaces. The modelling results indicate that the column provides effective confining pressure to reinforce the surrounding rocks and increase the pore convergence degree of the rock mass by its self-weight and the mechanical interaction at the interfaces between the column and the surrounding rocks.

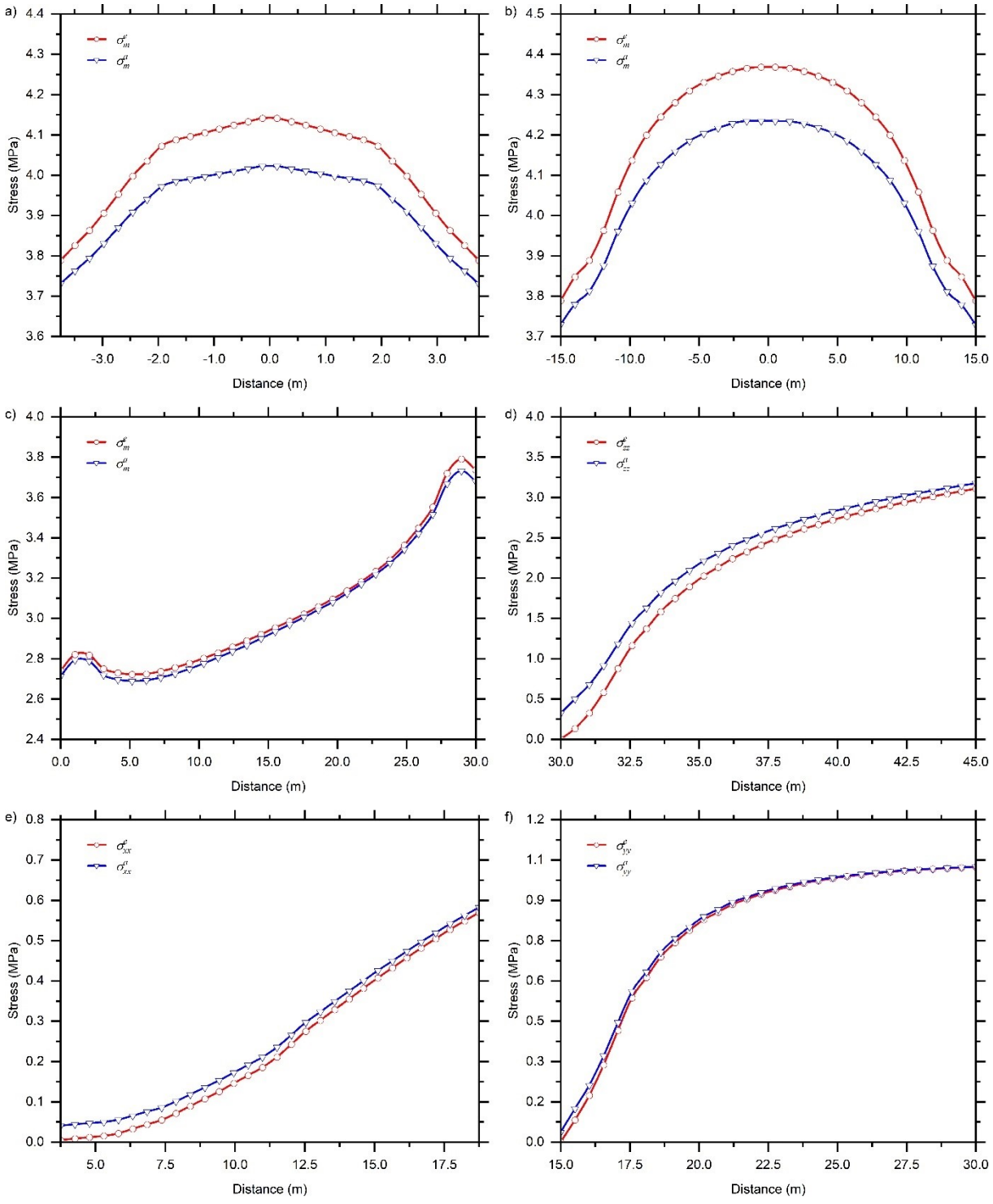

Fig. 7.11 Effect of the backfilling process on the stress distribution along the monitoring lines in the FD model of the surrounding rocks at the natural lateral earth pressure state: a) σ_m^a along the monitoring line BA, b) σ_m^a along the monitoring line AC, c) σ_m^a along the

monitoring line DA, d) σ_{zz} along the monitoring line EF, e) σ_{xx} along the monitoring line GH, and f) σ_{yy} along the monitoring line IJ.

Fig. 7.12 and Fig. 7.13 show the displacement distribution at the CCS of the FD model of the surrounding rocks at different lateral earth pressure states after the single vertical stope backfilled with the CRF column. The modelling results indicate that at both the at-rest and natural states, the displacement in the surrounding rocks in the z-direction, d_{zz}^{r} and d_{zz}^{a}, show the same distribution pattern at both the CCS of the surrounding rocks on the xz- and yz- planes. During the settlement and consolidation processes of the column, the overburden pressure from the column and the shear effect at the interfaces drive the surrounding rocks to gain a downtrend movement, leading the significant displacement, d_{zz}^{r} and d_{zz}^{a}, in the z-direction in the surrounding rocks. However, as can be seen in Fig. 7.12c and Fig. 7.12d, in the surrounding rocks at the at-rest state, the displacement in the x- and y- directions, d_{xx}^{r} and d_{yy}^{r}, are both extremely small at the CCS of the surrounding rocks on either the xz- or yz- plane because the CRF column has a great self-supporting ability, and relatively no horizontal displacement transferring occurs at the interfaces between the CRF column and the surrounding rocks. In contrast, Fig. 7.13c and Fig. 7.13d show that, naturally, along the depth of the CRF column, the lateral earth pressure switch from the at-rest state to the active state, leading to significant displacement transferring at the interface between the CRF column and the surrounding rocks. And then, under the combined effect of the overburden pressure from the CRF column and the shear effect at the interfaces, the bottom part of the CRF column has a trend of pushing the surrounding rocks away, leading to the significant increase in the displacement in the x- and y-

directions, d_{xx}^{r} and d_{yy}^{r}, at both the CCS of the surrounding rocks on the xz- and yz-planes.

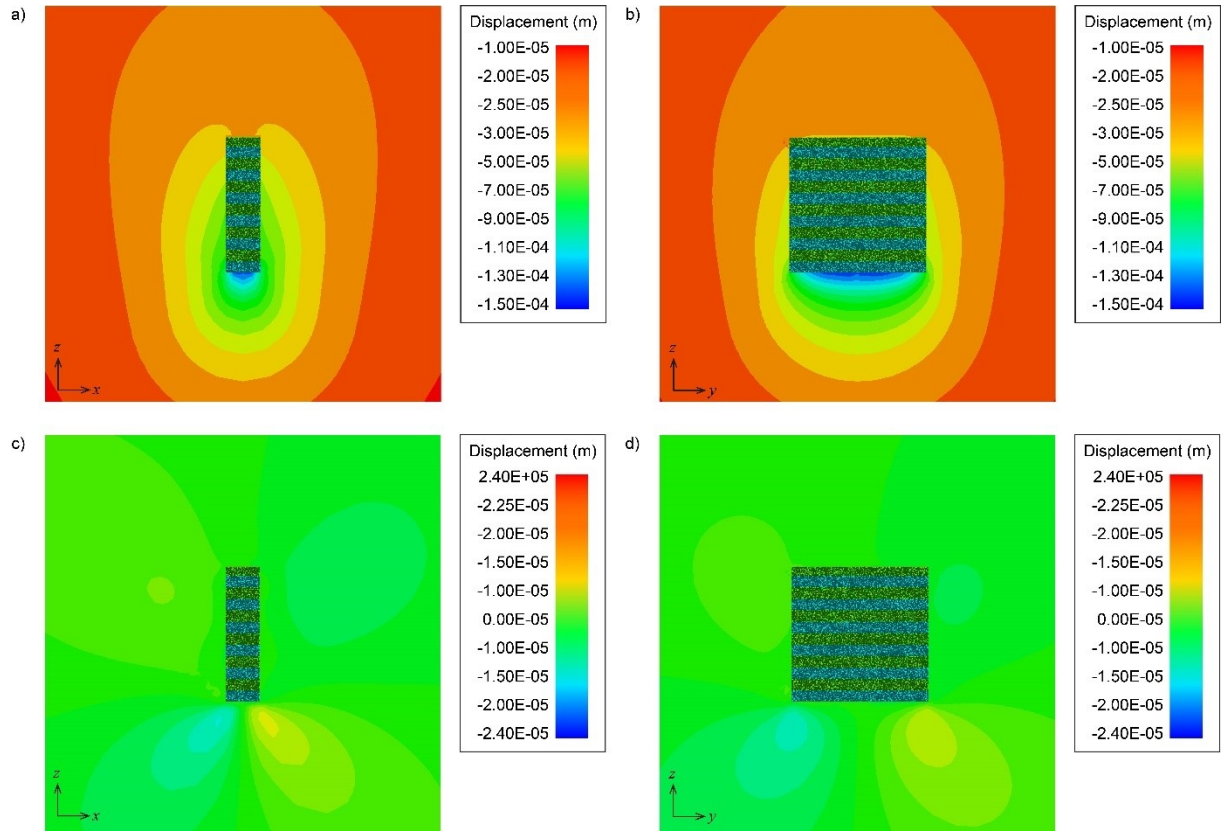

Fig. 7.12 Displacement distribution at the CCS of the FD model of the surrounding rocks at the at-rest lateral earth pressure state: a) d_{zz}^{r} on the xz-plane, b) d_{zz}^{r} on the yz-plane, c) d_{xx}^{r} on the xz-plane, and d) d_{yy}^{r} on the yz-plane.

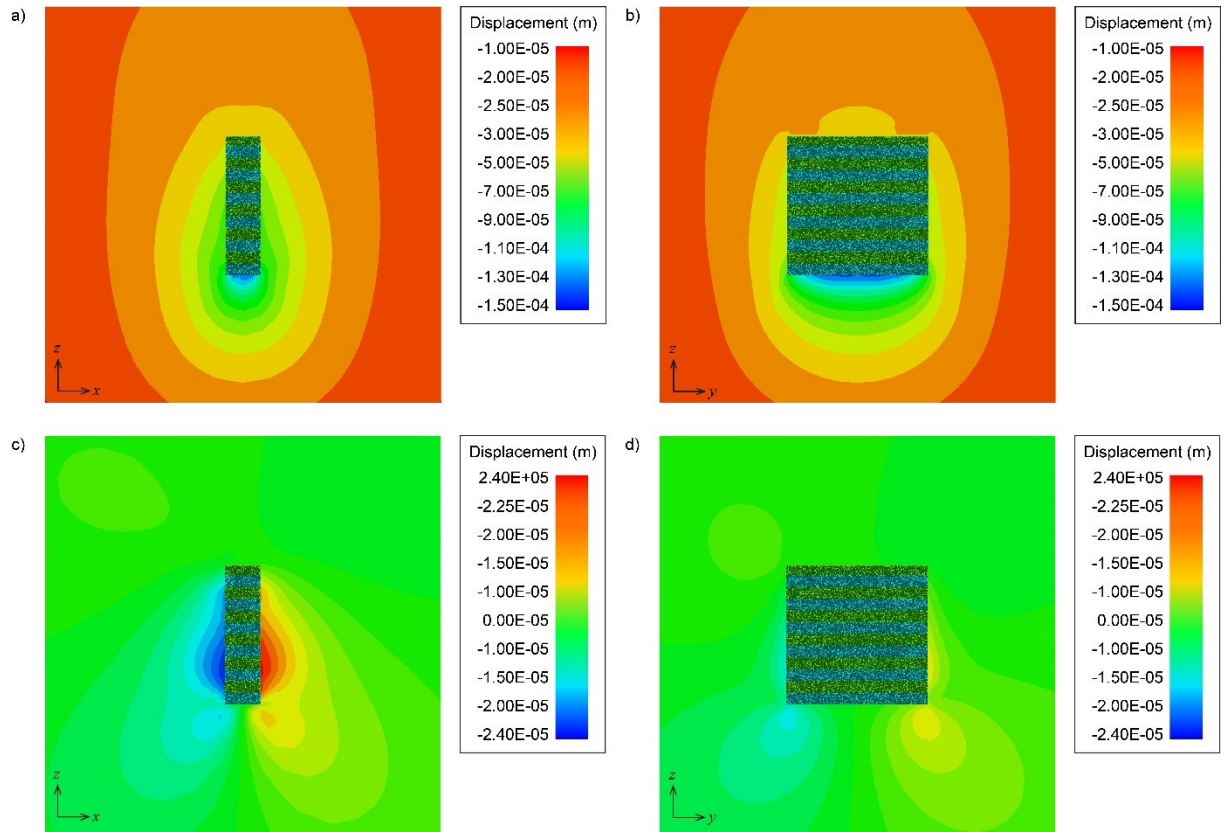

Fig. 7.13 Displacement distribution at the CCS of the FD model of the surrounding rocks at the active lateral earth pressure state: a) d_{zz}^{a} on the xz-plane, b) d_{zz}^{a} on the yz-plane, c) d_{xx}^{a} on the xz-plane, and d) d_{yy}^{a} on the yz-plane.

7.5 Conclusions

In this study, the coupled finite difference (FD) and discrete element (DE) method were successfully used to simulate a single underground stope backfilled with a cemented rockfill (CRF) column, considering the frictional-bonded interfaces between the CRF column and the surrounding rocks. This work proved the feasibility of applying the coupled FD-DE method in simulating the mechanical interaction and response between two different geo-materials involved with interfaces.

The modelling results indicate that the shear effect significantly influences the stress and displacement distribution at the single backfilled stope at the interfaces between the CRF column and the surrounding rocks. Naturally, as the CRF column fully settles and consolidates, the lateral earth pressure of the CRF column switch from the at-rest state at the shallow depth to the active state at the medium depth and bottom of the column. Due to the arching phenomenon in the CRF column, a significant deduction can be found in both the vertical and horizontal stresses in the CRF column, owing to the resistant forces from the shear effect at the interfaces between the CRF column and the surrounding rocks.

Meanwhile, the modelling results demonstrate that at both the at-rest and natural lateral earth pressure states, the CRF column provides confining pressure and supporting effect to the surrounding rocks, resulting in the shrinkage of the stress concentration zones and the decrease in the maximum principal stress in the surrounding rocks. The modelling results confirm that backfilling the primary single-stope can efficiently reduce the rockburst risk in surrounding rocks and improve the stability of the underground mined-out areas.

Chapter 8 Coupled finite difference and discrete element method for modelling multiple stopes backfilled with the cemented rockfill

In this chapter, multiple stopes backfilled with the cemented rockfill (CRF) columns at the natural lateral earth pressure state were modelled with the coupled finite difference (FD) and discrete element (DE) method, considering the frictional-bonded interfaces between the CRF columns and the surrounding rocks. Meanwhile, the primary/secondary manner of the mining/backfilling activities was modelled to study the influence of the sequence of the mining/backfilling activities on the stress and displacement distribution in the CRF columns and around the surrounding rocks at these multiple backfilled stopes. The modelling results indicate that backfilling the extracted stopes can efficiently enhance the stability of the underground mined-out area and adjacent rock pillars at the hard rock mine, and the mining/backfilling sequence can have a significant influence on the stress and displacement distribution in the CRF columns and around the surrounding rocks. Furthermore, the CRF columns with different numbers of exposed sidewalls were also modelled with the DE method in this chapter to study the fracture development and failure pattern caused by the overburden pressure from a constant displacement rate at the top surface of the CRF column. The modelling results show that the measured uniaxial compressive strength (UCS) and cohesion of the CRF columns at the hard rock mine are much higher than the required UCS and cohesion calculated with the modified Mitchell's analytical solution (1982), and the CRF columns can have decent stability when they are subjected to the adjacent mining activities, even for these CRF columns with the lowest UCS. Meanwhile, the modelling results indicate that as the mined-out area or the total width of the multiple backfilled stopes increase, the deduction in the maximum principal stress at the stress concentration zones around the surrounding rocks increases, resulting

from a relatively higher supporting effect from the CRF columns at the multiple backfilled stopes.

8.1 Introduction

At underground mines where the backfilling method is adopted, the mining/backfilling activities are usually executed in a sequence (primary/secondary manner) at the adjacent multiple stopes (Sepehri et al., 2017). For example, in the blasthole stoping (BHS) mining method, the primary stopes are extracted first, leaving the adjacent stopes as rock pillars to support the overburden pressure from the overhead rock strata. And then, the primary stopes are backfilled with the cement backfill material and cured for more than 28 days to form backfill columns. As backfill columns settle, consolidate, and gain strength, the secondary stopes, which are the adjacent rock pillars, can then be recovered, leaving the primary backfill columns to support the overburden and lateral pressures from surrounding rocks, providing work platform for the future mining activities at the meantime.

The primary/secondary manner of mining/backfilling activities can significantly influence the stress and displacement distribution in backfill columns and around the surrounding rocks. Numerical modelling is very efficient in comprehensively understanding the stress distribution law. Many researchers have created numerical models with the continuum or discontinuum method to study the effect of the mining/backfilling sequence on the stability of the underground mined-out area. These numerical models can be calibrated with analytical solutions to predict the instability and potential geohazards induced by the sequential mining/backfilling activities (Liu et al., 2016; Sepehri et al., 2017). In Mkadmi's FE model, saturated backfill layers were added

on the top of the pre-drained and settled backfill layers until the stope was wholly backfilled (Mkadmi et al., 2013). The modelling results show that a higher sequential backfilling rate results in higher total stress at the base of backfilled stopes due to the accumulation of pore water pressure, and lower normal stress can be observed at a slower backfilling rate since the drainage and binder hydration can occur sequentially in backfill columns. In some other FD models, two adjacent stopes were extracted and backfilled in a primary/secondary manner (Falaknaz et al., 2015). The modelling results indicate that the stress distribution in the second backfilled stope tends to behave like in a single backfilled stope and is in good agreement with the analytical solution developed by Li and Aubertin (2009), while the stress in the first backfilled stope can show an evident redistribution, which is significantly influenced by the neighbouring excavation and backfilling operations (Newman, 2018). Previous studies by Newman (2018) and Falaknaz et al. (2015) both show that during the excavation of the second stope, the vertical stress in the first backfilled stope tends to decrease, especially near the mid-height, while the horizontal stress increases first and then decreases owing to the movement of the surrounding walls. During the backfilling process of the second stope, the horizontal stress in the first backfilled stope tends to increase with the backfilling sequence, while the corresponding vertical stress becomes insensitive to the backfilling process. It should be mentioned here that most of the previous studies adopted the continuum approach due to its high computation performance (Falaknaz et al., 2015; Emad et al., 2018; Liu et al., 2016), while in very few studies (Hasan et al., 2017), the discontinuum approach has been selected to evaluate the stress redistribution within multiple stopes backfilled with uncemented backfill materials.

For underground mines, gaining an in-depth understanding of the stability of multiple backfilled stopes is one of the most crucial research objectives for mining engineers. Backfilling the underground mined-out area can reduce the risks in ground subsidence, ore dilution, pillar failure and rockburst (Abdellah et al., 2020; Heib et al., 2010; Yang et al., 2015). To study the backfill column stability, Mitchell (1982) proposed a solution based on the limit equilibrium analysis of a wedge block model, in which the required UCS of the backfill column is only related to the stope geometry and the height of the exposed sidewall. Li and Aubertin (2012) proposed a modified Mitchell's solution, which can be applied to backfilled stopes with rectangular shapes and overcomes several limitations of the original Mitchell's analytical model. For example, in the modified model, the internal friction angle of the backfill column can be nonzero, and the interface cohesion can be considered a portion of the cohesion of the backfill column. Meanwhile, a safety factor is introduced to evaluate the backfill column stability, calculated as the ratio of resistant force and driving force on the failure plane (Li and Aubertin, 2012). It must be mentioned here more details about Mitchell's analytical models are discussed in section 8.2.2.

Many previous studies have shown that underground mined-out voids are backfilled to minimize the ground subsidence and control the overlying strata movement, especially in many coal mines. The main factors that influence the stability of backfilled stopes at a coal mine include the deformation modulus and thickness of the stope roof, the overlying strata pressure, the advancement distance and work face width, and foundation coefficients of backfill columns (Sun et al., 2019; Yang et al., 2017). Yang et al. (2017) built a FE model of multiple backfilled stopes with the same geometry as the stopes at an

underground iron mine to evaluate the surface vertical and horizontal deformation at the mine site due to the subsidence. The modelling results indicate that as underground stopes are backfilled, the ground deformation can be lower than critical values and fall into a controllable range. It shows that backfilling the stopes with the cemented paste backfill (CPB) can be feasible and effective in subsidence control. Zhang et al. (2018) created a physical model of multiple backfilled stopes in the laboratory with the same cemented paste backfill and rock materials from a coal mine to reproduce the movement of overlying strata in a mining/backfilling sequence. The test results indicate that the overburden pressure from the overhead coal seams on the top surface of backfill columns increases first and then keeps stable. Backfilling underground stopes can limit the overlying rock strata's deformation and avoid the caved zones' appearance. Yang et al. (2015) created a physical model of two adjacent backfilled stopes in the laboratory with the same cemented paste backfill material from an iron mine to study the stope stability at different stages in the mining/backfilling sequence. The test results reveal that the stability of the primary backfilled stope is the worst when the secondary stope is extracted and one sidewall of the primary backfill column is exposed. Lu et al. (2018) conducted field monitoring and numerical modelling to study the stress redistribution caused by the excavation and backfilling of multiple stopes. The study indicates that shear stress can be concentrated at the interfaces between backfill columns and the surrounding rocks, and the corners of the backfilled stopes are the critical positions of shear and maximum principal stress concentration zones.

The rock pillar failure is a common engineering disaster at the underground mined-out area. Many researchers combined in-situ monitoring and numerical modelling to study

the supporting effect of backfill columns on rock pillars' stability. Heib et al. (2010) instrumented total earth pressure cells on rock pillars based on a gypsum mine and found that adjacent backfill columns can induce confining pressures on rock pillars. Building the DE model of multiple backfilled stopes adjacent to fractured rock pillars indicates that backfill columns can induce the horizontal and vertical stress that contributes to the cracks and fracture closure inside rock pillars. The induced stress depends on the backfill material consolidation, pillar deformation, pillar fracture presence, and the mechanical properties of the interfaces between backfill columns and the surrounding rocks (Heib et al., 2010; Yin et al., 2017). Tesarik et al. (2009) analyzed the monitoring data from biaxial stress meters instrumented in rock pillars to study the long-term stability of backfilled stopes in an underground lead-zinc mine. The test results indicate that backfill columns can limit dilation and improve the stability of rock pillars. The total strain measured inside rock pillars supported by backfill columns is significantly smaller than unconfined rock pillars (Tesarik et al., 2009; Zhang et al., 2017).

In this study, multiple underground stopes backfilled with the CRF columns at the natural lateral earth pressure state were modelled with the coupled FD-DE method, considering the frictional-bonded interfaces between the CRF columns and the surrounding rocks. Meanwhile, the primary/secondary manner of the mining/backfilling activities was simulated to study the effect of the mining/backfilling sequence on the stress and displacement distribution in the CRF columns and around the surrounding rocks at these multiple backfilled stopes. The CRF columns with different numbers of exposed sidewalls were also modelled with the DE method to study the fracture development and failure

pattern caused by the overburden pressure from a constant displacement rate at the top surface of the CRF columns.

8.2 Background and methodology

8.2.1 Mining and backfilling methods

In Chapter 3, Chapter 6, and Chapter 7, the mining and backfilling methods at the Canadian hard rock mine have been discussed in detail. At the mine, the blasthole stoping (BHS) method was adopted to extract the orebody, and then the cemented rockfill (CRF) was used to backfill the underground mined-out openings (Sepehri et al., 2017). Fig. 6.1 in Chapter 6 depicts the primary/secondary mining/backfilling activities at the hard rock mine. Two drifts of overcut and undercut were developed at the bottom and top of the stope, respectively, for mining and transportation of the ore products. As the stope was entirely mined out, the CRF material was then used in the extracted stope to provide support to the adjacent rock pillars. As the primary stopes were extracted and backfilled, the secondary stopes, which were the adjacent rock pillars, could be mined, leaving the primary CRF columns to prevent the mined-out area from catastrophic disasters of subsidence or rock pillar failure.

8.2.2 Mitchell's analytical model

Mitchell (1982) first proposed an analytical model to evaluate the stability of the backfill column based on a limit equilibrium analysis of a wedge block model. Li and Aubertin (2012) proposed a modified Mitchell's solution suitable for the backfilled stopes with rectangular shapes and overcame the limitations of original Mitchell's analytical model. In the modified Mitchell's solution, the internal friction angle of the backfill column can be nonzero, the contact between the backfill column and the unexposed surrounding walls

can be nonnegligible, and the interface cohesion can be considered a part of the cohesion of the backfill column. Meanwhile, A factor of safety (FS) is introduced to evaluate the backfill column stability, calculated as the resistance force's and driving force's ratio on the failure plane (Li and Aubertin, 2012). Fig. 8.1 shows the schematic diagram of a typical vertical backfill column, of which the front sidewall is exposed to the adjacent extracted stope. H, B, and L are the height, width, and length of the backfill column, respectively. H_r is the height of the main backfill column with a unit weight of γ, a cohesion of c, and an internal friction angle of φ. H_p is the height of the backfill column plug with a unit weight of γ_p, a cohesion of c_p, and an internal friction angle of φ_p. p_o is the surcharge pressure that acts on the top surface of the backfill column.

For the failure plane of the backfill column, two possibilities can be considered due to the difference in the mechanical properties of the two parts of the backfill column. One is the failure plane that entirely falls in the part of the backfill column plug, and the other one is the failure plane intersects with the interface between the main backfill column part and the backfill column plug. It must be mentioned that, in this study, the mechanical properties of the backfill column plug are assumed to be the same as the main backfill column part. Thus, the cohesion (c_p) of the backfill column plug can be equal to the main backfill column part (c_f), and the cohesion at the interface between the backfill column and the surrounding walls (c_i) is assumed to be a portion of the backfill column's cohesion (c):

$$c_p = r_p c_f = c \qquad \textbf{(Eq. 8.1)}$$

$$c_{if} = c_{ip} = r_{if}c_f = r_{ip}c_p = c_i = r_i c \quad \textbf{(Eq. 8.2)}$$

where c_{if} and c_{ip} are the cohesions at the interfaces between the surrounding walls and the corresponding backfill column part and backfill column plug, respectively. r_p, r_{if}, r_{ip}, and r_i are the corresponding proportion coefficients for the interface cohesions.

When the failure plane entirely falls in the backfill column plug, then the net weight of the wedge block above the failure plane (W_n) can be given as:

$$W_n = p_o BL + (\gamma L - 2c_{if})H_f B + (\gamma_p L - 2c_{ip})H^r B \quad \textbf{(Eq. 8.3)}$$

where the reference height H^r is given by:

$$H^r = H_p - H_s - \frac{B \tan \alpha}{2} \quad \textbf{(Eq. 8.4)}$$

According to Mitchell's analytical model, a factor of safety (FS) is introduced to evaluate the stability of the backfill column by considering the stress equilibrium of the wedge block. It is defined as the ratio between the resisting forces and the driving forces on the failure plane. In the situation that the failure plane of the backfill column entirely falls in the backfill column plug, the FS can be deduced as:

$$FS = \frac{F_r}{F_d} = \frac{\tan \varphi}{\tan \alpha} + \frac{2c_p LB}{W_n \sin 2\alpha} = \frac{\tan \varphi}{\tan \alpha} + \frac{2r_p c}{p_n \sin 2\alpha} \quad \textbf{(Eq. 8.5)}$$

In this equation, α is the angle between the failure and horizontal planes in the backfill column. The sub-term of α and p_n are given as:

$$\alpha = 45° + \frac{\phi}{2} \quad \textbf{(Eq. 8.6)}$$

$$p_n = p_o + \left(\gamma - \frac{2r_{if}c}{L}\right)H_f + \left(\gamma_p - \frac{2r_{ip}r_p c}{L}\right)H^r \quad \textbf{(Eq. 8.7)}$$

Meanwhile, in this situation, the required cohesion c_r of the backfill column is given by:

$$2c_r = \frac{p_o + \gamma H_f + \gamma_p H^r}{\frac{\gamma_p}{(FS - \tan\phi/\tan\alpha)\sin 2\alpha} + \gamma_{if}\frac{H_f}{L} + r_{ip}r_p\frac{H^r}{L}} \quad \textbf{(Eq. 8.8)}$$

The second possibility is that the failure plane of the backfill column intersects with the interface between the main backfill column part and the backfill column plug. In this situation, the net weight of the wedge block above the failure plane (W_n) can be given as:

$$W_n = p_o BL + (\gamma L - 2c_{if})BH^R + (\gamma_p L - 2c_{ip})\frac{(H_p - H_s)^2}{2\tan\alpha} \quad \textbf{(Eq. 8.9)}$$

where the reference height H^R is given by:

$$H^R = H_f - \frac{(B\tan\alpha - H_p + H_s)^2}{2B\tan\alpha} \quad \textbf{(Eq. 8.10)}$$

In this situation, considering the stress equilibrium of the wedge block in the tangential and perpendicular directions along the failure plane of the backfill column, the FS can be deduced as:

$$FS = \frac{\tan\phi}{\tan\alpha} + \frac{c}{\sin^2\alpha}\frac{\tan\alpha + (r_p - 1)\frac{H_p - H_s}{B}}{p_o + \left(\gamma - \frac{2r_{if}}{L}c\right)H^R + \left(\gamma_p - \frac{2r_{ip}r_p}{L}c\right)\frac{(H_p - H_s)^2}{2B\tan\alpha}} \quad \textbf{(Eq. 8.11)}$$

Meanwhile, in this situation, the required cohesion c_r of the backfill column is given by:

$$c_r = \frac{p_o + \gamma H^R + \gamma_p \dfrac{\left(H_p - H_s\right)^2}{2B\tan\alpha}}{\dfrac{\tan\alpha + \left(r_p - 1\right)\dfrac{H_p - H_s}{B}}{\left(FS - \dfrac{\tan\phi}{\tan\alpha}\right)\sin^2\alpha} + \dfrac{2}{L}\left[r_{ij}H^R + r_{ip}r_p\dfrac{\left(H_p - H_s\right)^2}{2B\tan\alpha}\right]} \qquad \textbf{(Eq. 8.12)}$$

If the backfill column plug has the same mechanical properties as the main backfill column part, then the FS and the required cohesion of the backfill column in the two failure possibilities inside the backfill column can be simplified to:

$$FS = \frac{\tan\phi}{\tan\alpha} + \frac{2c}{p_o + \left(\gamma - \dfrac{2r_{if}c}{L}\right)\left(H - \dfrac{B\tan\alpha}{2}\right)\sin\alpha} \qquad \textbf{(Eq. 8.13)}$$

$$2c_r = \frac{p_o + \gamma\left(H - \dfrac{B\tan\alpha}{2}\right)}{\left[\left(FS - \dfrac{\tan\phi}{\tan\alpha}\right)\sin 2\alpha\right]^{-1} + \dfrac{r_{if}}{L}\left(H - \dfrac{B\tan\alpha}{2}\right)} \qquad \textbf{(Eq. 8.14)}$$

Thus, the required uniaxial compressive strength, $(UCS)_r$, can be expressed from the Mohr-Coulomb strength criterion by introducing the required cohesion of the backfill column:

$$(UCS)_r = 2c\tan\left(45° + \frac{\phi}{2}\right) \qquad \textbf{(Eq. 8.15)}$$

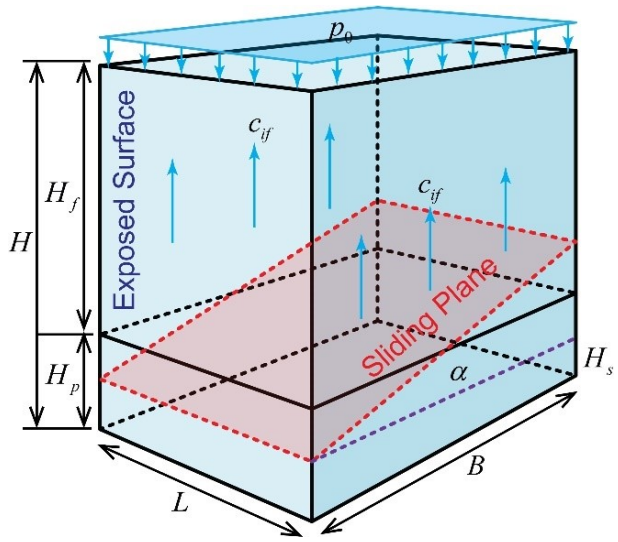

Fig. 8.1 Interaction between a typical cemented backfill column with an exposed sidewall and the surrounding rocks.

8.3 Numerical simulation

8.3.1 Model establishment

Fig. 8.2 shows the geometry, boundary conditions, and establishment procedure of the three-dimensional coupled FD-DE model of multiple stopes backfilled with the CRF columns, which were constructed in Itasca software FLAC3D and PFC3D. In this study, the dimensions, mechanical properties, boundary conditions, and geo-stress balance of the FD model of the orebody (surrounding rocks) are the same as those descriptions of the FD model of the surrounding rocks in Chapter 7. The dimensions of the FD model are large enough to eliminate the scale effect from the boundary conditions efficiently, and then the mechanical properties of kimberlite rock listed in Table 5.1 in Chapter 5 were assigned to the FD model of the surrounding rocks directly. Each stope, excavated in the FD model according to the mining/backfilling sequence at the hard rock mine, has the same dimensions as the single stope described in Chapter 7.

As shown in Fig. 8.2b, in the coupled FD-DE model of the multiple backfilled stopes, there are three primary and two secondary stopes. The mining/backfilling activities in the coupled FD-DE model were executed in 7 stages, as indicated in Fig. 8.2b. First, the primary stope A was extracted and backfilled with the CRF column A (stage 1 and stage 2), and then the primary stope B and C were mined-out and backfilled with the CRF columns B and C, sequentially (stage 3 to stage 6). Finally, the secondary stope D and E were excavated (stage 7), leading the CRF column A to stand alone without support from adjacent rock pillars. Meanwhile, a constant quasi-static displacement rate of 0.5 mm/min was added on the top surface of the DE model of the CRF column A, B and C, respectively, after the stope D and E was extracted, to study the stability of the CRF columns subjected to different numbers of exposed sidewalls. In addition, two groups of the mechanical properties of the CRF material, which are listed in Table 8.1, were assigned to the DE model of the CRF columns to study the effect of the strength characteristics on the fracture development and failure pattern of the columns. During these stages of the mining/backfilling sequence, the stress and displacement redistribution were measured and recorded along the predefined monitoring points, lines, and cross-sections in both the DE model of the CRF columns and the FD model of the surrounding rocks, which are marked in Fig. 8.2c to Fig. 8.2d.

Table 8.1 Physical-mechanical properties of the CRF columns.

Category	With the average uniaxial compressive strength	With the lowest compressive strength
Unit weight (MN/m³)	0.028	0.028
Young's modulus (GPa)	4.45	3.00

Poisson's ratio	0.24	0.24
Uniaxial compressive strength (MPa)	6.69	4.95

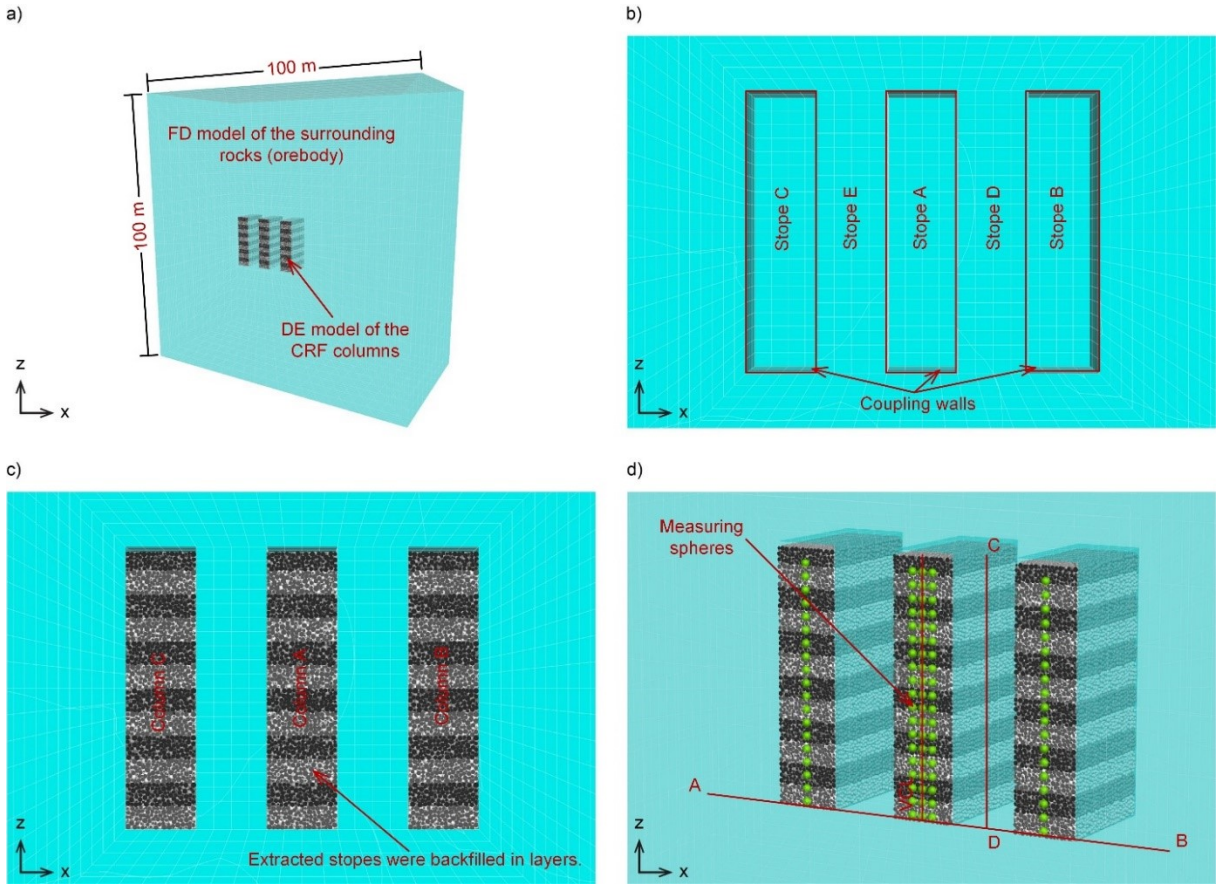

Fig. 8.2 Coupled FD-DE model of multiple stopes backfilled with the CRF columns: a) perspective view, b) mining sequence, c) backfilling sequence and d) measuring method.

8.3.2 Parameter determination

For the FD model of the surrounding rocks, the Mohr-Coulomb constitutive model was applied, and the mechanical properties listed in Table 5.1 in Chapter 5 were directly assigned to the FD model. For the DE model of the CRF columns, firstly, a series of numerical uniaxial and triaxial compression tests were conducted on the DE model of the

CRF specimens, which were generated according to the simplified particle size distribution to determine the microstructural parameters in the parallel bond (PB) contact model. These numerical tests can ensure the overall mechanical properties and stress-strain behaviour of the DE model are the same as the real CRF specimens in the laboratory. Next, the discrete particles of the DE model of the CRF columns were generated in layers with a simplified particle size distribution using the particle diameter scaling method. As a result, a total of 226,977 discrete particles were generated, with diameters ranging from 0.18 m to 0.3 m, and the DE model of the CRF columns was simulated to have a natural lateral earth pressure state. And then, these determined microstructural parameters, which were listed in Table 4.2 in Chapter 4, were assigned to the PB contact model among the discrete particles of the DE model of the CRF columns. Meanwhile, numerical the direct shear tests on the coupled FD-DE model of the combined rock-cemented rockfill (R-CRF) specimens were designed to determine the microstructural parameters at the interfaces between the DE model of the CRF columns and the FD model of the surrounding rocks (Wei et al., 2022). As a result, the microstructural parameters of the interfaces in the coupled FD-DE model of multiple backfilled stopes have been determined and listed in Table 5.3 in Chapter 5.

8.4 Results and discussion

8.4.1 Stress and displacement distribution in the DE model of the CRF columns

Fig. 8.3 shows the stress distribution along the VCL of the DE model of the CRF column A during the mining/backfilling sequence of stope B to E. It indicates that the primary/secondary manner of the mining/backfilling activities can significantly influence the stress states in the CRF columns at different stages in the sequence. At stage 2, the

discrete particles of the DE model of the CRF column A were placed into the extracted stope A by layers. At the natural lateral earth pressure state, as the PB contact model which was applied among the discrete particles was activated, the horizontal (σ_{xx}^{a}) and vertical stresses (σ_{zz}^{a}) in the x- and z- directions, respectively, increased along the VCL of column A, due to multiple stages of compression and consolidation under the overburden pressure from the overlying CRF layers. However, at a random depth of column A, the σ_{xx}^{a} and σ_{zz}^{a} were smaller than the corresponding natural lateral earth pressure (p_h) and overburden pressure (p_v), respectively, due to the shear effect at the interfaces between the DE model of the CRF column A and the FD model of the surrounding rocks.

At stage 3, as the adjacent stope B was extracted, σ_{xx}^{a} along the VCL of the DE model of the CRF column A decreased since the rock pillar D tended to bend to the extracted stope B, which led to the decrease in the confining pressure at the interface between the DE model of the CRF column A and the FD model of the stope D. As can be seen from Fig 8.3a that at the shallow depth, along the VCL of column A, σ_{xx}^{a} decreased to zero, showing an at-rest lateral earth pressure state, and at the middle height, σ_{xx}^{a} became tensile, indicating a more unstable lateral earth pressure state. It also shows that the excavation of stope B hastened column A to transfer from active to at-rest lateral earth pressure state, especially at the shallow and middle height of the column. Meanwhile, as can be seen from Fig. 8.3b, along the VCL of column A, σ_{zz}^{a} increased during stage 3 since the excavation of stope B accelerated the downtrend movement of the discrete particles of column A and weakened the shear effect at the interface between column A and stope D.

During stage 4, the excavated stope B was backfilled, σ_{xx}^{a} along the VCL of the DE model of the CRF column A increased significantly, especially at the shallow and middle depth,

since backfilling the stope B recovered part of the horizontal elastic strain that was stored in the rock pillar D. But σ_{xx}^{a} along the VCL of the column, A can never recover to its original value and lateral earth pressure state before the excavation of stope B. Meanwhile, σ_{zz}^{a} almost decreased to its original value and stress state before the excavation of stope B, since that backfilling the stope B contributed to the increase in the confining pressure and shear stress at the interface between the column A and the stope D. At the stage 5 and stage 6, the law of the stress redistribution along the VCL of the DE model of the CRF column A are similar to the stage 3 and stage 4. As stope C was excavated and backfilled, σ_{xx}^{a} Increased positively as tensile stress and then decreased slightly to around zero, especially at the shallow and middle height of column A, and σ_{zz}^{a} Increased firstly and then decreased. However, neither σ_{xx}^{a} and σ_{zz}^{a} can recover to its original value and stress state before the excavation of stope C due to the realization of the elastic strain stored in the rock pillar E. However, it also indicates that at stage 5, the CRF column A DE model can have the worst stability condition due to the further development of tensile stress zones, especially at the shallow and middle height of the column.

As can be seen in Fig. 8.3, at stage 7, rock pillars in the stope D and E were extracted at the same time, and significant stress redistribution can be found both in σ_{xx}^{a} and σ_{zz}^{a} along the VCL of the DE model of the CRF column A. During stage 7, σ_{xx}^{a} decreased to zero, especially at column A's shallow and middle depth, due to the disappearance of the confining pressure and supporting effect from the adjacent rock pillars. Meanwhile, σ_{zz}^{a} increased significantly to the overburden pressure (p_v), which is only related to the density and height of the column, due to the disappearance of the resistance from the shear effect at the interfaces between the column A and the stope D and stope E.

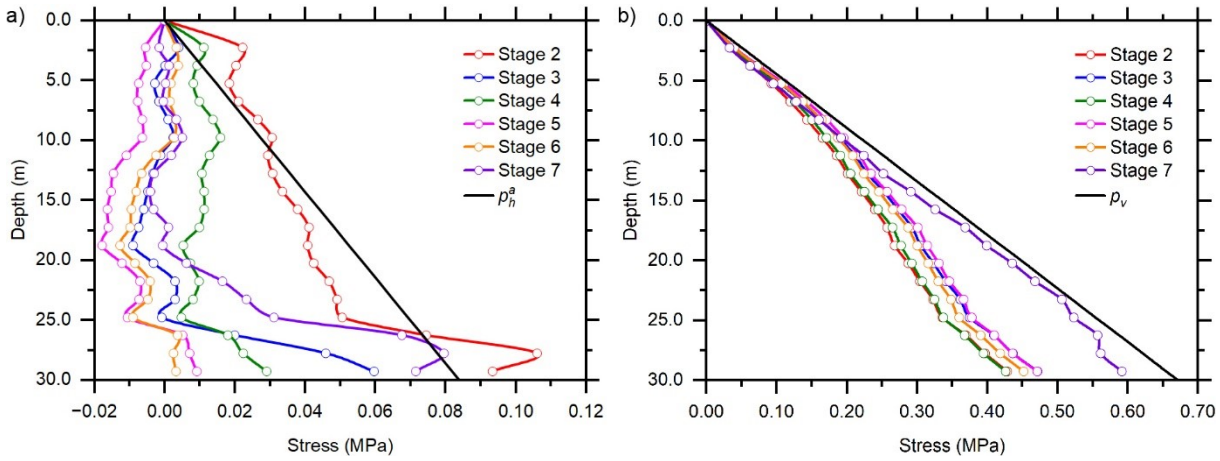

Fig. 8.3 Stress distribution along the VCL of the DE model of the CRF column A at the natural lateral earth pressure state during the mining/backfilling sequence of the stope B to E: a) σ_{xx}^a, and b) σ_{zz}^a.

Fig. 8.4 shows the effect of stope D and E mining sequence on the displacement distribution at the CCS of the DE model of the CRF columns. At the natural lateral earth pressure state, before the stope D and E were extracted, the arching phenomenon can be observed in the DE model of the CRF columns A, B, and C, due to the shear effect at the interfaces between the DE model of the CRF columns and the FD model of the surrounding rocks. Thus, the distribution of the displacement in the z-direction (d_{zz}^a) in all three columns can show as concaved-down shape arches, since d_{zz}^a was larger at the locations near the VCLs of the columns and smaller at the locations near the surrounding rocks. However, along the VCLs of the columns, d_{zz}^a in column A was slightly larger than the columns B and C at the same height due to the irreversible downtrend movement and settlement of the discrete particles during the mining/backfilling process of stope B and C. Along the VCLs of the DE model of the CRF columns, d_{xx}^a at the bottom part of the

column, A was slightly larger than columns B and C at the same location due to a further expansion of the column width during the mining/backfilling process of stope B and C.

Fig. 8.4b shows that the mining sequence of stope D and E significantly influences the displacement distribution at the CCS of the DE model of the CRF columns. After the excavation of the stope D and E, the confining pressure and supporting effect from the adjacent rock pillars to the CRF columns disappeared, resulting in the disappearance of the shear effect at the interfaces between the DE model of the CRF columns and the FD model of the surrounding rocks. Thus, a further downtrend movement and settlement of the discrete particles in the columns occurred, leading to an increase in d_{zz}^{a} in the columns, especially the parts near the extracted stope D and E. Meanwhile, after the excavation of D and E, the DE model of the CRF columns A, B, and C all tended to slide into the adjacent mined-out area, leading to an increase in d_{xx}^{a}, especially at the shallow and middle parts of the columns. It shows that the excavation of stope D and E reduced the stability of the columns, leading to the formation of the potential failure planes in the DE model of the CRF columns.

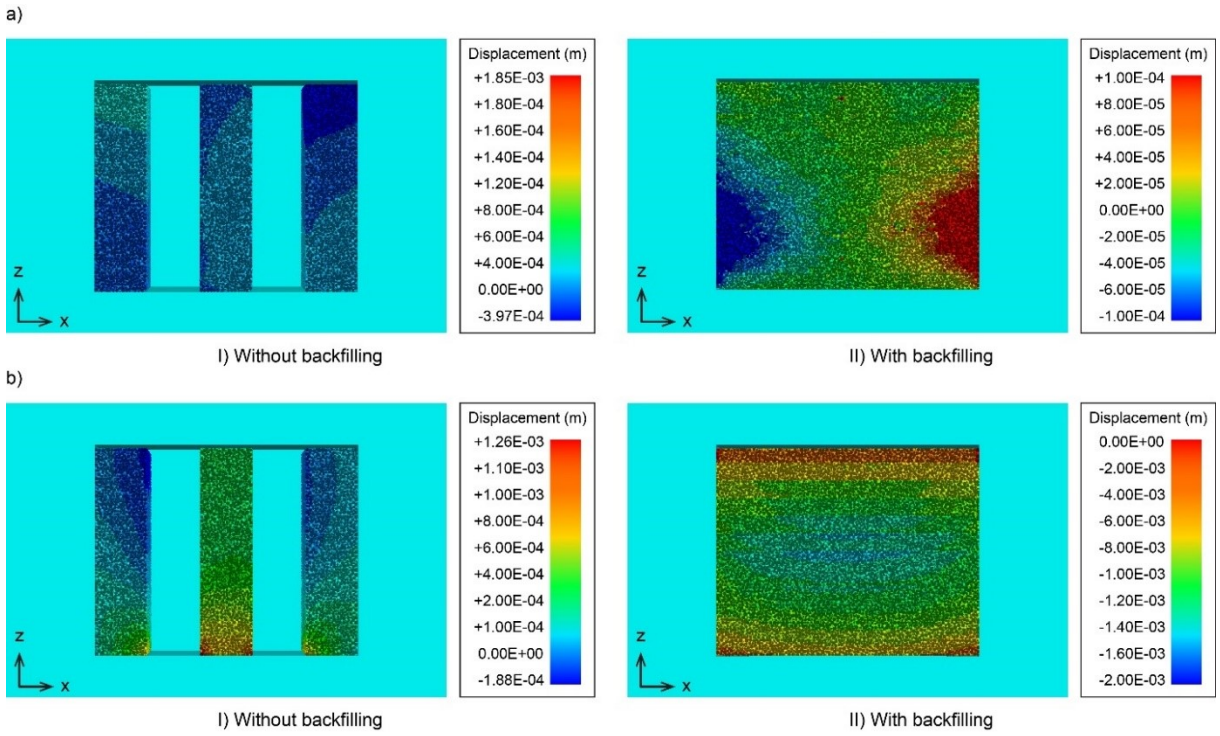

Fig. 8.4 Effect of the mining/backfilling sequence of the stope D to E on the displacement distribution at the CCS of the DE model of the CRF columns at the natural lateral earth pressure state: a) d_{xx}^{a} on the xz-plane, and b) d_{zz}^{a} on the xz-plane.

Fig. 8.5 and Fig. 8.6 show the failure pattern, fragment and force chains development of the DE model of the CRF columns with different mechanical properties and different numbers of the exposed sidewalls under the constant displacement control at the top surface of the columns. It should be mentioned here that the colour of the discrete particles in the DE model of the CRF columns indicates the order in which the fragments appear, and the green and blue colour indicates the tension and compression contact forces, respectively, in the parallel bond between two discrete particles in the DE model of the CRF columns. The modelling results show that when the adjacent stope was extracted, the DE model of the CRF columns with the average and the lowest UCS values were strong enough to stand steadily under the overburdened pressure from their self-

weight. It indicates that although naturally, the UCS of different parts of the CRF columns distributes dispersedly from 4.95 MPa to 8.78 MPa, which was discussed in Chapter 3, the CRF columns at the hard rock mine can still maintain stability, and no potential failure risk occurs.

And then, as the constant displacement rate was added at the top surface of the DE model of the CRF columns, the extra overburden pressure was loaded until the column reached its critical failure state. Fig. 8.5 shows that the DE model of the CRF columns B and C, which were with one exposed sidewall to the adjacent mined-out area, both have the same failure pattern of sliding shear mode, while the columns with the lowest UCS value reached failure faster due to its weaker load-bearing capacity. In the beginning, both columns B and C tended to slide into the adjacent extracted stope, and then the fragment started to develop from the foot end of the columns and gradually formed a wedge block. As the extra overburden pressure loaded on the top of the columns increased, the wedge block started to fall off from the failure plane, which appeared in both the columns, with average failure angles of 66.5 ^{o} and 65.2^{o}, respectively, for the columns with average and the lowest UCS. According to the modified Mitchell's analytical model, the calculated failure angle of the failure plane is 70.5^{o}, which is very close to the observation on the two kinds of DE model of the CRF columns, with an average error of 6.6%.

Meanwhile, if the FS was assumed to be 1, the required cohesion and the required UCS of the CRF columns were calculated as 0.088 MPa and 0.5 MPa, respectively, which were much smaller than the lowest UCS from the laboratory test results. For the DE model of the CRF column A, which was with two exposed sidewalls to the adjacent extracted stope D and E, the failure was in the 'X' shear mode at the shallow depth of the column during

the loading of the overburden pressure on the top surface of the column. The modelling and calculation results indicate that the CRF columns at the hard rock mine have an excellent stability condition and no potential failure risks exist even though the segregation phenomenon was found in the CRF columns, leading to the dispersed distribution of the UCS of different parts of the CRF columns.

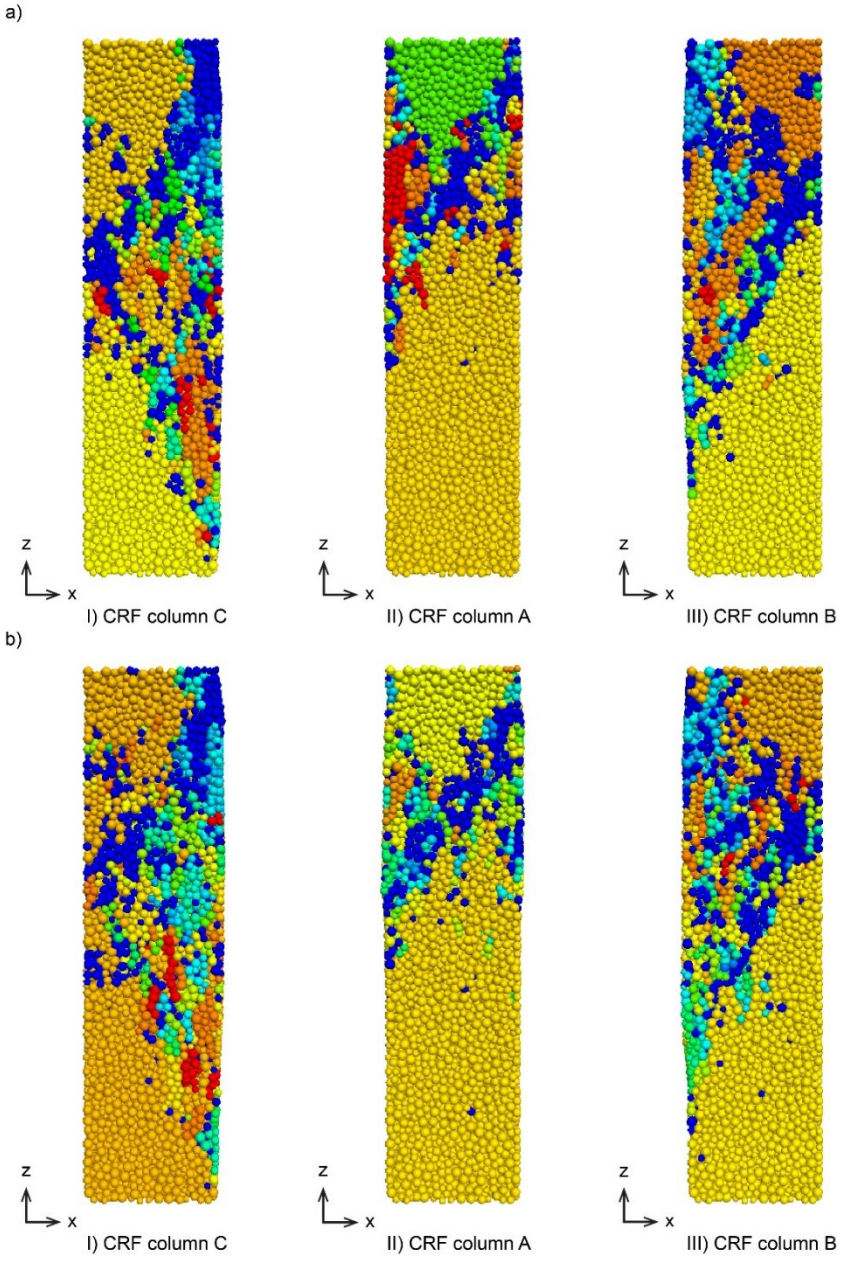

Fig. 8.5 Failure pattern of the DE model of the CRF columns with a) average UCS and b) lowest UCS, subjected to the overburden pressure.

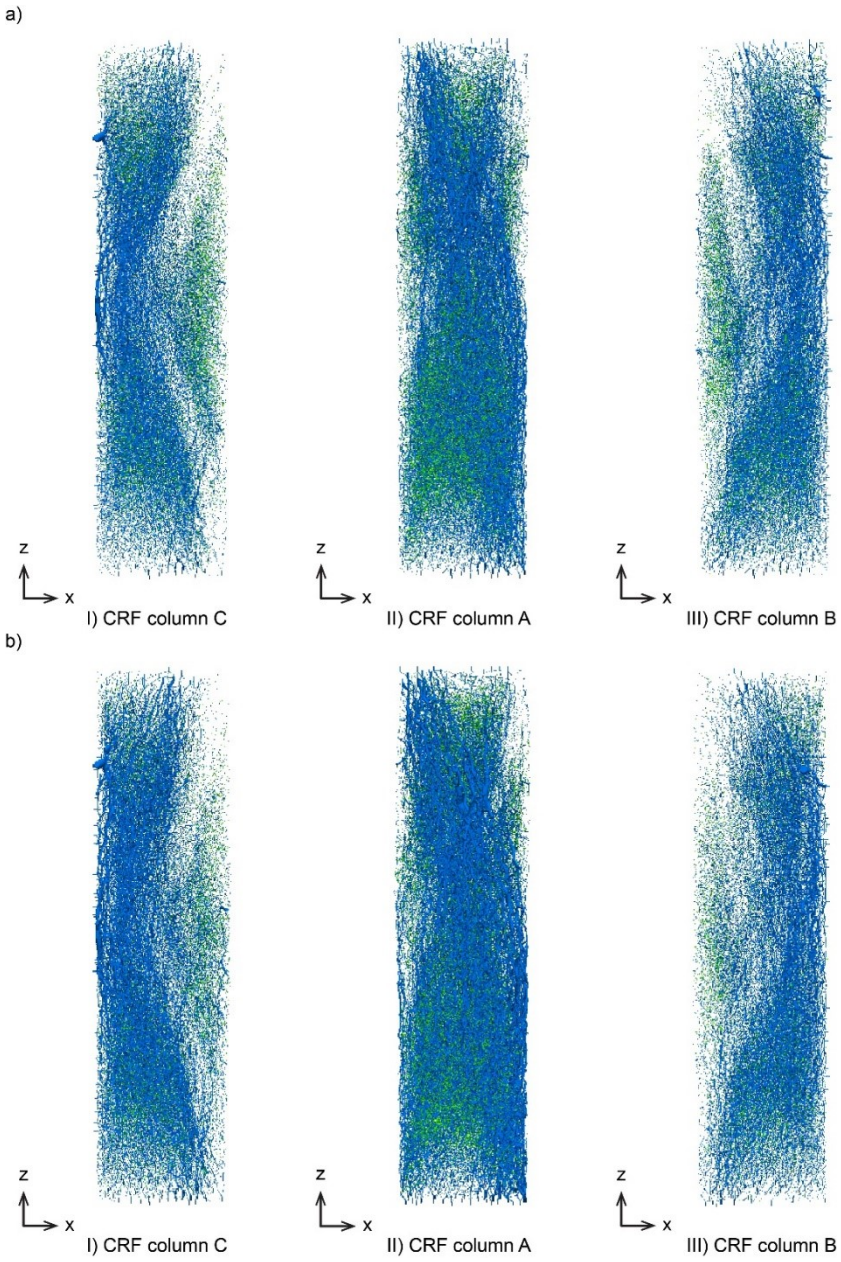

Fig. 8.6 Force chain of σ_n^c at the CCS of the DE model of the CRF columns with a) average UCS and b) lowest UCS, subjected to the overburden pressure.

8.4.2 Stress and displacement distribution in the FD model of the surrounding rocks

Fig. 8.7 and Fig. 8.8 present the distribution of the maximum principal stress (σ_m^a) along the monitoring lines and at the CCS of the coupled FD-DE model of the multiple backfilled stopes, which was influenced by the mining/backfilling sequence. Fig. 8.7a shows the distribution of σ_m^a along the monitoring line AB in the FD model of the surrounding rocks at the natural lateral earth pressure state during the mining/backfilling sequence of the stope A to E. During stage 1, stope A was excavated and stress concentration zones of σ_m^a were formed at the bottom corners of stope A. During stage 2, stope A was backfilled with the DE model of the CRF column A, and σ_m^a at the bottom corners of the stope, A decreased by 2.6%. As the stope B was excavated in stage 3, σ_m^a at the bottom corners of the stope A and B both increased again. However, due to the supporting effect from column A to the adjacent rock pillars, σ_m^a at the left bottom corner of the stope, A was 10.6% smaller than σ_m^a at the right bottom corner of stope B. And then, the stope B was backfilled with the column B in stage 4, and σ_m^a at the bottom right corner of the stope, B decreased by 2.5%.

The effect of the mining/backfilling sequence of the stope C on the distribution of σ_m^a along the monitoring line, AB is very similar to stope B due to the symmetric geometry of the coupled FD-DE model of the multiple backfilled stopes. During stage 5, stope C was excavated, and σ_m^a at all bottom corners of the columns increased, while σ_m^a at the right bottom corner of the stope B was 2.4% smaller than σ_m^a at the left bottom corner of stope C, due to the supporting effect from columns A and B. And then, stope C was backfilled with the column C in stage 6, and σ_m^aat the left bottom corner of the stope, C decreased by 2.5%.

Fig. 8.7b shows that the mining/backfilling sequence of the stope A to E has a significant influence on the distribution of σ_m^a along the monitoring line CD in the rock pillar E (stope E) in the FD model of the surrounding rocks at the natural lateral earth pressure state. Before the mining/backfilling activities in the FD model of the orebody, σ_m^a along the monitoring line CD in the stope E can be only related to the unit weight of the rock mass. At the stage 1, the stress concentration zones of σ_m^a formed at the top and bottom corners of the stope E due to the excavation of stope A. And then, σ_m^a decreased slightly during the stage B when stope A was backfilled with the DE model of CRF column A. At stage 3 the stope B was excavated, σ_m^a along the monitoring line CD increased significantly since the right sidewall of the stope E was exposed and the sudden increase in the overburden pressure at the top of the rock pillar E. Next, backfilling the stope B contributed to the decrease in σ_m^a at the bottom of the rock pillar E, while σ_m^a at the shallow depth of the pillar increased slightly. The mining/backfilling sequence of the stope C can have a similar effect on the distribution of σ_m^a along the monitoring line CD in stope E, compared with stope B, the effect can be smaller due to a farther distance. Fig. 8.7 and Fig 8.8 also indicate that backfilling the multiple stopes with the CRF columns can provide the confining pressure and supporting effect to the adjacent rock pillars and shrink the stress concentration zones improve the stability and the stress distribution state at the mined-out area.

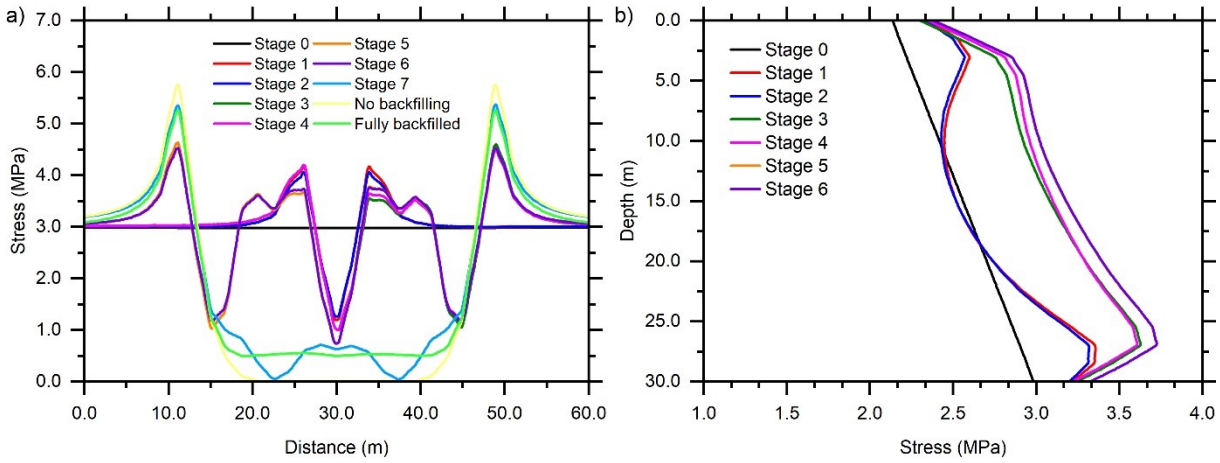

Fig. 8.7 Distribution of σ_m^a along the monitoring lines in the FD model of the surrounding rocks at the natural lateral earth pressure state during the mining/backfilling sequence of the stope A to E: a) monitoring line AB, and b) monitoring line CD.

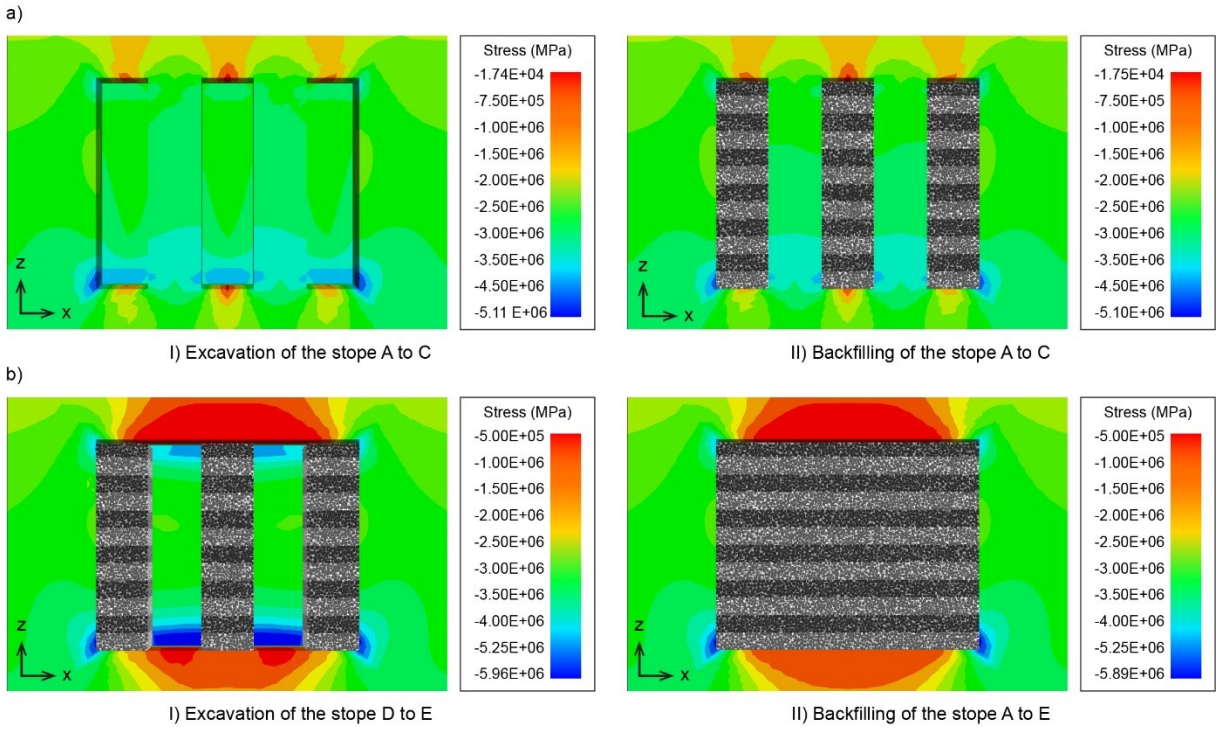

Fig. 8.8 Effect of the mining/backfilling sequence of a) stope A to C, and b) stope D to E, on the distribution of σ_m^a at the CCS of the FD model of the surrounding rocks at the natural lateral earth pressure state.

Fig. 8.9 presents the displacement distribution at the CCS of the FD model of the surrounding rocks at the natural lateral earth pressure with or without the stope A to C were backfilled. Fig. 8.9a indicates that at the natural lateral earth pressure state, the rock pillars D and E (stope D and E) tend to slide into the adjacent mined-out area. For the multiple stopes that were backfilled with the CRF columns, d_{xx}^{a} The stope D and E were smaller than the multiple stopes backfilled with the CRF columns, especially at the middle and bottom part of the rock pillars, leading to a lower failure risk. Fig. 8.9b and Fig. 8.9c show that as the stope A to C were backfilled, d_{zz}^{a} and d_{m}^{a} at the top part of the rock pillars, D and E slightly increased, while d_{zz}^{a} and d_{m}^{a} at the bottom of the multiple backfilled stopes decreased, compared with the multiple stopes that were not backfilled with the CRF columns.

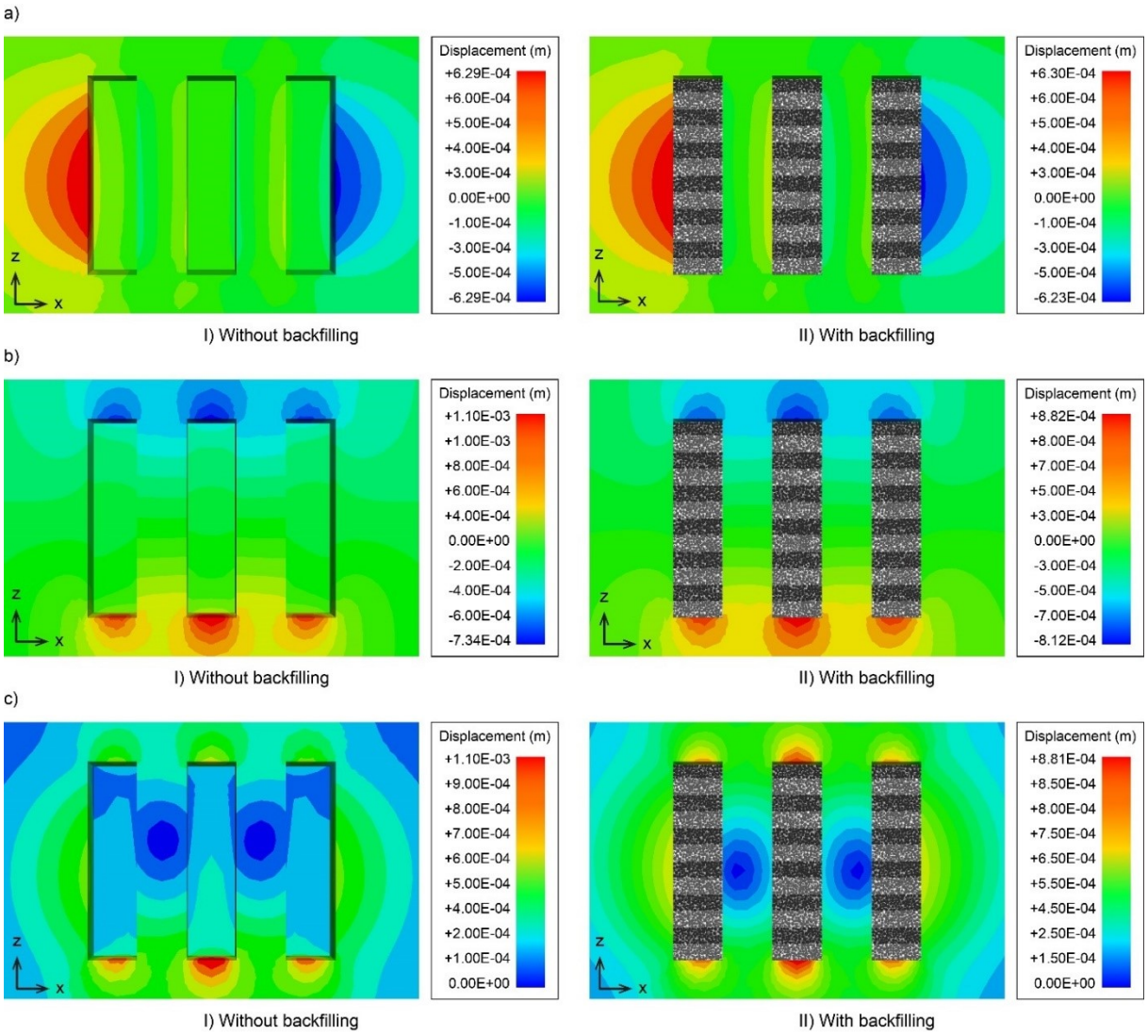

Fig. 8.9 Effect of the mining/backfilling sequence of the stope A to C on the displacement distribution at the CCS of the FD model of the surrounding rocks at the natural lateral earth pressure state: a) d_{xx}^{a} on the xz-plane, b) d_{zz}^{a} on the xz-plane, and c) d_{m}^{a} on the xz-plane.

Fig. 8.10 depicts the comparison of the displacement distribution at the CCS of the FD model of the surrounding rocks between the multiple stopes that were involved or not involved in backfilling activities during the mining/backfilling sequence. Fig. 8.10a shows that the as the multiple stopes were backfilled sequentially during the stage 1 to 7, d_{xx}^{a} in

the FD model, the surrounding rocks, especially at the lateral walls of stope 2 and 3, were smaller than the multiples stopes without backfilling activities at the natural lateral earth pressure state due to the confining pressure and supporting effect that were provided by the CRF column B and C. Fig. 8.10b and Fig. 8.10c show that as the multiple stopes were backfilled, d_{zz}^{a} and d_{m}^{a} at the roof of the FD model of the surrounding rocks have minimal changes, while d_{zz}^{a} and d_{m}^{a} at the bottom of the multiple backfilled stopes decreased, compared with the multiple stopes that were not backfilled with the CRF columns.

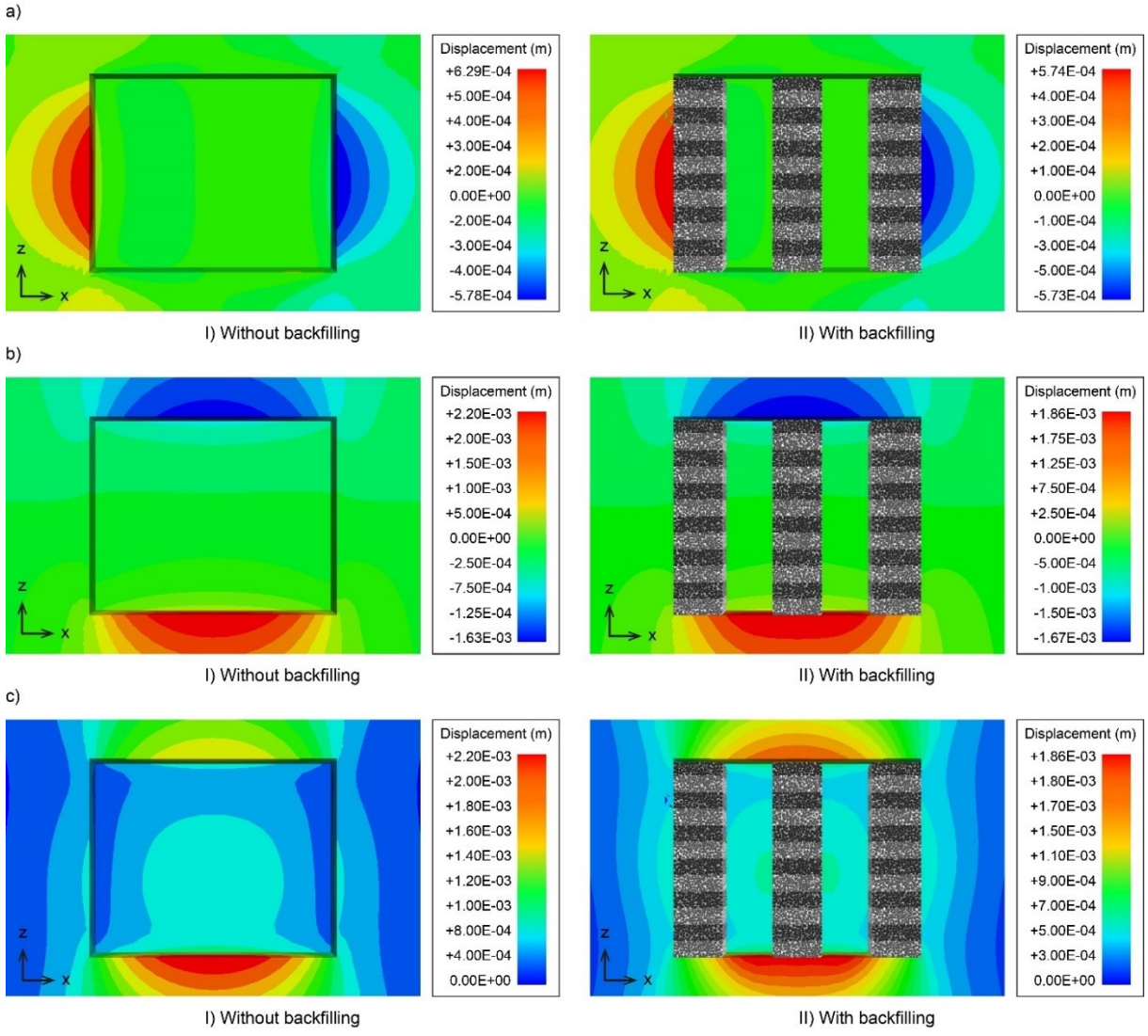

Fig. 8.10 Effect of the mining/backfilling sequence of the stope D to E on the displacement distribution at the CCS of the FD model of the surrounding rocks at the natural lateral earth pressure state: a) d_{xx}^{a} on the xz-plane, b) d_{zz}^{a} on the xz-plane, and c) d_{m}^{a} on the xz-plane.

8.5 Conclusions

In this study, the coupled finite difference (FD) and discrete element (DE) method were successfully used to simulate multiple underground stopes backfilled with the cemented rockfill (CRF) columns, considering the frictional-bonded interfaces between the CRF columns and the surrounding rocks, and the primary/secondary manner of the mining/backfilling activities. The modelling results indicate that the stress and displacement distribution in the CRF columns and around the surrounding rocks can be significantly influenced by the mining/backfilling sequence, leading to changes in the stability conditions at the multiple backfilled stopes. As a result, backfilling the multiple stopes with the CRF columns can decrease the maximum principal stress in the surrounding rocks, shrink the stress concentration zones occurring at the corners of the stopes, provide extra confining pressure and supporting effect to the adjacent rock pillars, and reduce the risk and potential damage from the overburden pressure to the underground mined-out area.

Chapter 9 Conclusions and recommendations

Five main conclusions can be summarized and highlighted here based on the laboratory test and numerical modelling results discussed in Chapters 3 to 8 in this thesis. Firstly, the strength characteristics and deformation properties of the field CRF material are heterogeneous at different parts of the CRF column, resulting from the segregation phenomenon during the settlement and consolidation processes of the CRF material due to the effects of the particle size distribution field curing conditions, and the workability of the CRF material. Secondly, the discrete element (DE) method, a discontinuum modelling approach, is verified to be feasible to simulate the elastoplastic behaviour of the CRF material, especially at the post-failure stage, by applying the parallel bond (PB) contact model and particle size scaling method. Thirdly, running the new-designed direct shear test on the coupled finite difference (FD) and discrete element (DE) model of the combined rock-cemented rockfill (R-CRF) specimen is verified to be an imperative step to determine the microstructural parameters of the PB contact model applied at the frictional-bonded interfaces between the CRF columns and the surrounding rocks. Fourthly, the stress and displacement distribution at the underground backfilled stopes is significantly influenced by the arching phenomenon, resulting from the shear effect at the interfaces between the CRF columns and the surrounding rocks. Next, the stress and displacement distribution at the underground backfilled stopes is significantly influenced by the primary/secondary manner of the mining/backfilling activities, leading to different stability conditions at different stages of the mining/backfilling sequence. It is verified that backfilling the underground stopes with the CRF columns can efficiently improve the

stress state and enhance the stability of the adjacent mining area. Finally, the coupled FD-DE method is proved to be an advanced hybrid discontinuum-continuum approach, with higher computation efficiency and precision, to simulate the mechanical interaction between different geo-materials involved with frictional, cohesive and bonded interfaces.

Meanwhile, three main aspects in the future work can be drawn here by comparing this research to the reality of the mining/backfilling activities at the Canadian hard rock mine. First, the determination of the microstructural parameters of the PB contact model at the interfaces with irregular profile shapes, different meshing sizes and numbers in the coupled FD-DE model of the underground stopes backfilled with the CRF columns. Second, the simulation of the CRF columns cured under the field conditions with the DE method by generating the discrete particles with different shapes, contacts and compositions. Thirdly, simulating the real-scale underground mined-out area backfilled with the CRF columns at the hard rock mine by connecting the Itasca software FLAC3D and PFC3D to the supercomputer with high computation efficiency.

Bibliography

Sivakugan, N., Rankine, R.M., Rankine, K.J. and Rankine, K.S., 2006. Geotechnical considerations in mine backfilling in Australia. Journal of Cleaner Production, 14(12-13), pp.1168-1175.

Abdellah, W.R.E., Hefni, M.A. and Ahmed, H.M., 2020. Factors influencing stope hanging wall stability and ore dilution in narrow-vein deposits: part 1. Geotechnical and Geological Engineering, 38(2), pp.1451-1470.

Al Heib, M.M., Didier, C. and Masrouri, F., 2010. Improving short-and long-term stability of underground gypsum mine using partial and total backfill. Rock mechanics and rock engineering, 43(4), pp.447-461.

Apel, Z., Vafaeian, B., Apel, D.B. and Hussain, A., 2021. Occlusal Stresses in Beveled versus Non-beveled Tooth Preparation. Biomedical Engineering Advances, p.100010.

ASTM, C., 2012. Standard test method for compressive strength of cylindrical concrete specimens. Chủ biên.

Aubertin, M., Li, L.S.T.B.M., Arnoldi, S., Belem, T., Bussière, B., Benzaazoua, M. and Simon, R., 2003. Interaction between backfill and rock mass in narrow stopes. Soil and rock America, 1(2), pp.1157-1164.

Bahaaddini, M., Hagan, P.C., Mitra, R. and Hebblewhite, B.K., 2015. Parametric study of smooth joint parameters on the shear behaviour of rock joints. Rock Mechanics and Rock Engineering, 48(3), pp.923-940.

Bahaaddini, M., Sharrock, G. and Hebblewhite, B.K., 2013. Numerical the direct shear tests to model the shear behaviour of rock joints. Computers and Geotechnics, 51, pp.101-115.

Bahaaddini, M., Sharrock, G., Hebblewhite, B.K. and Mitra, R., 2012, June. The direct shear tests to model the shear behavior of rock joints by PFC2D. In 46th US Rock Mechanics/Geomechanics Symposium. OnePetro.

Behera, S.K., Prashant, C.N., Mishra, D.P., Mandal, P.K., Verma, A., Mohanty, S., Mishra, K. and Singh, P.K., 2019. Slump test: laboratory and numerical simulation-based approach for consistency of mill tailings paste. Current Science, 117(2), p.235.

Belem, T. and Benzaazoua, M., 2008. Design and application of underground mine paste backfill technology. Geotechnical and Geological Engineering, 26(2), pp.147-174.

Belem, T., Benzaazoua, M. and Bussière, B., 2000, October. Mechanical behaviour of cemented paste backfill. In Proc. of 53rd Canadian Geotechnical Conference, Montreal (pp. 373-380).

Belem, T., Bussière, B. and Benzaazoua, M., 2001, January. The effect of microstructural evolution on the physical properties of paste backfill. In Proc. of Tailings and Mine Waste (Vol. 1, pp. 365-374).

Belinha, J. and Dinis, L.M.J.S., 2006. Elasto - plastic analysis of plates by the element free Galerkin method. Engineering Computations.

Benzaazoua, M., Bussière, B., Demers, I., Aubertin, M., Fried, É. and Blier, A., 2008. Integrated mine tailings management by combining environmental desulphurization and

cemented paste backfill: Application to mine Doyon, Quebec, Canada. Minerals engineering, 21(4), pp.330-340.

Bloss, M.L., 1996. Evolution of cemented rock fill at Mount Isa mines limited. Mineral Resources Engineering, 5(01), pp.23-42.

Bock, S. and Prusek, S., 2015. Numerical study of pressure on dams in a backfilled mining shaft based on PFC3D code. Computers and Geotechnics, 66, pp.230-244.

Boulekbache, B., Hamrat, M., Chemrouk, M. and Amziane, S., 2010. Flowability of fibre-reinforced concrete and its effect on the mechanical properties of the material. Construction and Building Materials, 24(9), pp.1664-1671.

Brady, B.H. and Brown, E.T., 2013. Rock mechanics: for underground mining. Springer science & business media.

Cai, M. and Kaiser, P.K., 2014. In-situ rock spalling strength near excavation boundaries. Rock Mechanics and Rock Engineering, 47(2), pp.659-675.

Cai, M. and Peng, H., 2011. Advance of in-situ stress measurement in China. Journal of Rock Mechanics and Geotechnical Engineering, 3(4), pp.373-384.

Cai, M., Kaiser, P.K., Morioka, H., Minami, M., Maejima, T., Tasaka, Y. and Kurose, H., 2007. FLAC/PFC coupled numerical simulation of AE in large-scale underground excavations. International Journal of Rock Mechanics and Mining Sciences, 44(4), pp.550-564.

Camborde, F., Mariotti, C. and Donzé, F.V., 2000. Numerical study of rock and concrete behaviour by discrete element modelling. Computers and geotechnics, 27(4), pp.225-247.

Chen, X., Shi, X., Zhang, S., Chen, H., Zhou, J., Yu, Z. and Huang, P., 2020. Fiber-reinforced cemented paste backfill: the effect of fiber on strength properties and estimation of strength using nonlinear models. Materials, 13(3), p.718.

Chokshi, A., Tielens, A.G.G.M. and Hollenbach, D., 1993. Dust coagulation. The Astrophysical Journal, 407, pp.806-819.

Cui, L. and Fall, M., 2016. An evolutive elasto-plastic model for cemented paste backfill. Computers and Geotechnics, 71, pp.19-29.

Cui, L. and Fall, M., 2018. Multiphysics modeling and simulation of strength development and distribution in cemented tailings backfill structures. International Journal of Concrete Structures and Materials, 12(1), p.25.

Deeb, R., Kulasegaram, S. and Karihaloo, B.L., 2014. 3D modelling of the flow of self-compacting concrete with or without steel fibres. Part I: slump flow test. Computational Particle Mechanics, 1(4), pp.373-389.

Deng, X., Zhang, J., Klein, B., Zhou, N. and Dewit, B., 2017. Experimental characterization of the influence of solid components on the rheological and mechanical properties of cemented paste backfill. International Journal of Mineral Processing, 168, pp.116-125.

Ding, X., Zhang, L., Zhu, H. and Zhang, Q., 2014. Effect of model scale and particle size distribution on PFC3D simulation results. Rock mechanics and rock engineering, 47(6), pp.2139-2156.

Du, X., Feng, G., Qi, T., Guo, Y., Zhang, Y. and Wang, Z., 2019. Failure characteristics of large unconfined cemented gangue backfill structure in partial backfill mining. Construction and Building Materials, 194, pp.257-265.

El Mkadmi, N., Aubertin, M. and Li, L., 2014. Effect of drainage and sequential filling on the behavior of backfill in mine stopes. Canadian Geotechnical Journal, 51(1), pp.1-15.

Emad, M.Z., Mitri, H. and Kelly, C., 2014. Effect of blast-induced vibrations on fill failure in vertical block mining with delayed backfill. Canadian Geotechnical Journal, 51(9), pp.975-983.

Emad, M.Z., Mitri, H. and Kelly, C., 2018. Dynamic model validation using blast vibration monitoring in mine backfill. International Journal of Rock Mechanics and Mining Sciences, 107, pp.48-54.

Emad, M.Z., Mitri, H.S. and Henning, J.G., 2012. Effect of blast vibrations on the stability of cemented rockfill. International Journal of Mining, Reclamation and Environment, 26(3), pp.233-243.

Ercikdi, B., Yılmaz, T. and Külekci, G., 2014. Strength and ultrasonic properties of cemented paste backfill. Ultrasonics, 54(1), pp.195-204.

Falaknaz, N., 2014. Analysis of the geomechanical behavior of two adjacent backfilled stopes based on two and three dimensional numerical simulations (Doctoral dissertation, École Polytechnique de Montréal).

Falaknaz, N., Aubertin, M. and Li, L., 2015. Numerical analyses of the stress state in two neighboring stopes excavated and backfilled in sequence. International Journal of Geomechanics, 15(6), p.04015005.

Falaknaz, N., Aubertin, M. and Li, L., 2015. Numerical investigation of the geomechanical response of adjacent backfilled stopes. Canadian Geotechnical Journal, 52(10), pp.1507-1525.

Fall, M. and Nasir, O., 2010. Mechanical behaviour of the interface between cemented tailings backfill and retaining structures under shear loads. Geotechnical and Geological Engineering, 28(6), pp.779-790.

Fall, M. and Samb, S.S., 2009. Effect of high temperature on strength and microstructural properties of cemented paste backfill. Fire Safety Journal, 44(4), pp.642-651.

Fall, M., Belem, T., Samb, S. and Benzaazoua, M., 2007. Experimental characterization of the stress–strain behaviour of cemented paste backfill in compression. Journal of materials science, 42(11), pp.3914-3922.

Fall, M., Benzaazoua, M. and Ouellet, S., 2005. Experimental characterization of the influence of tailings fineness and density on the quality of cemented paste backfill. Minerals engineering, 18(1), pp.41-44.

Fan, X., Li, K., Lai, H., Xie, Y., Cao, R. and Zheng, J., 2018. Internal stress distribution and cracking around flaws and openings of rock block under uniaxial compression: a particle mechanics approach. Computers and Geotechnics, 102, pp.28-38.

Fang, K. and Fall, M., 2018. Effects of curing temperature on shear behaviour of cemented paste backfill-rock interface. International Journal of Rock Mechanics and Mining Sciences, 112, pp.184-192.

Fang, K. and Fall, M., 2019. Chemically Induced Changes in the Shear Behaviour of Interface Between Rock and Tailings Backfill Undergoing Cementation. Rock Mechanics and Rock Engineering, 52(9), pp.3047-3062.

Fang, K. and Fall, M., 2020. Shear behavior of the interface between rock and cemented backfill: effect of curing stress, drainage condition and backfilling rate. Rock Mechanics and Rock Engineering, 53(1), pp.325-336.

Fang, K. and Fall, M., 2020. Shear Behaviour of Rock–Tailings Backfill Interface: Effect of Cementation, Rock Type, and Rock Surface Roughness. Geotechnical and Geological Engineering, pp.1-18.

Fang, K., Cui, L. and Fall, M., 2020. A coupled chemo-elastic cohesive zone model for backfill-rock interface. Computers and Geotechnics, 125, p.103666.

Farnam, Y., Moosavi, M., Shekarchi, M., Babanajad, S.K. and Bagherzadeh, A., 2010. Behaviour of slurry infiltrated fibre concrete (SIFCON) under triaxial compression. Cement and concrete research, 40(11), pp.1571-1581.

Feng, X., Zhang, Q. and Ali, M., 2020. 3D modelling of the strength effect of backfill-rocks on controlling rockburst risk: a case study. Arabian Journal of Geosciences, 13(3), p.128.

Feng, Z.Y., Lo, C.M. and Lin, Q.F., 2017. The characteristics of the seismic signals induced by landslides using a coupling of discrete element and finite difference methods. Landslides, 14(2), pp.661-674.

Frydman, S. and Keissar, I., 1987. Earth pressure on retaining walls near rock faces. Journal of Geotechnical Engineering, 113(6), pp.586-599.

Ghirian, A. and Fall, M., 2013. Coupled thermo-hydro-mechanical–chemical behaviour of cemented paste backfill in column experiments. Part I: physical, hydraulic and thermal processes and characteristics. Engineering Geology, 164, pp.195-207.

Gong, C., Li, C.H. and Zhao, K., 2014. Study on fractal dimension of acoustic emission during cemented backfill micro crack evolution process. In Applied Mechanics and Materials (Vol. 556, pp. 236-240). Trans Tech Publications Ltd.

Grabinsky, M.W., 2010, May. In situ monitoring for ground truthing paste backfill designs. In Proceedings of the 13th international seminar on paste and thickened tailings (pp. 3-6). Australian Centre for Geomechanics Nedlands.

Guo, S., Fall, M. and Haruna, S., 2020. Interface Shear Behavior of Cementing Underground Mine Backfill. International Journal of Geomechanics, 20(12), p.04020230.

Guo, Z.Q., Yuan, Q., Stroeven, P. and Fraaij, A.L.A., 2010, May. Discrete element method simulating workability of fresh concrete. In AIP Conference Proceedings (Vol. 1233, No. 1, pp. 430-435). American Institute of Physics.

Hærvig, J., Kleinhans, U., Wieland, C., Spliethoff, H., Jensen, A.L., Sørensen, K. and Condra, T.J., 2017. On the adhesive JKR contact and rolling models for reduced particle stiffness discrete element simulations. Powder Technology, 319, pp.472-482.

Hasan, A., Karrech, A. and Chareyre, B., 2017. Evaluating force distributions within virtual uncemented mine backfill using discrete element method. International Journal of Geomechanics, 17(7), p.06016042.

Hasan, A., Suazo, G., Doherty, J.P. and Fourie, A.B., 2014, May. In situ measurements of cemented paste backfilling in an operating stope at Lanfranchi Mine. In Proceedings of the Eleventh International Symposium on Mining with Backfill (pp. 327-336). Australian Centre for Geomechanics.

Helinski, M., Fahey, M. and Fourie, A., 2010. Behavior of cemented paste backfill in two mine stopes: measurements and modeling. Journal of geotechnical and geoenvironmental engineering, 137(2), pp.171-182.

Helinski, M., Fahey, M. and Fourie, A., 2010. Coupled two-dimensional finite element modelling of mine backfilling with cemented tailings. Canadian Geotechnical Journal, 47(11), pp.1187-1200.

Helms, W., 1988. Preparation and transportation systems for cemented backfill. Mining Science and Technology, 7(2), pp.183-193.

Hentz, S., Daudeville, L. and Donzé, F.V., 2004. Identification and validation of a discrete element model for concrete. Journal of engineering mechanics, 130(6), pp.709-719.

Hentz, S., Donzé, F.V. and Daudeville, L., 2004. Discrete element modelling of concrete submitted to dynamic loading at high strain rates. Computers & structures, 82(29-30), pp.2509-2524.

Hoornahad, H. and Koenders, E.A., 2012. Simulation of the slump test based on the discrete element method (DEM). In Advanced Materials Research (Vol. 446, pp. 3766-3773). Trans Tech Publications Ltd.

Hou, D., Lu, Z., Li, X., Ma, H. and Li, Z., 2017. Reactive molecular dynamics and experimental study of graphene-cement composites: Structure, dynamics and reinforcement mechanisms. Carbon, 115, pp.188-208.

Huang, Y.H., Yang, S.Q. and Zhao, J., 2016. Three-dimensional numerical simulation on triaxial failure mechanical behavior of rock-like specimen containing two unparallel fissures. Rock Mechanics and Rock Engineering, 49(12), pp.4711-4729.

Jahanbakhshzadeh A, Aubertin M, Li L. Numerical simulations to assess the stress state in backfilled stopes with inclined walls. In Proceeding of the Canadian geotechnical conference. GeoQuebec, Quebec, Canada 2015.

Jahanbakhshzadeh, A., Aubertin, M. and Li, L., 2017. A new analytical solution for the stress state in inclined backfilled mine stopes. Geotechnical and Geological Engineering, 35(3), pp.1151-1167.

Jahanbakhshzadeh, A., Aubertin, M. and Li, L., 2018. Analysis of the stress distribution in inclined backfilled stopes using closed-form solutions and numerical simulations. Geotechnical and Geological Engineering, 36(2), pp.1011-1036.

Jahanbakhshzadeh, A., Aubertin, M. and Li, L., 2018. Three-dimensional stress state in inclined backfilled stopes obtained from numerical simulations and new closed-form solution. Canadian Geotechnical Journal, 55(6), pp.810-828.

Jiang, H., Fall, M., Li, Y. and Han, J., 2019. An experimental study on compressive behaviour of cemented rockfill. Construction and Building Materials, 213, pp.10-19.

Johnson, J.C., Seymour, J.B., Martin, L.A., Stepan, M., Arkoosh, A. and Emery, T., 2015, November. Strength and elastic properties of paste backfill at the Lucky Friday Mine,

Mullan, Idaho. In 49th US Rock Mechanics/Geomechanics Symposium. American Rock Mechanics Association.

Johnson, K.L., Kendall, K. and Roberts, A., 1971. Surface energy and the contact of elastic solids. Proceedings of the royal society of London. A. mathematical and physical sciences, 324(1558), pp.301-313.

Jongpradist, P., Jumlongrach, N., Youwai, S. and Chucheepsakul, S., 2010. Influence of fly ash on unconfined compressive strength of cement-admixed clay at high water content. Journal of Materials in Civil Engineering, 22(1), pp.49-58.

Jongpradist, P., Youwai, S. and Jaturapitakkul, C., 2010. Effective void ratio for assessing the mechanical properties of cement-clay admixtures at high water content. Journal of Geotechnical and Geoenvironmental Engineering, 137(6), pp.621-627.

Jongpradist, P., Youwai, S. and Jaturapitakkul, C., 2011. Effective void ratio for assessing the mechanical properties of cement-clay admixtures at high water content. Journal of geotechnical and geoenvironmental engineering, 137(6), pp.621-627.

Kaklis, K.N., Agioutantis, Z.G., Mavrigiannakis, S.P. and Nomikos, P.P., 2018, August. A multi-stage triaxial test for cemented paste backfill. In 52nd US Rock Mechanics/Geomechanics Symposium. American Rock Mechanics Association.

Kemper, W.D. and Rosenau, R.C., 1986. Aggregate stability and size distribution.

Komurlu, E., Kesimal, A. and Demir, A.D., 2016. A numerical modelling study for determining ideal size and geometry of dog bone shaped direct tensile strength test rock specimens. EUROCK 2016 Rock Mechanics and Rock Engineering: From the Past to the Future–Ulusay et al. (Eds), pp.325-330.

Koupouli, N.J., Belem, T., Rivard, P. and Effenguet, H., 2016. The direct shear tests on cemented paste backfill–rock wall and cemented paste backfill–backfill interfaces. Journal of Rock Mechanics and Geotechnical Engineering, 8(4), pp.472-479.

Koupouli, N.J.F., Belem, T. and Rivard, P., 2017, October. Shear strength between cemented paste backfill and natural rock surface replicas. In Proceedings of the First International Conference on Underground Mining Technology (pp. 375-385). Australian Centre for Geomechanics.

Krenzer, K., Mechtcherine, V. and Palzer, U., 2019. Simulating mixing processes of fresh concrete using the discrete element method (DEM) under consideration of water addition and changes in moisture distribution. Cement and Concrete Research, 115, pp.274-282.

Kumar, D., Singh, U.K. and Singh, G.S.P., 2016. Laboratory characterization of cemented rock fill for underhand cut and fill method of mining. Journal of The Institution of Engineers (India): Series D, 97(2), pp.193-203.

le Roux, K., Bawden, W.F. and Grabinsky, M.F., 2005. Field properties of cemented paste backfill at the Golden Giant mine. Mining Technology, 114(2), pp.65-80.

Leveille, P., Sepehri, M. and Apel, D.B., 2017. Rockbursting potential of kimberlite: a case study of Diavik diamond mine. Rock Mechanics and Rock Engineering, 50(12), pp.3223-3231.

Li, K., Cheng, Y. and Fan, X., 2018. Roles of model size and particle size distribution on macro-mechanical properties of Lac du Bonnet granite using flat-joint model. Computers and Geotechnics, 103, pp.43-60.

Li, L. and Aubertin, M., 2009. A three-dimensional analysis of the total and effective stresses in submerged backfilled stopes. Geotechnical and Geological Engineering, 27(4), pp.559-569.

Li, L. and Aubertin, M., 2009. Numerical investigation of the stress state in inclined backfilled stopes. International Journal of Geomechanics, 9(2), pp.52-62.

Li, L. and Aubertin, M., 2012. A modified solution to assess the required strength of exposed backfill in mine stopes. Canadian Geotechnical Journal, 49(8), pp.994-1002.

Li, L. and Aubertin, M., 2014. An improved method to assess the required strength of cemented backfill in underground stopes with an open face. International Journal of Mining Science and Technology, 24(4), pp.549-558.

Li, L. and Aubertin, M., 2015. Numerical analysis of the stress distribution in symmetrical backfilled trenches with inclined walls. Indian Geotechnical Journal, 45(3), pp.278-290.

Li, L., Aubertin, M. and Belem, T., 2005. Formulation of a three-dimensional analytical solution to evaluate stresses in backfilled vertical narrow openings. Canadian Geotechnical Journal, 42 (6), pp. 1705-1717.

Li, L., Aubertin, M. and Belem, T., 2005. Formulation of a three-dimensional analytical solution to evaluate stresses in backfilled vertical narrow openings. Canadian Geotechnical Journal, 42(6), pp.1705-1717.

Li, S. and Liu, W.K., 2002. Meshfree and particle methods and their applications. Appl. Mech. Rev., 55(1), pp.1-34.

Li, Y., Hao, J., Jin, C., Wang, Z. and Liu, J., 2021. Simulation of the flowability of fresh concrete by discrete element method. Frontiers in Materials, 7, p.603154.

Lian, C.Q., Yan, Z.G. and Beecham, S., 2011. Modelling pervious concrete under compression loading–a discrete element approach (Vol. 168, pp. 1590-1600). Trans Tech Publications.

Lin, H., Cao, P. and Zhou, Y., 2010. Numerical simulation for direct shear test of joint in rock mass. International Journal of Image, Graphics and Signal Processing, 2(1), p.39.

Lingga, B.A. and Apel, D.B., 2018. Shear properties of cemented rockfills. Journal of Rock Mechanics and Geotechnical Engineering, 10(4), pp.635-644.

Lingga, B.A., 2018. Investigation of cemented rockfill properties used at a Canadian diamond mine.

Lingga, B.A., Apel, D.B., Sepehri, M. and Pu, Y., 2019. Assessment of digital image correlation method in determining large scale cemented rockfill strains. International Journal of Mining Science and Technology, 29(5), pp.771-776.

Liu, G., Li, L., Yang, X. and Guo, L., 2017. Numerical analysis of stress distribution in backfilled stopes considering interfaces between the backfill and rock walls. International Journal of Geomechanics, 17(2), p.06016014.

Liu, G., Li, L., Yao, M., Landry, D., Malek, F., Yang, X. and Guo, L., 2017. An investigation of the uniaxial compressive strength of a cemented hydraulic backfill made of alluvial sand. Minerals, 7(1), p.4.

Liu, L., Zhu, C., Qi, C., Zhang, B. and Song, K.I., 2019. A microstructural hydration model for cemented paste backfill considering internal sulfate attacks. Construction and Building Materials, 211, pp.99-108.

Liu, Q., Liu, D., Tian, Y. and Liu, X., 2017. Numerical simulation of stress-strain behaviour of cemented paste backfill in triaxial compression. Engineering geology, 231, pp.165-175.

Liu, Y. and You, Z., 2009. Visualization and simulation of asphalt concrete with randomly generated three-dimensional models. Journal of Computing in Civil Engineering, 23(6), pp.340-347.

Liu, Y., You, Z. and Zhao, Y., 2012. Three-dimensional discrete element modeling of asphalt concrete: size effects of elements. Construction and Building Materials, 37, pp.775-782.

Ljunggren, C., Chang, Y., Janson, T. and Christiansson, R., 2003. An overview of rock stress measurement methods. International Journal of Rock Mechanics and Mining Sciences, 40(7-8), pp.975-989.

Lu, R., Ma, F., Guo, J. and Zhao, H., 2018. Monitoring and analysis of ground subsidence and backfill stress distribution in Jinchuan Mine, China. CURRENT SCIENCE, 115(10), p.1970.

Ma, Y., Sheng, Q., Zhang, G. and Cui, Z., 2019. A 3D discrete-continuum coupling approach for investigating the deformation and failure mechanism of tunnels across an active fault: a case study of xianglushan tunnel. Applied Sciences, 9(11), p.2318.

Manaras, S., 2009. Investigations of backfill-rock mass interface failure mechanisms (Doctoral dissertation).

Marston, A., 1930. Theory of external loads on closed conduits in the light of the latest experiments. In Highway research board proceedings (Vol. 9).

Martin, C.D., Kaiser, P.K. and Christiansson, R., 2003. Stress, instability and design of underground excavations. International Journal of Rock Mechanics and Mining Sciences, 40(7-8), pp.1027-1047.

Mechtcherine, V. and Shyshko, S., 2015. Simulating the behaviour of fresh concrete with the Distinct Element Method–Deriving model parameters related to the yield stress. Cement and Concrete Composites, 55, pp.81-90.

Mitchell, R.J., 1989. Stability of cemented tailings backfill. Computer and physical modelling in geotechnical engineering. Balkema, Rotterdam, pp.501-507.

Mitchell, R.J., Olsen, R.S. and Smith, J.D., 1982. Model studies on cemented tailings used in mine backfill. Canadian Geotechnical Journal, 19(1), pp.14-28.

Nasir, O. and Fall, M., 2008. Shear behaviour of cemented pastefill-rock interfaces. Engineering Geology, 101(3-4), pp.146-153.

Nasir, O. and Fall, M., 2010. Coupling binder hydration, temperature and compressive strength development of underground cemented paste backfill at early ages. Tunnelling and Underground Space Technology, 25(1), pp.9-20.

Newman, C.R., 2018. Numerical analysis of stress distributions for multiple backfilled stopes.

Nishiura, D., Sakai, H., Aikawa, A., Tsuzuki, S. and Sakaguchi, H., 2018. Novel discrete element modeling coupled with finite element method for investigating ballasted railway track dynamics. Computers and Geotechnics, 96, pp.40-54.

Oñate, E., Zárate, F., Miquel, J., Santasusana, M., Celigueta, M.A., Arrufat, F., Gandikota, R., Valiullin, K. and Ring, L., 2015. A local constitutive model for the discrete element method. Application to geomaterials and concrete. Computational particle mechanics, 2(2), pp.139-160.

Ouellet, J., Hassani, F. and Zhu, Z., 2005, January. Study of the cemented pastefill and rock mass interaction and behavior in backfilled stopes. In Alaska Rocks 2005, The 40th US Symposium on Rock Mechanics (USRMS). American Rock Mechanics Association.

Ouellet, J., Hassani, F. and Zhu, Z., 2005, June. Study of the cemented pastefill and rock mass interaction and behavior in backfilled stopes. In Alaska Rocks 2005, The 40th US Symposium on Rock Mechanics (USRMS). OnePetro.

Parry, R.H., 2004. Mohr circles, stress paths and geotechnics. CRC Press.

PETERSON, S., SZYMANSKI, J., PLANETA, S. and PARASZCZAK, J., 1996. A NEW TECHNIQUE FOR CEMENTED ROCKFILL DISTRIBUTION IN BULK MINING. Mineral Resources Engineering, 5(02), pp.129-137.

Pirapakaran, K. and Sivakugan, N., 2007. A laboratory model to study arching within a hydraulic fill stope. Geotechnical Testing Journal, 30(6), pp.496-503.

Potyondy, D.O. and Cundall, P.A., 2004. A bonded-particle model for rock. International journal of rock mechanics and mining sciences, 41(8), pp.1329-1364.

Potyondy, D.O., 2015. The bonded-particle model as a tool for rock mechanics research and application: current trends and future directions. Geosystem Engineering, 18(1), pp.1-28.

Pu, Y., Apel, D.B., Chen, J. and Wei, C., 2019. A Gaussian process machine learning model for cemented rockfill strength prediction at a diamond mine. Neural Computing and Applications, pp.1-9.

Qi, C. and Fourie, A., 2019. Cemented paste backfill for mineral tailings management: Review and future perspectives. Minerals Engineering, 144, p.106025.

Rankine, R.M. and Sivakugan, N., 2007. Geotechnical properties of cemented paste backfill from Cannington Mine, Australia. Geotechnical and Geological Engineering, 25(4), pp.383-393.

Roussel, N., 2005. Steady and transient flow behaviour of fresh cement pastes. Cement and concrete research, 35(9), pp.1656-1664.

Roussel, N., 2006. A thixotropy model for fresh fluid concretes: theory, validation and applications. Cement and concrete research, 36(10), pp.1797-1806.

Saiang, D., 2010. Stability analysis of the blast-induced damage zone by continuum and coupled continuum–discontinuum methods. Engineering Geology, 116(1-2), pp.1-11.

Sainsbury, B.A., Sainsbury, D.P., Western, J., Petrie, P.E. and Mutton, V., 2014, January. Pillar recovery adjacent to stabilised rockfill at the Ballarat Gold Project. In AusRock 2014: Proceedings of the Third Australasian Ground Control in Mining Conference 2014 (pp. 1-18). AUSIMM.

Sainsbury, D.P. and Sainsbury, B.L., 2014, January. Design and implementation of cemented rockfill at the Ballarat Gold Project. In Mine Fill 2014 Proceeding of the 11th International Symposium on Mining with Backfill.

Salazar, A., Sáez, E. and Pardo, G., 2015. Modeling the direct shear test of a coarse sand using the 3D Discrete Element Method with a rolling friction model. Computers and Geotechnics, 67, pp.83-93.

Sepehri, M., Apel, D.B. and Hall, R.A., 2017. Prediction of mining-induced surface subsidence and ground movements at a Canadian diamond mine using an elastoplastic finite element model. International Journal of Rock Mechanics and Mining Sciences, 100, pp.73-82.

Sheshpari, M., 2015. A review of underground mine backfilling methods with emphasis on cemented paste backfill. Electronic Journal of Geotechnical Engineering, 20(13), pp.5183-5208.

Standard, A.S.T.M., 2013. C192: Standard Practice for Making and Curing Concrete Test Specimens in the Laboratory. Annual Book of ASTM Standards, ASTM International, West Conshohocken, PA.

Standard, A.S.T.M., C39, 2018, "Standard Test Method for Compressive Strength of Cylindrical Concrete Specimens," ASTM International, West Conshohocken, PA, 2018, DOI: 10.1520/C0039_C0039M-18.

Suazo, G. and Villavicencio, G., 2018. Numerical simulation of the blast response of cemented paste backfilled stopes. Computers and Geotechnics, 100, pp.1-14.

Suchorzewski, J., Tejchman, J. and Nitka, M., 2018. Discrete element method simulations of fracture in concrete under uniaxial compression based on its real internal structure. International Journal of Damage Mechanics, 27(4), pp.578-607.

Sun, J., Liu, X. and Ren, T., 2019. Overburden stability of an inclined backfill stope in the context of the nonlinear elastic mechanical properties of the backfill body. Environmental Earth Sciences, 78(24), p.719.

Sun, Q., Cai, C., Zhang, S., Tian, S., Li, B., Xia, Y. and Sun, Q., 2019. Study of localized deformation in geopolymer cemented coal gangue-fly ash backfill based on the digital speckle correlation method. Construction and Building Materials, 215, pp.321-331.

Sun, W., Hou, K., Yang, Z. and Wen, Y., 2017. X-ray CT three-dimensional reconstruction and discrete element analysis of the cement paste backfill pore structure under uniaxial compression. Construction and Building Materials, 138, pp.69-78.

Swan, G., 1985. A new approach to cemented backfill design. CIM bulletin, 78(884), pp.53-58.

Talbot, A.N., Brown, H.A. and Richart, F.E., 1923. The strength of concrete: its relation to the cement aggregates and water (No. 137-138). University of Illinois.

Terzaghi, K., 1943. Earth pressure and shearing resistance of plastic clay: a symposium: liner-plate tunnels on the Chicago (IL) subway. Transactions of the American Society of Civil Engineers, 108(1), pp.970-1007.

Terzaghi, K., 1943. Liner-Plate Tunnels on the Chicago (Il) Subway. Transactions of the American Society of Civil Engineers, 108(1), pp.970-1007.

Tesarik, D.R., Seymour, J.B. and Yanske, T.R., 2009. Long-term stability of a backfilled room-and-pillar test section at the Buick Mine, Missouri, USA. International Journal of Rock Mechanics and Mining Sciences, 46(7), pp.1182-1196.

Thompson, B.D., Bawden, W.F. and Grabinsky, M.W., 2012. In situ measurements of cemented paste backfill at the Cayeli Mine. Canadian Geotechnical Journal, 49(7), pp.755-772.

Thompson, B.D., Grabinsky, M.W., Bawden, W.F. and Counter, D.B., 2009, May. In-situ measurements of cemented paste backfill in long-hole stopes. In Proceedings of the 3rd CANUS rock mechanics symposium, Toronto (pp. 197-198).

Thompson, B.D., Grabinsky, M.W., Veenstra, R. and Bawden, W.F., 2011, April. In-situ pressures in cemented paste backfill–a review of fieldwork from three mines. In Proceedings of the 14th International Seminar on Paste and Thickened Tailings, Perth, Australia (pp. 5-7).

Ting, C., 2011. Arching in granular materials with particular reference to inclined mine stopes (Doctoral dissertation, James Cook University).

Ting, C.H., Shukla, S.K. and Sivakugan, N., 2011. Arching in soils applied to inclined mine stopes. International Journal of Geomechanics, 11(1), pp.29-35.

Ting, C.H., Sivakugan, N. and Shukla, S.K., 2012. Laboratory simulation of the stresses within inclined stopes. Geotechnical Testing Journal, 35(2), pp.280-294.

Tran, V.T., Donzé, F.V. and Marin, P., 2011. A discrete element model of concrete under high triaxial loading. Cement and Concrete Composites, 33(9), pp.936-948.

Turichshev, A., Cotesta, L., Brummer, R. and Beauvais, M., 2017. Estimation of fill strength requirements using bonded particle modelling for mining under cemented rockfill.

Vennes, I., 2014. Determination of Cemented Rockfill Strength with Large Scale UCS Tests under In-Situ Conditions (Doctoral dissertation, McGill University Libraries).

Wang, C., Deng, A. and Taheri, A., 2018. Three-dimensional discrete element modeling of direct shear test for granular rubber–sand. Computers and Geotechnics, 97, pp.204-216.

Wang, J., Dove, J.E. and Gutierrez, M.S., 2007. Discrete-continuum analysis of shear banding in the direct shear test. Géotechnique, 57(6), pp.513-526.

Wang, X.M., Bin, Z.H.A.O., Zhang, C.S. and Zhang, Q.L., 2009. Paste-like self-flowing transportation backfilling technology based on coal gangue. Mining Science and Technology (China), 19(2), pp.137-143.

Wang, Y.M., Huang, M.Q., Wu, A.X., Yao, G.H. and Hu, K.J., 2013. Rock backfill and hazard control of abandoned stopes: A case study. In Applied Mechanics and Materials (Vol. 368, pp. 1726-1731). Trans Tech Publications Ltd.

Wang, Z., Lin, F. and Gu, X., 2008. Numerical simulation of failure process of concrete under compression based on mesoscopic discrete element model. Tsinghua Science and Technology, 13(S1), pp.19-25.

Wei, C., Apel, D. and Katsaga, T., 2022. Coupled Finite-Difference and Discrete-Element Method for Modelling The direct shear tests on Combined Rock-Cemented Rockfill Specimens. Mining, Metallurgy & Exploration, 39(1), pp.89-109.

Wu, H., 2015. Modelling of non-linear shear displacement behaviour of soil–geotextile interface. International Journal of Geosynthetics and Ground Engineering, 1(2), pp.1-10.

Wu, J., Feng, M., Mao, X., Xu, J., Zhang, W., Ni, X. and Han, G., 2018. Particle size distribution of aggregate effects on mechanical and structural properties of cemented rockfill: experiments and modeling. Construction and Building Materials, 193, pp.295-311.

Wu, L. and Qu, F.Z., 2009. Discrete element simulation of mechanical characteristic of conditioned sands in earth pressure balance shield tunneling. Journal of Central South University of Technology, 16(6), pp.1028-1033.

Wu, S. and Xu, X., 2016. A study of three intrinsic problems of the classic discrete element method using flat-joint model. Rock Mechanics and Rock Engineering, 49(5), pp.1813-1830.

Xia, R., Li, B., Wang, X., Li, T. and Yang, Z., 2019. Measurement and calibration of the discrete element parameters of wet bulk coal. Measurement, 142, pp.84-95.

Yang, L., Qiu, J., Jiang, H., Hu, S., Li, H. and Li, S., 2017. Use of cemented super-fine unclassified tailings backfill for control of subsidence. Minerals, 7(11), p.216.

Yang, L., Xu, W., Yilmaz, E., Wang, Q. and Qiu, J., 2020. A combined experimental and numerical study on the triaxial and dynamic compression behavior of cemented tailings backfill. Engineering Structures, 219, p.110957.

Yang, Z., Zhai, S., Gao, Q. and Li, M., 2015. Stability analysis of large-scale stope using stage subsequent filling mining method in Sijiaying iron mine. Journal of Rock Mechanics and Geotechnical Engineering, 7(1), pp.87-94.

Yao, Y., Cui, Z. and Wu, R., 2012. Development and challenges on mining backfill technology. Journal of Materials Science Research, 1(4), p.73.

Yilmaz, E. and Fall, M. eds., 2017. Paste tailings management (pp. 1-303). Cham, Switzerland: Springer International Publishing.

Yilmaz, E., Belem, T. and Benzaazoua, M., 2015. Specimen size effect on strength behavior of cemented paste backfills subjected to different placement conditions. Engineering Geology, 185, pp.52-62.

Yin, W., Li, M., Gao, R., Zhong, S. and Quan, K., 2017. Stability analysis of surrounding rock and pillar design in roadway backfill mining method. Mining Technology, 126(3), pp.177-184.

You, Z., Adhikari, S. and Kutay, M.E., 2009. Dynamic modulus simulation of the asphalt concrete using the X-ray computed tomography images. Materials and Structures, 42(5), pp.617-630.

Zelelew, H.M. and Papagiannakis, A.T., 2010. Micromechanical modeling of asphalt concrete uniaxial creep using the discrete element method. Road Materials and Pavement Design, 11(3), pp.613-632.

Zhang, H. and Li, C.C., 2019. Effects of Confining Stress on the Post-Peak Behaviour and Fracture Angle of Fauske Marble and Iddefjord Granite. Rock Mechanics and Rock Engineering, 52(5), pp.1377-1385.

Zhang, J., Deng, H., Taheri, A., Deng, J. and Ke, B., 2018. Effects of superplasticizer on the hydration, consistency, and strength development of cemented paste backfill. Minerals, 8(9), p.381.

Zhang, J.W., Wang, H.L. and Chen, S.J., 2018. Bearing capacity of backfill body and roof stability during strip coal pillar extracted with paste backfill. Geotechnical and Geological Engineering, 36(1), pp.235-245.

Zhang, J.X., Huang, P., Zhang, Q., Li, M. and Chen, Z.W., 2017. Stability and control of room mining coal pillars—taking room mining coal pillars of solid backfill recovery as an example. Journal of Central South University, 24(5), pp.1121-1132.

Zhang, L. and Thornton, C., 2007. A numerical examination of the direct shear test. Geotechnique, 57(4), pp.343-354.

Zhang, Q.L. and Wang, X.M., 2007. Performance of cemented coal gangue backfill. Journal of Central South University of Technology, 14(2), pp.216-219.

Zhang, X., Zhang, Z., Li, Z., Li, Y. and Sun, T., 2020. Filling capacity analysis of self-compacting concrete in rock-filled concrete based on DEM. Construction and Building Materials, 233, p.117321.

Zhang, X.P. and Wong, L.N.Y., 2012. Cracking processes in rock-like material containing a single flaw under uniaxial compression: a numerical study based on parallel bonded-particle model approach. Rock Mechanics and Rock Engineering, 45(5), pp.711-737.

Zhao, B., Liu, Y., Huang, T. and Wang, X., 2019. Experimental Study on Strength and Deformation Characteristics of Rock–Concrete Composite Specimens Under Compressive Condition. Geotechnical and Geological Engineering, 37(4), pp.2693-2706.

Zhu, W., Yu, S., Xuan, D., Shan, Z. and Xu, J., 2018. Experimental study on excavating strip coal pillars using caving zone backfill technology. Arabian Journal of Geosciences, 11(18), p.554.